

# **Turbulence studies in TCV using the Correlation ECE diagnostic**

**THÈSE N° 9016 (2018)**

PRÉSENTÉE LE 2 NOVEMBRE 2018  
À LA FACULTÉ DES SCIENCES DE BASE  
SPC - PHYSIQUE DU TOKAMAK TCV  
PROGRAMME DOCTORAL EN PHYSIQUE

**ÉCOLE POLYTECHNIQUE FÉDÉRALE DE LAUSANNE**

POUR L'OBTENTION DU GRADE DE DOCTEUR ÈS SCIENCES

PAR

**Matteo FONTANA**

acceptée sur proposition du jury:

Prof. F. Courbin, président du jury  
Prof. A. Fasoli, Dr L. Porte, directeurs de thèse  
Prof. A. White, rapporteuse  
Dr T. Happel, rapporteur  
Dr S. Brunner, rapporteur



ÉCOLE POLYTECHNIQUE  
FÉDÉRALE DE LAUSANNE

Suisse  
2018



... there was no such thing as absolute control, not in a fully functioning universe.

There was just a variable amount of lack of control

— Terry Pratchett

Alla mia famiglia





# Abstract

In this thesis work, the flexibility of the tokamak à configuration variable (TCV) is exploited to study the influence of various plasma parameters on turbulent fluctuations. The correlation electron cyclotron emission (CECE) diagnostic is used to measure low amplitude, large bandwidth radiative temperature fluctuations, associated with the anomalous transport terms that constitute the largest contribution to heat and particle loss in tokamak plasmas. In a series of L-mode limited plasmas, fluctuations are characterized over a large range of plasma parameters, obtained varying collisionality, electron-ion temperature ratio and plasma triangularity. The influence of negative triangularity on confinement and fluctuations over this large parameter space is also investigated.

Temperature fluctuations profiles have been measured in low density, ohmic, positive and negative triangularity discharges, with matched current and density profiles. Strong suppression of fluctuations is observed in negative triangularity discharges from the plasma edge to the plasma mid radius. This is despite triangularity quickly decreasing when moving away from the edge. The existence of a region of low stiffness at the plasma edge is postulated to be responsible for the unexpected radial penetration of the effects of triangularity. Negative triangularity is thus confirmed having beneficial effects on confinement and reducing fluctuations amplitude in regimes with high  $T_e/T_i$ .

For the first time on TCV, the neutral beam injector (NBI) has been used on positive and negative triangularity discharges in order to study the effect of negative triangularity on plasmas where  $T_e/T_i \sim 1$ . This condition is of particular interest since future reactor-like tokamaks are expected to work with thermalized electrons and ions. A pair of discharges with positive and negative triangularity has been realized, where matched temperature profiles are attained with  $\sim 385$  kW and  $\sim 145$  kW of NBI power respectively for the two shapes. This is evidence of negative triangularity improving plasma confinement also in conditions of low  $T_e/T_i$ . In these discharges, CECE measurements find reduced fluctuation amplitudes in the negative triangularity discharges.

Linear, flux tube, gyrokinetic simulations show that, in the same plasmas, the dominant turbulent regime is a mix of ion temperature gradient (ITG) instabilities and trapped electron modes (TEM). This is different with respect to all previous works in TCV, in which no ion heating had been available and only pure TEM regimes were observed. The results of the linear simulations indicate that, also in this mixed turbulence regime, negative triangularity has a stabilizing effect on instabilities. Stabilization is more visible for radial positions closer to the plasma edge, where the magnitude of triangularity is higher.

---

A database of fluctuations measurements has been constructed from a series of discharges with positive and negative triangularity covering a large range of plasma conditions, particularly focusing on the effects of different combinations of collisionality and the  $T_e/T_i$  ratio. Collisionality is found to be the main parameter to control the relative suppression of fluctuations in negative with respect to positive triangularity plasmas. No direct effect of the  $T_e/T_i$  ratio on the fluctuation amplitudes is observed in the explored parameter range.

Measurements taken in positive and negative triangularity plasmas, with comparable conditions and matched normalized temperature scale lengths ( $R/L_{Te}$ ) still show reduced fluctuation levels for the negative  $\delta$  cases. Since the normalized scale lengths are the main drive for the turbulent instabilities, this difference suggests that negative triangularity could increase the gradient threshold for the onset of fluctuations or reduce the sensitivity of fluctuations to increasing gradients once the threshold has been exceeded.

**Key words:** plasma, fusion, magnetic confinement, tokamak, microwaves, electron cyclotron emission, turbulence, plasma shaping, collisionality, stiffness, radiative temperature, negative triangularity.

# Sinossi

In questo lavoro, la flessibilità del *tokamak à configuration variable* (TCV) è stata sfruttata per studiare l'influenza di alcuni parametri del plasma sulle fluttuazioni turbolente. Il *correlation electron cyclotron emission* (CECE) è stato utilizzato per misurare fluttuazioni della temperatura radiativa di bassa ampiezza e larga banda, associate ai termini di trasporto anomalo che costituiscono il contributo principale alle perdite di particelle e calore nei tokamak. Le fluttuazioni sono state caratterizzate in plasmi limited in L-mode che coprono un grande intervallo di parametri di plasma, ottenuti variando la collisionalità, il rapporto tra le temperature ioniche ed elettroniche e la triangolarità. All'interno dello stesso spazio di parametri, è stata inoltre indagata l'influenza della triangolarità negativa sul confinamento e sulle fluttuazioni. I profili di fluttuazioni di temperatura sono stati misurati in scariche ohmiche a bassa densità con triangolarità positiva e negativa in cui la corrente di plasma e i profili di densità sono stati mantenuti invariati. Si è osservata una forte soppressione delle fluttuazioni per le scariche con triangolarità negativa a partire dal bordo del plasma fino a metà del raggio. Questo nonostante la triangolarità cali rapidamente nel muoversi dal bordo verso il centro del plasma. Si ritiene che ad essere responsabile di questa inattesa penetrazione radiale degli effetti della triangolarità sia l'esistenza di una zona del plasma cosiddetta *non-stiff*. Queste misure confermano che la triangolarità negativa ha un effetto benefico sul confinamento e riduce l'ampiezza delle fluttuazioni in plasmi con alto  $T_e/T_i$ .

Per la prima volta in TCV, il *neutral beam injector* (NBI) è stato utilizzato per studiare gli effetti della triangolarità negativa in plasmi a triangolarità positiva e negativa in cui  $T_e/T_i \sim 1$ . Questa è una condizione particolarmente interessante per il fatto che i futuri tokamak *reactor-like* opereranno in condizioni in cui ioni ed elettroni saranno termalizzati. Due scariche con triangolarità positiva e negativa sono state prodotte, in cui si sono ottenuti profili di temperatura confrontabili utilizzando, rispettivamente nelle due forme,  $\sim 385$  kW e  $\sim 145$  kW di riscaldamento NBI. Questo dimostra che la triangolarità negativa migliora il confinamento anche per plasmi con basso  $T_e/T_i$ . In queste scariche le misure effettuate col CECE mostrano una ridotta ampiezza per le fluttuazioni nei plasmi a triangolarità negativa.

Simulazioni girocinetiche lineari, *flux tube*, mostrano che in questi plasmi il regime di turbolenza dominante è un misto di instabilità *ion temperature gradient* (ITG) e *trapped electron modes* (TEM). In tutti i precedenti lavori compiuti su TCV quando ancora il riscaldamento ionico non era disponibile, invece, solo regimi puramente TEM erano stati osservati. I risultati delle simulazioni lineari indicano che, anche in questo regime di turbolenza misto, la triangolarità ha un effetto stabilizzante sulle instabilità. La stabilizzazione è tanto più forte quanto

---

più le simulazioni sono compiute su posizioni radiali prossime al bordo del plasma, dove il valore assoluto della triangolarità è massimo.

A partire da una serie di scariche che copre un'ampia varietà di plasmi con condizioni diverse sia in triangolarità negativa che positiva, è stato costruito un database di misure di fluttuazioni, concentrandosi in particolare sugli effetti delle differenti combinazioni di collisionalità e  $T_e/T_i$ . Si è osservato che la collisionalità è il fattore più importante nel determinare la riduzione dell'ampiezza delle fluttuazioni in plasmi a triangolarità negativa rispetto a quelli con triangolarità positiva. All'interno dello spazio di parametri esplorato in questi esperimenti, non si è osservato alcun effetto diretto del rapporto  $T_e/T_i$  sull'ampiezza delle fluttuazioni.

Anche confrontando plasmi a triangolarità positiva e negativa con condizioni confrontabili e pari scale caratteristiche dei profili ( $R/L_{Te}$ ), è stato osservato che l'ampiezza delle fluttuazioni in triangolarità negativa è sempre minore che in triangolarità positiva. Dato che le scale caratteristiche sono ritenute essere il termine principale che genera la turbolenza, questa differenza suggerisce che la triangolarità negativa possa aumentare la soglia necessaria per i gradienti prima che le fluttuazioni turbolente comincino a svilupparsi. In alternativa la triangolarità negativa potrebbe ridurre la sensibilità delle fluttuazioni al crescere dei gradienti.

**Parole chiave:** plasma, fusione, confinamento magnetico, tokamak, microonde, electron cyclotron emission, turbolenza, plasma shaping, collisionalità, stiffness, temperatura radiativa, triangolarità negativa.

# Contents

<b>Abstract (English/Français/Deutsch)</b>	<b>v</b>
<b>List of figures</b>	<b>xi</b>
<b>List of tables</b>	<b>xxi</b>
<b>1 Introduction</b>	<b>1</b>
1.1 Nuclear fusion . . . . .	1
1.2 The tokamak . . . . .	4
1.3 Motivation of the thesis . . . . .	9
1.4 Thesis outline . . . . .	11
<b>2 Tokamak à configuration variable (TCV) and experimental apparatus</b>	<b>13</b>
2.1 Auxiliary heating systems . . . . .	13
2.1.1 Electron Cyclotron Resonance Heating system . . . . .	13
2.1.2 NBI . . . . .	17
2.2 TCV diagnostics . . . . .	17
2.2.1 Magnetic probes . . . . .	17
2.2.2 Far infrared interferometer . . . . .	18
2.2.3 Thomson scattering . . . . .	19
2.2.4 Electron cyclotron emission (ECE) and Correlation ECE diagnostics . . .	19
2.2.5 Charge Exchange Recombination Spectroscopy . . . . .	20
<b>3 Electron Cyclotron Emission (ECE) and Correlation ECE diagnostics principles and their application in TCV</b>	<b>23</b>
3.1 Introduction: diagnostic applications of ECE . . . . .	23
3.2 Heterodyne radiometry . . . . .	26
3.3 Correlation ECE technique for the study of small $T_e$ fluctuations . . . . .	27
3.3.1 Wavenumber sensitivity . . . . .	29
3.3.2 Effects of density fluctuations on CECE fluctuations measurements . . .	30
3.4 ECE diagnostics in TCV . . . . .	31
3.5 Correlation ECE in TCV . . . . .	33
3.5.1 Lines of sight and radiometers . . . . .	34
3.5.2 Intermediate frequency section . . . . .	36

## Contents

---

3.6	CECE signal processing . . . . .	39
3.6.1	Signal normalization . . . . .	39
3.6.2	Calculation of the emission volumes and signals calibration . . . . .	40
3.6.3	Correlation analysis . . . . .	41
3.7	Summary . . . . .	44
<b>4</b>	<b>Triangularity effects on fluctuations in ohmic tokamak plasmas</b>	<b>45</b>
4.1	Transport in negative triangularity plasmas in TCV . . . . .	45
4.1.1	Numerical simulations . . . . .	46
4.1.2	Profile stiffness . . . . .	49
4.1.3	Fluctuations measurements in previous experiments . . . . .	52
4.2	Flucuations measurements using an upper lateral line of sight . . . . .	54
4.2.1	Description of the experimental conditions . . . . .	54
4.2.2	Temperature fluctuations profiles . . . . .	56
4.3	Fluctuations measurements using a horizontal line of sight . . . . .	63
4.3.1	Linear GENE simulations . . . . .	66
4.4	Conclusions . . . . .	69
<b>5</b>	<b>Matching discharges with <math>T_e/T_i &lt; 1</math></b>	<b>73</b>
5.1	Introduction . . . . .	73
5.2	Development of matching NBI heated discharges with positive and negative $\delta$	74
5.2.1	Measurements of temperature fluctuations . . . . .	83
5.2.2	Linear GENE simulations . . . . .	85
5.3	Conclusions . . . . .	90
<b>6</b>	<b>Effects of collisionality and <math>T_e/T_i</math> on fluctuations in positive and negative <math>\delta</math> plasmas</b>	<b>93</b>
6.1	Introduction . . . . .	93
6.2	Experimental method . . . . .	94
6.3	Results . . . . .	95
6.4	Conclusions . . . . .	103
<b>7</b>	<b>Conclusions and outlook</b>	<b>105</b>
<b>A</b>	<b>Calculation of the emission volumes position</b>	<b>109</b>
<b>B</b>	<b>Commissioning of the radiometers</b>	<b>113</b>
B.1	LFS ECE transmission lines . . . . .	113
B.2	CECE RF stage . . . . .	113
B.3	CECE IF stage . . . . .	115
B.3.1	Routine testing the IF stage of the Correlation ECE . . . . .	115
<b>C</b>	<b>Estimation of the propagation velocity of fluctuations using CECE measurements</b>	<b>119</b>
C.1	Principles . . . . .	119
C.2	Estimation of $\Delta s$ . . . . .	119

C.3	Propagation velocity estimate . . . . .	121
C.4	Comparison with CXRS measurements . . . . .	122
<b>D</b>	<b>Simple modelling of fluctuations and application of a synthetic diagnostic</b>	<b>127</b>
D.1	Simple model for fluctuations . . . . .	127
D.2	CECE synthetic diagnostic . . . . .	128
D.3	Applications of the fluctuations model and the synthetic diagnostic . . . . .	129
D.3.1	Emission volume size and wavenumber sensitivity . . . . .	129
D.3.2	Wavenumber sensitivity of different lines of sight . . . . .	131
D.3.3	Effects of positive and negative $\delta$ equilibria on wavenumber sensitivity .	133
D.4	Conclusions . . . . .	134
	<b>Bibliography</b>	<b>144</b>
	<b>Curriculum Vitae</b>	<b>145</b>
	<b>Acknowledgements</b>	<b>147</b>





# List of Figures

1.1	Average binding energy per nucleon for different mass numbers. Net energy can be produced by splitting heavier atoms into lighter fragments (fission) or combining very light nuclei into bigger atoms (fusion). Public Domain, <a href="https://commons.wikimedia.org/w/index.php?curid=1540082">https://commons.wikimedia.org/w/index.php?curid=1540082</a> . . . . .	2
1.2	Reactivity for three different fusion reactions as functions of the ions temperature. Licensed under Creative Commons 2.5. . . . .	2
1.3	Cross section of a torus with representation of cylindrical ( $R, \Phi, Z$ ) and toroidal ( $r, \theta, \Phi$ ) coordinates . . . . .	5
1.4	Representation of the main coils in a tokamak and the fields they produce. Poloidal coils around the vessel produce the toroidal field (in blue). Current is ramped into the central ohmic coils to induce the plasma current and the poloidal field (all in green). Finally, horizontal poloidal field coils are used to improve stability and tailor the plasma shape and position. Source: EUROfusion website . . . . .	6
1.5	Examples of shapes obtained varying $\kappa$ and $\delta$ in equations 1.12 for $a = 0.25$ and $R_0 = 0$ . . . . .	8
2.1	Sketch of TCV with some of its main components highlighted. A) Central solenoid, acting as a transformer primary circuit in the induction of the plasma current. B) Toroidal field coils. C) Vacuum vessel. D) Shaping coils, also called poloidal field coils. E) Ports for access into TCV. F) In-vessel poloidal field coils. . . . .	14
2.2	Drawing of the different positions available to ECRH launchers in TCV. . . . .	14
2.3	Schematic of the launchers directing ECRH power into TCV. The injected beam can be rotated over $\theta$ and $\phi$ . . . . .	16
2.4	Drawing of the NBI system in TCV with the designed shape of the produced beam. . . . .	17
2.5	Layout of the magnetic probes of TCV in the poloidal and toroidal arrays [1] . . . . .	18
2.6	a) In green the optical path of the Thomson scattering diagnostic laser into a TCV plasma. In red the fraction of the beam path covered by the lines of sight of the diagnostic, shown in blue. b) Lines of the FIR diagnostic in TCV measuring the integrated electron density. In red the central line used for real time density control of the plasma discharges [2]. . . . .	20
2.7	Viewlines of three of the CXRS systems of TCV [2]. . . . .	21

## List of Figures

---

3.1	Intensity of the magnetic field over the cross-section of the vessel of TCV. Particles in plasma regions of constant B will emit EC radiation at the same frequency $\propto 1/R$ where R is the major radius. . . . .	24
3.2	Simple representation of the optical depth seen by the collection optics for emission along a ray identified by the curvilinear coordinate s. . . . .	25
3.3	Schematics of the main components of a heterodyne radiometer for ECE applications. . . . .	27
3.4	Schematics of the RF section of the standard LFS ECE radiometer on TCV. . . .	31
3.5	Schematics of one of the two IF sections of the standard LFS ECE of TCV. Each of these twelve channel sets is connected to a different branch characterized by a different LO frequency. . . . .	32
3.6	Picture of one of the two IF sections available for the LFS ECE diagnostic on TCV.	32
3.7	Summary of the CECE system in TCV from the vessel to the RF sections of the radiometers. . . . .	33
3.8	Picture of one of the two RF sections available for the CECE on TCV. Radiation enters the high pass filter after the notch filters and, after mixing and amplification, is transferred to the IF section. . . . .	34
3.9	Picture of the entrance of the horizontal $z = 0$ and $z = 21$ cm LFS lines of sight for the ECE systems. The $z = 0$ one looks through a polyethylene lens directly into the plasma. The one above it looks into a gaussian horn connected to a piece of waveguide rising up to $z = 21$ cm. . . . .	35
3.10	Antenna pattern calculated for the $z = 0$ LFS horizontal line. The solid line represents the distance from the axis where $\sim 95\%$ of the beam power is contained ( $2\sigma$ ), the two dashed lines contain respectively 3 and 4 $\sigma$ . The beam propagation has been calculated using gaussian beam theory starting from the aperture of the waveguide. . . . .	35
3.11	(a) Schematics of the whole transmission line for the steerable receiver including the antenna, the polarizers, and the telescope coupling the power gathered by the steerable line of sight to the CECE and the DBS reflectometer. (b) Details of the telescope. . . . .	37
3.12	Schematics of the IF section of the CECE diagnostic on TCV. . . . .	37
3.13	Picture of CECE IF stage where the six YIG filters are visible. After rectification in the Schottky diodes, the signals are sent to the video stage. . . . .	38
3.14	Emission volumes of six channels for a discharge in which the horizontal $z=0$ line of sight has been used calculated with TORAY, and the corresponding emission peaks over the flux coordinate $\rho$ . . . . .	40
3.15	Example of CPSD for two CECE signals acquired through the upper lateral line of sight and whose channels' center frequencies were separated by 500 MHz. The three curves are the CPSD of the flat top phase, that of the baseline ( $CPSD_{ft}$ and $CPSD_{bl}$ respectively), and $CPSD_{ft}$ with the average of the [300 350] kHz region subtracted from it to define the noise floor at 0 dB. . . . .	42

3.16	Coherence and phase of two CECE signals coming from different channels. Together they are used to select the frequency range over which the fluctuations amplitude will be evaluated, represented in this case by the vertical black lines.	43
4.1	Radial profiles in two plasmas with positive and negative triangularity in which comparable $T_e$ (a) and $n_e$ (b) have been achieved with only half of the ECH power in the latter case. c) $T_i$ d) $q$ e) $Q_e$ f) $\chi_e$ . From [3]	46
4.2	Electron heat diffusivity $\chi_e$ as a function of the effective collisionality $\nu_{eff}$ measured at $\rho_{vol} = 0.55$ for the discharges in [3]. The difference between positive and negative $\delta$ plasmas is largest at low $\nu_{eff}$ and becomes almost indistinguishable for high collisionality. From [3].	47
4.3	Ratio between $\chi_e$ for positive and negative $\delta$ plasmas as calculated from the experiments (blue rectangle) and from non-linear GS2 simulations. Agreement is found within errorbars for $\rho = 0.7$ . From [4]	48
4.4	Logarithmic plot of electron pressure profiles for a series of ohmic TCV discharges with varying plasma current. The experimental Thomson measurements have been fit using a constant gradient for the non-stiff region ( $\rho_{vol} > 0.8$ ), a constant logarithmic gradient for the stiff region and constant pressure inside the sawteeth inversion radius. From [5]	49
4.5	Sketches of possible interpretations of confinement improvement in negative $\delta$ plasmas consistent with the observations in [5]. Improvement in the plasma non stiff region could be due to a change in stiffness (a), critical gradient (b) or a combination of both. From [6].	50
4.6	(a) Heat fluxes at three different radial positions resulting from non linear, flux tube GENE simulations in which gradients have been varied to study the influence of negative triangularity on transport. Full markers represent the experimental gradient values. For the sake of clarity, the fluxes for each radial positions are plotted on different scales in (b) $\rho_{tor} = 0.5$ , (c) $\rho_{tor} = 0.7$ and (d) $\rho_{tor} = 0.9$ . Dashed black lines represent the experimental heat fluxes. From [6].	51
4.7	Relative density fluctuations profile in positive and negative triangularity plasmas with matched heating (a). The same points have also been plotted as a function of the local normalized inverse density (b) and temperature (c) scale lengths to highlight the different threshold behaviour for different shapings. From [7].	53
4.8	Relative density fluctuations in ohmic and EC heated plasmas during a scan from positive to negative $\delta$ as a function of triangularity (a) and $\nu_{eff}$ (b). From [7].	54

## List of Figures

---

4.9	Profiles of the model discharges for the two most extreme shapes ( $\delta = 0.5$ and $\delta = -0.4$ ). a) Electron density. b) Electron temperature. c) Ion temperature. d) Electron/ion temperature ratio. e) Normalized density scale-length. f) Normalized electron temperature scale length. g) Normalized ion temperature scale length. h) Inverse effective collisionality. The electron profiles are calculated from Thomson scattering measurements while ion temperature and $Z_{eff}$ from charge exchange recombination spectroscopy measurements. . . . .	56
4.10	Electron temperature and density profiles of the model discharges ( $z_{axis} = 23$ cm) and corresponding plasmas repeated at $z = 0$ to have CXRS measurements across the whole radial profile. . . . .	57
4.11	Electron temperature ratio between the $\delta = -0.4$ and $\delta = +0.5$ discharges. . . . .	57
4.12	Profiles obtained for the repetitions of the target $\delta = +0.5$ discharge. Radial profiles of electron temperature (a) electron density (b) and inverse effective collisionality (c) . . . . .	58
4.13	Plasma cross sections and position of the CECE emission volumes for the measurements taken with $\delta = 0.5$ (a) and $\delta = -0.4$ (b). . . . .	59
4.14	Cross Power Spectral Density obtained from correlation analysis over 100 ms of CECE signals coming from couples of neighbouring channels ( $\Delta f = 0.5$ GHz) at $\rho_{vol} = 0.8$ and $\rho_{vol} = 0.4$ , in positive and negative triangularity. The noise level is at 0 dB for all the curves. . . . .	60
4.15	Phase difference between the same couples of neighbouring channels shown in figure 3.15. A negative phase corresponds to fluctuations moving from channels closer to the edge towards those closer to the plasma core. . . . .	60
4.16	a) Radial profiles of relative radiative temperature fluctuations amplitude for different triangularity values. The fluctuations amplitude is reduced changing shape from positive to negative triangularity and the effects extends up to $\rho_{vol} = 0.5$ . A similar effect can be observed also in the absolute fluctuations profiles (b). The same data are plotted against the normalized inverse density (c, e) and temperature (d, f) scale lengths. Notice that these data points combine measurements taken over a wide fraction of the radial profile. . . . .	62
4.17	Correlation coefficient for couples of channels at $\rho_{vol} \sim 0.8$ in positive and negative $\delta$ plasmas. The former show a much higher correlation level, while both of them indicate that fluctuations are observed first in the outermost channels (negative $\tau$ for the maximum correlation), with a slightly different delay. . . . .	63
4.18	Correlation coefficient as a function of $\tau$ for increasingly separated couples of channels inside discharges with (a) positive $\delta$ and (b) negative $\delta$ . Take notice of the different color scales in the two pictures. . . . .	64
4.19	Plasma geometries and emission volumes for the $z_{axis}=0$ discharges matching the $z_{axis} = 25$ cm ones. In this discharge the emission volumes were distributed in three pairs at $\Delta f = 500 MHz$ separated by 3 GHz . . . . .	65

4.20	Cross power spectral density of neighbouring channels around $\rho_{vol}=0.65$ in negative and positive triangularity plasmas measured using the horizontal line of sight (a). Fluctuations are strongly reduced in both amplitude and frequency range with respect to those observed with upper lateral line of sight (figure 3.15). Nonetheless, higher fluctuations amplitude is still observed in positive triangularity discharges with respect to negative triangularity ones. . . . .	65
4.21	Examples of the changes in the emission volumes extension when changing the aperture angle of the horizontal line of sight from $2^\circ$ (a) to $5^\circ$ (b). The emission volumes are represented over the norm of the fluctuating structure obtained superimposing modes with $m$ from 1 to 32. (c) Sensitivity of the diagnostic to varying $m$ modes for increasing line of sight aperture angle. The sensitivity to higher order modes is reduced while the antenna pattern is widened. . . . .	66
4.22	Norm of the fluctuating field ( $m$ from 1 to 32) and emission volumes for the simulation of the the upper lateral (a) and horizontal (b) lines of sight looking at $\rho_\psi = 0.7$ . (c) Estimated sensitivity to the different modes for the two lines. . . .	67
4.23	Normalized linear growth rate ( $\gamma * R/c_s$ ) and frequency ( $\omega * R/c_s$ ) of the most unstable mode for each wavenumber in three radial positions: $\rho_{tor} = 0.6$ (a), $\rho_{tor} = 0.7$ (b), $\rho_{tor} = 0.8$ (c). In the $\omega$ plots, full markers correspond to modes that propagate in the electron diamagnetic direction (TEM or ETG). . . . .	68
4.24	Linear growth rate ( $\gamma$ ) and frequency ( $\omega$ ), in real units, of the most unstable mode for each wavenumber in three radial positions: $\rho_{tor} = 0.6$ (a), $\rho_{tor} = 0.7$ (b), $\rho_{tor} = 0.8$ (c). In the $\omega$ plots, full markers correspond to modes that propagate in the electron diamagnetic direction (TEM or ETG). Horizontal lines in the $\gamma$ plots represent the estimated $E \times B$ shearing rate, with its uncertainty shown as the dashed line. . . . .	70
5.1	Plasma geometry and CECE emission volumes for the positive and negative $\delta$ discharges (a and b) and a zoomed detail of the CECE channels (c and d). . . .	75
5.2	Safety factor ( $q$ ) profiles for the positive and negative triangularity discharges calculated with ASTRA (c). . . . .	75
5.3	Time traces for plasma current $I_p$ , line averaged density $n_{av}$ , core temperature $T_{e0}$ and density $n_{e0}$ , NBI power absorbed by the bulk plasma $P_{NBI \rightarrow i,e}$ , $\beta_{tor}$ and energy confinement time $\tau_E$ for the reference discharge with $\delta < 0$ . Highlighted is the time interval over which correlation analysis has been computed. . . . .	76
5.4	Time traces for plasma current $I_p$ , line averaged density $n_{av}$ , core temperature $T_{e0}$ and density $n_{e0}$ , NBI power absorbed by the bulk plasma $P_{NBI \rightarrow i,e}$ , $\beta_{tor}$ and energy confinement time $\tau_E$ for the discharges with $\delta > 0$ . Highlighted are the time intervals over which correlation analysis has been computed, corresponding to the two different NBI power levels. . . . .	77

## List of Figures

---

5.5	Time traces of the ohmic power $P_{ohm}$ and breakdown of the distribution of NBI power in the negative triangularity discharge ( $\delta=-0.4$ ). Starting from the nominal $P_{NB}$ , the losses in the beam duct reduce it to $P_{NB,inj}$ ; after shine through and first orbit losses $P_{NB,conf}$ remains and, taking into account charge exchange losses, $P_{NB \rightarrow i,e}$ is the actual power transferred to ions and electrons. Highlighted is the time interval over which correlation analysis has been computed. . . . .	79
5.6	Same as figure 5.5 but for $\delta=+0.4$ . Highlighted are the two time intervals over which correlation analysis has been computed. . . . .	80
5.7	Profiles and normalized scale lengths for electron density (a and e), electron temperature (b and f) and ion temperature (c and g), electron to ion temperature ratio (d) and inverse effective collisionality (h). The profiles of the negative $\delta$ case, heated with 300 kW (blue), are compared with those of the positive $\delta$ case heated with 300kW (red). . . . .	81
5.8	Profiles and normalized scale lengths for electron density (a and e), electron temperature (b and f) and ion temperature (c and g), electron to ion temperature ratio (d) and inverse effective collisionality (h). The profiles of the negative $\delta$ case, heated with 300 kW (blue), are compared with those of the positive $\delta$ case heated with 1000 kW (green). . . . .	82
5.9	Emissivity profiles for the CECE channels in the positive and negative $\delta$ plasmas, calculated as detailed in appendix A. . . . .	84
5.10	Cross power spectral density of fluctuations for two neighbouring channels at $\rho_{vol} \sim 0.75$ . . . . .	84
5.11	Relative (a) and absolute (b) amplitude of the fluctuations obtained by integrating the CPSD of neighbouring channels between 25 and 50 kHz. . . . .	85
5.12	Toroidal angular speed of the carbon ions in the plasma as measured by the CXRS in the ohmic discharges presented in paragraph 4.3 (a) and in the NBI heated discharges presented in this chapter (b). . . . .	86
5.13	Normalized linear growth rate ( $\gamma * R/c_s$ ) and frequency ( $\omega * R/c_s$ ) of the most unstable mode for each wavenumber in three radial positions: $\rho_{tor} = 0.6$ (a), $\rho_{tor} = 0.685$ (b), $\rho_{tor} = 0.8$ (c). In the $\omega$ plots, full markers correspond to modes that propagate in the electron diamagnetic direction (TEM or ETG). . . . .	87
5.14	Linear growth rate ( $\gamma$ ) and frequency ( $\omega$ ), in real units, of the most unstable mode for each wavenumber in three radial positions: $\rho_{tor} = 0.6$ (a), $\rho_{tor} = 0.685$ (b), $\rho_{tor} = 0.8$ (c). In the $\omega$ plots, full markers correspond to modes that propagate in the electron diamagnetic direction (TEM or ETG). Simulations have been run using the same electrons and ions profiles, changing the plasma equilibrium from negative triangularity (blue) to positive triangularity (red). Horizontal lines in the $\gamma$ plots represent the estimated $E \times B$ shearing rate, with its uncertainty shown as the dashed line. . . . .	88

5.15	Normalized linear growth rate ( $\gamma$ ) and frequency ( $\omega$ ) of the most unstable mode for each wavenumber with different impurity content of the plasma: no impurities (circles); carbon in concentration measured by CXRS (squares); carbon in concentration to match $Z_{eff} = 2.91$ (triangles); carbon with concentration measured by CXRS and iron to match $Z_{eff} = 2.91$ (stars). The simulations have been run using the profiles of the $\delta = -0.4$ plasma at $\rho_{tor} = 0.685$ . . . . .	90
6.1	Inverse effective collisionality $1/\nu_{eff}$ for each channel time interval and discharge included in the database, plotted versus the radial location of the measurement. The different subfigures represent different windows of $T_e/T_i$ . The shade of color is related to the total nominal power in the discharge ( $P_{ECH} + P_{NBI} + P_{Ohm}$ ). . . . .	95
6.2	H-factor H98(y,2) for each time interval and discharge considered in the database. The data are divided in windows according to the electron-ion temperature ratio at the plasma core. . . . .	96
6.3	Relative $T_e$ fluctuations (in %) in positive and negative triangularity as a function of $1/\nu_{eff}$ for various radial positions ( $\Delta\rho = 0.05$ ). The colors of the different points are related to the nominal power ( $P_{ohm} + P_{ECH} + P_{NBI}$ ) used in the discharges, with lighter colors corresponding to higher power. The black lines represent the estimated sensitivity limit for fluctuations detection, below which fluctuations are indistinguishable from noise. . . . .	97
6.4	Relative $T_e$ fluctuations (in %) in positive and negative triangularity as a function of $1/\nu_{eff}$ for all radial positions. The colors of the different points are related to the nominal power ( $P_{ohm} + P_{ECH} + P_{NBI}$ ) used in the discharges, with lighter colors corresponding to higher power. The black lines represent the estimated sensitivity limit for fluctuations detection, below which fluctuations are indistinguishable from noise. Only points corresponding to discharges for which $T_e/T_i \leq 1.1$ at the core are plotted. . . . .	98
6.5	Relative $T_e$ fluctuations (in %) in positive and negative triangularity as a function of $T_e/T_i$ for different combinations of radial positions ( $\Delta\rho = 0.05$ ) and $1/\nu_{eff}$ . The colors of the different points are related to the nominal power ( $P_{ohm} + P_{ECH} + P_{NBI}$ ) used in the discharges, with lighter colors corresponding to higher power. The black lines represent the estimated sensitivity limit for fluctuations detection, below which fluctuations are indistinguishable from noise. . . . .	100
6.6	Relative $T_e$ fluctuations (in %) in positive and negative triangularity as a function of $T_e$ for different combinations of radial positions ( $\Delta\rho = 0.05$ ) and $1/\nu_{eff}$ . The colors of the different points are related to the nominal power ( $P_{ohm} + P_{ECH} + P_{NBI}$ ) used in the discharges, with lighter colors corresponding to higher power. The black lines represent the estimated sensitivity limit for fluctuations detection, below which fluctuations are indistinguishable from noise. . . . .	101



## List of Figures

---

6.7	Relative $T_e$ fluctuations (in %) in positive and negative triangularity as a function of $R/L_{T_e}$ for all radial positions. The colors of the different points are related to the nominal power ( $P_{ohm}+P_{ECH}+P_{NBI}$ ) used in the discharges, with lighter colors corresponding to higher power. . . . .	102
A.1	Starting positions of the rays generated by TORAY ( $s = 0$ ). The red points represent the central ray and the four extremes that contain 95% of the emitted/collected power. In this plot $z$ is the vertical direction and $y$ a direction tangential to the magnetic axis. . . . .	110
B.1	Transmission loss in the LFS ECE transmission lines from the TCV vessel to the radiometer input. . . . .	114
B.2	Transmission loss in the pre-mixing stage of the two independent CECE front ends. The measurements include the notch filters (82.7 and 118.3 GHz), a directional coupler splitting the power between the two front ends and the image reject high-pass filter. . . . .	114
B.3	Insertion loss for the six channels of the CECE centered around the same frequency (12.1 GHz). . . . .	115
B.4	Insertion loss of the CECE channels for various frequencies setting of the YIG filters, in dB. . . . .	116
B.5	Insertion loss of the CECE channels for various frequencies setting of the YIG filters, in real units. . . . .	117
C.1	Definition of the angles used in the estimation of the propagation velocity. . . .	120
C.2	Definition of $\theta_{rf}$ and representation of the distance separating two emission volumes in the R/Z plane ( $\Delta r$ ) and along a flux surface ( $\Delta s$ ). . . . .	121
C.3	Schematic representation of the four different cases corresponding to the combinations of signs for $\theta_{rf}$ and $\Phi$ . The sign of the resulting velocity can be interpreted as the direction of propagation of the fluctuation along the flux surface. A negative velocity corresponds to counter-clockwise rotation, while negative velocity to clockwise. . . . .	122
C.4	Comparison of the propagation velocity of fluctuations estimated using the phase difference between neighbouring channels (blue) or the time of maximum correlation (red). . . . .	123
C.5	Volumes 53667. . . . .	124
C.6	Poloidal and toroidal velocities of the carbon ions in TCV in the two phases where the NBI was on (yellow) and off (blue) respectively. . . . .	124
C.7	Phase and vflux 53667. . . . .	125
C.8	Phase and vflux 53667. . . . .	126
D.1	(a) Real part of the mode $m=4$ as defined in D.1. (b) Norm of a superposition of modes with $m$ going from 1 to 8 from equation D.3 with $A_0(R, Z) = 1$ . . . . .	128



D.2	(a) Norm of a superposition of modes with $m$ going from 1 to 8 from equation D.3 with $A_0(R, Z)$ composed by two gaussians in both poloidal and radial directions. The former is centered on $\theta = 0$ and the latter on $\rho = 1$ . (b) Norm of the fluctuating structure shown in a interpolated over two emission volumes. (c) Emissivity $G$ over one of the emission volumes. . . . .	130
D.3	CPSD of two synthetic channels at $\rho_{psi} = 0.7$ separated by 500 MHz, looking at fluctuations generated by moodses with $m$ from 1 to 32, rotating at constant angular velocity $\omega$ . The actual characteristics of the CECE diagnostic of TCV have been used in this test (optics, $B_{IF}$ , $f_{acq}$ , $B_{vid}$ ). . . . .	131
D.4	Examples of the changes in the emission volumes extension when changing the aperture angle of the horizontal line of sight from $2^\circ$ (a) to $5^\circ$ (b). The emission volumes are represented over the norm of the fluctuating structure obtained superimposing modes with $m$ from 1 to 32. (c) Sensitivity of the diagnostic to varying $m$ modes for increasing line of sight aperture angle. The sensitivity to higher order modes is reduced while the antenna pattern is widened. . . . .	132
D.5	Amplitude of the fluctuations measured for varying aperture angle $\alpha$ for several poloidal modes and corresponding fits with confidence intervals, calculated according to the model in [8]. . . . .	132
D.6	Norm of the fluctuating field ( $m$ from 1 to 32) and emission volumes for the simulation of the the upper lateral (a) and horizontal (b) lines of sight looking at $\rho_\psi = 0.7$ . (c) Estimated sensitivity to the different modes for the two lines of sight.	133
D.7	Norm of a superposition of modes with $m$ going from 1 to 32 from equation D.3 with $A_0(R, Z) = 1$ over the equilibria of positive (a) and negative (b) $\delta$ plasmas, together with the simulated emission volumes. (c) Fluctuations amplitude of modes of order $m$ obtained in the two cases. . . . .	134



## List of Tables

2.1	Main TCV technical specs and plasma parameters. [2]	15
5.1	Summary of nominal and effective ohmic and auxiliary power injected in the positive and negative $\delta$ plasmas described in paragraph 5.2.	78



# 1 Introduction

## 1.1 Nuclear fusion

One of the biggest challenges humanity has to face in the next decades is finding how to satisfy the ever growing world energy demand in a way that is sustainable for the planet and human societies. Fossil fuels, currently the most widespread source of energy, are limited in quantity and they produce large quantities of carbon dioxide, currently considered the main responsible for anthropic global warming. Renewable energy sources, like wind or solar technology, are considered by many as possible alternatives. In the last decades they developed considerably, becoming much more efficient, affordable and widespread. Nonetheless, they are still limited by their intermittent nature and by a very low energy density. Finally, nuclear fission power plants are an emission free technology, developed and refined over more than fifty years, but, for the current technologies at least, fuel reserves remain limited. Moreover, the problem of long living radioactive waste is still far from being solved and, after a series of accidents with far reaching consequences, the public opinion in many countries seems to strongly oppose the construction of this kind of reactors, hindering their implementation. One possible way to sustainably produce energy, not yet exploited, are nuclear fusion reactions. These are reactions in which two light nuclei combine creating a heavier, more stable, product. A nucleus is more stable the higher its binding energy per nucleon (protons and neutrons) is. The values of binding energy per nucleon with increasing atomic number are shown in figure 1.1. When converting reactants into products with higher binding energy, the resulting nuclei will have a lower total mass than the starting ones. The difference in mass between the starting nuclei and the products is converted to energy according to  $E = \Delta mc^2$ . This is the same principle that allows to exploit nuclear fission reactions to produce energy. In that case, though, a heavy, relatively unstable nucleus is made to split into several lighter, more stable products. To have nuclear fusion reactions, the positively charged nuclei need to have enough energy to approach each other at less than  $10^{-15}$  m, where the strong nuclear force overcomes Coulomb repulsion. In nature, nuclear fusion reactions are mainly found in stars, where the extreme pressure due to gravitational force allows nuclei to overcome the electric repulsion and fuse. Reproducing this kind of reactions on Earth, is no simple task.

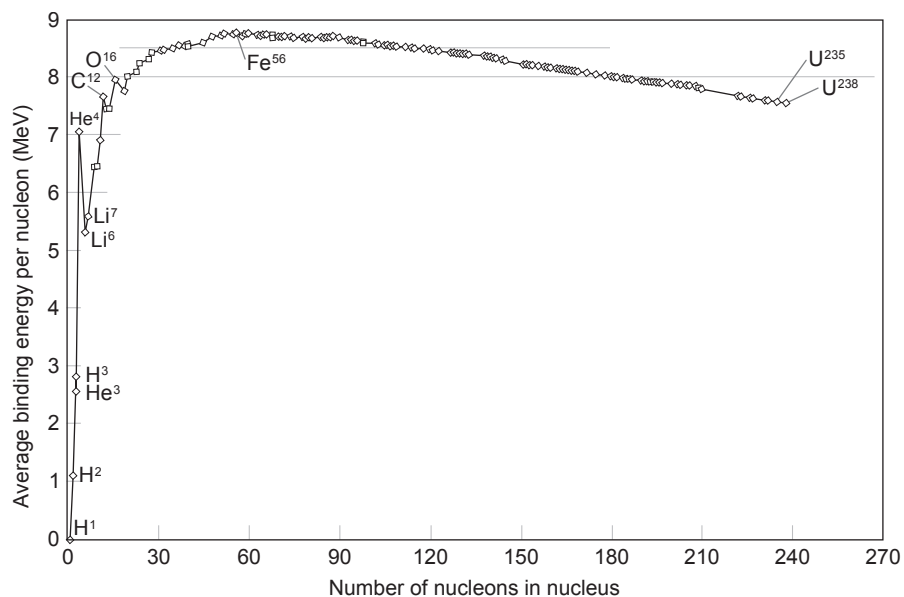


Figure 1.1 – Average binding energy per nucleon for different mass numbers. Net energy can be produced by splitting heavier atoms into lighter fragments (fission) or combining very light nuclei into bigger atoms (fusion). Public Domain, <https://commons.wikimedia.org/w/index.php?curid=1540082>

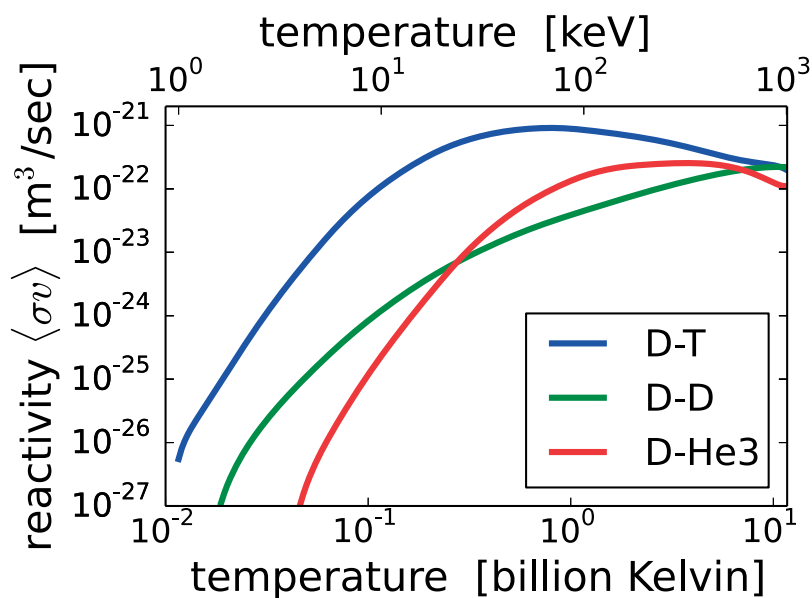


Figure 1.2 – Reactivity for three different fusion reactions as functions of the ions temperature. Licensed under Creative Commons 2.5.

Looking at the cross sections for several fusion reactions, shown in figure 1.2, it can be noticed how relatively high values can be obtained only for energies higher than 10 keV. In particular, the reaction that presents the highest cross section, at the lowest energy, is:



A reactor based on this type of reaction would have very high energy density, would emit no greenhouse gas and its fuel supplies would be widespread and relatively abundant. Deuterium can be easily extracted from water, while tritium, after an initial quantity required for the startup of the first of such machines, can be produced by having lithium react with neutrons produced by the fusion reactions.

At energies around 10 keV, matter cannot exist in any of the conventional three states (solid, liquid or gas) but only in the plasma state. At such high energies, in fact, atoms are stripped of their electrons producing strongly ionized gases, composed by free electrons and ions, susceptible to electromagnetic fields. It is common use in plasma physics, due to the high energies involved, to express temperatures in terms of electron volts according to:  $E[eV] = k_B T[K]$ , where  $k_B$  is Boltzmann constant. One eV corresponds then to 11605 K.

Plasmas are globally quasi-neutral, meaning that, if an unbalanced charge should develop, electrons would quickly redistribute to compensate for it. The characteristic distance at which charge unbalance can exist without being shielded by the neighbouring particles is called the Debye length:

$$\lambda_D = \sqrt{\frac{\epsilon_0 T}{ne^2}}, \quad (1.2)$$

where  $n$  is the plasma density,  $T$  the plasma temperature (the electrons and ions populations composing it are considered to be in thermal equilibrium),  $\epsilon_0$  is the vacuum dielectric constant and  $e$  is the electric charge of an electron. The natural frequency of the oscillations that develop in a plasma if a charge were to be displaced is called the plasma frequency:

$$\omega_p = \sqrt{\frac{ne^2}{\epsilon_0 m_e}}, \quad (1.3)$$

where  $m_e$  is the electron mass. Normally a plasma is defined as such when  $\lambda_D \ll L$ ,  $n\lambda_D \gg 1$ , and  $\omega_p \gg \nu_{en}$ , where  $L$  is the characteristic size of the system and  $\nu_{en}$  the collision frequency between electrons and neutrals. The dominance of collective effects, such as charge shielding, with respect to binary interactions, is one of the defining characteristics of a plasma.

To build a machine that exploits nuclear fusion reactions in order to produce electric energy, it is necessary to develop a reactor design that is able to produce a plasma at the required temperatures, confine it for a definite period of time and, finally, convert the produced thermal energy into electric energy so that it can be injected into the electric network.

## 1.2 The tokamak

Calculations based on a simple power balance model can be used to obtain a useful criterion guiding the design of a reactor exploiting nuclear fusion reactions [9]. The model considers a steady-state, uniform plasma, half deuterium and half tritium, of density  $n$ , at a temperature  $T$ , identical for ions and electrons. The balance assumes that the electrically charged  $\alpha$  particles, produced by the D-T fusion reactions, deposit all their energy ( $E_\alpha = 3.5$  MeV) in the plasma and that this energy is sufficient to compensate the losses by radiation and conduction. This condition, in which the plasma maintains its burning state without any energy injection from the outside, is called 'ignition'. If a confinement time is defined as  $\tau_e = \frac{W}{P_{loss}}$ , where  $W$  is the energy density stored in the plasma and  $P_{loss}$  represents the power loss by radiation and conduction, this simple power balance yields a minimum threshold for the triple product  $nT\tau_E$  [9][10]:

$$nT\tau_e \geq \frac{12}{E_\alpha} \frac{k_B T^2}{\langle \sigma v \rangle} \quad (1.4)$$

where  $\langle \sigma v \rangle$  represents the product between the reaction cross section and the relative velocity of the reacting nuclei averaged over the particles distribution. Since  $\langle \sigma v \rangle$  depends in turn on temperature, a minimum for  $\frac{k_B T^2}{\langle \sigma v \rangle}$  can be found. For D-T fusion this occurs for  $T \sim 14$  keV. If  $T$  is assumed to be close to this value, the condition then becomes:

$$nT\tau_E \geq 3 \cdot 10^{21} \text{ keV} \cdot \text{s} / \text{m}^3 \quad (1.5)$$

These requirements can be relaxed if the reactor is allowed to use external power  $P_{ext}$  together with the  $\alpha$  particles for plasma heating. The power plant would act as an energy amplifier, characterized by the parameter  $Q = P_{fus} / P_{ext}$ , where  $P_{fus}$  is the thermal energy supplied by the reactor.

Once  $T$  is constrained to reside around the optimum value for the reactivity, it is evident that equation 1.5 can be satisfied with either high density and low confinement time or, viceversa, with a high confinement time but low density. The latter is the approach that has received more attention in the last fifty years. The main idea is to employ strong magnetic fields to contain the plasma in a well defined volume, with confinement times of the order of one second or larger, while, at the same time, heating it up to 10-20 keV. This is made possible by the properties of the motion of electrically charged particles in magnetic fields.

A charged particle of species  $s$ , characterized by mass  $m_s$  and charge  $q_s$ , moving in a magnetic field  $B$ , describes a helical orbit around the field lines. The frequency of this motion for a particle of mass  $m_s$  and charge  $q_s$  is called cyclotron frequency:

$$\Omega_{c,s} = \frac{q_s B}{m_s}, \quad (1.6)$$

The radius of the resulting helix, called Larmor radius, depends on  $v_\perp$ , the particle velocity



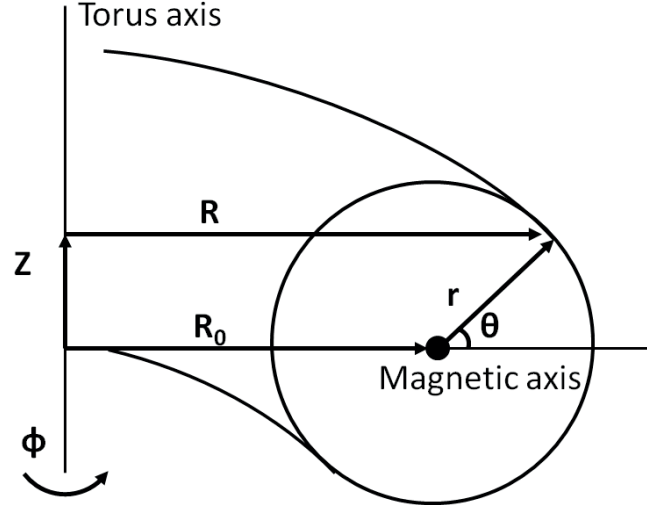


Figure 1.3 – Cross section of a torus with representation of cylindrical ( $R, \Phi, Z$ ) and toroidal ( $r, \theta, \Phi$ ) coordinates

component perpendicular to the magnetic field line, and on the magnetic field intensity.

$$\rho_{L,s} = \frac{v_{\perp,s}}{\Omega_{c,s}}, \quad (1.7)$$

In an infinitely long, cylindrical, uniform magnetic field, particles would then be confined in the direction perpendicular to the magnetic field lines (for distances corresponding to their Larmor radii) but would be unconfined in the parallel direction, leading to large plasma losses and poor confinement.

In magnetic confinement fusion, the most widespread machine concepts tackle this problem by closing the magnetic field lines on themselves in a toroidal shape. Points in a toroidal geometry can be identified using cylindrical coordinates ( $R, Z, \phi$ ) or pseudo-toroidal ( $r, \theta, \phi$ ), as shown in figure 1.3.  $\theta$  and  $\phi$  are called poloidal and toroidal directions respectively.

One of the most successful variations of this idea is the tokamak. Its main components and principle are shown in figure 1.4. It consists of a toroidal vacuum chamber, and several sets of coils used to generate the magnetic configuration that will confine the plasma. The name tokamak, in fact, is the transliteration of a russian acronym that stands for '*toroidal chamber with magnetic coils*'. The vacuum vessel is surrounded by a set of vertical coils that generate the toroidal magnetic field  $B_\phi$ . Neglecting the disuniformities in the toroidal directions due to the finite number of coils, the field in a tokamak is axisymmetric with respect to the torus axis. In such a configuration, though, the magnetic field can not be uniform across the torus cross section. Inside the vacuum vessel  $B_\phi \propto 1/R$  where  $R$  is the major radius of the torus. For this reason, it is common to refer to the inboard and outboard sides of the torus cross section as the high field side (HFS) and the low field side (LFS) respectively. The resulting field gradient and its curvature introduce forces that make the charged particles drift perpendicularly to the

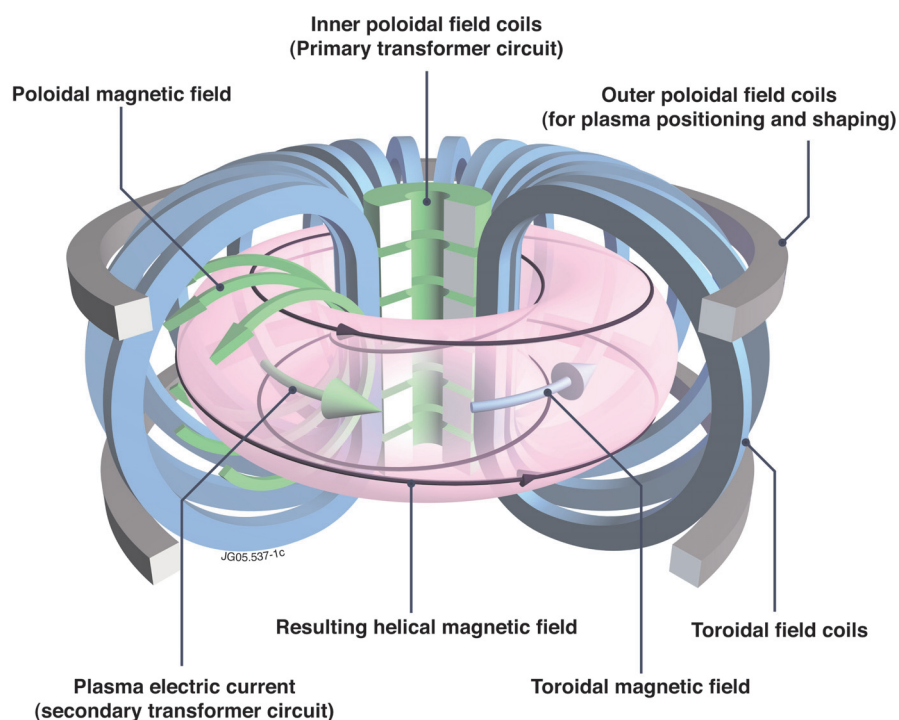


Figure 1.4 – Representation of the main coils in a tokamak and the fields they produce. Poloidal coils around the vessel produce the toroidal field (in blue). Current is ramped into the central ohmic coils to induce the plasma current and the poloidal field (all in green). Finally, horizontal poloidal field coils are used to improve stability and tailor the plasma shape and position. Source: EUROfusion website

magnetic field:

$$\mathbf{v}_{\nabla B} = \frac{1}{2} \frac{m v_{\perp}^2}{q B} \frac{\mathbf{B} \times \nabla B}{B^2}, \quad \mathbf{v}_c = \frac{m v_{\parallel}^2}{q R_c^2} \frac{\mathbf{R}_c \times \mathbf{B}}{B^2} \quad (1.8)$$

where  $R_c$  is the radius of curvature of the magnetic field lines. Since these drifts depend on the particles' charge, in a tokamak they tend to separate vertically electrons and ions. This generates electric fields that consequently add an outward radial drift that would degrade confinement:

$$\mathbf{v}_{E \times B} = \frac{\mathbf{E} \times \mathbf{B}}{B^2}, \quad (1.9)$$

To counter this, a more complicated magnetic field structure is necessary, as shown in figure 1.4. A poloidal magnetic field ( $B_{\theta}$ ) is generated by inducing a current that flows inside the plasma. To do so, current is ramped inside the inner poloidal field coils that act as the primary circuit of a transformer, while the plasma acts as the secondary. It is important to notice that a tokamak requires induced currents to work, hence will not be able to work continuously. Other strategies are being investigated to overcome this problem for the development of a reactor-like machine whose operation is not intrinsically pulsed [11]. Finally, vertical fields ( $B_v$ ) are also added to provide further stabilization and to help control plasma shaping and position inside the vacuum vessel. In general  $B_{\phi} \gg B_{\theta} \gg B_v$  and the resulting magnetic field is helical. The exact pitch of the magnetic field lines varies across the plasma cross section and is described using the safety factor  $q$ : the number of toroidal turns necessary for a magnetic field line to complete a poloidal turn.

Confining the plasma implies the generation of a pressure gradient and, with it, a force that opposes the confinement. In magnetic confinement devices, this force is balanced by the action of the magnetic field:

$$\nabla p = \mathbf{j} \times \mathbf{B}, \quad (1.10)$$

where  $\mathbf{j}$  is the plasma current density. This force balance implies that  $\mathbf{B} \cdot \nabla p = 0$  and so the magnetic field lines lie on surfaces of constant pressure. Defining flux surfaces as surfaces such that  $\mathbf{B}$  is in every point perpendicular to their normal, then all surfaces with constant  $p$  are flux surfaces. In toroidal topology these flux surfaces appear as nested surfaces, The same property is valid for the fluxes of the toroidal and poloidal components of the magnetic field, respectively  $\psi$  and  $\Phi$ . These fluxes are often used to label the magnetic surfaces defining radial coordinates such as:

$$\rho_{\psi} = \sqrt{\frac{\psi - \psi_0}{\psi_{LCFS} - \psi_0}}, \quad \text{or} \quad \rho_{tor} = \sqrt{\frac{\Phi - \Phi_0}{\Phi_{LCFS} - \Phi_0}}, \quad (1.11)$$

where  $\psi_0$  ( $\Phi_0$ ) and  $\psi_{LCFS}$  ( $\Phi_{LCFS}$ ) are, respectively, the poloidal (toroidal) fluxes at the magnetic axis and at the last closed flux surface (LCFS), the last flux surface inside which the

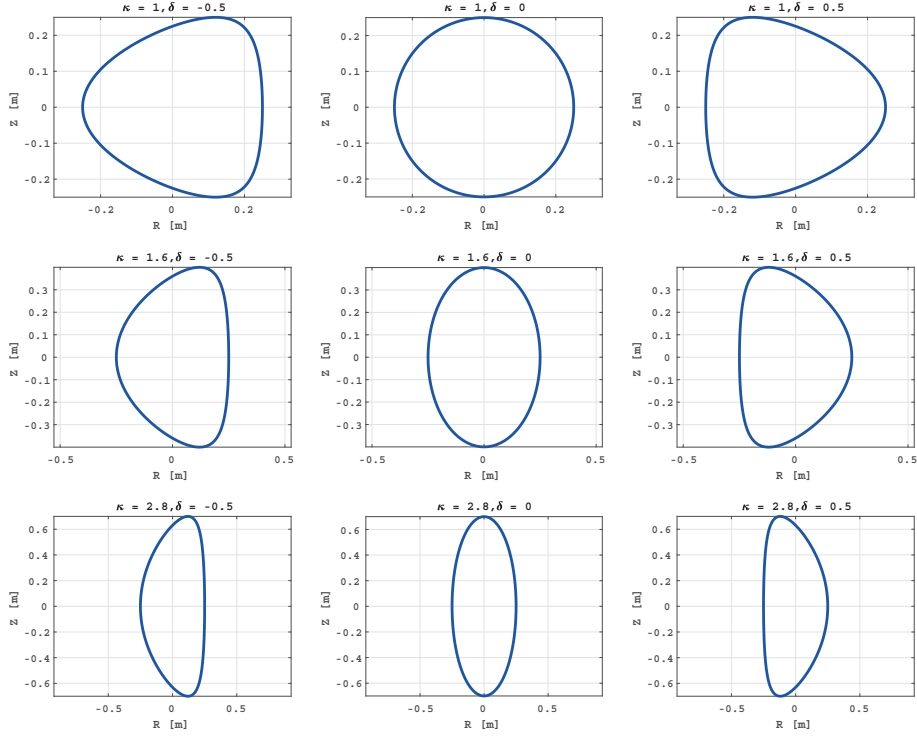


Figure 1.5 – Examples of shapes obtained varying  $\kappa$  and  $\delta$  in equations 1.12 for  $a = 0.25$  and  $R_0 = 0$

plasma is effectively confined. In this way flux surface quantities can be described with a simple 1D model, as functions of the radial variable  $\rho$ . Another commonly used normalization for the plasma minor radius is  $\rho_{vol}$ , defined as  $\sqrt{V/V_{LCFS}}$  where  $V_{LCFS}$  is the plasma volume included in the last closed flux surface.

Tokamaks can generate plasmas with different poloidal cross section shapes and this has been found to strongly influence stability and transport. The two most important shaping parameters are elongation  $\kappa$  and triangularity  $\delta$  [12]. They can be seen as the first two moments of the sinusoidal expansion of the poloidal cross section of a given flux surface. For a tokamak with major radius  $R_0$ , minor radius  $a$ , the analytic form of the last close flux surface is:

$$\begin{aligned} R(\theta) &= R_0 + a \cos(\theta + \delta \sin(\theta)) \\ Z(\theta) &= Z_0 + a\kappa \sin(\theta) \end{aligned} \tag{1.12}$$

Examples of the possible plasma shapes that can be obtained varying  $\kappa$  and  $\delta$  in equations 1.12 are shown in figure 1.5. Both elongation and triangularity have been found to strongly influence the plasma stability [13] and to increase the maximum achievable normalized

pressure  $\beta = \frac{p}{B^2/2\mu_0}$ . For a given plasma current, in fact, it is found that an upper boundary to  $\beta$  exists [14]:  $\beta = \beta_N / (I_p / a B_0)$  where  $B_0$  is the magnetic field in T,  $I_p$  the plasma current in MA,  $a$  the minor radius in m and  $\beta_N$  is the normalized  $\beta$ . The value of  $\beta_N$  has been estimated to be  $\sim 3.5$  but it can vary for different operational regimes [15]. Plasmas with higher elongation and triangularity allow the increase of plasma current beyond the limits for circular plasma, related to the approaching of the edge safety factor to  $q_{95} = 2$ , significantly improving the energy confinement [16]. The possibility of obtaining plasmas with negative triangularity has been significantly less explored, but several studies have shown consistent improvements of confinement with respect to symmetric, positive triangularity plasmas [17]. The effects of negative triangularity on stability and transport are central to the scope of this thesis and will be presented in chapters 4, 5 and 6.

### 1.3 Motivation of the thesis

One of the long standing issues in the quest for building a reactor powered by nuclear fusion reactions is achieving sufficiently high energy and particles confinement. One of the problems to be tackled is the radial transport of particles and energy. *Neoclassical* transport models, which take into account the diffusion caused by Coulomb collisions between particles in the particular case of toroidal geometries, fail to predict the transport level experimentally measured in magnetic confinement fusion machines. Diffusion coefficients are found to be higher than neoclassical predictions by an order of magnitude or more [18]. This at the time unexplained contribution is called *anomalous* transport and is widely accepted to be due to turbulent phenomena driven by microinstabilities inside the plasma. The plasmas studied for nuclear fusion applications, are far from thermodynamic equilibrium. The steep gradients, consequence of confinement, can act as sources of free energy for a broad class of unstable modes on microscopic scales, of the order of the electron and ion gyroradius. These microinstabilities cause fluctuations in temperature, density, and in the electric and magnetic fields ( $\tilde{n}$ ,  $\tilde{T}$ ,  $\tilde{E}$ ,  $\tilde{B}$ ). Those, in turn, affect particle drifts, generating also fluctuations in particles velocities and plasma currents ( $\tilde{j}$ ). Depending on their relative phase, these fluctuations can couple and generate non-negligible fluxes of particles ( $\Gamma$ ) and energy ( $Q$ ) [18]:

$$\begin{aligned}
\Gamma_j^e &= \frac{\langle \tilde{E}_\theta \tilde{n}_j \rangle}{B_\Phi} \\
\Gamma_j^b &= -\frac{\langle \tilde{j}_\parallel \tilde{B}_r \rangle}{e B_\Phi} \\
Q_j^e &= \frac{3}{2} k_B n \frac{\langle \tilde{E}_\theta \tilde{T}_j \rangle}{B_\Phi} + \frac{3}{2} k_B T_j \frac{\langle \tilde{E}_\theta \tilde{n}_j \rangle}{B_\Phi} \\
Q_j^b &= g_j \left( \frac{\tilde{B}_r}{B_\Phi} \right) \nabla T_j.
\end{aligned} \tag{1.13}$$

In equation 1.13,  $g$  is a function whose precise form depends on the plasma collisional regime and the strength of the turbulence (see [18]), and  $\langle \cdot \rangle$  represents ensemble averaging. The subscript  $j$  indicates the particle species and the superscripts  $e$  and  $b$  refer to electrostatic and electromagnetic components of the fluxes respectively. The former, in particular, has been found to account for most of the observed particle and energy transport [19][20][21].

While plasma fluctuations have been measured in a variety of magnetic confinement machines and conditions, connections between turbulence characteristics and macroscopic plasma parameters are still being actively investigated, both experimentally and with the use of numerical codes based on theoretical models. Thanks to its flexibility, the *Tokamak à Configuration Variable* (TCV) [22] is particularly suited for the study of the effects of plasma shaping on fluctuations. TCV is a medium sized tokamak (major radius  $R = 0.88$  m, minor radius  $a = 0.25$  m) with up to 1.53 T magnetic field on axis and up to 1 MA plasma current. Its main asset is the unparalleled shaping capability that allows the investigation of plasmas with elongation  $0.9 < \kappa < 2.8$  and triangularity [12]  $-0.7 < \delta < 1$ . A more detailed description of TCV is presented in chapter 2.

These shaping capabilities have been exploited in past experiments, where it was found that one parameter strongly influencing electron heat transport is the plasma triangularity ( $\delta$ ) [17]. In particular, it has been observed that it is possible to get similar electron density and temperature profiles in symmetric positive and negative  $\delta$  plasmas using only half of the auxiliary heating power in the latter case [23][3]. In those experiments, the electron heat transport has been found to be strongly reduced from the edge to  $\rho_{vol} = 0.4$  [3]. This is despite the fact that the magnitude of  $\delta$  (positive or negative) decreases quickly when moving from the edge to the plasma interior. These earlier works, however, only focused on macroscopic quantities related to transport (electron heat flux, electron heat conductivity and electron energy confinement time) due to the lack of fluctuations measurements on TCV at the time [17][23][3].

The effects of negative triangularity on transport have also been investigated with ion-scale, electromagnetic gyrokinetic simulations, using the GS2 [24] and GENE [25] codes. Linear simulations starting from the experimental profiles found trapped electrons modes (TEM) to be the dominant source of instability in these discharges. Non-linear, local simulations found a partial stabilization of TEMs in negative triangularity discharges and managed to reproduce the flux reduction in the edge with respect to the positive triangularity plasmas [4] [6]. Global simulations qualitatively reproduce the transport reduction also closer to the plasma core [26], but they are limited by their very high computational costs.

More recently, experimental fluctuations studies have been performed in TCV. The tangential phase contrast imaging (TPCI) diagnostic has been exploited to investigate the difference between density fluctuations in positive and negative triangularity [7]. A marked suppression of fluctuations has been observed in a large radial fraction, also in positions where the absolute value of triangularity is vanishing. These measurements have been taken in L-mode discharges

with only electron cyclotron resonance heating as auxiliary heating power. Linear gyrokinetic simulations showed TEMs to be the dominant instability also in these cases.

The substantial confinement improvements that have been observed make the idea of designing a negative triangularity fusion reactor an attractive possibility [27][28]. Plasma conditions in a reactor-scale machine are expected to be very different with respect to those in TCV. In particular it is foreseen that confinement time will be sufficiently high to allow thermalization of ions and electrons, obtaining  $T_e/T_i \sim 1$  in the whole plasma. This condition is expected to make ion temperature gradient (ITG) driven modes the dominant instability. Even though not many studies have been performed with negative  $\delta$  plasmas in these conditions until now, first results appear promising [29][30]. A more thorough investigation of the effects of different dominant turbulence regimes on fluctuations suppression in negative  $\delta$  plasmas is necessary.

TCV has been recently upgraded with a 1 MW neutral beam (NB) heating system. It can be used to explore a wide range of previously unattainable operation spaces, especially characterized by  $T_e/T_i \leq 1$ . The core of this thesis work consists in the study of fluctuations in TCV, in varying conditions of collisionality and  $T_e/T_i$ . In particular, the effect of negative triangularity in plasmas characterized by low  $T_e/T_i$  has been investigated.

Fluctuations measurements have been obtained with the use of the correlation electron cyclotron emission (CECE) diagnostic of TCV. This diagnostic is able to measure small ( $< 1\%$ ) electron temperature fluctuations with low wavenumber ( $k < 1.12 \text{ cm}^{-1}$ , corresponding to  $k\rho_i \sim 0.5$  and  $k\rho_e \sim 0.01$ ) in a wide range of plasma configurations. More information on the CECE technique and its application in TCV will be presented in chapter 3.

## 1.4 Thesis outline

Chapter 2 presents the main characteristics of TCV, its auxiliary heating systems, and the main diagnostics whose measurements were used in the experimental data analysis.

Chapter 3 contains a simple description of the principles of electron cyclotron emission (ECE) and its application in plasma diagnostics, together with the basic concepts of heterodyne radiometry. The correlation ECE (CECE) technique, used to measure small scale fluctuations over a large bandwidth, and its main limitations are also introduced. The chapter continues with a description of the ECE and CECE diagnostics in TCV and of the analysis procedure that is used to process the CECE measurements.

The results of fluctuation measurements in a series of ohmic discharges with positive and negative triangularity, using different lines of sight for the CECE diagnostic, are detailed in chapter 4. Fluctuations were found to be strongly suppressed in negative triangularity discharges, corroborating the results of previous works on similar plasmas. In chapter 5 the study of the effect of triangularity on confinement and fluctuations is extended to plasmas with dominant ion heating, studied with both experimental measurements and linear gyroki-

netic fluctuations. Also in this regime, previously unexplored in TCV, negative triangularity was found to have beneficial effects on confinement and to suppress fluctuations. A larger database of fluctuation measurements, coming from discharges covering a large range of plasma parameters, is analyzed in chapter 6. Negative triangularity is found to have beneficial effects on confinement over a large range of collisionality and electron-ion temperature ratio. Conclusions drawn from this work are presented in chapter 7.

This thesis is closed by some appendices. In appendix A, the method used to calculate the emission volumes of the ECE channels is explained in detail. Appendix B presents some of the characterization of waveguides and components of the ECE radiometers, performed as part of this thesis work. In appendix C a method is presented to exploit the variety of plasma positions available in TCV and the flexibility of the CECE lines of sight to estimate the rotation velocity of the plasma using the propagation speed of fluctuations between the CECE channels. Finally, a model to test the sensitivity of the different lines of sight of TCV over a simple fluctuating field is introduced in appendix D.



## 2 Tokamak à configuration variable (TCV) and experimental apparatus

The work contained in this thesis is based on experiments performed at the Swiss Plasma Center (SPC) on the *Tokamak à Configuration Variable* (TCV) [22]. A sketch of the tokamak is shown in figure 2.1. TCV is a medium-sized tokamak whose main characteristic is the possibility of studying plasmas in a large variety of shapes, including extreme elongation and negative triangularity. This is possible thanks to its elongated vessel ( $\sim 0.5$  m of width versus  $\sim 1.5$  m of height), labeled by C in figure 2.1, and its unique set of 16 shaping coils (D). These coils are distributed evenly between the LFS and HFS and have independent power supplies, thus allowing the realization of complex magnetic field geometries. Beyond obtaining extreme values of elongation and triangularity, they also allow the exploration of exotic divertor configurations. The inner wall of TCV is covered with graphite tiles. Carbon, released by the tiles, constitutes the main impurity in the plasmas. The main parameters of TCV are summarized in table 2.1.

### 2.1 Auxiliary heating systems

TCV is equipped with a very versatile auxiliary heating system, that allows the exploration of a large range of plasma parameters in the many different configurations that the tokamak can reproduce. It comprises both an electron cyclotron resonance heating (ECRH) system and a neutral beam injector (NBI or NBH) for ion heating.

#### 2.1.1 Electron Cyclotron Resonance Heating system

The Electron Cyclotron Resonance Heating (ECRH) system of TCV consists of seven gyrotrons. Four produce microwaves at 82.7 GHz for heating at the second harmonic of the electron cyclotron resonance frequency, and three at 118 GHz to heat instead at the third harmonic. All are equipped with gratings in the matching optics units (MOUs) that can control the polarization of the radiation entering the vessel to optimize the coupling to the plasma. In particular, extraordinary mode (X-mode) shows better absorption at the second and third

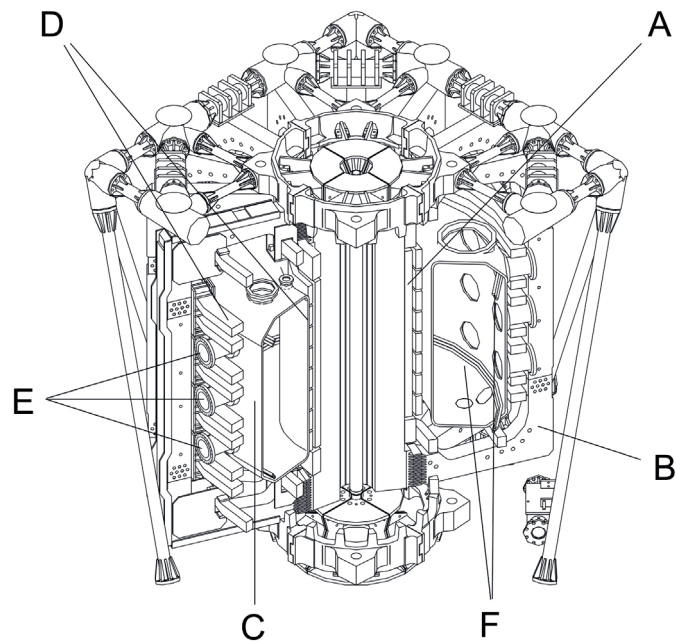


Figure 2.1 – Sketch of TCV with some of its main components highlighted. A) Central solenoid, acting as a transformer primary circuit in the induction of the plasma current. B) Toroidal field coils. C) Vacuum vessel. D) Shaping coils, also called poloidal field coils. E) Ports for access into TCV. F) In-vessel poloidal field coils.

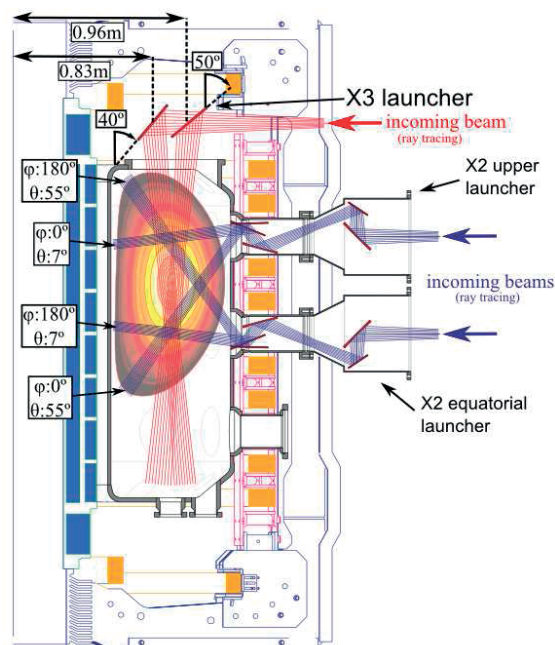


Figure 2.2 – Drawing of the different positions available to ECRH launchers in TCV.

## 2.1. Auxiliary heating systems

Parameter	Symbol	Value
Major radius	$R_0$	0.88 m
Minor radius	$a$	0.255 m
Aspect ratio	$1/\epsilon = R_0/a$	$\leq 3.5$
Vessel height	$h$	1.54 m
Vessel elongation	$\kappa_{TCV}$	3
Vessel base vacuum	$p_{TCV}$	$\leq 10^{-7}$ mbar
Toroidal field on axis	$B_0$	$\leq 1.54$ T
Loop voltage	$V_{loop}$	1-2 V
Plasma current	$I_p$	$\leq 1$ MA
Ohmic heating power	$P_{OH}$	$\leq 1$ MW
NBH heating	$P_{NBH}$	$\leq 1$ MW
ECRH X2 heating	$P_{X2}$	$\leq 2.4$ MW
ECRH X3 heating	$P_{X3}$	$\leq 1.4$ MW
Plasma species		D (He,H)
Main impurities		C,B
Plasma elongation	$\kappa_a$	0.9-2.8
Plasma triangularity	$\delta_a$	-0.8 +0.9
Electron density	$n_e$	$\leq 2 \cdot 10^{20} \text{ m}^{-3}$
Electron temperature (OH)	$T_e$	$\leq 2$ keV
Electron temperature (ECRH)	$T_e$	$\leq 15$ keV
Ion temperature (OH-ECRH)	$T_i$	$\leq 1$ keV
Ion temperature (+ NBH)	$T_i$	$\leq 3.7$ keV
Plasma frequency	$f_{pe}$	30-120 Ghz
Electron Larmor radius	$\rho_e$	50-250 $\mu\text{m}$
Ion Larmor radius	$\rho_i$	2-7 mm

Table 2.1 – Main TCV technical specs and plasma parameters. [2]

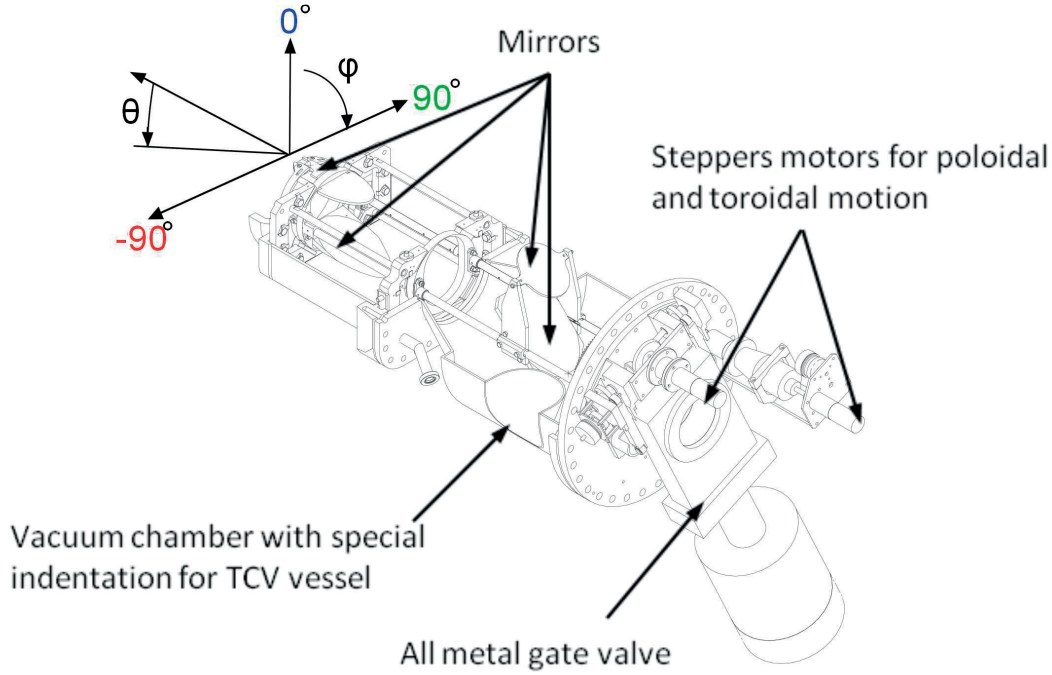


Figure 2.3 – Schematic of the launchers directing ECRH power into TCV. The injected beam can be rotated over  $\theta$  and  $\phi$ .

harmonic than ordinary mode (O-mode) and is hence used in TCV. Furthermore, using X-mode allows the X2 gyrotrons to inject radiation from the LFS avoiding cutoff layers. Two X2 gyrotrons are connected to equatorial launchers, while the remaining two are connected to upper lateral launchers, as shown in figure 2.2. The launchers' schematics and movable angles are shown in figure 2.3. The last of their four mirrors can rotate between 7 and 55 degrees ( $\theta$ ) allowing one to select the absorption location of EC radiation on the resonant layer. The launchers can also rotate around their axis ( $\phi$ ), adding a toroidal component to the injected radiation that can induce additional current inside the plasma. This is called Electron Cyclotron Current Drive (ECCD). The radiation produced by the three X3 gyrotrons is instead directed by a mirror positioned at the top of the vessel, as shown in figure 2.2. This mirror can be displaced radially (only between one discharge and the next) and rotated (also during a discharge). The X3 gyrotrons are normally used to heat the plasmas in discharges where density is too high and X2 radiation cannot reach its resonance due to the presence of cutoff layers. Two of the X2 gyrotrons produce up to 750 kW, the other two up to 450 kW. Each of these couples of gyrotrons has access to an equatorial and an upper lateral launcher, as shown in figure 2.2. The X3 gyrotrons can produce up to 450 kW.

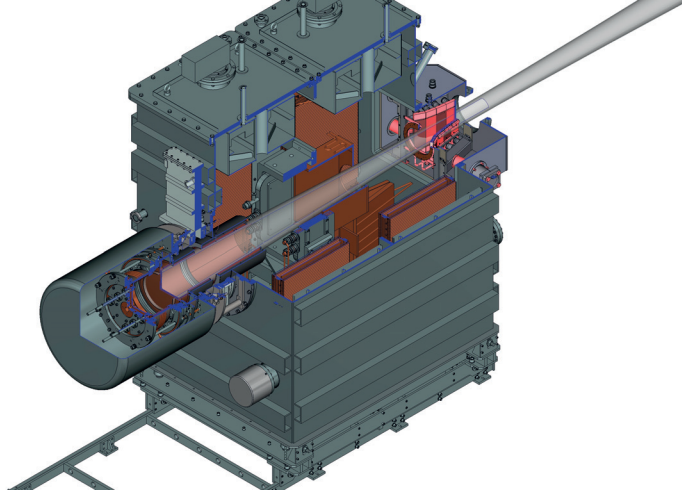


Figure 2.4 – Drawing of the NBI system in TCV with the designed shape of the produced beam.

### 2.1.2 NBI

A NBI heating system, whose 3D render is shown in figure 2.4, has been installed in TCV in 2015 [31]. It is able to produce up to 1 MW of ion heating through the injection of fast deuterium atoms. The exact energy of the ions varies with the injected power from  $\sim 10$  keV at 100 kW to 24 keV at 1 MW. The beam injects neutrals tangentially with respect to the plasma, thus acting also as a strong source of momentum. This addition opened the possibility to study plasmas characterized by  $T_e/T_i \leq 1$ . Previous standard scenarios of TCV were instead characterized by  $T_e \gg T_i$ . This is of particular interest since in a future reactor-like machine the confinement time should be high enough to guarantee equilibrium between ions and electrons temperatures.

## 2.2 TCV diagnostics

TCV is equipped with a large set of diagnostics able to measure numerous plasma characteristics. These diagnostics have been specifically designed to be able to achieve meaningful measurements in all the combinations of shapes and plasma positions available to TCV. In the following, the main diagnostics of TCV, whose measurements have been used in this work, will be briefly introduced.

### 2.2.1 Magnetic probes

Magnetic measurements in TCV are taken by a total of 228 magnetic probes, measuring the poloidal magnetic field tangent to the vessel. They are positioned inside the vacuum vessel, behind the graphite tiles, in several poloidal and toroidal arrays. Four poloidal sections of the machine, separated by  $90^\circ$ , are equipped with thirty-eight probes each, as shown in figure

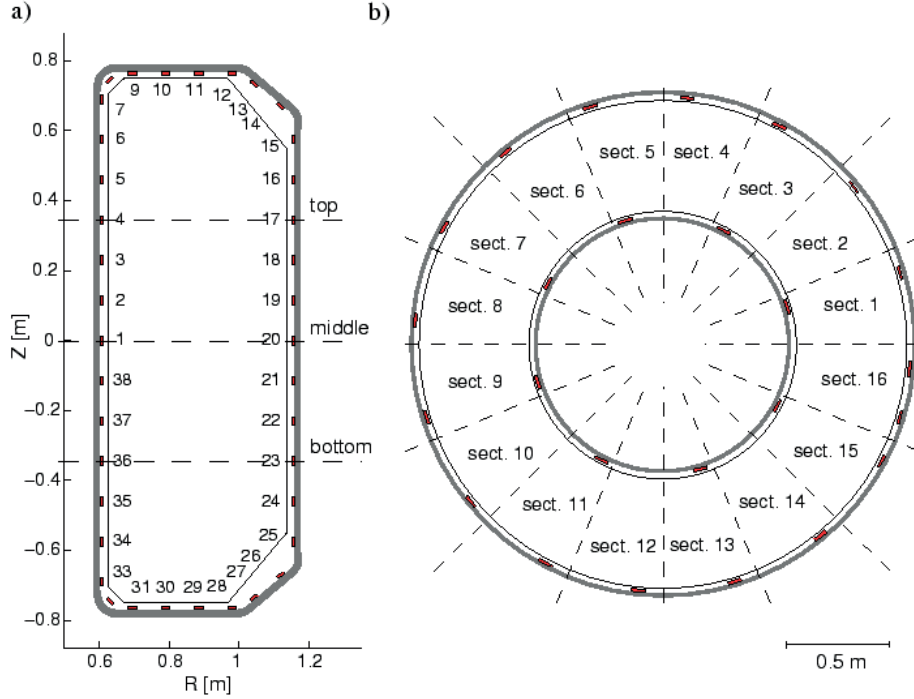


Figure 2.5 – Layout of the magnetic probes of TCV in the poloidal and toroidal arrays [1]

2.5a. They provide data used for equilibrium reconstruction. The other probes are divided in six toroidal arrays. Three are located on the LFS, at the equatorial plane of the machine and 35 cm above and below it. Each consists of sixteen equidistant probes, plus a seventeenth at an irregular distance to increase the resolution of toroidal mode numbers. The remaining three toroidal arrays, consisting of only eight equidistant probes each, are located on the HFS at vertical positions equivalent to the LFS ones [1]. An example of the LFS and HFS toroidal arrays is shown in figure 2.5b. In addition to these arrays, TCV is also equipped with three toroidal arrays of eight saddle coils to measure the radial flux derivative (used to deduce  $B_R$ ), again at  $z = 0$ ,  $z = -35$  cm and  $z = 35$  cm. Acquisition frequency for all of these probes can reach up to 1 MHz but is routinely set at 250 kHz.

The main applications of these measurements is to provide data for the plasma equilibrium reconstruction, using the Grad-Shafranov solver LIUQE [32][33][34], estimate the plasma current and detect MHD activity during discharges.

### 2.2.2 Far infrared interferometer

A 14 channel Mach-Zender interferometer, based on a continuous wave far infrared (FIR) laser, emitting at  $184.3 \mu\text{m}$ , is used on TCV to obtain line-integrated electron density measurements along 14 vertical chords, shown in figure 2.6b [35]. For the laser frequency and polarization selected, the phase difference between a reference beam and those that have traversed the

plasma can be directly related to the line-integrated electron density. The interferometer signals are acquired at 20 kHz. The signal coming from its central line (entering the plasma at  $R = 0.9$  m), shown in red in figure 2.6b, is used for real time control of plasma density during the discharges.

### 2.2.3 Thomson scattering

The main source of local measurements of electron density and temperature in TCV is the Thomson scattering system [36]. The diagnostic is based on the collection of scattered laser radiation by the plasma electrons. Electromagnetic radiation interacts with charged particles by accelerating them. In turn, they emit radiation in all directions as scattered light [37]. If the laser wavelength is negligible with respect to the Debye length, then the emissions from different electrons will be uncorrelated and the process is called incoherent Thomson scattering. In this case, the intensity of the scattered radiation is proportional to the local electron density, while the spectral broadening of the scattered radiation with respect to the incident laser light can be used to measure the electron temperature. TCV is equipped with three Nd-YAG lasers emitting 1064 nm light at up to 20 Hz with almost overlapped optical paths. The laser beams enter the vessel from the bottom at  $R \sim 0.9$  m. Wide angle lenses positioned in three different horizontal ports focus some of the scattered radiation onto sets of optical fibres connected to 96 spectrometers. The lines of sight cover the vessel from -0.35 m to 0.55 m, as shown in figure 2.6a, allowing the reconstruction of temperature and density profiles in TCV plasmas. Each channel covers between 6 and 12 mm along the laser line. The three lasers can be triggered independently to reach a 60 Hz sampling frequency, or simultaneously, to obtain a higher signal-to noise ratio in low density plasmas. The diagnostic is regularly calibrated using Raman scattering on  $N_2$  filling the TCV vessel. Furthermore special reference discharges are used to verify the existence of drifts. Correction factors for the density measurements are obtained through the comparison with the line integrated density measurements obtained using the FIR.

### 2.2.4 Electron cyclotron emission (ECE) and Correlation ECE diagnostics

While the Thomson scattering system provides accurate, local, measurements of electrons temperature and density, its temporal resolution is limited by the lasers firing rate. To study faster modifications of the electrons temperature profile, such as MHD modes, TCV is equipped with an ECE diagnostic. It analyses the EC spectrum passively emitted by the plasma electrons. The different frequency components of this spectrum correspond to different radial positions. The intensity of these components, if the plasma can be considered "optically thick", can be related to the local electron temperature. In TCV the ECE diagnostic uses 24 channels, acquired at 200 kHz.

In addition to a standard ECE diagnostic, TCV is also equipped with a six channels Correlation ECE system. This is a fluctuations diagnostic, sensitive to low-wavenumber modes. Using



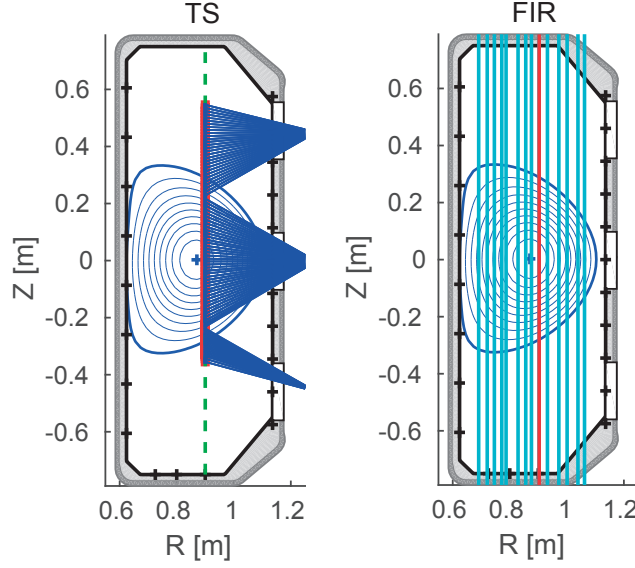


Figure 2.6 – a) In green the optical path of the Thomson scattering diagnostic laser into a TCV plasma. In red the fraction of the beam path covered by the lines of sight of the diagnostic, shown in blue. b) Lines of the FIR diagnostic in TCV measuring the integrated electron density. In red the central line used for real time density control of the plasma discharges [2].

spectral decorrelation techniques, it is able to measure small electron temperature fluctuations ( $\delta T_e / T_e < 1\%$ ) over a large fraction of TCV cross section. More details on these diagnostics and their working principles are presented in chapter 3.

### 2.2.5 Charge Exchange Recombination Spectroscopy

TCV is equipped with a charge exchange recombination spectroscopy (CXRS) diagnostic that is used to obtain local measurements of impurity temperature, density and rotation velocity [2]. The diagnostic is based on the collection and analysis of line radiation emitted by recombined impurity ions going through a charge exchange reaction with an energetic neutral hydrogen atom. In TCV these fast neutrals are supplied by a low power ( $\leq 80$  kW) diagnostic neutral beam (DNB) that injects  $\sim 50$  keV hydrogen atoms radially into the tokamak. Due to its low power, the plasma is not significantly perturbed by the DNB. This allows the study of intrinsic plasma rotation in discharges without external momentum sources. In TCV the main impurity is carbon coming from the graphite tiles, so emission at the CVI line (529.06 nm) is normally used in CXRS measurements. The CXRS diagnostic of TCV is made up of four different systems: two toroidal, looking at the plasma from the LFS and HFS respectively, and two poloidal, one of which specifically designed to take measurements in the plasma periphery. The lines of sight of three of these systems are summarized in figure 2.7. The measurements used in this work have been taken using system 1, also known as LFS CXRS. The time resolution of the diagnostic is limited, by photon statistics, to 30-60 ms.



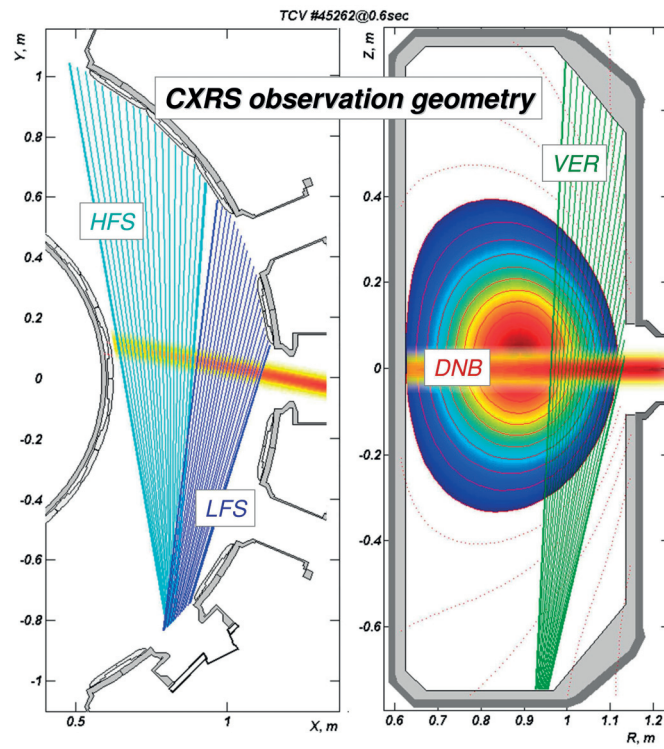


Figure 2.7 – Viewlines of three of the CXRS systems of TCV [2].



## 3 Electron Cyclotron Emission (ECE) and Correlation ECE diagnostics principles and their application in TCV

### 3.1 Introduction: diagnostic applications of ECE

Many plasma diagnostics work by deriving information on plasma characteristics from passive or stimulated electromagnetic radiation emission. An important component of the passively radiated power in plasmas is the so called Electron Cyclotron Emission (ECE). In plasmas, electrons continuously emit electron cyclotron radiation at their gyration frequency  $\Omega_c = q_e B / m_e$  depending mainly on the intensity of the local magnetic field. Since in magnetic confinement machines the magnetic field is externally imposed through the toroidal field coils and its value at each point can be reconstructed (starting from magnetic probes measurements), different frequency components of the ECE spectrum can be associated with specific emission volumes. In a tokamak, for example, the total magnetic field is dominated by its toroidal component, which decreases monotonously ( $B \propto 1/R$ ) from the high field side to the low field side as shown in figure 3.1. Thus, higher ECE frequencies will correspond to an emission layer at lower R positions and vice versa. For any given frequency, the emission layer will always have a finite radial width due to broadening effects. The most important, in a tokamak plasma, are Doppler and relativistic broadening [38]. In ECE diagnostic applications, radiation is usually collected using lines of sight perpendicular to the main magnetic field, thus greatly reducing the effects of doppler broadening.

Relativistic broadening is related to the fact that electrons at a specific radial location do not have uniform energy but, instead, a distribution of energies around a mean value. The distribution will include electrons whose energy is sufficient to make relativistic mass increase non negligible in the calculation of their cyclotron frequency:

$$\Omega_{ce} = \frac{eB}{\gamma m_e} \quad \text{with} \quad \gamma = \frac{1}{\sqrt{1 - (\frac{v}{c})^2}} \quad (3.1)$$

Energetic electrons will hence emit at reduced frequencies. This effect is commonly referred

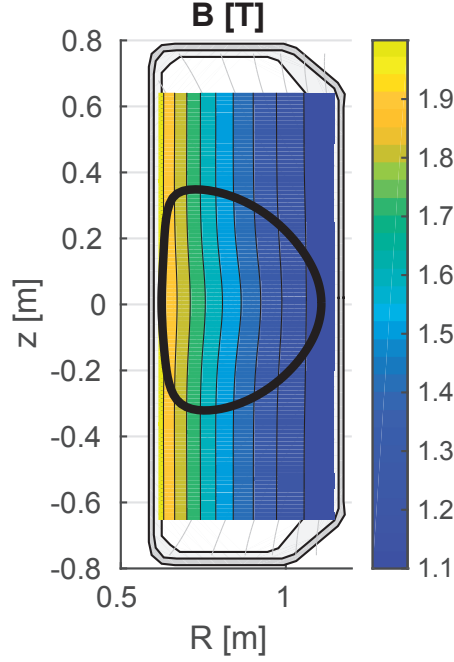


Figure 3.1 – Intensity of the magnetic field over the cross-section of the vessel of TCV. Particles in plasma regions of constant  $B$  will emit EC radiation at the same frequency  $\propto 1/R$  where  $R$  is the major radius.

to as relativistic downshift. Every frequency component of the ECE spectrum will then contain contributions coming from energetic electrons residing on the neighbouring layers on the HFS. This causes a broadening of the effective emission volume. This effect is stronger the higher the electron temperature. An expression for relativistic broadening is [39][40]:

$$\frac{\Delta f_{rel}}{f} = \frac{4.1 e T_e}{m_e c^2}, \quad (3.2)$$

where  $f$  is the detection frequency and  $T_e$  the electron temperature in eV. Taking as an example a plasma with  $T_e = 1 \text{ keV}$ , the relative frequency variation would be  $\frac{\Delta f_{rel}}{f} \sim 0.8\%$ , corresponding, for a resonance at 80 GHz, to  $\sim 640 \text{ MHz}$ . Such a broadening, for TCV, would expand the ideal emission line by  $\sim 0.75 \text{ cm}$ . In more unfavourable conditions, these broadening mechanisms, can widen the ideal line emission by several centimetres. Still, more precise radial localization of ECE emission would still be possible, if the plasma can be considered to be optically thick. The definition of optical thickness (or optical depth) is related to the radiation transport properties of plasmas.

A body that emits a certain radiation spectrum, also absorbs it in the same frequency range. Hence, part of the EC radiation emitted at a frequency  $\omega$  is reabsorbed before reaching the collection optics. For an antenna looking at a plasma slab, as shown in figure 3.2, one can consider the balance between the emission and absorption processes along a ray trajectory

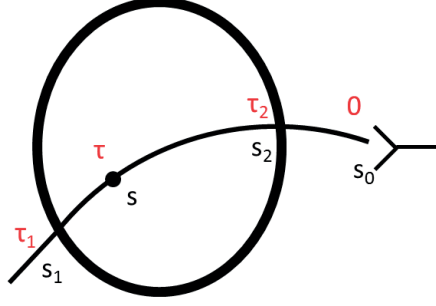


Figure 3.2 – Simple representation of the optical depth seen by the collection optics for emission along a ray identified by the curvilinear coordinate  $s$ .

characterized by the curvilinear coordinate  $s$  [37][38]:

$$\frac{dI}{ds} = j(\omega) - I\alpha(\omega) \quad (3.3)$$

Here  $\alpha(\omega)$  is the absorption coefficient,  $j(\omega)$  is the plasma emissivity and  $I(\omega)$  the radiation intensity. Defining the optical depth as:

$$\tau(s) = \int_{s_0}^s \alpha(\omega, s) ds, \quad (3.4)$$

the intensity of the radiation leaving a medium, with uniform  $j/\alpha$ , at a position  $s_2$  can be expressed as [37]:

$$I(s_2) = I(s_1)e^{-(\tau_1 - \tau_2)} + \int_{\tau_1}^{\tau_2} (j/\alpha)e^{-(\tau - \tau_2)} d\tau \quad (3.5)$$

where  $I(s_1)$  is the radiation incident to the medium along the ray. If  $\tau_1 - \tau_2 \gg 1$  all contributions coming from outside the medium are dampened, together with the radiation originating in the body farther from the collection optics. It is normally assumed that radiation emitted from plasma regions for which  $\tau > 2$  will be almost completely reabsorbed before reaching the collection optics. For a broadened ECE layer, then, only radiation emitted from regions where  $\tau \leq 2$  will effectively contribute to the collected radiation intensity. Plasmas are then said to be optically thick for a given frequency if  $\tau \geq 2$ . The plasma, in this case, behaves like a blackbody at the frequency considered since it is perfectly absorbing. This implies that, if the electrons can be considered to be in thermodynamic equilibrium, for low frequencies such that  $\hbar\omega \ll kT$ , the plasma emits according to Rayleigh-Jeans classical limit for Planck's radiation formula:

$$I(\omega) = \frac{\omega^2 T}{8\pi^3 c^2}. \quad (3.6)$$

This is particularly convenient in the case of ECE from an optically thick plasma. The measured intensity of the collected radiation, in fact, will be proportional to the temperature of the electrons that have emitted it. Once the antenna pattern of the collection optics is well

### **Chapter 3. Electron Cyclotron Emission (ECE) and Correlation ECE diagnostics principles and their application in TCV**

---

established, its intersection with the emission layer defines the emission volumes for a specific frequency. More details on the calculation of the plasma absorption coefficient and the estimate of the emission volumes in TCV is presented in appendix A.

In conclusion, collection and analysis of ECE in magnetic confinement machines has an important diagnostic value. The ECE spectrum can be divided into frequency components which will correspond to emission from localized plasma volumes, and their intensity will give information on the local electron temperature. A common method of collection and analysis of ECE in magnetic fusion devices is heterodyne radiometry which will be the subject of the next section.

## **3.2 Heterodyne radiometry**

ECE has been measured since the 60s [41] and its potential as an electron temperature diagnostic was realized in the following decade [42][43][44]. Since then, the techniques used have evolved considerably, converging, in the more recent devices, on the use of heterodyne radiometry, even though some exceptions still exist [45].

The ECE from plasmas relevant for nuclear fusion studies usually covers the range from 30 to 200 GHz, corresponding to the millimeter-wave range. A heterodyne radiometer collects radiation in a given frequency band, the radio frequency (RF) band, and shifts it to a lower frequency one, called intermediate frequency band (IF), where simpler components can be used to process it. The collected RF is downconverted using a mixer: a non-linear device that combines two inputs in the RF range and outputs power at the sum and difference frequencies. In this kind of application, ECE radiation is combined with the monochromatic emission of a coherent local oscillator (LO). Often a filter is placed before the mixer to select only RFs either higher or lower than the LO frequency. These radiometers are called single-sideband receivers, otherwise double-sideband receivers. Of particular importance is that the mixing process is linear (power in the IF is proportional to power in the RF) and phase-coherent (especially valuable for applications in interferometry and reflectometry).

The main components of a heterodyne radiometer are shown in figure 3.3. The first section of a radiometer, up to the mixer, is normally referred to as the RF section. After that, the downconverted signal is usually amplified, band-pass filtered and rectified, in what is called the IF section. Note that, for a fixed LO frequency, the IF filter bandwidth is what eventually selects the RF bandwidth whose intensity the radiometer will measure. Multiple IF branches, each with a band-pass filter centred on a different frequency, constitute the different channels of a heterodyne radiometer. The place of origin of the power sent to each channel, and thus the spatial localisation of the measurement, is determined by the bandwidth of the IF filters. What comes after the detection is the video stage of the radiometer. There the signal is further amplified and then usually low-pass filtered to improve the signal to noise ratio, defining the bandwidth of the rectified signal before the acquisition.

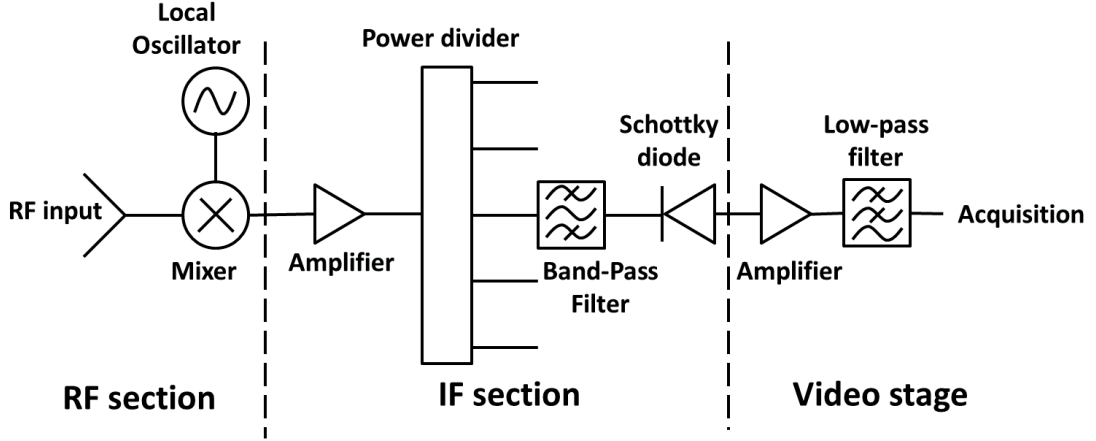


Figure 3.3 – Schematics of the main components of a heterodyne radiometer for ECE applications.

The very high sensitivity, good spatial localisation and possibility of having high temporal resolution have made heterodyne radiometry the technique of choice for the study of ECE emission from plasmas[46].

### 3.3 Correlation ECE technique for the study of small $T_e$ fluctuations

One of the main limits of ECE radiometry is the relatively high minimum detectable temperature fluctuation, due to the presence of thermal noise in the receiver [38]:

$$\left(\frac{\delta T_e}{T_e}\right)^2 \sim \frac{2B_{vid}}{B_{IF}}. \quad (3.7)$$

where  $B_{vid}$  is the video bandwidth and  $B_{IF}$  the IF filter bandwidth. The factor 2 in the numerator arises when  $B_{vid}$  is small with respect to  $B_{IF}$  [47]. For example, for a radiometer that works with  $B_{vid} = 100$  kHz and  $B_{IF} = 750$  MHz, as in TCV, this would result in a minimum detectable fluctuation  $\frac{\delta T_e}{T_e} \sim 1.6\%$ . In tokamak plasmas, fluctuations of interest for the study of core turbulent transport are expected to have relative amplitudes well below 1%, thus impossible to detect with a similar configuration. Furthermore, using a 750 MHz wide IF filter significantly limits the spatial resolution of the channel as seen in section 3.1. In the following it will be assumed that the conditions mentioned in section 3.1 are respected and so fluctuations in the ECE signals can be interpreted as electron temperature fluctuations. The case of plasmas with lower optical depth is treated in section 3.3.2.

In the 1990s several groups independently proposed the idea to use cross correlation analysis techniques to overcome the minimum detectable fluctuation limitations [48][49]. The main idea is to combine two ECE signals  $S_1$  and  $S_2$  containing the same information about plasma temperature and its fluctuations ( $\delta T$ ), but independent thermal noise ( $N_1$  and  $N_2$ ) such that

### Chapter 3. Electron Cyclotron Emission (ECE) and Correlation ECE diagnostics principles and their application in TCV

---

$\langle N\delta T \rangle = 0$  and  $\langle N_1 N_2 \rangle = 0$ , where  $\langle \cdot \rangle$  represents the cross correlation calculated over a finite time period [39]. In this way one obtains:

$$\langle S_1 S_2 \rangle = \langle (\delta T)^2 \rangle + \langle N_1 \delta T \rangle + \langle N_2 \delta T \rangle + \langle N_1 N_2 \rangle \sim \langle (\delta T)^2 \rangle \quad (3.8)$$

When this type of analysis is performed, the minimum detectable fluctuations is reduced depending on the number of time samples of the signals that were cross-correlated,  $N_s$ :

$$\left( \frac{\delta T_e}{T_e} \right)^2 \sim \frac{1}{\sqrt{N_s}} \frac{2B_{vid}}{B_{IF}}. \quad (3.9)$$

In equation 3.3, there are two main components on which one can act to reduce the minimum detectable fluctuation level. The first is maximizing the number of samples used in the correlation analysis  $N_s$ . This requires to work with discharges as stable as possible and an acquisition system with high sample frequency. For example, on TCV, the acquisition frequency is set at 1.75 MHz so that averaging over 500 ms would reduce the minimum detectable fluctuation by more than a factor 30. It is important to notice that averaging over relatively long time records means the loss of temporal resolution for the fluctuations measurements.

To optimize the second term, one would have to work with a high  $B_{IF}$  and a low  $B_{vid}$  but, as it has already been mentioned,  $B_{IF}$  needs to be small enough to actually resolve fluctuating structures. For tokamaks, fluctuations are known to exist in a wide range of scales that goes from the electron gyroradius to several times the ion gyroradius, corresponding, in the core of TCV, to  $\sim 60 \mu m$  and  $\sim 3 mm$  respectively. To be able to resolve at least the fluctuations on the ion gyroradius scale, where  $k_\perp \rho_i \leq 1$ , it is necessary to use filters with  $B_{IF}$  small enough to guarantee that the radial extension of the emission volumes would be smaller than 1 cm. For most machines this requires using filters with  $100 MHz < B_{IF} < 200 MHz$ . At the same time  $B_{vid}$  needs to include the whole frequency range where the fluctuations of interest are observed, possibly extending over several hundreds of kHz. On TCV  $B_{IF} = 100 MHz$  and  $B_{vid} = 450 kHz$ .

Different techniques have been developed and successfully employed to obtain ECE signals apt for correlation analysis: spectral decorrelation and detector decorrelation. In the detector decorrelation technique, the two ECE signals to be correlated come from exactly the same plasma volume and hence contain the same information on temperature fluctuations. This can be achieved by having two identical radiometers with crossed lines of sight, viewing the same plasma volume with sufficient angular separation to obtain decorrelated thermal noise in the two channels. This technique was originally developed in the stellarator W7-AS [49]. Spectral decorrelation systems, instead, use a single radiometer and line of sight. The signals to be correlated come from two different channels whose IF filters are narrow and centered around frequencies close to each other, while still not overlapped. The idea is to probe plasma volumes that are physically separated (thus emitting uncorrelated thermal noise) but close enough to contain the same local temperature fluctuations. This can be achieved using



channel separation of the order of the expected fluctuations' correlation length. This design was first used on TEXT [48] and has become the most widespread design in other machines such as TCV [50], Alcator C-Mod [51], Asdex Upgrade [52], DIII-D [53], LHD [54].

#### 3.3.1 Wavenumber sensitivity

The spectrum of the detectable fluctuations is not only limited by the radiometer characteristics, but also by those of the line of sight through which the plasma is observed. The finite size of the plasma emission volumes limits the spectrum of wavenumbers that can be observed both in the radial and in the poloidal directions. Fluctuating structures are normally considered to be strongly elongated along the magnetic field lines, so the effects of finite emission volume dimensions are normally negligible in the direction parallel to the magnetic field. The effect of finite spatial resolution in a given channel can be taken into account using a simple model [8]. For a quantity  $n_{true}(\mathbf{r}, t)$ , the measured signal  $n_m$  is considered to be an average weighted by a three dimensional gaussian profile whose  $1/e$  folding lengths are  $w_x$ ,  $w_y$  and  $w_z$ :

$$n_m(\mathbf{r}, t) = \frac{1}{\pi^{3/2} w_x w_y w_z} \int d\mathbf{r}' e^{-\left(\frac{x-x'}{w_x}\right)^2} e^{-\left(\frac{y-y'}{w_y}\right)^2} e^{-\left(\frac{z-z'}{w_z}\right)^2} n_{true}(\mathbf{r}', t) \quad (3.10)$$

Consequently, the measured spectral power density  $S_m(\mathbf{k}, \omega) = |n_m(\mathbf{k}, \omega)/\bar{n}|^2$  will differ from the real one  $S_{true}$  according to:

$$S_m(\mathbf{k}, \omega) = e^{-\frac{(k_x w_x)^2}{2}} e^{-\frac{(k_y w_y)^2}{2}} e^{-\frac{(k_z w_z)^2}{2}} S_{true}(\mathbf{k}, \omega) \quad (3.11)$$

Thus the measured spectral power is attenuated by a factor  $e^{-(\mathbf{k}\mathbf{w})^2/2}$ . The diagnostic is said to be sensitive only to modes with wavenumbers [8][39]:

$$k_{x,y,z} \leq 2/w_{x,y,z} \quad (3.12)$$

As already mentioned in section 3.1, the dominant contributions to the radial width of the emission volumes, apart from the IF filter bandwidth and when the line of sight is perpendicular to the magnetic field, is relativistic broadening. This is often negligible in standard ECE radiometry applications, where the bandwidth of each channel is usually of several hundreds MHz, but not in Correlation ECE applications, where channel bandwidths are often 100-200 MHz. The dimensions of the emission volumes in the other directions are instead fixed by the antenna pattern.

### 3.3.2 Effects of density fluctuations on CECE fluctuations measurements

One of the main difficulties in the interpretation of the radiative temperature fluctuations measured by CECE diagnostics is to properly take into account the effects of plasma density fluctuations. For emission at the second X-mode harmonic the absorption coefficient  $\alpha$ , and hence the optical depth  $\tau$ , depend on density and temperature. If  $\tau$  is not high enough at the emission volume position, then density fluctuations contribute to a non-negligible fraction of the measured fluctuating power [55]:

$$\frac{\delta I}{I} = [1 + A_2(\tau, \chi)] \frac{\delta T_e}{T_e} + A_2(\tau, \chi) \frac{\delta n_e}{n_e} \quad (3.13)$$

In this formula  $A_2$  is a function of the optical depth and the reflectivity of the machine walls  $0 < \chi < 1$ . It is defined as:

$$A_2(\tau, \chi) = \frac{\tau \exp(-\tau)}{1 - \exp(-\tau)} \left( 1 - \chi \frac{1 - \exp(-\tau)}{1 - \chi \exp(-\tau)} \right) \quad (3.14)$$

It approaches 0 when the plasma is optically thick.

By applying correlation analysis to two signals, each with its own fluctuations  $\delta I_1$  and  $\delta I_2$ , to extract the common fluctuations one obtains:

$$\begin{aligned} \left( \frac{\delta I_1 \delta I_2}{I^2} \right) = & [1 + A_2(\tau, \chi)]^2 \left( \frac{\delta T_e}{T_e} \right)^2 + A_2(\tau, \chi)^2 \left( \frac{\delta n_e}{n_e} \right)^2 + \\ & + 2[1 + A_2(\tau, \chi)] A_2(\tau, \chi) \left( \frac{Re[\langle \delta T_e \delta n_e \rangle]}{T_e n_e} \right) \end{aligned} \quad (3.15)$$

Here the first two terms contain the contributions of temperature and density fluctuations respectively, while the third term represents an additional contribution related to the cross-correlation of density and temperature fluctuations. This result implies that, to be able to precisely associate ECE radiation fluctuations with temperature fluctuations in an optically thin plasma, it is necessary to have simultaneous measurements of the density fluctuations from the same plasma volume. For high reflectivity machines (normally with metal walls  $\chi > 0.9$ ),  $\tau \geq 2$  is usually considered a sufficient condition to interpret the radiative temperature measurements as electron temperature. The requirements on  $\tau$  are stricter when considering fluctuations. Assuming density and temperature fluctuations to be perfectly in phase ( $\langle \delta T_e \delta n_e \rangle = \delta T_e \delta n_e$ ), equation 3.15 can be used to estimate the maximum contribution of density fluctuations to the measured fluctuations, as a function of the ratio  $\frac{\delta T_e}{T_e} / \frac{\delta n_e}{n_e}$  [56]. Due to the relatively low optical thickness of TCV plasmas at the edge, measurements of the CECE diagnostic will be interpreted only as fluctuations of radiative temperature. An estimation of the maximum contribution of density fluctuations on the measured radiative temperature fluctuations will be presented.

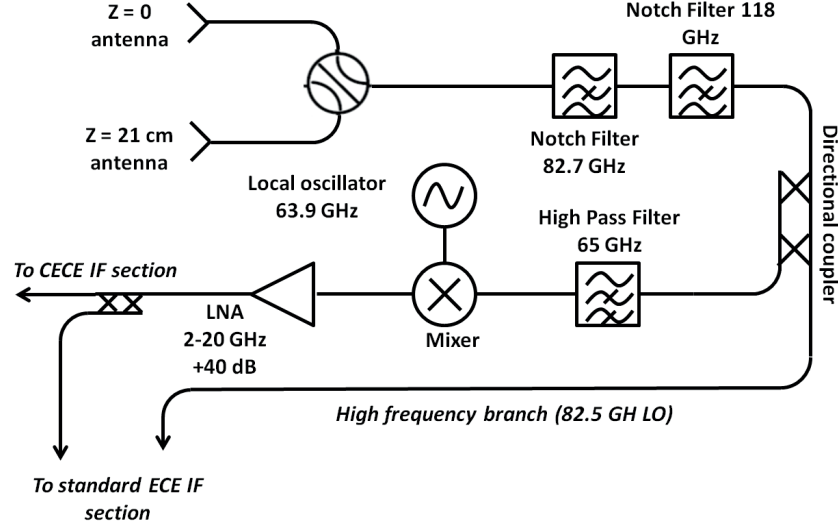


Figure 3.4 – Schematics of the RF section of the standard LFS ECE radiometer on TCV.

### 3.4 ECE diagnostics in TCV

TCV is equipped with several ECE diagnostics, all detecting emission at the second harmonic of the extraordinary mode (X2). A standard ECE radiometer views the plasma from the low field side (LFS), perpendicular to the magnetic field, with two alternative lines of sight: one at the vessel midplane, the other 21 cm above it. The two lines of sight are designed to optimize the ECE measurements in plasmas whose axis lie in the two most common positions used in TCV ( $z_{axis} = 0$  and  $z_{axis} = 0.23$  m). A picture of the end of these lines, where they interface with the TCV vessel is shown in figure 3.9. A more detailed description of these lines will be provided in 3.5.1. The radiometer's 24, 750 MHz wide, channels cover the 66-102 GHz range, corresponding to the whole plasma cross-section for discharges with standard magnetic field in TCV ( $B_{axis} = 1.45$  T). The incoming signals are digitized at 200 kHz. The raw measurements are cross-calibrated against the Thomson scattering measurements [57]. This radiometer is mainly used for the reconstruction of temperature profiles with 200 kHz temporal resolution. Each channel covers a fraction of the normalized minor radius between 0.005 and 0.1, depending on its frequency. Schematics of the RF and IF stages of the standard ECE radiometer of TCV can be found in figures 3.4 and 3.5. A similar radiometer, with higher frequency local oscillators (covering the 78-114 GHz range), views the plasma from the HFS, again alternatively from  $z = 0$  or  $z = 21$  cm. The choice of having two radiometers viewing plasmas from two different sides was made to allow a greater flexibility in the possible applications of the system. The LFS system makes it possible to study the bulk plasma temperature even in conditions where ECRH or ECCD generate a significant fraction of suprathermal electrons, as mentioned in section 3.1. Radiation emitted from suprathermal particles in fact, whose frequency is downshifted due to relativistic effects, is reabsorbed by lower frequency resonant layers when propagating towards the LFS. Emission from these electrons can instead propagate towards the HFS without being reabsorbed. Thus, the HFS system can observe radiation emitted by these fast particles, giving

**Chapter 3. Electron Cyclotron Emission (ECE) and Correlation ECE diagnostics principles and their application in TCV**

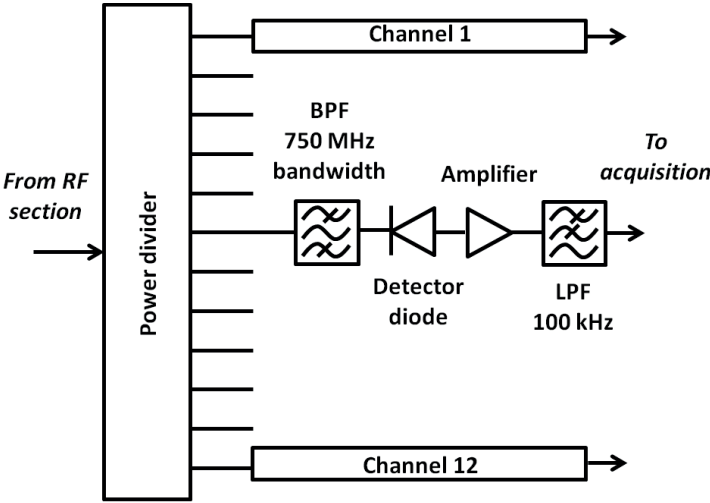


Figure 3.5 – Schematics of one of the two IF sections of the standard LFS ECE of TCV. Each of these twelve channel sets is connected to a different branch characterized by a different LO frequency.

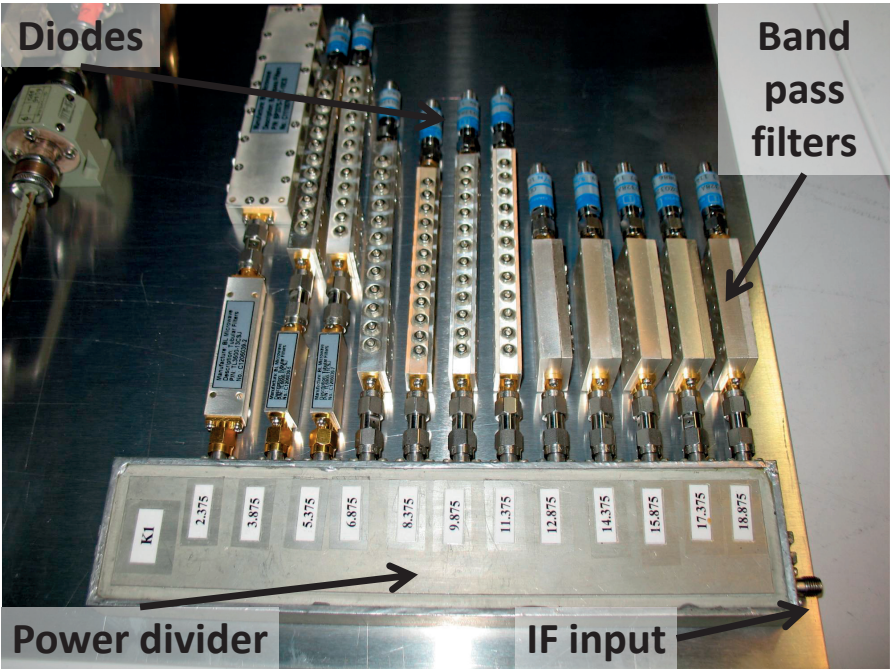


Figure 3.6 – Picture of one of the two IF sections available for the LFS ECE diagnostic on TCV.

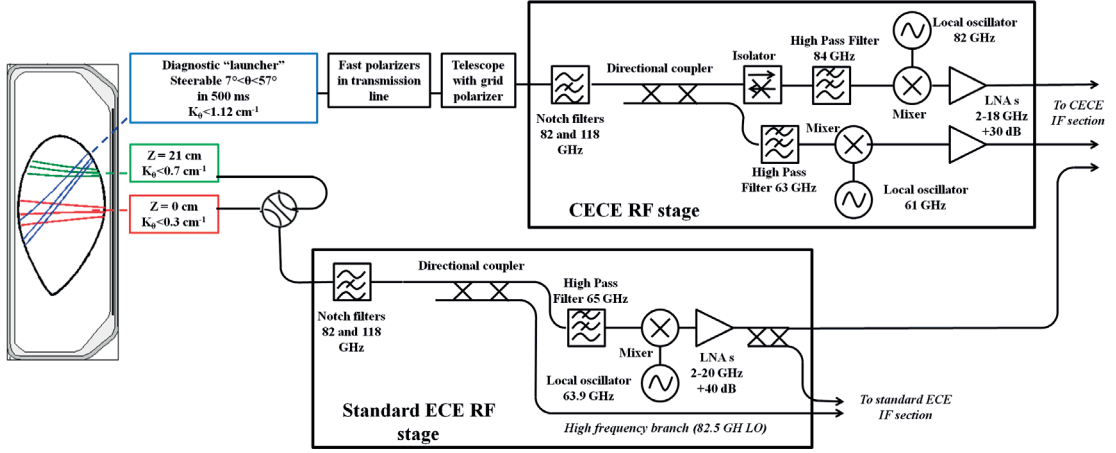


Figure 3.7 – Summary of the CECE system in TCV from the vessel to the RF sections of the radiometers.

the possibility to compare the results between LFS and HFS data coming from similar volumes in the plasma [58][59].

A vertical line of sight is also available on TCV [60]. It consists of a focusing ellipsoidal mirror and a telescope system with a view from the top of the vessel, perpendicular to the magnetic field. A beam dump (reflectivity  $< 0.1\%$ ) is placed at the bottom of the vacuum chamber. This line of sight can be considered to be looking along a surface of constant magnetic field. The broadening of the ECE spectrum measured by this line of sight is produced by the distribution of electrons' energies along the line of sight. These signals can then be used to gather information on the suprathermal electron population. [61]. This antenna is presently connected with two independent radiometers with six channels each, still undergoing commissioning.

Stray radiation injected by the gyrotrons, would damage the mixers if collected. To

### 3.5 Correlation ECE in TCV

TCV is equipped with a CECE diagnostic, detecting X2 radiation. Its main features include a steerable line of sight, shared with a reflectometry system, and a set of six independently frequency tunable, narrow band IF filters. The main goal of this system is to study electron temperature fluctuations in a large section of the radial profile and in a variety of plasma configurations, exploiting the flexibility provided by the multiple lines of sight and the possibility of precisely choosing the measurement location for each channel in every discharge. Part of this thesis work consisted in the commissioning of the CECE radiometers, upgraded in 2016. After testing the components' performances at the frequencies of operation, the radiometers have been assembled and connected to the dedicated waveguides in TCV. Details on these tests and their results are presented in appendix B.



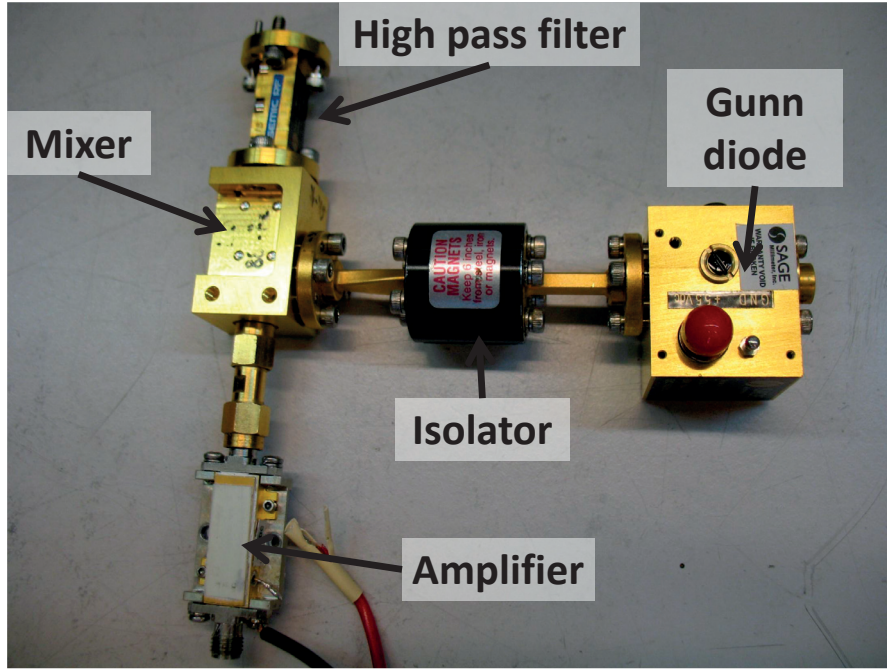


Figure 3.8 – Picture of one of the two RF sections available for the CECE on TCV. Radiation enters the high pass filter after the notch filters and, after mixing and amplification, is transferred to the IF section.

### 3.5.1 Lines of sight and radiometers

A schematic diagram of the different lines of sight available to the CECE in TCV and the corresponding radio frequency sections is shown in figure 3.7. The CECE system can use three different lines of sight. The first two are the horizontal lines of sight already mentioned in the description of the standard LFS ECE diagnostics in section 3.4. The equatorial line employs a Teflon lens focusing the emitted radiation into a circular 2.5 cm waveguide. The  $z = 21$  cm line, instead, uses a Gaussian horn and an elliptical mirror to focus radiation into a similar waveguide. Due to their antenna pattern, the  $z = 0$  and  $z = 21$  cm antennas are sensitive to modes with  $k_\theta < 0.4 \text{ cm}^{-1}$  and  $k_\theta < 0.3 \text{ cm}^{-1}$  respectively [8], where  $k_\theta$  is the poloidal wave number, as used in equation 3.11. Calculations for the gaussian beam propagation at 80 GHz have been used to compute the maximum wavenumber limit for the  $z = 0$  line. Their result is shown in figure 3.10. The choice of the viewing line is made using a remotely controlled waveguide switch. As mentioned in section 3.4, these horizontal lines carry radiation to the standard LFS ECE radiometer. This radiometer, as shown in figure 3.4, has two RF sections with different LO frequencies. The power going into the lower frequency branch (63.9 GHz LO) is split in two by a directional coupler after the mixing stage: half of it goes into the standard ECE channels while the other half can be directed to the IF section of the CECE as shown in figure 3.7.

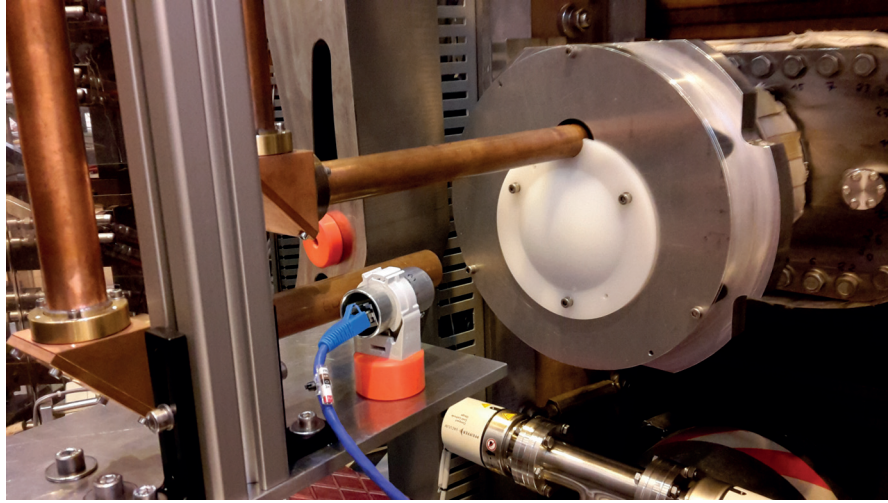


Figure 3.9 – Picture of the entrance of the horizontal  $z = 0$  and  $z = 21$  cm LFS lines of sight for the ECE systems. The  $z = 0$  one looks through a polyethylene lens directly into the plasma. The one above it looks into a gaussian horn connected to a piece of waveguide rising up to  $z = 21$  cm.

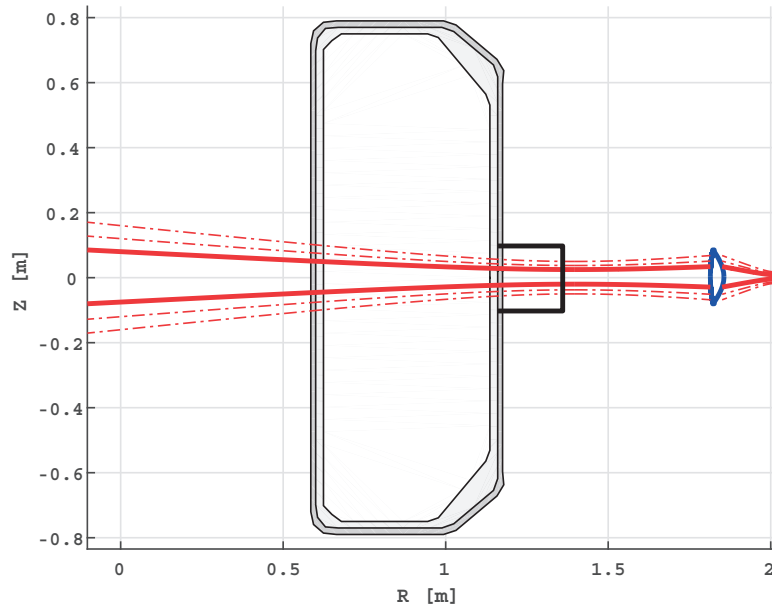


Figure 3.10 – Antenna pattern calculated for the  $z = 0$  LFS horizontal line. The solid line represents the distance from the axis where  $\sim 95\%$  of the beam power is contained ( $2\sigma$ ), the two dashed lines contain respectively 3 and 4  $\sigma$ . The beam propagation has been calculated using gaussian beam theory starting from the aperture of the waveguide.

### Chapter 3. Electron Cyclotron Emission (ECE) and Correlation ECE diagnostics principles and their application in TCV

---

#### Steerable antenna

The third line of sight available to the CECE system is based on a steerable antenna. Its schematics are shown in figure 2.3. The antenna is located on the LFS, perpendicular to the wall, 45 cm above the chamber mid plane. It is a converted ECRH launcher and its position mirrors that of the upper lateral launchers of TCV shown in figure 2.3. Its line of sight can be moved by changing the angle of the last mirror ( $\theta$  in figure 2.3) and by rotating the whole antenna body around its axis (angle  $\phi$  in figure 2.3). The angle  $\theta$  can be varied between  $7^\circ$  and  $55^\circ$  with respect to the antenna axis, while  $\phi$  can vary between  $-90^\circ$  and  $90^\circ$  with respect to the horizontal plane perpendicular to the LFS vessel wall. This allows one to accurately select the measurement location in all plasma configurations in TCV and, additionally, to perform oblique ECE measurements [62]. The effective vertical size of the emission volumes observed with this line strongly depends on  $\theta$ , the selected channels' frequencies and the plasma position. In optimal conditions it can resolve modes with  $k_\theta < 1.12 \text{ cm}^{-1}$  at 70 GHz.

The collected radiation is transmitted to the CECE along a HE11 63.5 mm inner diameter corrugated waveguide, shown in figure 3.11a. To guarantee optimal coupling between the emitted radiation and the diagnostic systems in all discharges, the transmission line contains two remotely controlled polarizers, one linear and one elliptical, whose orientation can be varied during a discharge (0.1 s for  $90^\circ$  polarization rotation) [63]. They are needed to obtain optimal coupling between the X-mode emission coming from the plasma and the transmission line. Given a reference discharge it is possible to calculate the optimal polarizers setting for the selected viewing angle [64]. The transmission line is coupled to the diagnostic through a telescope, shown in figure 3.11b. A pair of elliptical mirrors direct the radiation to a grid polarizer that separates vertical and horizontal polarizations. The two halves of the incoming signal are directed to two gaussian horns, respectively connected to WR-10 and WR-15 rectangular waveguides. The former is connected to the CECE RF section which is made up of two separate front ends with different local oscillators (working at 61 GHz and 82 GHz respectively) as shown in figure 3.7. The mixing stage can be switched between discharges. A picture of one of these RF sections is shown in figure 3.8.

The WR-15 horn is instead connected to a reflectometer [65]. The presence of this system in parallel with the CECE allows the design of discharges where simultaneous measurements of temperature and density fluctuations in the same plasma volume can be performed. By applying correlation analysis techniques to such signals it is possible to calculate the n-T fluctuations crossphase. Even though it is not the main topic of this thesis, this measurement is of particular interest since it relates directly to the turbulent transport terms shown in equations 1.13 and can be compared with the predictions of gyrokinetic simulations [66].

#### 3.5.2 Intermediate frequency section

The downconverted radiation coming from the CECE RF section is passed into the CECE IF section, whose schematics are presented in figure 3.12 and whose picture is shown in figure



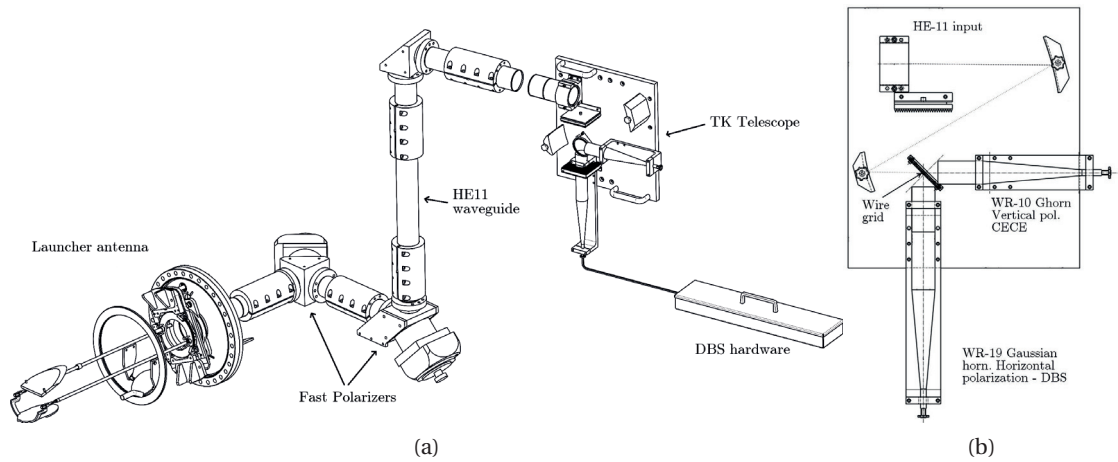


Figure 3.11 – (a) Schematics of the whole transmission line for the steerable receiver including the antenna, the polarizers, and the telescope coupling the power gathered by the steerable line of sight to the CECE and the DBS reflectometer. (b) Details of the telescope.

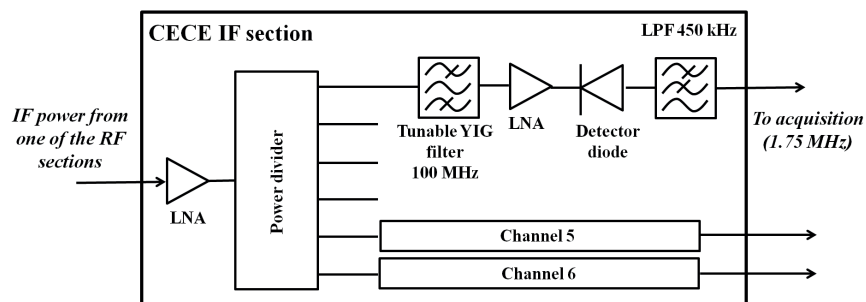


Figure 3.12 – Schematics of the IF section of the CECE diagnostic on TCV.

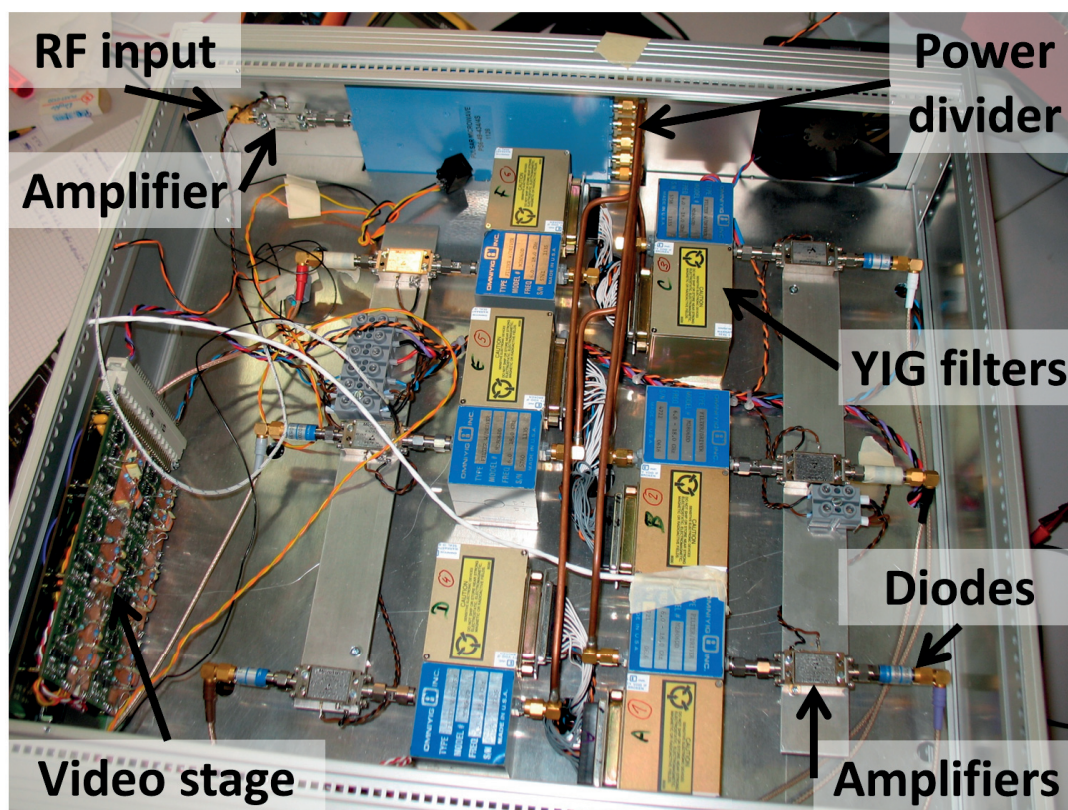


Figure 3.13 – Picture of CECE IF stage where the six YIG filters are visible. After rectification in the Schottky diodes, the signals are sent to the video stage.

3.13, using flexible RF cables. The signal is amplified with a 30 dB low noise amplifier (LNA) connected to a six way power divider that splits the signal into six identical channels. Each channel consists of a YIG (yttrium iron garnet) filter, an additional amplification stage (20 dB LNA) and finally a schottky diode for rectification. The filters are OMNYIG M2806DD. They have 3 dB bandwidth of 100 MHz and their center frequencies are independently tunable with a 12 bit digital controller, in the 6-18 GHz range. After rectification, the signals are amplified with electronically controlled gain and low pass filtered in a fifth order butterworth filter at 450 kHz before being digitised at 1.75 MHz. With these parameters, over the whole 450 kHz band, the minimum detectable fluctuation when correlation analysis is performed over 100 ms period is  $\delta T_e / T_e \sim 0.45\%$ .

## 3.6 CECE signal processing

As already mentioned in section 3.3, the high sampling rate and video bandwidth of the CECE combined with the narrow IF filters, make this diagnostic an ideal choice to study electron temperature fluctuations with high radial resolution over a large bandwidth. To do so three steps are necessary:

- The signals are normalized turning the time traces into oscillations around zero over a stationary plasma phase identified as the flat top.
- The position of the emission volume for each channel is calculated and the normalized signals calibrated using as reference the Thomson scattering measurements.
- The normalized signals are used to calculate spectral quantities such as the cross power spectral density and correlation coefficient. These, together with information on the emission volumes position, are necessary to calculate the fluctuation amplitude profile, correlation lengths and propagation speed and direction.

All these steps will be described in more details in the following.

### 3.6.1 Signal normalization

To study fluctuations the first step is to find a stationary phase in the plasma long enough to allow detection of microturbulence, referred to as flat-top. Once this is selected, the raw signals  $S_{ft}$  are normalized:

$$S_{ft}^n = \frac{S_{ft} - \overline{S_{ft}}}{\overline{S_{ft}} - \overline{S_{bl}}} \quad (3.16)$$

$S_{ft}^n$  is the normalized signal in the selected flat-top phase, oscillating around 0,  $\overline{S_{ft}}$  is the average of the raw signal in that same phase and  $\overline{S_{bl}}$  is the baseline, defined as the average of

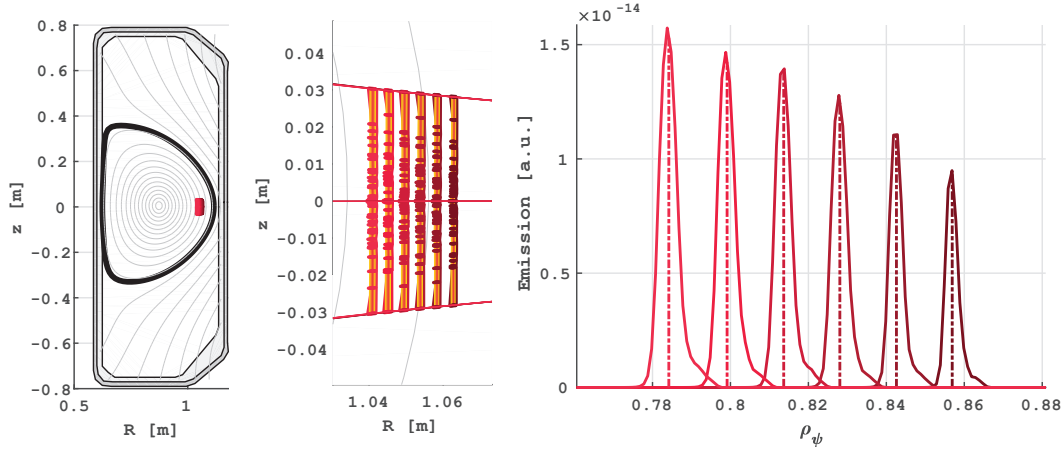


Figure 3.14 – Emission volumes of six channels for a discharge in which the horizontal  $z=0$  line of sight has been used calculated with TORAY, and the corresponding emission peaks over the flux coordinate  $\rho$ .

the signal over a time window where plasma has not yet started. To convert these normalized signals into temperature fluctuations, it is necessary to reconstruct the plasma emission volume for each channel. The normalized signals are then multiplied by the local electron temperature as measured by the Thomson scattering diagnostic.

### 3.6.2 Calculation of the emission volumes and signals calibration

The emission volumes are determined by the intersection of the resonant layers corresponding to the IF filters bandwidth with the antenna pattern of the line of sight. The latter is calculated using the ray tracing code TORAY [67][68]. In this way the effects of refraction of the emitted wave by the plasma between the emission location and the antenna are taken into account. One set of rays, for each channel, is propagated into the plasma taking into account the geometry of the launchers. Emissivity for X2 ECE is calculated along these rays and the emission volumes are estimated as the union of each ray's section that contains 95% of the integral emissivity. Finally, for each channel, the emission volumes are described through averaged values of the plasma characteristics ( $T_e$ ,  $n_e$ ,  $B$ ,  $\rho$ ) and their uncertainties, related to the emission volumes' finite extension. This technique also allows the estimation of the maximum detectable wavenumber during a particular plasma phase. Being  $d_{x,y,z}$  the dimensions of the emission volumes calculated by TORAY, it can be shown that the diagnostic is sensitive only to modes with  $k \leq 2/(d_{x,y,z}/2)$ . Details of this procedure can be found in appendix A.

An example of the emission volumes of six channels generated with this procedure and the corresponding emission regions in  $\rho$  are shown in figure 3.14.

### 3.6.3 Correlation analysis

Once all the channels' signals have been properly calibrated, correlation analysis can be used to extract information on the fluctuations in the plasma. The cross power spectral density (CPSD) for two signals  $S_1$  and  $S_2$  is calculated using Welch's method [69]. The signals are divided into  $n$  intervals of duration  $T$  and their Fourier transforms are averaged:

$$P_{12}(f) = \frac{2}{nT} \sum_{k=1}^n \hat{S}_{1k}^*(f, T) \hat{S}_{2k}(f, T) \quad (3.17)$$

Where  $\hat{S}$  is the Fourier transform of  $S$  and  $\hat{S}^*$  its complex conjugate. If  $S_1 = S_2$  one obtains the auto power spectrum.

The CPSD of signals coming from distinct channels is a complex quantity:  $P_{xy}(f) = |P_{xy}(f)|e^{i2\pi\phi_{xy}(f)}$ . The norm of the CPSD represents the power of the fluctuations' frequency components<sup>1</sup>, while its phase is proportional to the speed of propagation of the fluctuation between the two channels.

An example of the spectra obtained with these procedures for CECE channels on the flat top phase of a TCV plasma is shown in figure 3.15 as  $CPSD_{ft}$ . This is the standard appearance of CECE spectra on TCV: a strong low frequency component (0-10 kHz) related to slow, macroscopic oscillations (MHD modes, Sawteeth, *etc...*) followed by a broad and decaying feature that contains the effects of higher frequency fluctuations, normally associated with turbulence. At frequencies greater than approximately 200 kHz no physical fluctuations are normally observed so, to further improve the definition of the noise level of the system, the average of the norm of the CPSD over a frequency range where fluctuations are not expected to appear (normally 300-350 kHz), is treated as noise floor and subtracted from the whole CPSD ( $CPSD_{ft} - \langle CPSD_{NF} \rangle$  in figure 3.15). For even higher frequencies, the 450 kHz low pass filter in the video stage should eliminate any remaining power coming from the plasma. The residual observed power is due to the radiometer video stage electronics. It is indeed identical to the spectrum of the plasma baseline ( $CPSD_{bl}$  in figure 3.15), calculated over a time window in which the plasma had not yet started.

The temperature fluctuations amplitude, over a certain range of frequencies, can be calculated integrating the CPSD over the same frequency range. If the CPSD has been obtained from calibrated signals, then this will result in an absolute fluctuation level (*i. e.* in eV). This value can then be divided by the local electron temperature (obtained after the calculation of the emission volumes) to get the relative temperature fluctuations amplitude:

$$\frac{\delta T_{rad}}{T_e} = \frac{1}{T_e} \sqrt{\int_{f_a}^{f_b} P_{12}(f) df} \quad (3.18)$$

In this formula  $f_a$  and  $f_b$  define the frequency range of the fluctuations whose amplitude

<sup>1</sup>If the signals are in temperature units the norm of the CPSD is  $eV^2s$

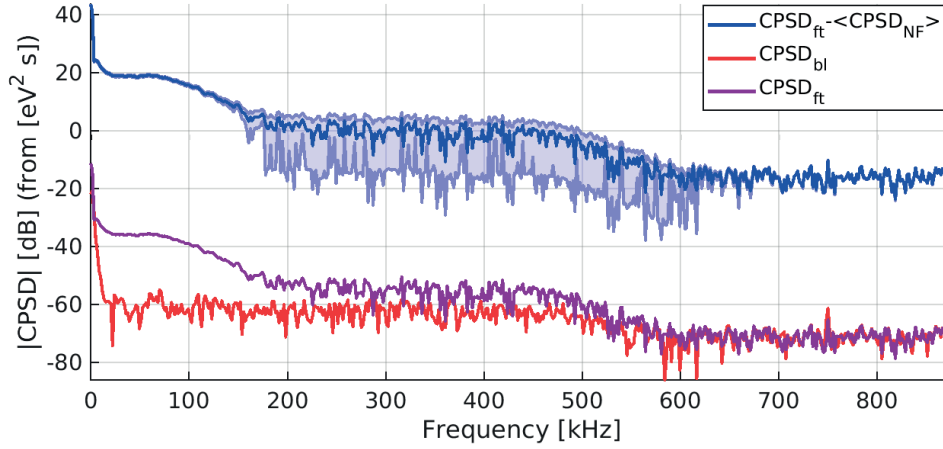


Figure 3.15 – Example of CPSD for two CECE signals acquired through the upper lateral line of sight and whose channels' center frequencies were separated by 500 MHz. The three curves are the CPSD of the flat top phase, that of the baseline ( $CPSD_{ft}$  and  $CPSD_{bl}$  respectively), and  $CPSD_{ft}$  with the average of the [300 350] kHz region subtracted from it to define the noise floor at 0 dB.

is to be calculated. As already mentioned, the [20 200] kHz region of the spectra shown in figure 3.15 is where turbulent micro fluctuations are expected to be observed in TCV. That corresponds to the frequency range normally chosen for the integration of equation 3.18. The low frequency range (0-20 kHz) could still contain fluctuations, like zonal flows, that are known to influence the saturated turbulence amplitude [70], but it is normally not taken into account in TCV due to the strength of low frequency components (MHD modes, sawteeth). The most common way to identify the frequency range to evaluate the fluctuations is to make use of the coherence or the phase of the correlation. The coherence, defined as:

$$\gamma_{12}^2(f) = \frac{|P_{12}(f)|^2}{|P_{11}(f)P_{22}(f)|} \quad (3.19)$$

contains similar information to the CPSD and is used in the calculation of uncertainties for many of the quantities introduced in this chapter. The phase of the CPSD between signals coming from different channels is normally characterized by stable values (related to the fluctuations propagation speed) and very low error bars for frequencies where fluctuations are coherent, while phase angle of noise assumes random values in the  $[-\pi \pi]$  range. These two quantities can thus be used to determine the lower and upper boundaries of frequency over which the fluctuations amplitude will be calculated as shown in figure 3.16.

While the quantities introduced up to now give information on the spectral composition of the fluctuations, another interesting approach is to compare the correlation between signals



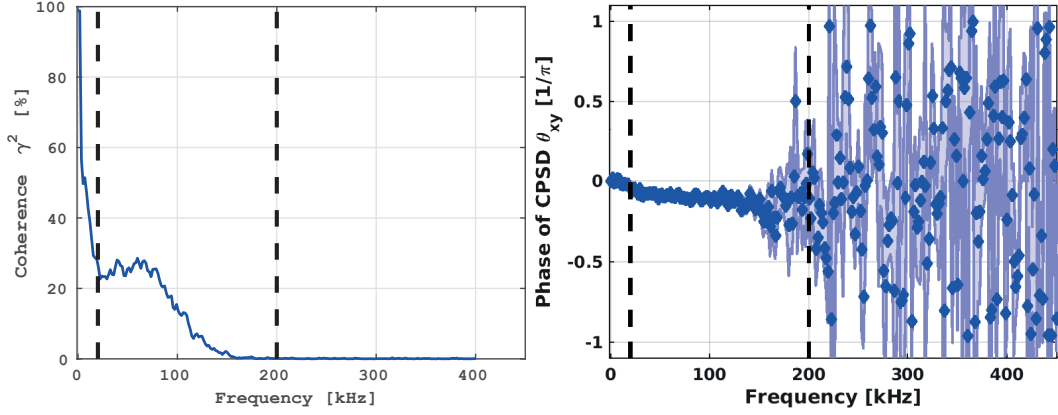


Figure 3.16 – Coherence and phase of two CECE signals coming from different channels. Together they are used to select the frequency range over which the fluctuations amplitude will be evaluated, represented in this case by the vertical black lines.

at different time delays. This is done using the correlation function, normally defined as:

$$R_{12}(\tau) = \frac{1}{T} \int_0^T S_1(t) S_2(t + \tau) dt \quad (3.20)$$

Another way of calculating this quantity allows to select the same frequency range that has already been used when integrating the CPSPD:

$$\begin{aligned} R_{12}(\tau) &= \frac{1}{2} \int_{f_l}^{f_h} P_{12}(f) e^{i2\pi f\tau} df + \frac{1}{2} \int_{f_l}^{f_h} P_{12}^*(f) e^{-i2\pi f\tau} df \\ &= \int_{f_l}^{f_h} \{ \Re(P_{12}(f) \cos(2\pi f\tau) + \Im(P_{12}(f) \sin(2\pi f\tau)) \} df \end{aligned} \quad (3.21)$$

Equation 3.21 is the one that will be used in this work.

Once the correlation function is known, the correlation coefficients for various pairs of channels can be calculated similarly to the coherence defined above.

$$\rho_{12}(\tau) = \frac{|R_{12}(\tau) - \overline{S_1 S_2}|}{\sqrt{(R_{11}(\tau) - \overline{S_1})(R_{22}(\tau) - \overline{S_2})}} \quad (3.22)$$

Due to the way the signals have been normalized this reduces to:

$$\rho_{12}(\tau) = \frac{|R_{12}(\tau)|}{\sqrt{R_{11}(\tau) R_{22}(\tau)}} \quad (3.23)$$

The correlation coefficients between different pairs of channels in the same plasma discharge, separated by  $\Delta \mathbf{r}$  are used to estimate the correlation length  $L_c$  of the fluctuations according to:

### Chapter 3. Electron Cyclotron Emission (ECE) and Correlation ECE diagnostics principles and their application in TCV

---

$$\rho_{12}(\tau = 0, \Delta r) = \rho_0 e^{-\left(\frac{\Delta r}{L_c}\right)^2} \quad (3.24)$$

To estimate  $L_c$ , the values of  $\rho_{12}(\tau = 0, \Delta r)$  for all couples of channels inside the discharge (1-2, 1-3,...1-6, 2-3... *etc.*) are plotted as a function of the channels' separation  $\Delta r^2$  and fitted with an exponential.

The statistical uncertainty in G, R, and  $\gamma^2$  is calculated using the formulas presented in [71]. The errors on derived quantities have been computed using error propagation.

### 3.7 Summary

ECE diagnostics are a fundamental part of most machines for nuclear fusion research. They can provide electron temperature measurements with high temporal resolution and spatial localisation. TCV is equipped with a 24 channel (750 MHz bandwidth) ECE radiometer that can view plasmas perpendicularly to the magnetic field, through two alternative horizontal lines of sight, at  $z = 0$  and  $z = 21$  cm above the vessel midplane. It is used to reconstruct electron temperature profiles with better temporal resolution than the Thomson scattering system. Correlation analysis can be applied to signals coming from an ECE diagnostic to study microfluctuations on the ion scale ( $k \cdot \rho_i \leq 1$ ). In the spectral decorrelation technique the signals coming from channels closely spaced are correlated. Fluctuations whose correlation length is of the order of the two emission volumes' separation distance will be detected by both channels. Using the cross-correlation technique, these fluctuations are enhanced while the incoherent noise is strongly suppressed. This technique allows the study of fluctuations  $\delta T_e / T_e < 1\%$ . The TCV CECE system can view the plasma through an upper lateral, steerable antenna and its IF section consists of six frequency tunable YIG filters (100 MHz bandwidth). Its high flexibility in the choice of the measurement locations, combined with the wide range of plasma shapes that can be explored in TCV, allows the study of microfluctuations with high sensitivity ( $\delta T_e / T_e < 0.5\%$ ) and spatial localisation ( $w_r \leq 1$  cm,  $w_z \sim 4$  cm for  $f_{ECE} = 70$  GHz) in a large range of radial positions.



## 4 Triangularity effects on fluctuations in ohmic tokamak plasmas

### 4.1 Transport in negative triangularity plasmas in TCV

One of the main goals of TCV is to study the effects of plasma shaping on confinement. Early studies meant to build a wide database of shape classes with different combinations of elongation,  $\kappa$ , and triangularity,  $\delta$ . These studies covered L-mode, limited, ohmic [17] and EC heated plasmas [16]. Increasing elongation was found to be always beneficial for the electron energy confinement time  $\tau_E$ . The effect of triangularity, instead, was found to depend on its sign. While positive triangularity degraded confinement with respect to a circular plasma, negative  $\delta$  discharges were found to present a comparable or higher  $\tau_E$ . In these studies the electron heat flux was modelled as [23]:

$$Q_e = -n_e \chi_e \langle |\nabla \rho|^2 \rangle \frac{\partial T_e}{\partial \rho}, \quad (4.1)$$

where  $\chi_e$  is the electron heat diffusivity, and  $\langle |\nabla \rho| \rangle$  is the flux surface averaged gradient of  $\rho$ . A direct effect of shaping on  $\chi_e$  was excluded in these earlier studies [17]. The observed higher  $\tau_E$  in negative with respect to positive  $\delta$  plasmas was, instead, attributed to changes in the gradient geometrical factor, with the positive  $\delta$  plasmas having a larger volume characterized by lower local temperature gradients, hence lower thermal conduction [17].

Further studies on EC heated discharges [23] investigated possible effects of shaping on the electron heat diffusivity,  $\chi_e$ . In equally heated discharges with comparable density and safety factor profiles, negative  $\delta$  plasmas showed reduced  $\chi_e$  with respect to positive  $\delta$ , thus attaining higher electron temperatures and ion temperatures profiles. The lower  $\chi_e$ , observed at equal heat flux, was postulated to be mainly related to the different temperature gradients resulting from the different shaping. Flux surface compression, in these cases, seemed not to have an effect. The confinement improvement observed in these discharges allowed to obtain quasi-identical  $T_e$  profiles using only half the heating power (0.6 MW instead of 1.3 MW) in a negative  $\delta$  plasma with respect to its matched positive  $\delta$  case, as shown in figure 4.1[3].

For all shapes in this set of discharges, the dependence of  $\chi_e$  on electron density  $n_e$ , tem-

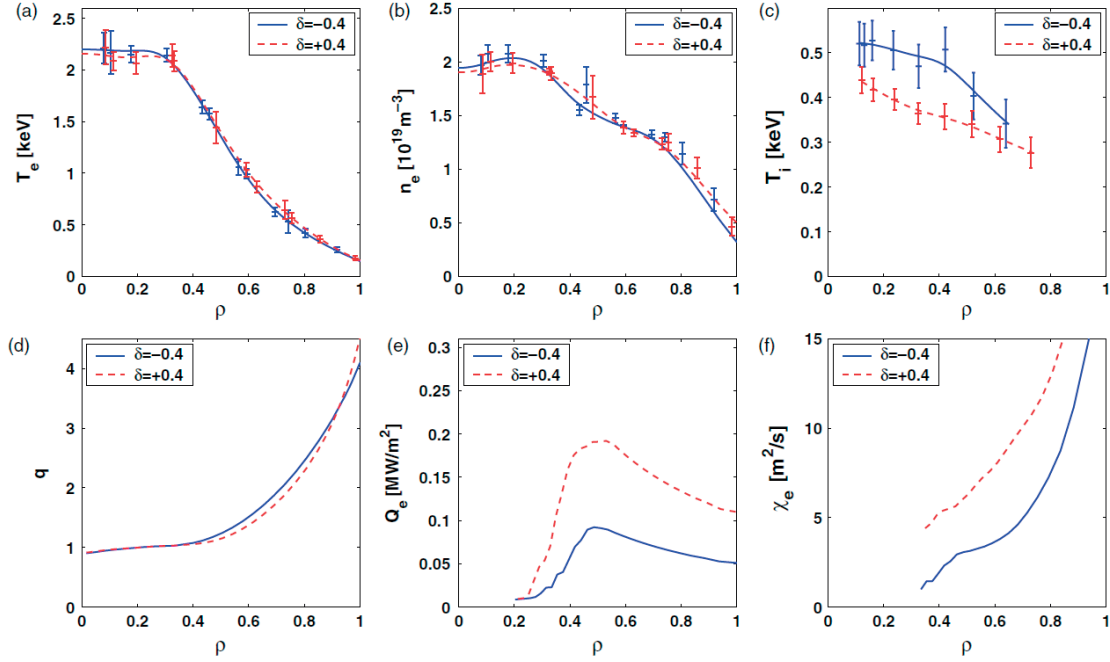


Figure 4.1 – Radial profiles in two plasmas with positive and negative triangularity in which comparable  $T_e$  (a) and  $n_e$  (b) have been achieved with only half of the ECH power in the latter case. c)  $T_i$  d)  $q$  e)  $Q_e$  f)  $\chi_e$ . From [3]

perature  $T_e$  and effective charge  $Z_{eff}$  was found to be well summarized into a dependence on the effective collisionality  $\nu_{eff} = \nu_{ei}/\omega_{De} \sim 0.1 R n_e Z_{eff} / T_e^2$  [23], the ratio between the electron-ion collision rate and the electron curvature drift frequency. This dependence was highlighted in figure 4.2 [3]. The decrease of  $\chi_e$  in plasmas with negative  $\delta$ , with respect to those with positive  $\delta$ , was particularly evident for cases with comparable  $\nu_{eff}$ . It is noteworthy to observe that, for increasing collisionality, the effect of  $\delta$  becomes weaker up to the point where no difference between positive and negative triangularity discharges is observed. This could explain why, in previous studies, a dependence of  $\chi_e$  on  $\delta$  was excluded [17]. At the time of these studies, no fluctuations diagnostics were operational on TCV, so the influence of shaping on turbulence could not be investigated experimentally [17][16][23][3].

#### 4.1.1 Numerical simulations

These experiments were accompanied by gyro-fluid (GLF23 [72]) and gyro-kinetic (LORB5 [73]) simulations, carried out using experimental equilibria and matched profiles. Trapped electron modes (TEMs) were identified as the dominant source of turbulence in all considered experimental cases, for the low to medium  $k$  in the wavenumber spectrum. TEMs are expected to be stabilized by collisions, so these results are consistent with the experimental observation of a  $\chi_e$  reduction for increasing  $\nu_{eff}$  [3]. The global, gyro-kinetic, collisionless simulations performed using the LORB5 code, demonstrated changes in growth rate and perpendicular

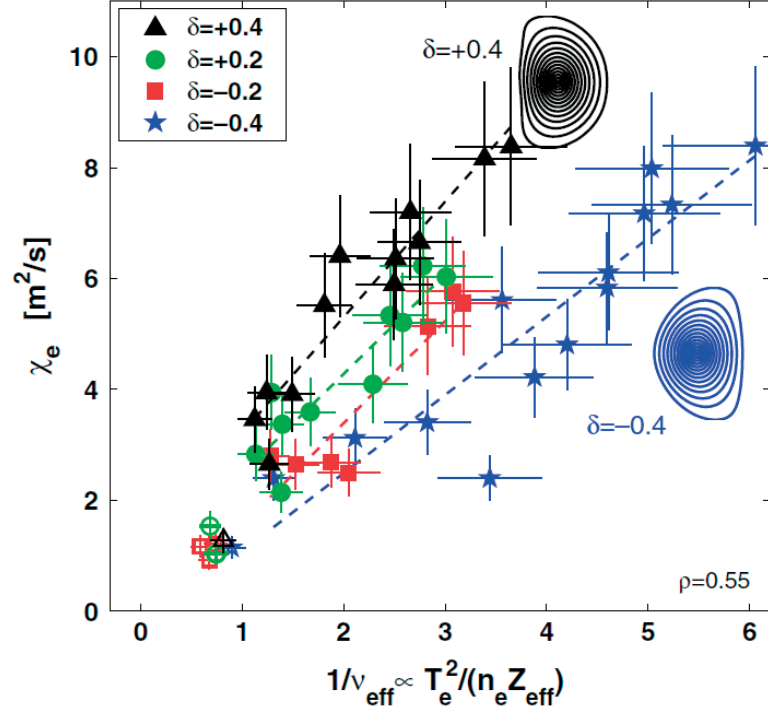


Figure 4.2 – Electron heat diffusivity  $\chi_e$  as a function of the effective collisionality  $\nu_{eff}$  measured at  $\rho_{vol} = 0.55$  for the discharges in [3]. The difference between positive and negative  $\delta$  plasmas is largest at low  $\nu_{eff}$  and becomes almost indistinguishable for high collisionality. From [3].

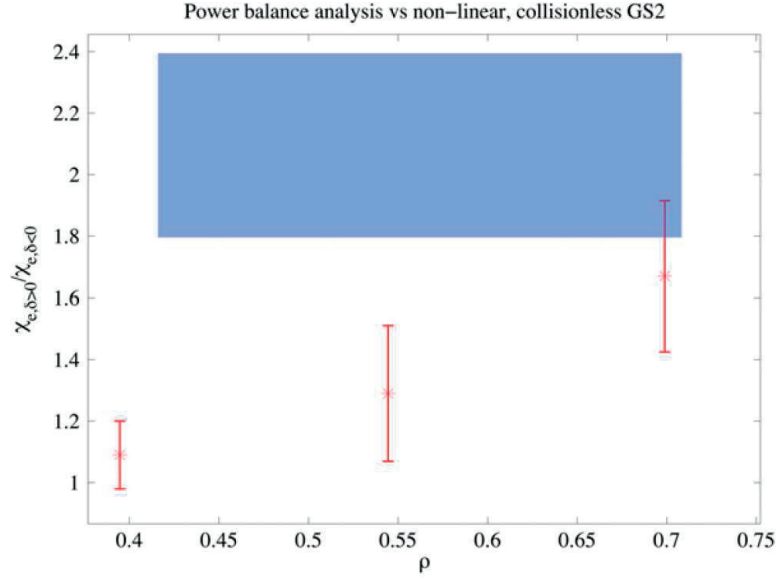


Figure 4.3 – Ratio between  $\chi_e$  for positive and negative  $\delta$  plasmas as calculated from the experiments (blue rectangle) and from non-linear GS2 simulations. Agreement is found within errorbars for  $\rho = 0.7$ . From [4]

wave vector between positive and negative  $\delta$  plasmas. The structure of the electrostatic potential fluctuations was observed to change with  $\delta$ , moving towards the plasma core for negative  $\delta$  discharges [3].

Further gyrokinetic simulations have been performed to better understand the effects of shaping on turbulence. All these simulations were limited to the ion scale, hence excluding Electron Temperature Gradient driven modes (ETG), taking into account impurities and electromagnetic effects. The latter, though, were found to be unimportant. The experimental profiles and the equilibria of the matched profiles case from [3] were used as inputs [4][6]. Local, non-linear, collisionless simulations, run with the flux tube GS2 code [24], confirmed TEMs to be the dominant instability [4]. These simulations reproduced the  $\chi_e$  variation between positive and negative  $\delta$  plasmas within error bars for  $\rho_{vol} = 0.7$ , as shown in figure 4.3, and found a partial TEM stabilization in the negative triangularity case [4].

Other local, linear and non-linear simulations, run with the GENE code [25] and this time including collisions, again found TEM dominated fluctuations and have qualitatively reproduced the heat flux reduction in negative  $\delta$  plasmas in the outer core [26][6]. The fact that the measured transport reduction in positions closer to the core could not be reproduced was attributed to the local nature of the simulations. In fact, the local triangularity quickly decreases in inner flux surfaces so, for those positions, the input equilibria of the different simulations are very similar.

Successive gradient driven, global simulations, this time run with only two kinetic species, managed to also qualitatively reproduce the heat flux reduction for positions closer to the

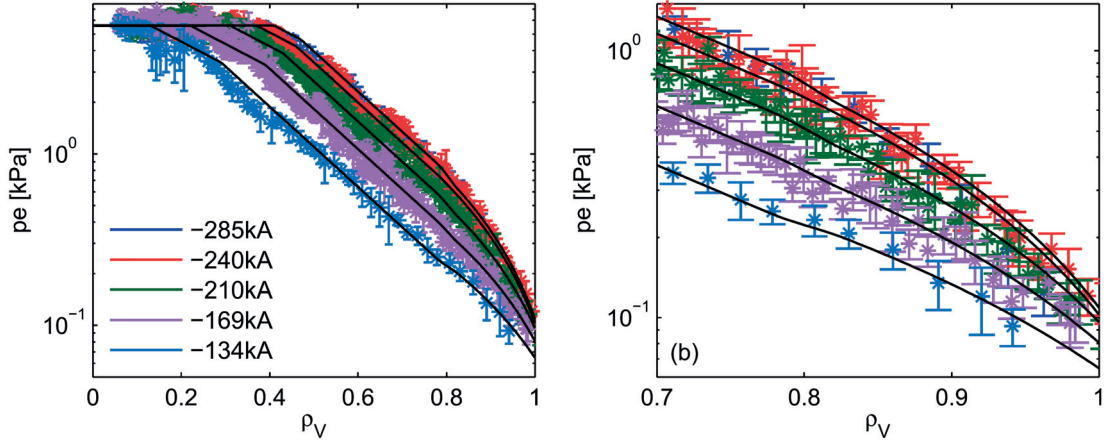


Figure 4.4 – Logarithmic plot of electron pressure profiles for a series of ohmic TCV discharges with varying plasma current. The experimental Thomson measurements have been fit using a constant gradient for the non-stiff region ( $\rho_{vol} > 0.8$ ), a constant logarithmic gradient for the stiff region and constant pressure inside the sawteeth inversion radius. From [5]

plasma core. This suggested that the observed stabilizing effect on fluctuations could be due to non-local effects *i. e.* those related to the finite value of  $\rho_* = \rho_{Li}/a$  typical of TCV ( $\sim 1/80$ ) [26].

#### 4.1.2 Profile stiffness

The confinement improvement observed in [23] and [3] extended well into the core ( $\rho_{vol} < 0.5$ ), despite the fact that the magnitude of  $\delta$  (positive or negative) decreases quickly when moving from the edge to the plasma interior. A coherent picture emerged based on a distinction between regions of different stiffness within the plasma.

In this work, stiffness is defined, as in [5], as the resistance the plasma opposes to attempts to peak its temperature profile when increasing the central heating or, more generally, to modify the shape of its profiles. In practice, this translates into the existence of a critical value for the temperature inverse scale length ( $R/L_{T_e} = R\nabla \log(T_e)/T_e$ ) [74]. When this value is reached, increasing the input heat flux almost exclusively increases the power dissipation across the plasma profile, instead of further peaking the temperature profile. This mechanism is explained by the onset of turbulent fluctuations after reaching the critical gradient that add anomalous terms to the heat transport. The higher the increase in dissipated power necessary to modify the shape of the profile, the stiffer a plasma is said to be.

Signs of stiffness defined in this sense have been observed in several tokamaks [75][76][77]. In TCV it has been noticed, particularly in L-mode limited plasmas, that a region exists around the plasma mid-radius (typically from the sawtooth inversion radius to  $\rho_{vol} \sim 0.8$ ), where the  $T_e$  and  $n_e$  scale lengths are generally insensitive to various plasma parameters, including edge

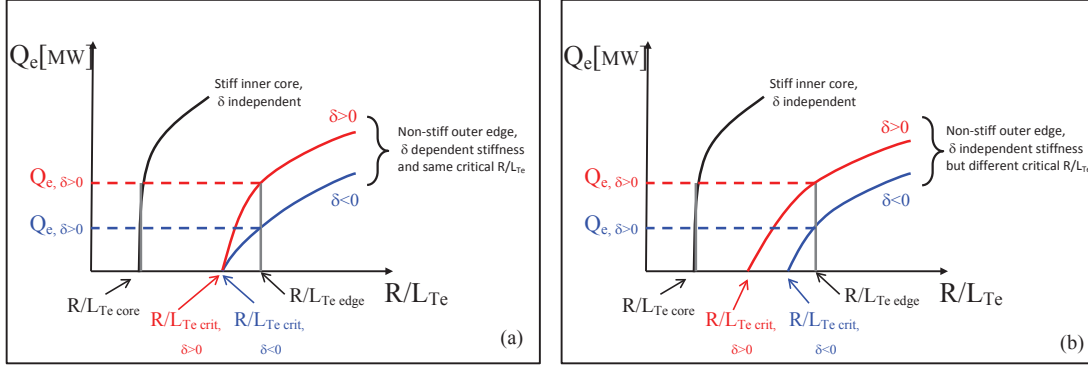


Figure 4.5 – Sketches of possible interpretations of confinement improvement in negative  $\delta$  plasmas consistent with the observations in [5]. Improvement in the plasma non stiff region could be due to a change in stiffness (a), critical gradient (b) or a combination of both. From [6].

triangularity [5]. This will be referred to in the following as the stiff region. Beyond this region ( $\rho_{vol} > 0.8$ ), the profiles can be fit with a radially uniform gradient that is found to change when changing plasma conditions ( $I_p$ , ECRH power,  $n_e$ ,  $\delta$ ) and thus this plasma region is considered to be non-stiff. An example of this distinction, taken from [5] is shown in figure 4.4. According to this observation, even if the magnitude of the local flux-surface triangularity quickly decreases when moving towards the core, a localised confinement improvement at the plasma edge, up to the outer limit of the stiff region, would raise temperature all the way across the profile. Indeed a higher  $\nabla T_e$  at the outer edge of the stiff region would imply a higher  $T_e$  well inside the plasma core, thanks to the constant normalized gradient [5].

In [6] a possible interpretation for the effects of negative triangularity in this frame was proposed. Figure 4.5 shows two different ways in which different heat fluxes, in the two different shapes, could still lead to comparable profiles (in this case matched  $R/L_{Te}$ ), as was experimentally observed [23]. In figure 4.5a, negative triangularity plasmas are assumed to have a higher stiffness with respect to positive triangularity ones in the non-stiff region. In figure 4.5b, instead, it is postulated that negative  $\delta$  plasmas present a higher critical gradient. Both these interpretations assume the existence of a stiff region, closer to the plasma core, as shown by the black curve in the figures. These figures represent only two extreme cases. A combination of these two effects could also justify the same final result. This interpretation of the role of negative triangularity in confinement improvement is in agreement with some of the results of the non-linear, flux tube GENE simulations mentioned in paragraph 4.1.1. The results of these runs, shown in figure 4.5 [6], suggest that, towards the plasma edge, where flux surface triangularity is high, negative  $\delta$  plasmas could present higher critical gradients for the saturated heat flux [6] with respect to positive  $\delta$  plasmas.

The argument that negative triangularity only improves confinement close to the plasma edge seems to be in contradiction with the experimental observation of a lower  $\chi_e$  in the plasma

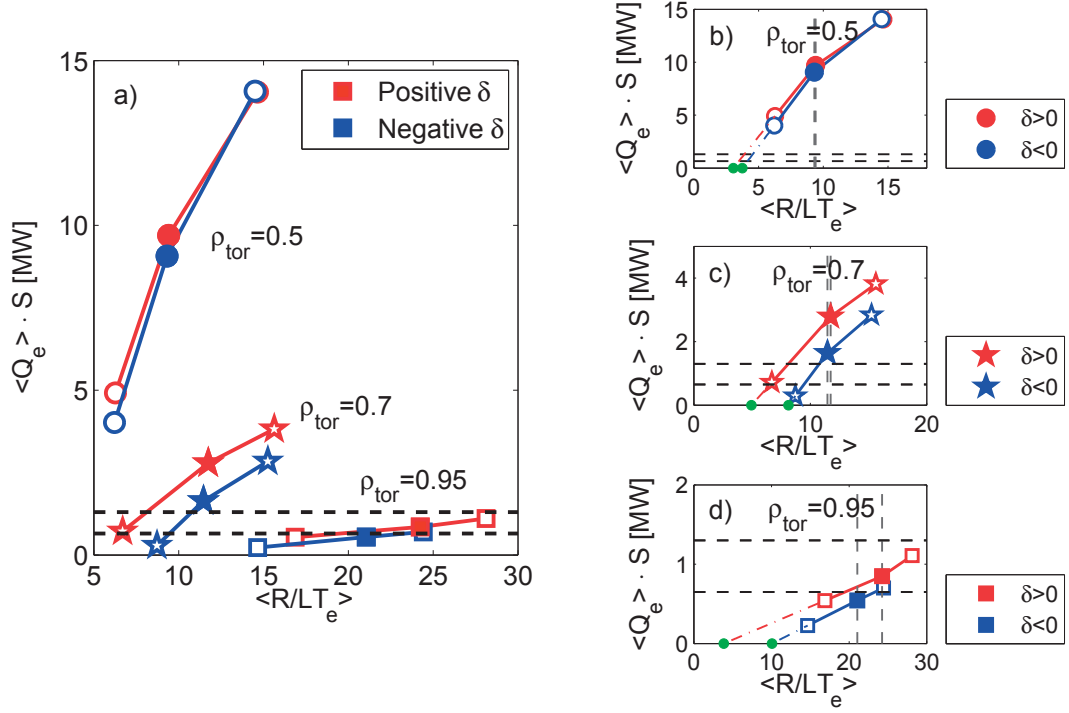


Figure 4.6 – (a) Heat fluxes at three different radial positions resulting from non linear, flux tube GENE simulations in which gradients have been varied to study the influence of negative triangularity on transport. Full markers represent the experimental gradients values. For the sake of clarity, the fluxes for each radial positions are plotted on different scales in (b)  $\rho_{tor} = 0.5$ , (c)  $\rho_{tor} = 0.7$  and (d)  $\rho_{tor} = 0.9$ . Dashed black lines represent the experimental heat fluxes. From [6].

core [3] mentioned in paragraph 4.1. This confusion is due to how electron heat conductivity is calculated in the experiments. Experimentally two main ways exist to calculate the heat diffusivity at a point in the plasma, power balance and perturbative analysis [78]. In [3], power balance analysis was used:

$$\chi_e = -\frac{Q_e}{n_e |\nabla T_e|} \quad (4.2)$$

In situations such as those represented in figure 4.5, the value of  $\chi_e$  calculated using power balance analysis can be seen simply as  $Q_e/(R/L_{Te})$ . This method would then have produced two different estimates of  $\chi_e$  in the core for positive and negative  $\delta$ , even in the presence of comparable stiffness and critical gradients (black curves in both figures 4.5a and 4.5b). The experimental results are then consistent with the possibility that negative  $\delta$  only influences confinement in a non-stiff region closer to the plasma edge, where the magnitude of triangularity is higher, and that this results in higher temperature across a large fraction of the radial profile due to the constant normalized scale length characteristic of the stiff region of the plasma.

### 4.1.3 Fluctuations measurements in previous experiments

With the installation of core fluctuations diagnostics on TCV, namely the tangential phase contrast imaging (TPCI) [7] and CECE, further experimental study of the effects of negative  $\delta$  and collisionality on fluctuations have been undertaken.

Discharges with positive and negative triangularity were studied using the TPCI diagnostic both in matched heating and matched profiles conditions [7]. These experiments showed a suppression of relative density fluctuations, stronger at the plasma edge but reduced fluctuations were observed up to  $\rho_{vol} = 0.5$  (figure 4.7). The normalized gradients of these discharges suggested the presence of differences in the stiffness of positive and negative triangularity plasmas, in both matched profiles and matched heating experiments. The fluctuations data were plotted as a function of the local temperature and density scale lengths to investigate possible effects of shaping on the critical gradients. Fluctuation amplitudes, for all shapes, were observed to be almost constant for increasing normalized gradients up to a value, after which they began to rise quickly, as shown in figure 4.7b and 4.7c. This value corresponds to the gradient in the stiff region of the plasma, where normalized gradients were observed to remain constant, and was identified as the critical gradient, as defined in [5]. These observations suggested that plasma triangularity had an effect on the fluctuations characteristic. In negative  $\delta$  cases, a higher critical gradient than in positive  $\delta$  discharges was observed. Furthermore, negative triangularity seemed to reduce profile stiffness, in the sense that higher temperature gradients could be reached at the expense of a smaller increase in the fluctuations level with respect to positive triangularity plasmas, as seen in particular in figure 4.7c. This is in partial agreement with what was observed in numerical simulations [6]. It is important to stress that this kind of representation is not equivalent to the results of the GENE runs mentioned in



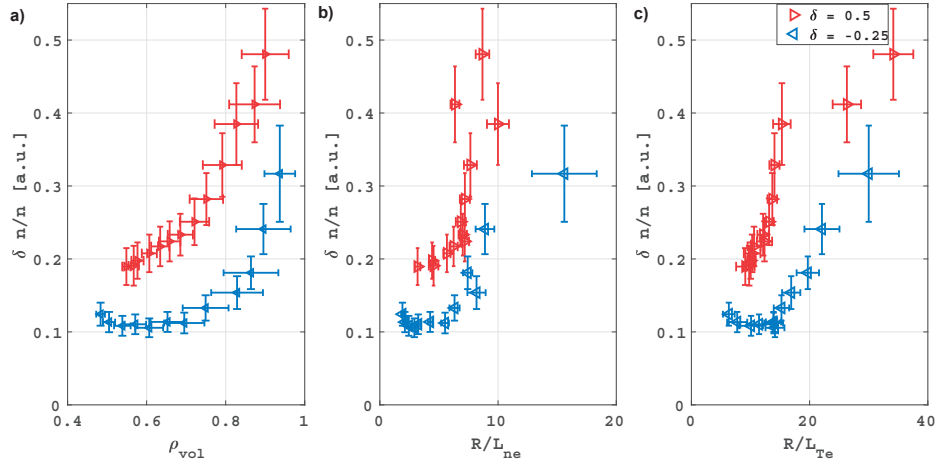


Figure 4.7 – Relative density fluctuations profile in positive and negative triangularity plasmas with matched heating (a). The same points have also been plotted as a function of the local normalized inverse density (b) and temperature (c) scale lengths to highlight the different threshold behaviour for different shapings. From [7].

4.1.1 and shown in figure 4.6. In that case the critical gradients that are estimated belong to a specific flux surface, while the experimental fluctuation measurements have been collected from a large fraction of the radial profile. The fluctuations spectra indicated that negative  $\delta$  affected mainly the lower frequencies ( $f < 200$  kHz). A reduction of the decorrelation time and correlation length, with respect to positive  $\delta$  plasmas, was observed in negative  $\delta$  discharges.

The effect of collisionality on fluctuations was investigated in another set of measurements, performing a triangularity scan in an ohmic and an EC heated discharge [7]. In the first case density fluctuations were found to decrease going from positive to negative triangularity, while collisionality remained constant (both  $n_e$  and  $T_e$  increased slightly). In the EC heated discharge, instead, the scan towards negative  $\delta$  caused almost no change in the measured fluctuations level. When moving to negative triangularity, in fact, temperature rose, thus reducing collisionality. This in turn favoured the increase in fluctuation amplitudes until an equilibrium was reached. These observations are consistent with previous transport studies [3] mentioned in 4.1. In high collisionality plasmas, such as the ohmic discharge in this case or the experiments in [17], the effect of triangularity is expected to be small, while confinement improvement becomes significant at lower collisionalities, as stated in [3].

In a separate campaign, the CECE diagnostic of TCV was used to measure radiative temperature fluctuations from ohmic, L-mode, limited discharges with  $\delta$  varying from -0.4 to +0.4 with the same plasma current [79]. Observations taken with the horizontal,  $z=0$  line of sight revealed a suppression of the radiative temperature fluctuations in negative triangularity discharges especially at the edge, but penetrating deep into the plasma core (up to  $\rho \sim 0.4$ ).

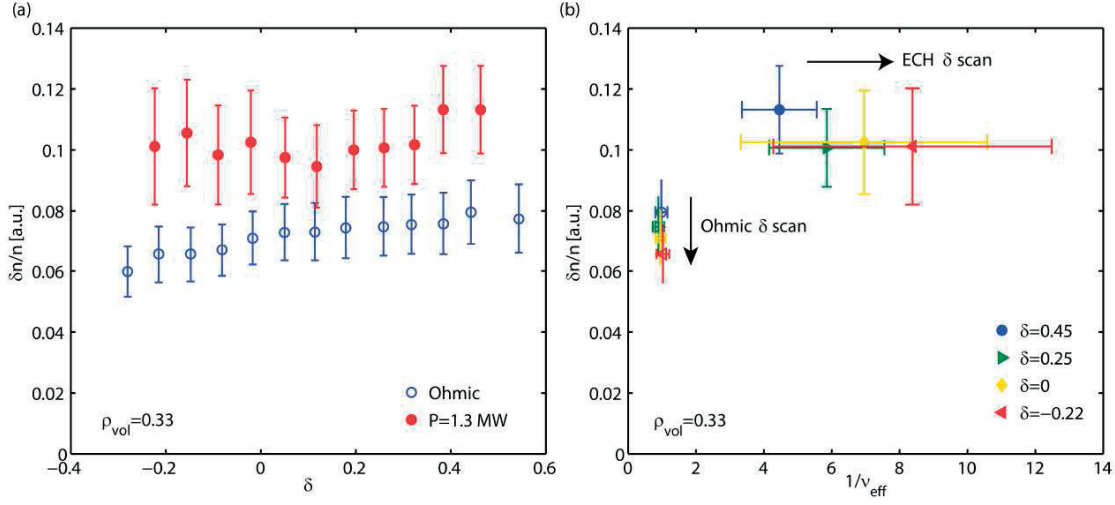


Figure 4.8 – Relative density fluctuations in ohmic and EC heated plasmas during a scan from positive to negative  $\delta$  as a function of triangularity (a) and  $v_{eff}$  (b). From [7].

## 4.2 Flucuations measurements using an upper lateral line of sight

### 4.2.1 Description of the experimental conditions

The goal of this study was to further investigate the effects of negative triangularity on radiative temperature fluctuations by expanding the measurement region. The discharge setup was based on those studied in [79]. Ohmic, limited, L-mode plasmas were realized in the upper part of the TCV vessel ( $z_{axis} = 0.25$  m and  $z_{axis} = 0.3$  m for negative and positive  $\delta$  discharges respectively) to optimize the CECE measurements taken with the upper lateral, steerable line of sight. Four different triangularities ( $\delta = +0.5, +0.3, -0.3, -0.4$ ) were explored at constant elongation ( $\kappa = 1.4$ ) and plasma current ( $I_p = 225$  kA), with comparable density profiles (line averaged density  $n_{e,av} = 2 \cdot 10^{19} m^{-3}$ ). The plasma temperature was left free to evolve. Due to the difference in shaping, the safety factor profile is different in the two discharges when using the same plasma current. Thus for the positive  $\delta$  and negative  $\delta$  discharges,  $q_{95} = 3.6$  and  $q_{95} = 3.3$  respectively. The carbon content, as measured by the CXRS diagnostic results in  $Z_{eff} =$

The resulting profiles are shown in figure 4.9. Electron temperature and density profiles shown here were deduced from measurements taken using the Thomson scattering diagnostic [57], while ion profiles and  $Z_{eff}$  values were obtained through the charge exchange recombination spectroscopy diagnostic of TCV [80]. Examples of the resulting plasma cross sections for the  $\delta = +0.5$  and  $\delta = -0.4$  discharges are shown in figure 4.13. All discharges had at least 500 ms of flat top where all the measurements were taken.

For discharges placed so high in the vessel, the CXRS could not provide full coverage of the plasma cross-section. The measurements shown in figure 4.9c were taken from a series of matching discharges reproduced at the vessel midplane ( $z_{axis} = 0$ ), where ion temperature and

density could be measured across the whole profile. In these discharges great care was taken to have density and temperature profiles very similar to those with  $z_{axis} = 25$  cm. An example of the profiles obtained in the  $z_{axis} = 0$  discharges is shown in figure 4.10. Plasma geometry and emission volumes position in these discharges are shown in figure 4.19. Error bars on the profiles are deduced from the experimental uncertainties of the Thomson scattering. For gradients, also the uncertainty in the radial localization of Thomson measurements was taken into account ( $\sigma_\rho \sim 0.01$ ) and the final error bar is calculated using error propagation.

As expected, the negative triangularity discharges showed a higher temperature over the whole profile. Note that this is despite the fact that the ohmic power, calculated as the product of the plasma current and the voltage measured by the flux loops around the vacuum vessel in a stationary phase, actually decreased in going from positive to negative triangularity. The higher temperature, in fact, modified the plasma resistivity, changing the ohmic power from 329 kW at  $\delta = +0.5$  to 287 kW at  $\delta = -0.4$ . The fact that  $T_e$  was considerably higher with respect to positive  $\delta$  even though the heating power was reduced by  $\sim 15\%$  is an additional sign of the improved confinement in negative triangularity plasmas. Looking at the ratio between electron temperature profiles of the discharges with  $\delta = +0.5$  and  $\delta = -0.4$ , a region where the temperature ratio was almost constant at  $\sim 1.4$  could be distinguished between  $0.45 < \rho_{vol} < 0.7$  (figure 4.11). This is what is expected to happen in the stiff region of a plasma [5], as mentioned in 4.1.2. A confirmation of this observation could be found by looking at the normalized temperature gradients for the differently shaped discharges (figure 4.9f). In the same radial range, despite the differences in the temperature profile, the value of the inverse temperature scale length was very similar across the different shapes considered. For  $\rho_{vol} > 0.75$ , instead,  $R/L_{Te}$  changed and the temperature gradient of the negative  $\delta$  discharges was larger than the positive  $\delta$  case. This was hence identified as the non-stiff region where the edge triangularity effectively exerted its influence [5].

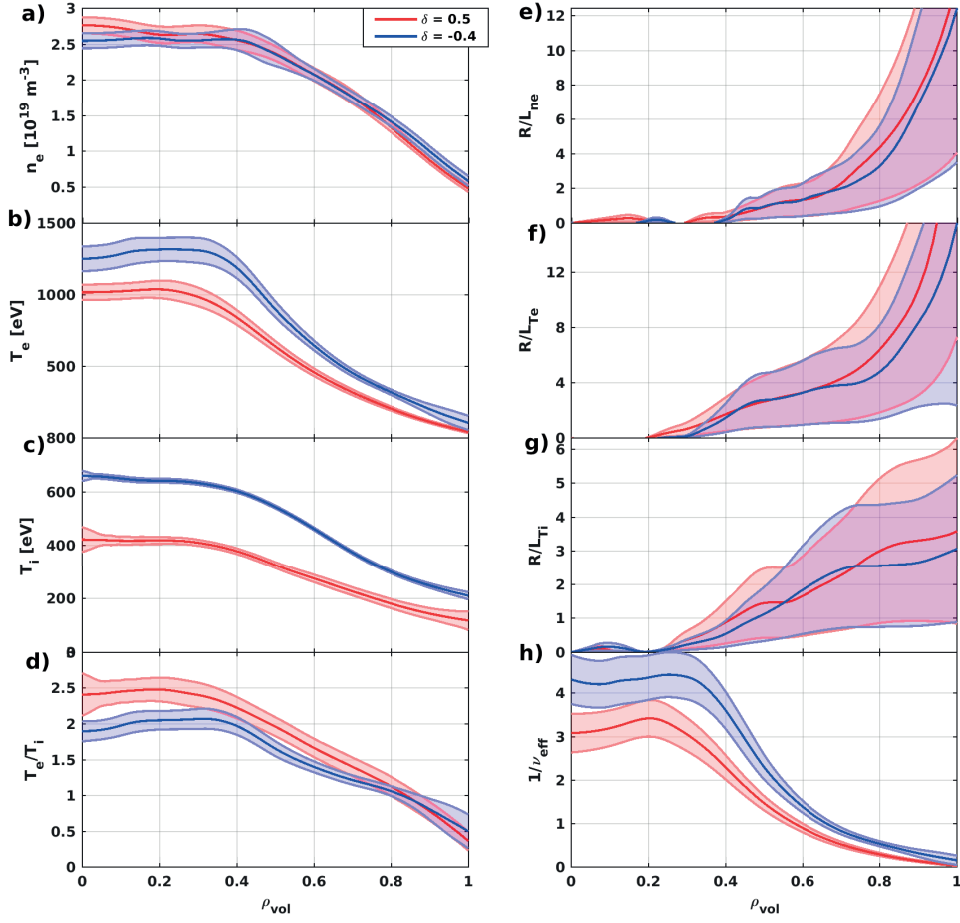


Figure 4.9 – Profiles of the model discharges for the two most extreme shapes ( $\delta = 0.5$  and  $\delta = -0.4$ ). a) Electron density. b) Electron temperature. c) Ion temperature. d) Electron/ion temperature ratio. e) Normalized density scale-length. f) Normalized electron temperature scale length. g) Normalized ion temperature scale length. h) Inverse effective collisionality. The electron profiles are calculated from Thomson scattering measurements while ion temperature and  $Z_{eff}$  from charge exchange recombination spectroscopy measurements.

These discharges were ideal targets to observe how fluctuations change in positive and negative triangularity plasmas. Care was taken in selecting the line of sight and the CECE channels frequencies to obtain fluctuations measurements both in the stiff and non-stiff regions of the plasma.

#### 4.2.2 Temperature fluctuations profiles

After the development of a target for the four different shapes, the corresponding plasma discharges were repeated three times each, with different frequency settings for the CECE channels. In this way it was possible to obtain measurements from eighteen plasma volumes covering the region  $0.3 < \rho_{vol} < 0.95$  and  $0.3 < \rho_{vol} < 0.85$  for the positive and negative

## 4.2. Fluctuations measurements using an upper lateral line of sight

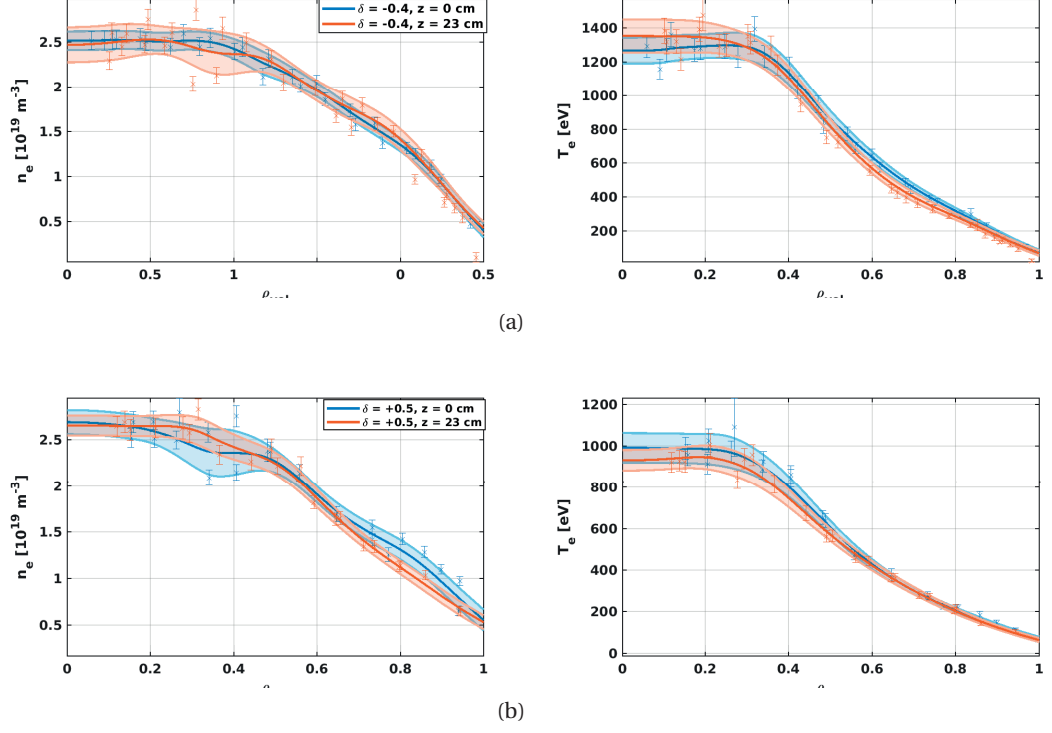


Figure 4.10 – Electron temperature and density profiles of the model discharges ( $z_{axis} = 23$  cm) and corresponding plasmas repeated at  $z = 0$  to have CXRS measurements across the whole radial profile.

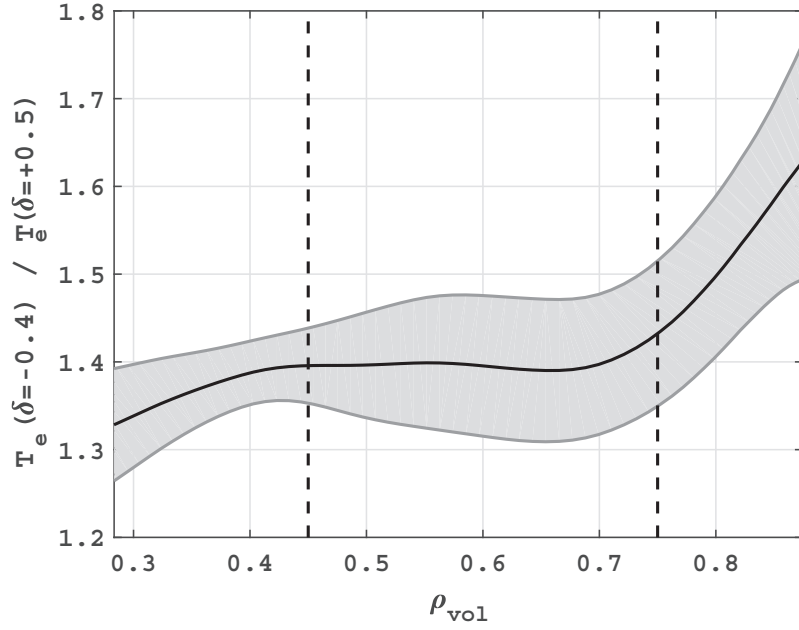


Figure 4.11 – Electron temperature ratio between the  $\delta = -0.4$  and  $\delta = +0.5$  discharges.

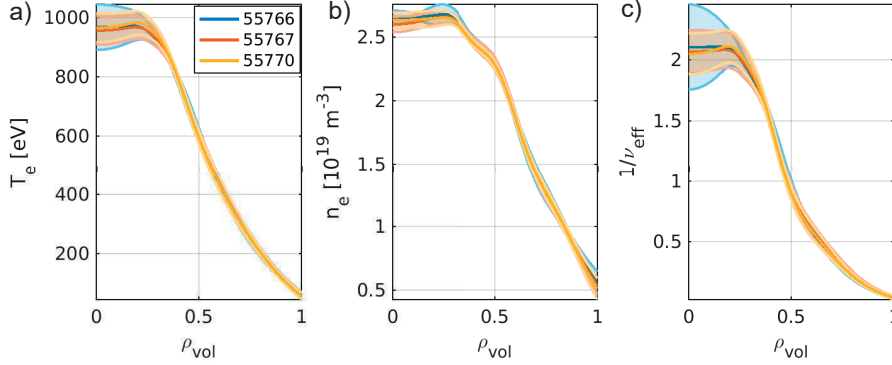


Figure 4.12 – Profiles obtained for the repetitions of the target  $\delta = +0.5$  discharge. Radial profiles of electron temperature (a) electron density (b) and inverse effective collisionality (c)

triangularity discharges, respectively. The position of the emission volume for each channel, in each different discharge was calculated via ray tracing, using the TORAY code [67] [68], as explained in appendix A. The discharges showed excellent reproducibility as is shown in figure 4.12 for the  $\delta = 0.5$  case.

In figure 4.13 the shapes of the two target discharges for  $\delta = +0.5$  and  $\delta = -0.4$  are shown together with the reconstructed position of the emission volumes of the whole set of measurements. The radial width of the emission volumes, taking into account the 100 MHz IF bandwidth of the filters, was  $\sim 3$  mm. Applying equation (3.12) together with the considerations in appendix A, the channels were sensitive to modes whose radial wavenumber  $k_r \leq \frac{2}{d_r/2} \sim 13 \text{ cm}^{-1}$ . The chosen frequency spacing of the channels (500 MHz) corresponded to physical distances varying from 0.8 cm for the outer channels to 0.65 cm for the inner ones. To appear in the cross-correlation analysis, a fluctuating structure needed to be large enough to be detected by both emission volumes involved. If the emission volumes lay on the magnetic flux surfaces, only fluctuations with radial correlation lengths larger than the volumes separation would be detectable. In these experiments, the channel separation is comparable with the ion larmor radii ( $\rho_{Li} \sim 2$  mm,  $k\rho_{Li} \sim 1$ ).

Cross-correlation analysis, following the procedure introduced in 3.6, was performed for each pair of adjacent channels (1-2, 2-3 etc...), over a 500 ms time period ( $N_s = 875$  kS). Examples of the cross power density (CPSD) spectra obtained with this technique are shown in figure 4.14. In these spectra the positive triangularity discharges showed a broadband feature between  $\sim 20$  and 160 kHz, absent in the negative triangularity case. This feature seemed to reduce in both amplitude and bandwidth moving towards the plasma core. A consistent behaviour could also be observed in the phase between the CECE signals coming from neighbouring channels, as shown in figure 4.15. In the same range of frequencies where coherent fluctuations were observed in the power spectra, positive triangularity discharges showed a negative phase difference, weakly increasing in magnitude with frequency. In the convention selected for these calculations, a negative phase signifies that the fluctuations were first observed in the

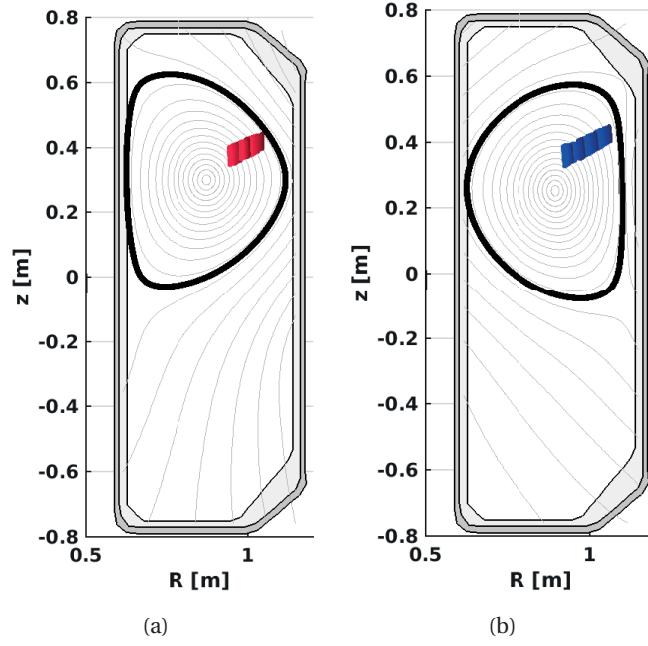


Figure 4.13 – Plasma cross sections and position of the CECE emission volumes for the measurements taken with  $\delta = 0.5$  (a) and  $\delta = -0.4$  (b).

outer channels, suggesting inward propagation. Moving from  $\rho_{vol} = 0.8$  to  $\rho_{vol} = 0.4$ , the absolute value of the phase decreased slightly. In the negative triangularity case, a qualitatively similar behaviour could be observed, but the results are less clear due to the lower signal to noise ratio in the measurements. Combining the cross-phase measurements with the reconstruction of the emission volumes in the plasma, it was possible to estimate the speed and the direction of propagation of the fluctuations between different channels. This is explained in details in appendix C.

The fluctuation amplitudes were calculated, from the integral of these spectra, over the 20-200 kHz range. This choice excluded the low frequency range where the spectrum is dominated by coherent fluctuations, and the high frequency range, where no fluctuations are expected to exist, as mentioned in 3.6.3. Furthermore, negative triangularity is known to have an effect on sawteeth period and amplitude [81], so differences in the low frequency range could not be directly associated with changes in the turbulence activity. In this case, anyway, negative and positive triangularity discharges showed comparable values of absolute fluctuations amplitude in the 0-20 kHz spectrum, over the whole range of measurements. The absolute fluctuations were normalized with respect to the mean of the electron temperature in the volumes from which the CECE signals that were being correlated were coming.

Taking into account the IF and video bandwidth of the system, and the averaging time, the minimum detectable fluctuation for these measurements can be calculated using equation

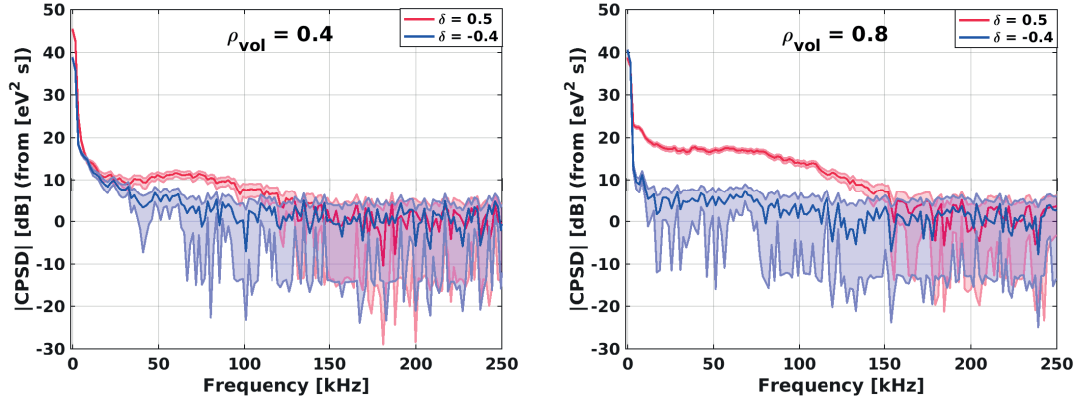


Figure 4.14 – Cross Power Spectral Density obtained from correlation analysis over 100 ms of CECE signals coming from couples of neighbouring channels ( $\Delta f = 0.5$  GHz) at  $\rho_{vol} = 0.8$  and  $\rho_{vol} = 0.4$ , in positive and negative triangularity. The noise level is at 0 dB for all the curves.

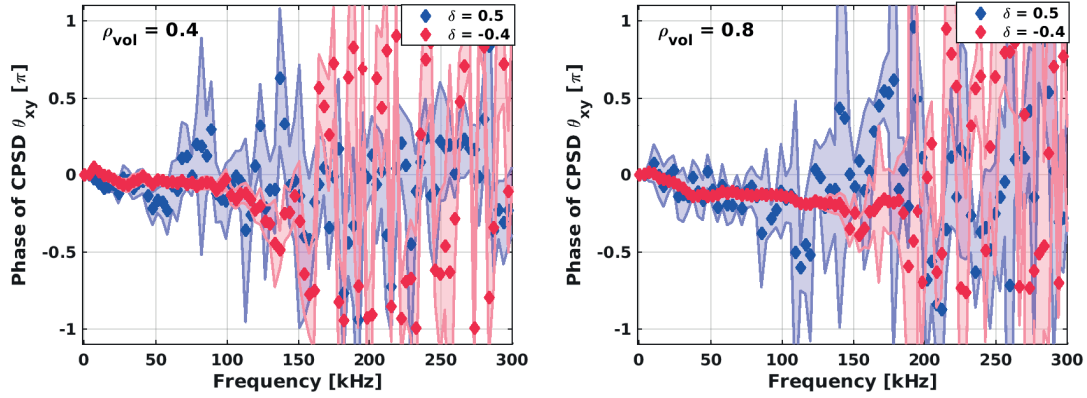


Figure 4.15 – Phase difference between the same couples of neighbouring channels shown in figure 3.15. A negative phase corresponds to fluctuations moving from channels closer to the edge towards those closer to the plasma core.



3.3:

$$\delta T_e / T_e = \sqrt{\frac{2B_{fluct}}{B_{IF}} \frac{1}{\sqrt{N_s}}} \approx 0.3\%. \quad (4.3)$$

where  $B_{fluct}$ , in this case, is the bandwidth over which the fluctuations were being integrated (180 kHz).

As already mentioned in 3.3.2, fluctuations measurements with the CECE diagnostic in TCV need to be interpreted taking into account the low optical depth of the plasmas. From the optical depth profiles for these experiments, calculated integrating  $\alpha(s)$  along the line of sight as detailed in appendix [?],  $\tau \sim 0.5$  at  $\rho_{vol} = 0.85$ . A conservative value for the reflectivity of the carbon tiles (as in TCV) is  $\chi \sim 0.76$  [82], resulting in  $A2(\tau, \chi) = 0.33$ . Preliminary non-linear, electromagnetic, gyrokinetic simulations suggest that in these discharges, the ratio  $\frac{\delta T/T}{\delta n/n}$  should be between 0.5 and 1. The latter was considered, in the frame of an upper limit estimation. The resulting maximum relative contribution of density on the measured fluctuation, obtained from equation 3.15, would then be below 20% at  $\rho_{vol} = 0.85$ . For radial positions closer to the core this value quickly decreased. In any case, in this work, an exact estimation of the electron temperature fluctuations is not attempted but, as already mentioned, only fluctuations of the radiative temperature are discussed.

The profiles of relative temperature fluctuations,  $\delta T_{rad} / T_e$ , are shown in figure 4.16a. A strong suppression of the fluctuations in negative triangularity compared to positive triangularity, especially close to the edge, could be observed. At  $\rho_{vol} \sim 0.8$  the fluctuation level in the  $\delta = -0.4$  case was less than one third of the one with  $\delta = 0.4$ . The suppression of the fluctuations could also be observed in the absolute fluctuations amplitude (figure 4.16b) showing that the difference in temperature was not the only factor responsible for this effect. For radial positions closer to the plasma core the difference quickly decreased, but it is interesting to note that fluctuations in positive  $\delta$  discharges remained measurably higher than those in negative  $\delta$  down to  $\rho_{vol} = 0.55$ , where the magnitude of the plasma triangularity has already decreased to less than  $\sim 40\%$  its edge value.

These measurements, taken over a wide fraction of the radial profile, were also used to study the dependence of the relative fluctuations on the normalized inverse density and temperature scale lengths, as shown in figure 4.16 b and c. Obviously, over the plasma region considered, these scale lengths were not the only parameters changing. Nonetheless, the measurements suggested that a threshold gradient was present in both temperature and density, corresponding to the point of sharp increase in fluctuation level. In the positive  $\delta$  discharges, the sharp fluctuation rise occurred in a small region, corresponding to the stiff region of the plasma, where fluctuations reached the level measured at the edge. A similar trend was not observed in negative triangularity discharges. It could be hypothesized that negative triangularity discharges have a higher critical gradient beyond the range explored in these experiments. This would be in agreement with the results of the non-linear gyrokinetic simulations performed in [6][26].

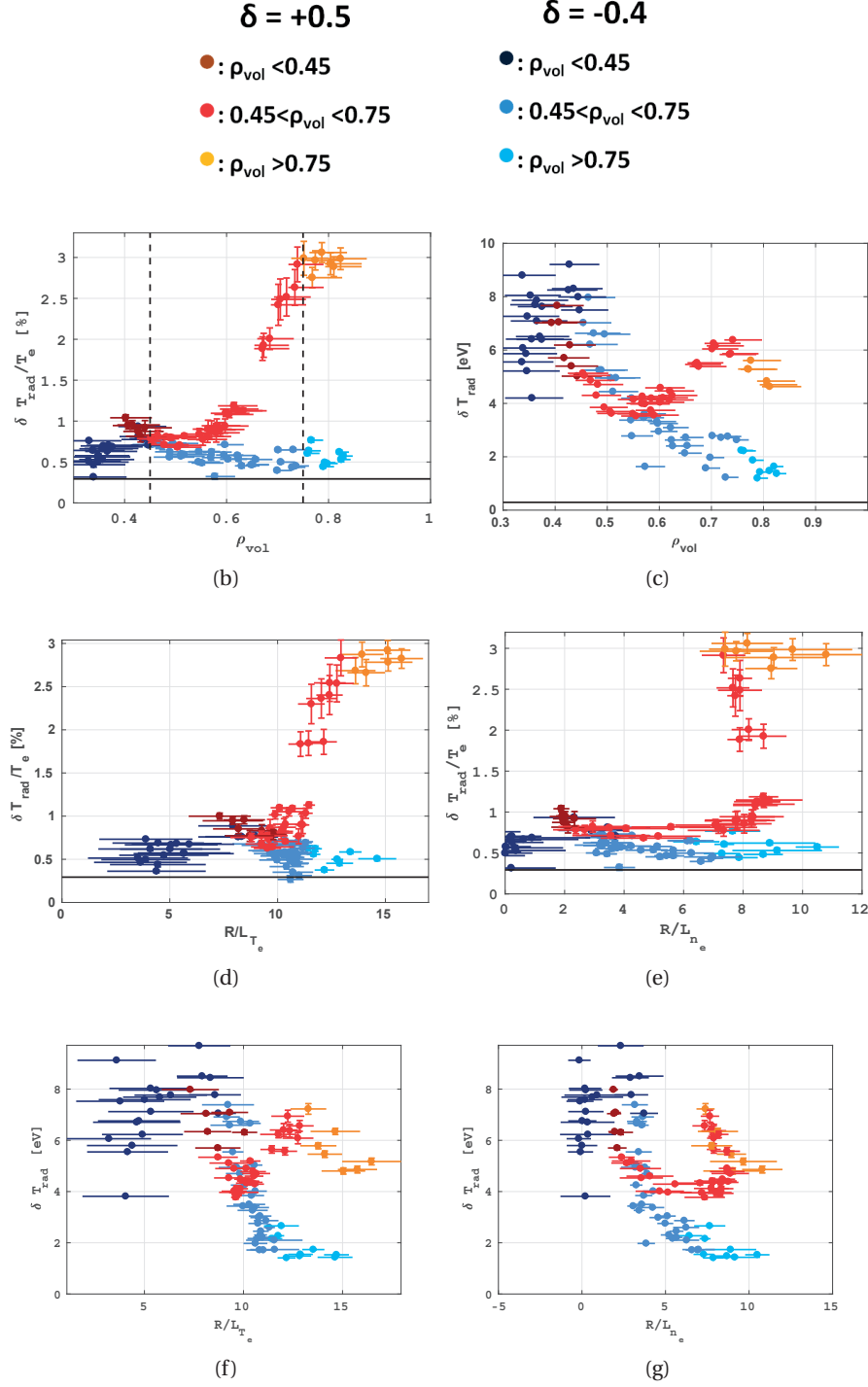


Figure 4.16 – a) Radial profiles of relative radiative temperature fluctuations amplitude for different triangularity values. The fluctuations amplitude is reduced changing shape from positive to negative triangularity and the effects extends up to  $\rho_{vol} = 0.5$ . A similar effect can be observed also in the absolute fluctuations profiles (b). The same data are plotted against the normalized inverse density (c, e) and temperature (d, f) scale lengths. Notice that these data points combine measurements taken over a wide fraction of the radial profile.

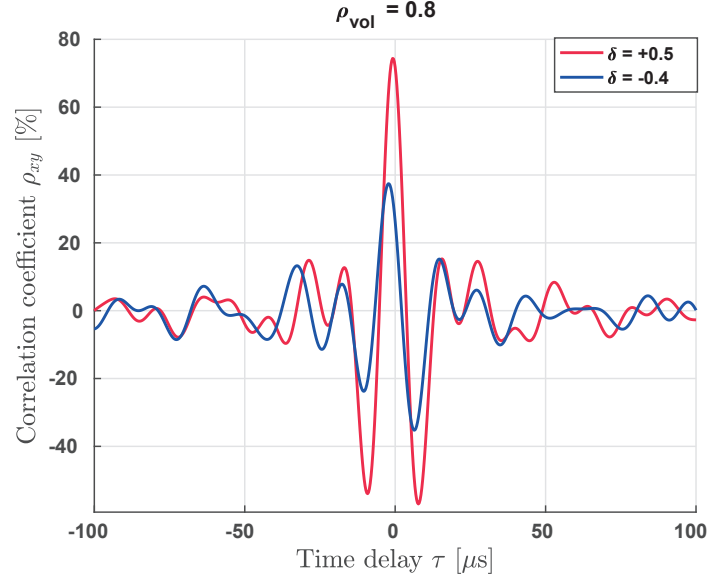


Figure 4.17 – Correlation coefficient for couples of channels at  $\rho_{vol} \sim 0.8$  in positive and negative  $\delta$  plasmas. The former show a much higher correlation level, while both of them indicate that fluctuations are observed first in the outermost channels (negative  $\tau$  for the maximum correlation), with a slightly different delay.

The correlation coefficients of pairs of neighbouring channels confirmed the higher coherence observed for positive  $\delta$  with respect to negative  $\delta$  discharges, as shown in figure 4.17 for the outermost channels of both series of plasmas. In this representation, a negative delay  $\tau$  corresponds to the fluctuations being detected first in the channel closer to the plasma edge.

Further information on the propagation of the fluctuations across the channels could be obtained by looking how  $\rho_{xy}(\tau)$  varies for increasingly separated pairs of channels (still within the same discharge). An example is shown in figure 4.18. For the positive  $\delta$  discharge, the growing time delay of maximum correlation ( $\tau_{max}$ ) for couples of channels further apart was particularly evident. The situation was less clear in the negative triangularity case, where the lower fluctuation level produced noisier correlation functions. Still, the fact that in negative  $\delta$  the correlation coefficient fell quickly to noise level when moving away from the reference channel was indicative of a lower correlation length of the fluctuations in this case.

### 4.3 Fluctuations measurements using a horizontal line of sight

As already mentioned, a series of discharges with matching shapes and profiles to those mentioned above was reproduced at the vessel midplane. The goal of these additional experiments was to obtain good measurements of the density and temperature of carbon in these plasmas. The profiles of carbon density, temperature and velocity obtained in this way were used as inputs for gyrokinetic simulations. Examples of this configuration are shown in figure 4.19, where also the emission volumes of the CECE are highlighted. As shown in figure 4.10, the

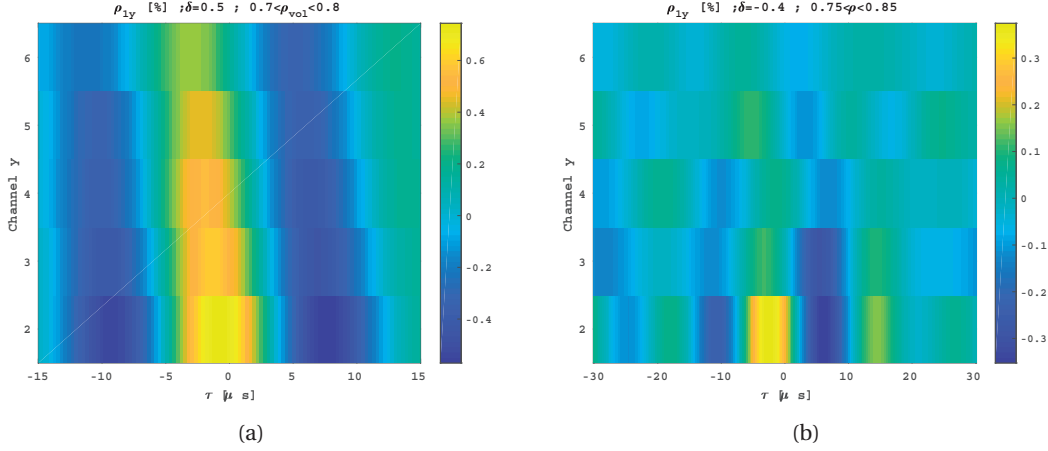


Figure 4.18 – Correlation coefficient as a function of  $\tau$  for increasingly separated couples of channels inside discharges with (a) positive  $\delta$  and (b) negative  $\delta$ . Take notice of the different color scales in the two pictures.

density and temperature profiles obtained in these discharges were comparable with the experiments described above. The resulting measures of  $T_i$  are shown in figure 4.9.

In this configuration, the intersection of the upper lateral line of sight with the plasma would have produced ECE emission volumes extended in the vertical direction, greatly impairing the diagnostic resolution. The  $z = 0$  cm horizontal line of sight was hence used to acquire CECE data. The volumes from which emission was collected are shown in figure 4.19. With respect to the discharges studied using the upper lateral line of sight, here lower correlation was observed between signals coming from neighbouring channels. The spectrum of fluctuations (most evidently for positive triangularity discharges) was substantially reduced, with respect to that observed using the upper lateral line of sight shown in figure 4.14, both in amplitude and in frequencies for corresponding radial positions as shown in figure 4.20a. Still, also in these cases, fluctuations measured in positive  $\delta$  discharges were stronger than in negative  $\delta$ . In the latter, barely any fluctuation above the noise level was observed (figure 4.20b).

The disagreement between the two sets of measurements could be explained in two possible ways. First the fluctuations intensity could depend on the poloidal angle, with increasing amplitude for increasing  $\theta$ . In fact when using the upper lateral line of sight, the emission volumes were estimated to be at  $30^\circ < \theta < 40^\circ$ . This argument was considered to be unrealistic since numerical simulations suggest that the fluctuations structure is ballooning, with a maximum near the outboard midplane. Second, the larger vertical extension of the horizontal line of sight would restrict the wavenumber spectrum that could be probed ( $k_\theta < 0.4 \text{ cm}^{-1}$  for the  $z = 0$  horizontal line of sight versus  $k_\theta < 1.12 \text{ cm}^{-1}$  for the upper lateral one). This effect could be modelled using a very simple model for the CECE diagnostic, described in D. By studying a superposition of modes with different poloidal number varying the aperture angle of the line of sight  $\alpha$ , the attenuation in the total power detected by the correlation became apparent

### 4.3. Fluctuations measurements using a horizontal line of sight

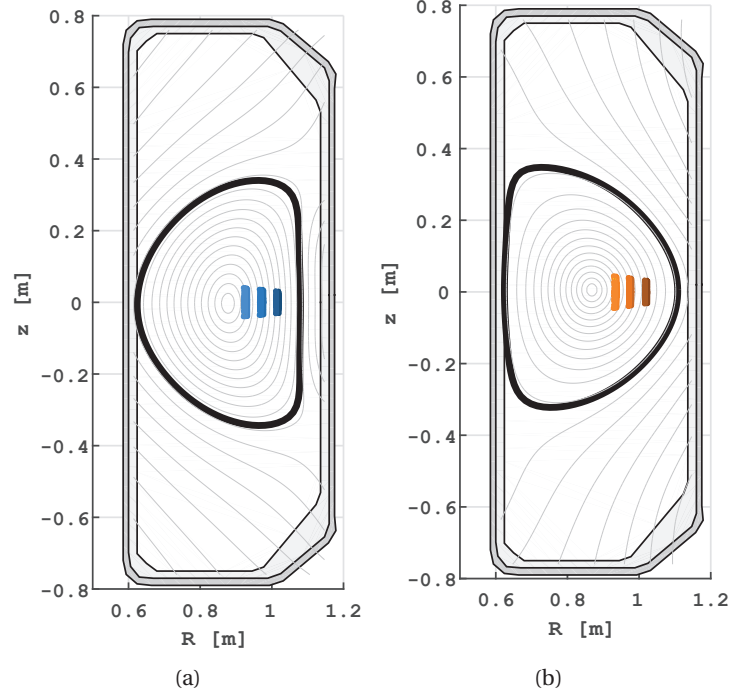


Figure 4.19 – Plasma geometries and emission volumes for the  $z_{axis}=0$  discharges matching the  $z_{axis} = 25$  cm ones. In this discharge the emission volumes were distributed in three pairs at  $\Delta f = 500$  MHz separated by 3 GHz

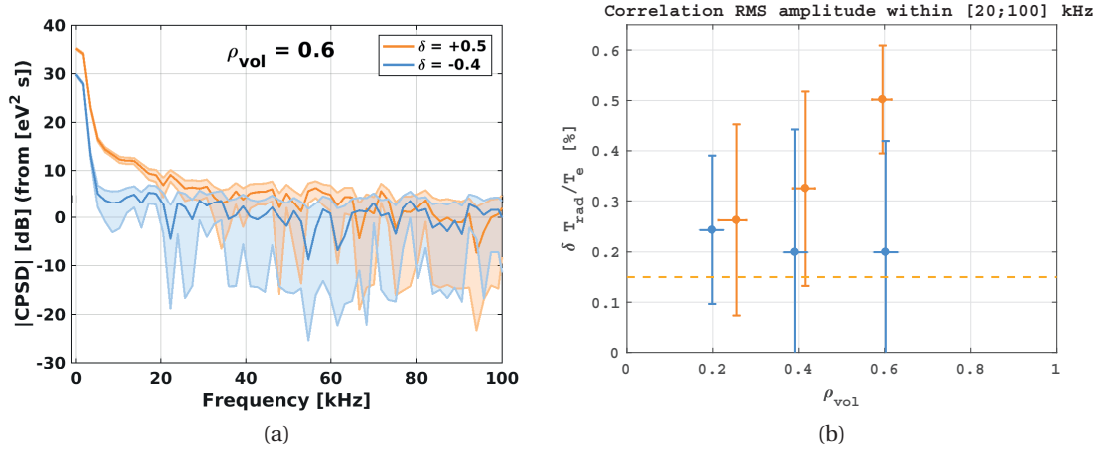


Figure 4.20 – Cross power spectral density of neighbouring channels around  $\rho_{vol}=0.65$  in negative and positive triangularity plasmas measured using the horizontal line of sight (a). Fluctuations are strongly reduced in both amplitude and frequency range with respect to those observed with upper lateral line of sight (figure 3.15). Nonetheless, higher fluctuations amplitude is still observed in positive triangularity discharges with respect to negative triangularity ones.

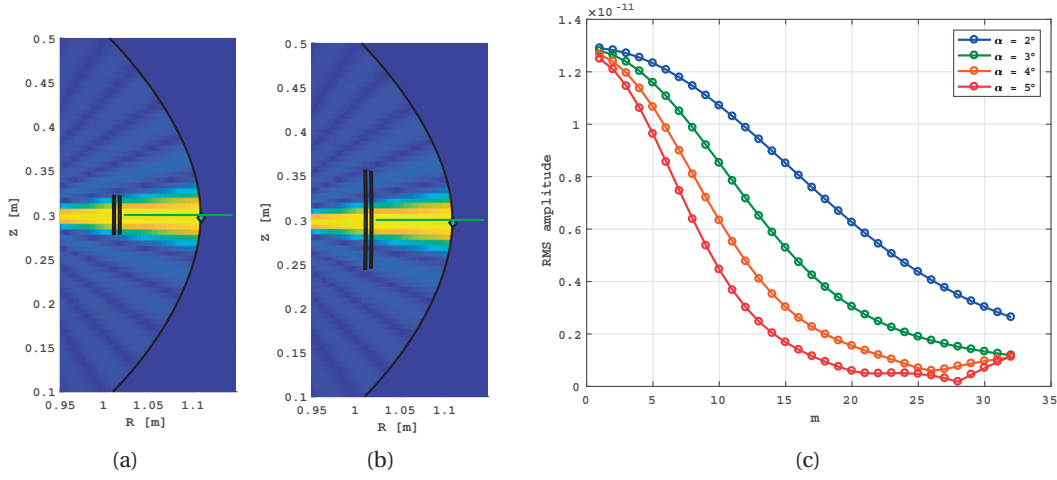


Figure 4.21 – Examples of the changes in the emission volumes extension when changing the aperture angle of the horizontal line of sight from  $2^\circ$  (a) to  $5^\circ$  (b). The emission volumes are represented over the norm of the fluctuating structure obtained superimposing modes with  $m$  from 1 to 32. (c) Sensitivity of the diagnostic to varying  $m$  modes for increasing line of sight aperture angle. The sensitivity to higher order modes is reduced while the antenna pattern is widened.

(figure 4.21).

The same model was used to try to study the difference between these different lines of sight, as shown in figure 4.22. When the experimental profiles, reconstructed plasma equilibrium, and the real antenna characteristics were taken into account, the model suggested that the configuration where the upper lateral line of sight was used was more sensitive to modes with higher  $m$ . This could justify, albeit qualitatively, the differences observed in the fluctuations spectra.

#### 4.3.1 Linear GENE simulations

A series of linear, flux tube gyrokinetic simulations, using the eulerian code GENE, has been performed to verify the dominant turbulence regime in the discharges presented in the previous section and to investigate the effects of triangularity on the linearly unstable modes. A first set of simulations used both the equilibrium and the profiles of the negative triangularity discharge. Another set, instead swapped the equilibrium and the temperature profile with the positive triangularity ones. The runs considered three fully kinetic species (deuterium ions, electrons and carbon) and included the effects of collisions and electromagnetic effects. The density and temperature profiles of carbon have been obtained by fitting the measurements of the CXRS and the same temperature profile was assumed for deuterium. The density profile of deuterium is determined imposing charge neutrality. The results are shown in figure 4.23 where, for three different radial positions ( $\rho_{tor} = [0.6, 0.7, 0.8]$ ), the linear growth rate  $\gamma$  and fre-

### 4.3. Fluctuations measurements using a horizontal line of sight

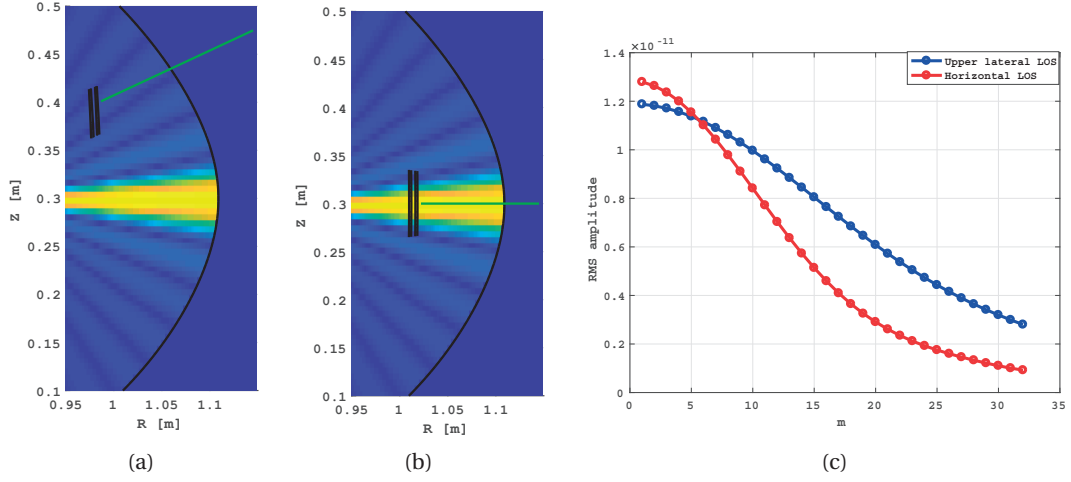


Figure 4.22 – Norm of the fluctuating field (m from 1 to 32) and emission volumes for the simulation of the the upper lateral (a) and horizontal (b) lines of sight looking at  $\rho_\psi = 0.7$ . (c) Estimated sensitivity to the different modes for the two lines.

quency  $\omega$  of the most unstable mode for each wavenumber  $k_y$  (corresponding to the direction perpendicular to the magnetic field lines) are shown, all in normalized units. In GENE,  $\gamma$  and  $\omega$  are normalized by  $c_s/R$  where  $R=0.88$  m is the major radius and  $c_s = \sqrt{T_e/m_D}$  is the ion sound speed. Wavenumbers are instead normalized by  $\rho_s = c_s \frac{m_D c}{qB}$ . At all three radii, smaller growth rates for the low wavenumber modes ( $k_y \rho_s < 1$ ) are found for negative triangularity compared with positive triangularity equilibria. All unstable modes were found to propagate in the electron diamagnetic direction allowing their identification as trapped electron modes (TEM) for lower values of  $k_y \rho_s$  or electron temperature gradient (ETG) driven modes for  $k_y \rho_s > 1$ . This situation is very similar to what had been observed in past experiences for gyrokinetic simulations run using the profiles of EC heated positive and negative triangularity plasmas. Also in those cases, in fact, the unstable modes were electron dominated for all wavenumbers [26][4].

The same data is shown in figure 4.24 in real units in the interval  $k_y < 2 \text{ cm}^{-1}$ . Here it is more evident how, in simulations run with negative triangularity equilibria, the linear growth rate for the most unstable mode is smaller than in simulations where the positive triangularity equilibrium was used. This effect is strongest for low wavenumbers and for radial positions closer to the plasma edge where, for selected wavenumbers,  $\gamma$  is up to 50% lower in the negative triangularity case. This is consistent with the fact that triangularity is a flux surface quantity that quickly decreases when moving from the edge to the plasma core.

Besides the variation in the linear growth rate of the most unstable modes, another way in which triangularity could affect the saturated turbulence regime is through changes in the  $E \times B$  shearing rate ( $\omega_{E \times B}$ ). It is in fact well known that  $\omega_{E \times B}$  contributes to the suppression of

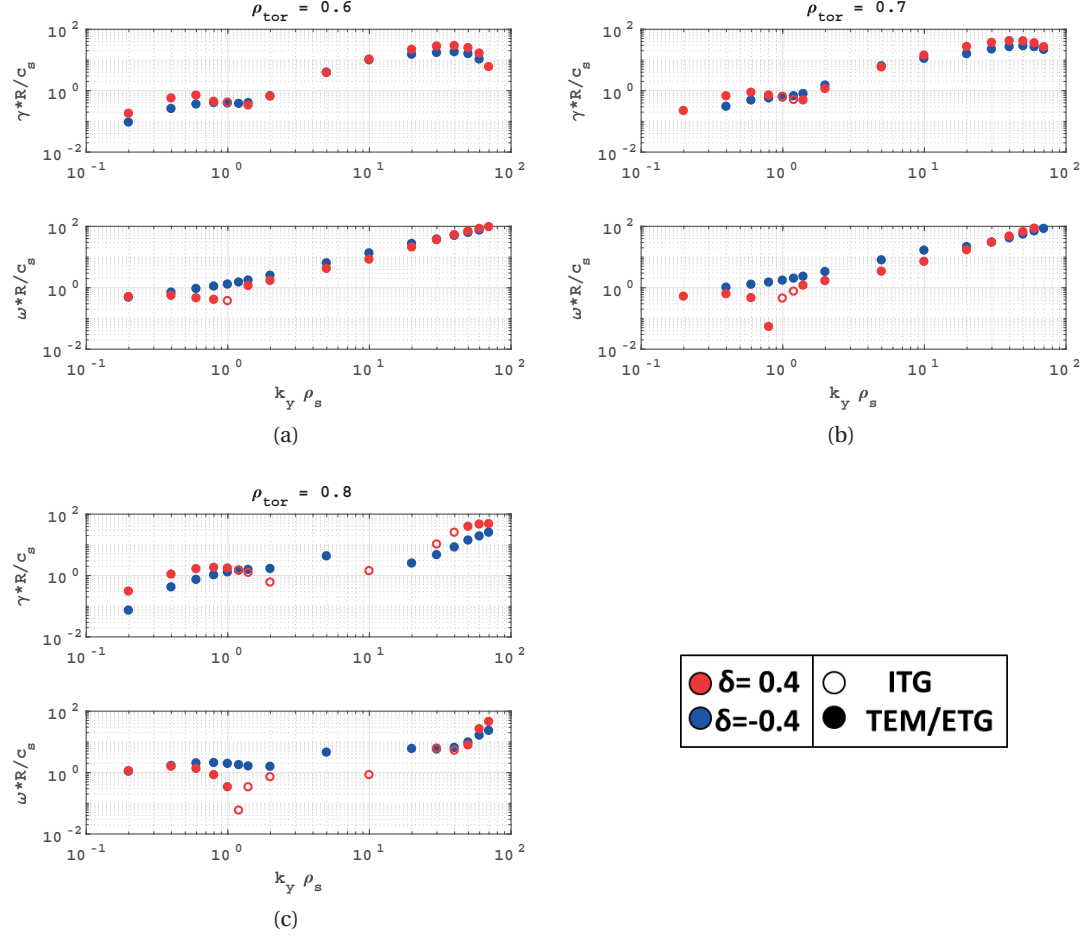


Figure 4.23 – Normalized linear growth rate ( $\gamma * R/c_s$ ) and frequency ( $\omega * R/c_s$ ) of the most unstable mode for each wavenumber in three radial positions:  $\rho_{tor} = 0.6$  (a),  $\rho_{tor} = 0.7$  (b),  $\rho_{tor} = 0.8$  (c). In the  $\omega$  plots, full markers correspond to modes that propagate in the electron diamagnetic direction (TEM or ETG).



turbulent eddies [83]. The growth rates were estimated with the definition used by GENE [25]:

$$\omega_{E \times B} = -\frac{r}{q} \frac{\partial \Omega_{tor}}{\partial r}, \quad (4.4)$$

where  $r$  is the radial coordinate centred on the plasma axis,  $q$  is the safety factor and  $\Omega_{tor}$  is the toroidal angular velocity. The latter is calculated dividing the toroidal velocity, measured by the CXRS system 1 on the outboard midplane, by the position on the major radius of the intersections of the lines of sight with the diagnostic NBI. It was then assumed that the toroidal angular velocity could be treated as a flux surface quantity. The calculated values of  $\omega_{E \times B}$  are shown in the  $\gamma$  plots of figure 4.24 as horizontal lines, with the dashed lines, showing the estimated uncertainty. Within errorbars, no difference in  $\omega_{E \times B}$  could be observed between positive and negative triangularity discharges. The uncertainty on these estimates, though, is very large ( $\frac{\sigma_{\omega_{E \times B}}}{\omega_{E \times B}} \sim 1$ ), encompassing  $\omega_{E \times B} \sim \gamma$  for lower wavenumber modes. It can then not be excluded that the  $E \times B$  shearing rate plays an important role in the final saturated state of the turbulence.

## 4.4 Conclusions

A series of discharges, with similar density profiles and plasma current, in which triangularity was varied from  $\delta = 0.5$  to  $\delta = -0.4$ , were produced and investigated in TCV. Fluctuation measurements over the region  $0.4 < \rho_{vol} < 0.9$  were performed using the CECE diagnostic. The data show a strong reduction in the fluctuations amplitude at the edge of plasmas with negative triangularity compared to positive triangularity (see figures 4.1.3a and 4.1.3b). This suppression seems to penetrate up to  $\rho_{vol} = 0.55$  where the local triangularity at this flux surface ( $\sim 0.12$ ) is already much lower than at the edge (less than  $\sim 40\%$  of the edge value) in both positive and negative triangularity plasmas.

When the fluctuation data are plotted versus the normalized scale lengths at the position of the emission volumes, a threshold behaviour is observed both on density and temperature for the positive triangularity discharges but not in the presence of negative triangularity (see figures 4.1.3c and 4.1.3d). These measurements were taken over a considerable extension of the minor radius where the scale lengths were not the only parameters varying. However, due to the extreme similarity of the profiles of many other quantities and the fact that these scale lengths are supposed to constitute the drives for the observed fluctuations, these trends show the presence of a higher threshold for fluctuations onset in negative triangularity plasmas. This is in agreement with the results of nonlinear gyrokinetic flux tube simulations.

Correlation analysis show lower correlation coefficients for negative triangularity plasmas. In both shapes fluctuations seem to propagate in the same direction, from the channels closest to the plasma edge towards the plasma interior. All these observations suggest that an underlying difference exists in the nature of the turbulence fluctuations between negative and positive triangularity plasmas.

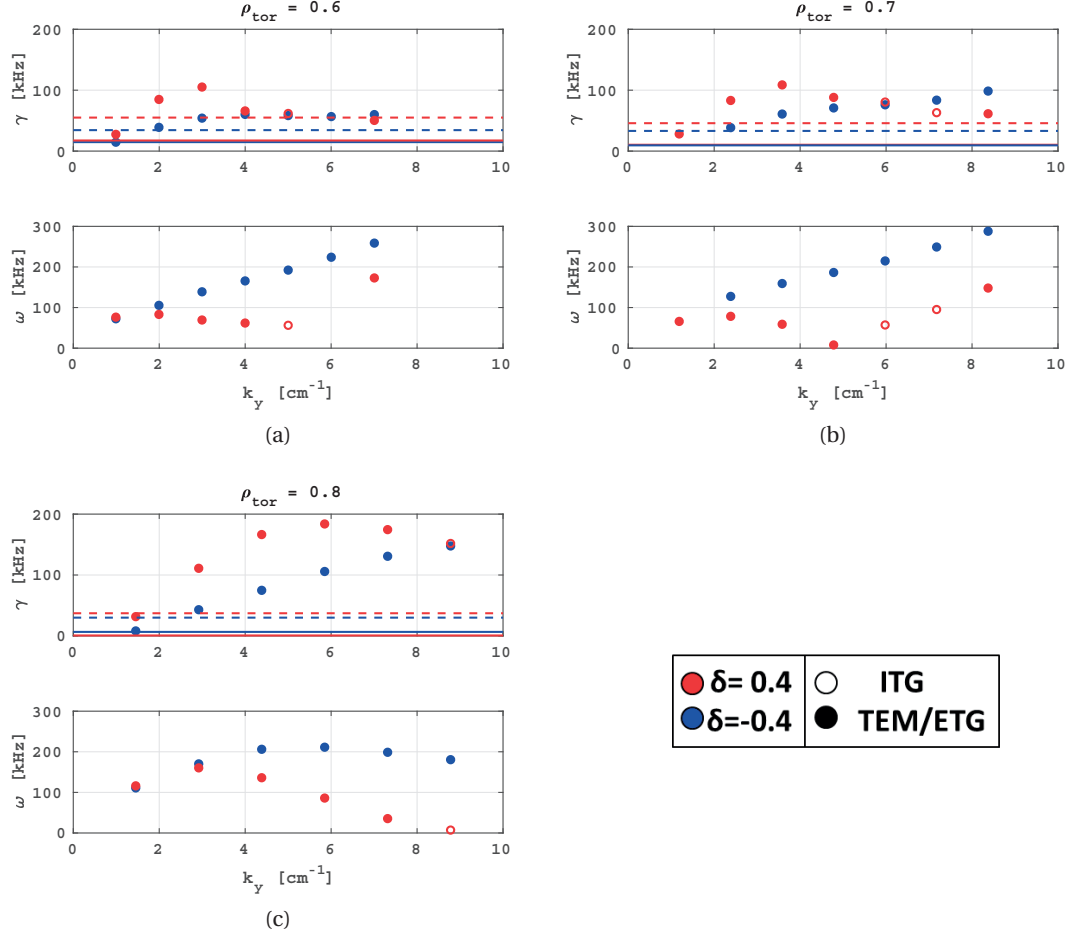


Figure 4.24 – Linear growth rate ( $\gamma$ ) and frequency ( $\omega$ ), in real units, of the most unstable mode for each wavenumber in three radial positions:  $\rho_{tor} = 0.6$  (a),  $\rho_{tor} = 0.7$  (b),  $\rho_{tor} = 0.8$  (c). In the  $\omega$  plots, full markers correspond to modes that propagate in the electron diamagnetic direction (TEM or ETG). Horizontal lines in the  $\gamma$  plots represent the estimated  $E \times B$  shearing rate, with its uncertainty shown as the dashed line.

A similar series of discharges was also developed at the vessel midplane to obtain profiles of ion density and temperature. The latter is found to increase in negative  $\delta$  plasmas similarly to electron temperature. The  $z = 0$  horizontal line was employed to obtain fluctuations measurements with results consistent with the measurements taken using the upper lateral line of sight. The reduced fluctuations amplitude observed in these cases can be attributed to a combined effect of the larger pattern of the horizontal antenna, and the different poloidal angle with respect to the emission volumes determined by the upper lateral line of sight.

The equilibria and profiles of these discharges were used as inputs for a series of linear gyrokinetic simulations using the GENE code. These wavenumber scans found electron driven modes (TEMs or ETGs) to be the dominant form of instability across the whole  $k_y$  spectrum. The linear growth rates calculated using the negative triangularity plasma profiles and equilibria were up to 50% smaller than those found when the equilibrium was swapped with that of the positive triangularity one. Estimates of the  $E \times B$  shearing rate did not highlight a direct effect of negative triangularity but suggested that  $\omega_{E \times B} \sim \gamma$  could have an effect on the saturated state of the turbulence already for these ohmic discharges.



## 5 Matching discharges with $T_e/T_i < 1$

### 5.1 Introduction

It has been suggested that negative  $\delta$  scenarios are interesting for the development of reactor-like tokamak machines [84][27][28]. These configurations could provide attractive advantages concerning the power handling problem, which is considered to be one of the major challenges[85][86]. One of the main reasons that makes power handling so critical is that future reactor-like machines are expected to operate in high-confinement mode (H-mode) [87], a scenario in which a transport barrier is formed close to the plasma edge. In this regime, the pressure in a narrow region inside of last closed flux surface is strongly increased, enhancing pressure across the whole plasma profile. This region is normally called the pedestal and is characterized by large pressure gradients. These gradients, though, are associated with the so called edge localized modes (ELMs) [88]. The ELMs are quasi-periodic relaxations of the transport barrier, causing the expulsion of large amounts of energy and particles from the plasma that can cause heat flux peaking on plasma facing components exceeding the material limits. In this context, negative triangularity scenarios present advantageous characteristics. A series of experiments performed in TCV show how, upon entering H-mode, negative  $\delta$  plasmas develop more frequent but less intense ELMs at the expense of a lower pedestal [89]. A similar effect on the pedestal height was also predicted using numerical codes [90]. In a negative triangularity tokamak (NTT), the peak heat flux on plasma facing components in the divertor region could be further reduced by moving the strike point position towards the low field side, thus increasing the surface over which the heat load is distributed [28][84]. To possibly counter this effect, though, other experimental [91] and numerical [92] works suggest that in negative  $\delta$  plasmas, the width of the scrape of layer may be reduced.

The observation of the suppression of fluctuations and of improved confinement with  $\delta < 0$  presented in chapter 4 constitutes another interesting argument that motivates research towards the NTT. However, the results obtained in previous experiments in TCV [16][23][7][93] can not simply be extrapolated to a reactor-like machine. One of the reasons is that the works cited above only investigated the effects of negative  $\delta$  on confinement in ohmic or EC-heated

discharges where, in the core, electron temperature is more than twice the ion temperature. In the ohmic discharges presented in chapter 4, for example,  $T_e/T_i \sim 1$  only for  $\rho_{vol} > 0.7$ . Instead, in a reactor-like tokamak, it is expected that the confinement time will be high enough to allow thermalization of electrons and ions, leading to  $T_e/T_i \sim 1$  across a large fraction of the radial profile. Recently, on DIII-D, L-mode discharges with negative triangularity, heated with both ECH and NBI, reaching  $T_e/T_i \sim 1$  were obtained. In these discharges, improved confinement and reduced fluctuations were observed [29]. Gyro-fluid simulations performed using the TGLF code [94] show that the resulting turbulence is dominated by trapped electron modes [29], similarly to what is observed in TCV [4][6][26].

This chapter focuses on measurements similar to those described in chapter 4 and in [93], studying the effect of negative  $\delta$  on fluctuations and confinement, in more reactor-like relevant regimes, characterized by  $T_e/T_i \sim 1$  and strong ion drive. To do so, the NBI system of TCV [31] was exploited to produce a pair of discharges with symmetric positive and negative  $\delta$  and comparable density and current density profiles, in which  $T_e/T_i \leq 1$  across a large fraction of the radial profile. The goal in this case was to obtain two discharges as similar as possible, except for the shapes, in order to compare confinement and fluctuations while excluding a strong influence of parameters other than triangularity. Furthermore, reduction in the value of  $T_e/T_i$  is considered one of the main factors that drives the change in the turbulence regime from electron to ion dominated, thus possibly allowing the study of fluctuations in an ITG dominated plasma or a mixed ITG/TEM regime. Linear, flux-tube gyrokinetic simulations, using the experimental profiles as inputs, were run to investigate the effective dominant turbulence regimes in these cases.

## **5.2 Development of matching NBI heated discharges with positive and negative $\delta$**

A reference discharge with negative triangularity, heated with NBI, was developed at the vessel midplane ( $z = 0$  cm) with the following characteristics: plasma current  $I_p = 230$  kA, line averaged density  $n_{av} = 2.9 \cdot 10^{19} \text{ m}^{-3}$ ,  $\delta = -0.4$ ,  $\kappa = 1.4$ . The plasma was heated with 300 kW of NBI for 1 s. NBI injection was on-axis since the plasma was centered at  $z = 0$ . A symmetric positive triangularity ( $\delta = +0.4$ ,  $\kappa = 1.4$ ) discharge was developed, with similar density and current profiles, for comparison. The geometry of the two plasmas are shown in figure 5.1a and 5.1b. To obtain equivalent  $\kappa$  and  $q$  profiles, in the positive triangularity discharge the plasma current was increased to 265 kA. The resulting  $q$  profiles for the two discharges, calculated using the 1D transport code ASTRA [95], are shown in figure 5.2. The positive  $\delta$  plasma was heated in two 0.4 s different NBI phases of 300 and 1000 kW. The time traces of the main parameters for the negative and positive  $\delta$  discharges are shown in figures 5.3 and 5.4 respectively.

The ASTRA code [95] has been used to simulate the total beam heating power deposition, the resulting current drive and the effective ohmic power in the different cases, as is shown in

## 5.2. Development of matching NBI heated discharges with positive and negative $\delta$

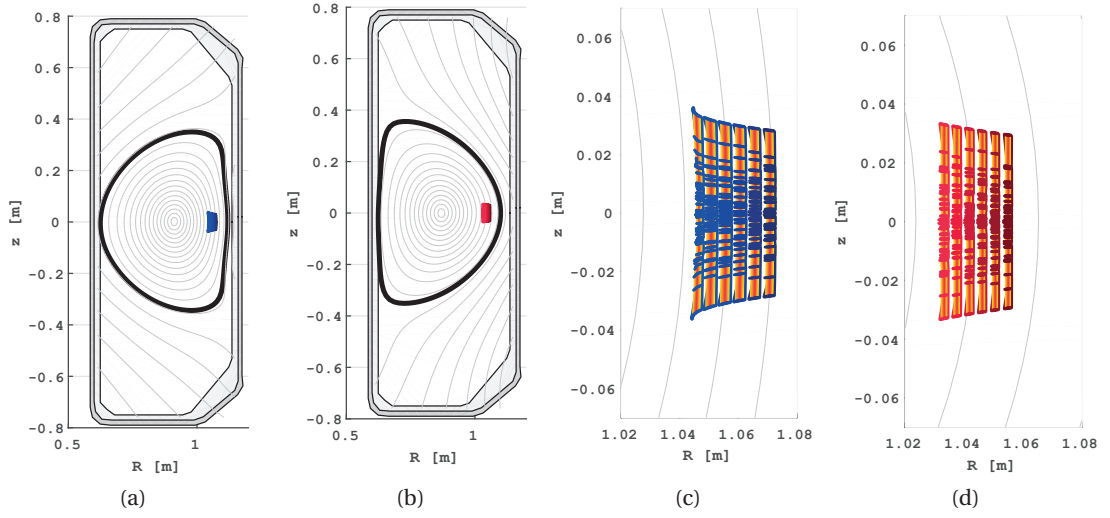


Figure 5.1 – Plasma geometry and CECE emission volumes for the positive and negative  $\delta$  discharges (a and b) and a zoomed detail of the CECE channels (c and d).

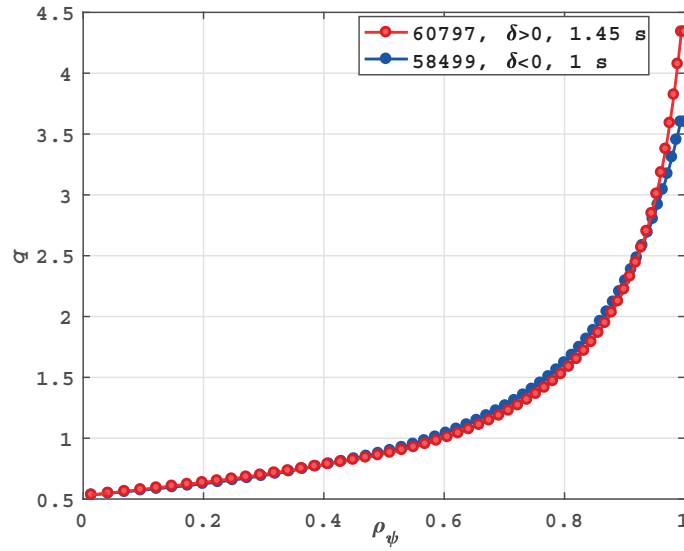


Figure 5.2 – Safety factor ( $q$ ) profiles for the positive and negative triangularity discharges calculated with ASTRA (c).

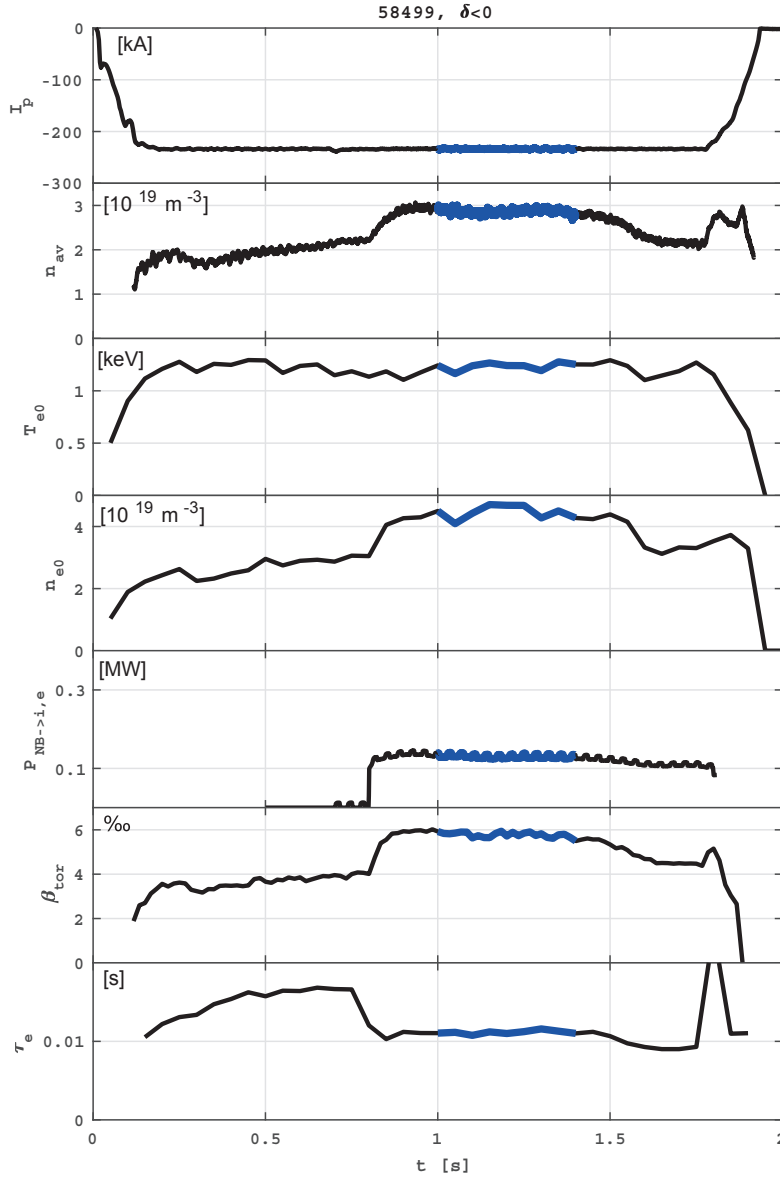


Figure 5.3 – Time traces for plasma current  $I_p$ , line averaged density  $n_{av}$ , core temperature  $T_{e0}$  and density  $n_{e0}$ , NBI power absorbed by the bulk plasma  $P_{NBI \rightarrow i,e}$ ,  $\beta_{tor}$  and energy confinement time  $\tau_E$  for the reference discharge with  $\delta < 0$ . Highlighted is the time interval over which correlation analysis has been computed.



## 5.2. Development of matching NBI heated discharges with positive and negative $\delta$

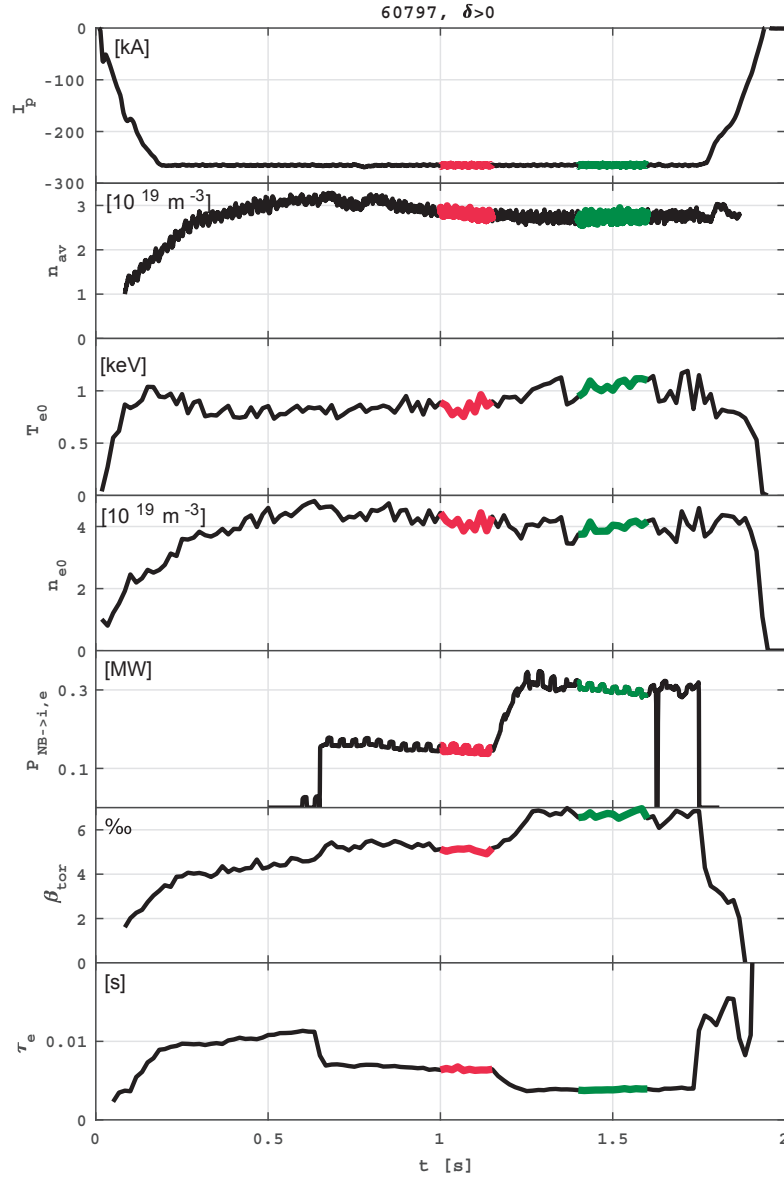


Figure 5.4 – Time traces for plasma current  $I_p$ , line averaged density  $n_{av}$ , core temperature  $T_{e0}$  and density  $n_{e0}$ , NBI power absorbed by the bulk plasma  $P_{NBI \rightarrow i,e}$ ,  $\beta_{tor}$  and energy confinement time  $\tau_E$  for the discharges with  $\delta > 0$ . Highlighted are the time intervals over which correlation analysis has been computed, corresponding to the two different NBI power levels.

	$I_p$ [kA]	$P_{NBI}$ nom. [kW]	$P_{NBI}$ eff. [kW]	$P_{ohm}$ [kW]	$P_{tot}$ [kW]
$\delta = -0.4$	230	300	145	185	330
$\delta = +0.4$	265	300	145	290	435
$\delta = +0.4$	265	1000	290	180	470

Table 5.1 – Summary of nominal and effective ohmic and auxiliary power injected in the positive and negative  $\delta$  plasmas described in paragraph 5.2.

figures 5.5 and 5.6 for the negative and positive triangularity discharge respectively. In TCV  $\sim 20\%$  of the NBI power is lost in interactions with the beam duct. Of the remaining power, a fraction between 8% and 20% escapes the plasma by shine-through or first orbit losses. The fast ions are then confined in the plasma and can transfer their energy to electrons or ions, but part of them (29% - 35%) also undergo charge exchange reactions, escaping confinement before they can transfer their energy to the bulk plasma.

In the negative  $\delta$  plasma discharge,  $P_{ohm} \sim 185$  kW. In the positive  $\delta$  phase with the same nominal heating ( $P_{NB} = 300$  kW), instead,  $P_{ohm} \sim 290$  kW due to the higher  $I_p$  and the lower temperature, that in turn increases the necessary  $V_{loop}$ . Adding the absorbed NB power,  $\sim 145$  kW in both cases, the total heating for the two differently shaped plasmas is then  $\sim 330$  kW ( $\delta < 0$ ) and  $\sim 435$  kW ( $\delta > 0$ ).

The resulting profiles for the negative  $\delta$  discharge ( $P_{NB} = 300$  kW) are compared with those for the first ( $P_{NB} = 300$  kW) and second ( $P_{NB} = 1000$  kW) phases of the positive  $\delta$  one in figures 5.7 and 5.8, respectively. In figure 5.7 it is possible to observe that even though the positive  $\delta$  plasma is subjected to  $\sim 100$  kW more of effective heating than the negative  $\delta$  one, the latter still presents higher electron and ion temperatures across the whole profile, as was observed for ohmic plasmas in chapter 4. Ion heating successfully increases the ion temperature to a point where  $T_e/T_i \sim 1$  across a large part of the radial profile, in contrast to the previously mentioned ohmic discharges, where  $T_e/T_i > 2$  in the core and  $T_e/T_i \sim 1$  only for  $\rho > 0.7$ .

In the 1 MW NBI phase of the positive  $\delta$  discharge,  $P_{ohm}$  decreases to  $\sim 180$  kW, and the net power injected by the beam is  $\sim 290$  kW for a total of  $\sim 470$  kW of heating power. In this phase, the electron and ion temperature profiles are almost matched with that of the negative  $\delta$  plasma, as shown in figure 5.8b 5.8c. This is despite the fact that the negative  $\delta$  plasma is effectively subjected to less than 70% effective heating power with respect to the high power positive  $\delta$  case. A summary of the nominal and effective power for each of the cases discussed until now is presented in table 5.1. These observations show that negative triangularity could maintain its beneficial effect on confinement also in plasmas closer to what is expected in a reactor-like machine with respect to past experiments in TCV.

## 5.2. Development of matching NBI heated discharges with positive and negative $\delta$

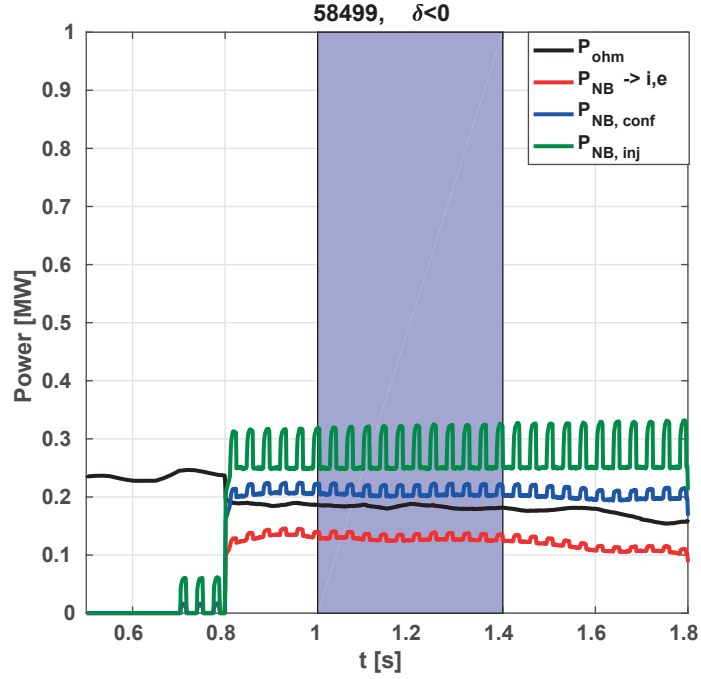


Figure 5.5 – Time traces of the ohmic power  $P_{ohm}$  and breakdown of the distribution of NBI power in the negative triangularity discharge ( $\delta=-0.4$ ). Starting from the nominal  $P_{NB}$ , the losses in the beam duct reduce it to  $P_{NB,inj}$ ; after shine through and first orbit losses  $P_{NB,conf}$  remains and, taking into account charge exchange losses,  $P_{NB \rightarrow i,e}$  is the actual power transferred to ions and electrons. Highlighted is the time interval over which correlation analysis has been computed.

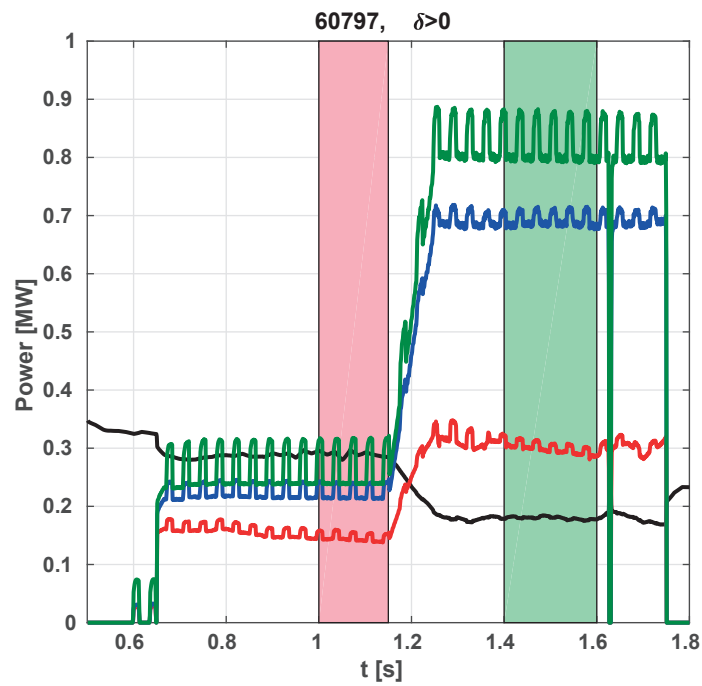


Figure 5.6 – Same as figure 5.5 but for  $\delta=+0.4$ . Highlighted are the two time intervals over which correlation analysis has been computed.

## 5.2. Development of matching NBI heated discharges with positive and negative $\delta$

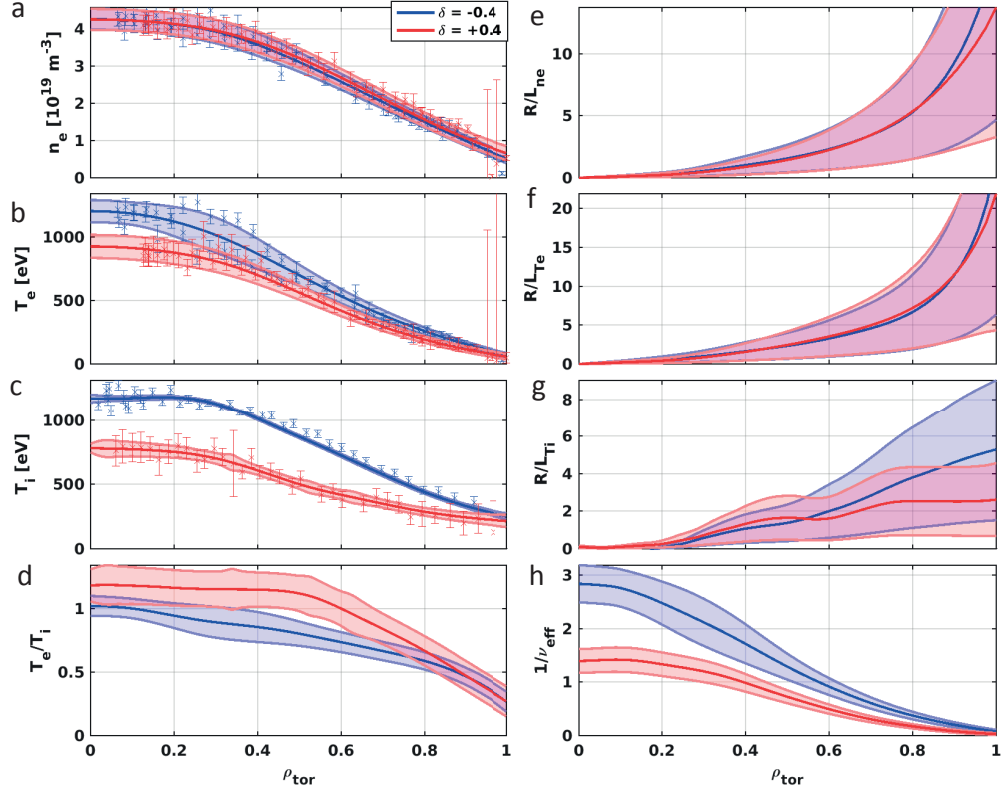


Figure 5.7 – Profiles and normalized scale lengths for electron density (a and e), electron temperature (b and f) and ion temperature (c and g), electron to ion temperature ratio (d) and inverse effective collisionality (h). The profiles of the negative  $\delta$  case, heated with 300 kW (blue), are compared with those of the positive  $\delta$  case heated with 300kW (red).

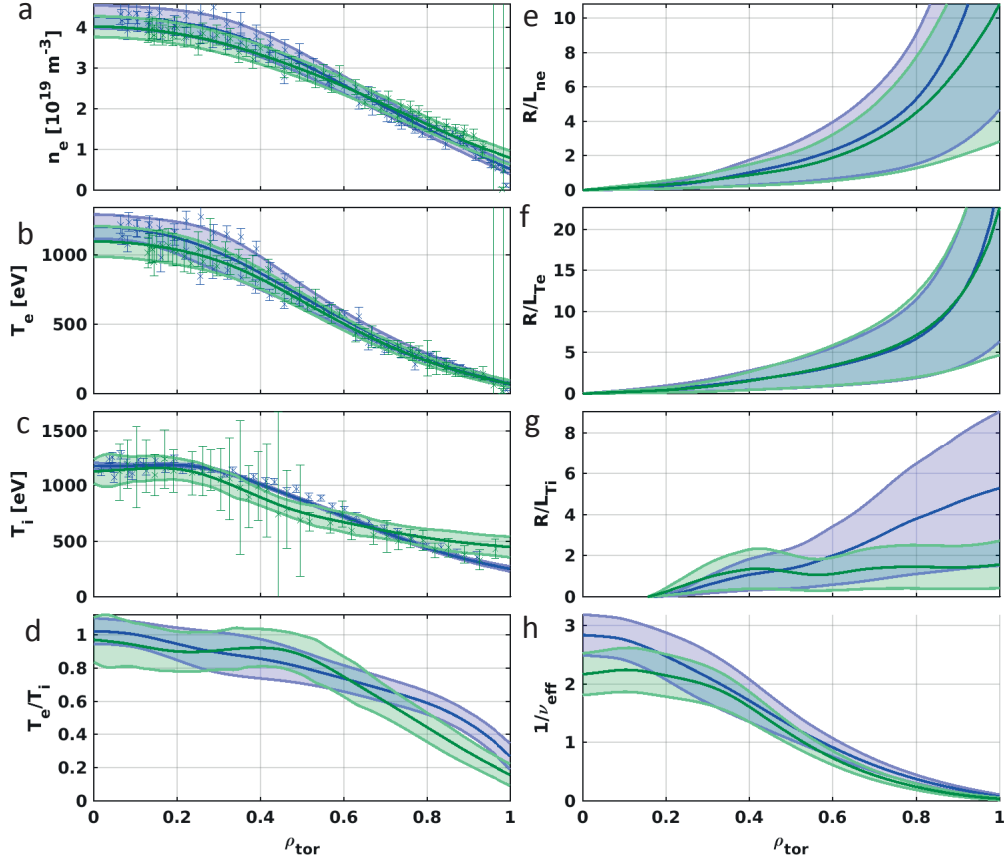


Figure 5.8 – Profiles and normalized scale lengths for electron density (a and e), electron temperature (b and f) and ion temperature (c and g), electron to ion temperature ratio (d) and inverse effective collisionality (h). The profiles of the negative  $\delta$  case, heated with 300 kW (blue), are compared with those of the positive  $\delta$  case heated with 1000 kW (green).

### 5.2.1 Measurements of temperature fluctuations

The CECE diagnostic was used to study radiative temperature fluctuations in these discharges. The horizontal line of sight located at the vessel midplane was selected to optimize the plasma coverage of the diagnostic. The frequency separation between the six channels was set to 300 MHz, covering the region  $0.57 < \rho_{vol} < 0.78$ . The emission volumes for the two shapes are shown in figure 5.1a and 5.1b and the corresponding emissivity profiles over the plasma normalized radius in figure 5.9. As already mentioned in chapter 4, the antenna pattern of this line of sight leads to poorer sensitivity to smaller fluctuating structures, compared to the steerable, upper lateral, line of sight. For plasmas centered at the vessel midplane, though, the angle between the upper lateral line of sight and the ECE resonance layers would be small enough to generate emission volumes strongly elongated in the vertical directions, compromising the localisation of the measurements.

The cross power spectral density obtained from cross correlation analysis of a pair of neighbouring channels at  $\rho_{vol} = 0.75$  is shown in figure 5.10. For the positive triangularity discharges, a higher level of fluctuations can be observed in the 20-50 kHz frequency range. The fluctuation amplitude, in figure 5.11a and 5.11b, is obtained by integrating the CPSD's over that frequency range. Fluctuations in the positive  $\delta$  plasma, in both NBI phases, are about twice as strong as those in the negative  $\delta$  one, similar to what has been observed in ohmic discharges when using the  $z = 0$  horizontal line of sight, described in paragraph 3.5.1, see figure 4.20b. The upper limit contribution of density fluctuations to the measured radiative temperature density fluctuations is calculated, as explained in 3.3.2 to be below 10% and 18% for negative and positive  $\delta$  discharges respectively.

Beside injecting energy, the NBI is also a strong source of momentum for the plasma, that drives rotation. The tangential NBI available to TCV, when used on plasmas centred around the vessel mid plane (on-axis heating) mainly induces strong toroidal rotation. This is shown in figures 5.12a and 5.12b. In the NBI heated discharges, in fact, the toroidal velocity is strongly increased with respect to the ohmic discharges.

The increased toroidal rotation observed for these discharges, could affect the CECE measurements due to Doppler effect broadening of the fluctuations spectrum. As a consequence, an observed reduction of the fluctuations amplitude could be due to the spectral broadening and not to a change in the turbulence characteristics of the plasma. In this case, though, a change in toroidal velocity cannot by itself explain the observed fluctuations suppression observed in the negative triangularity discharge. As seen in figure 5.12b, in the radial positions where CECE collected fluctuations measurements, the toroidal velocity in the high power phase of the positive triangularity discharge is higher than in the negative triangularity discharge. In any case, on TCV, is currently impossible to test separately the effects of rotation from the additional ion heating. To overcome this problem one possibility is to have two NBIs, injecting particles in the co- and counter- current directions respectively. In this way ion heating can be applied without driving any net rotation in the plasma. This technique was

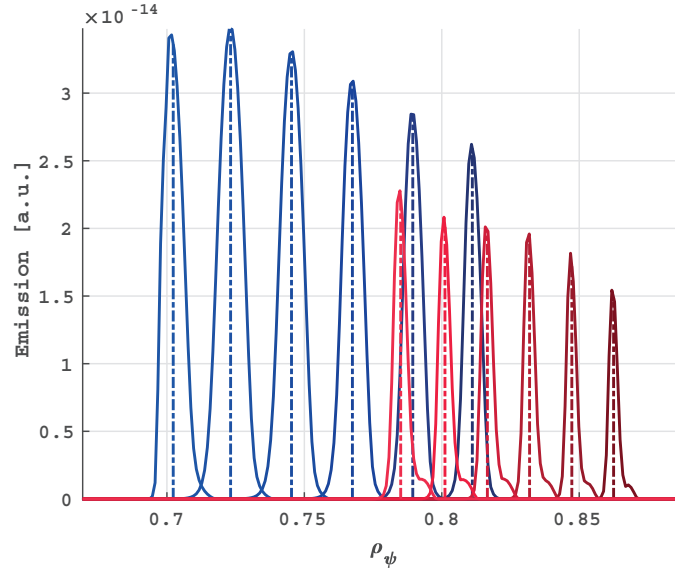


Figure 5.9 – Emissivity profiles for the CECE channels in the positive and negative  $\delta$  plasmas, calculated as detailed in appendix A.

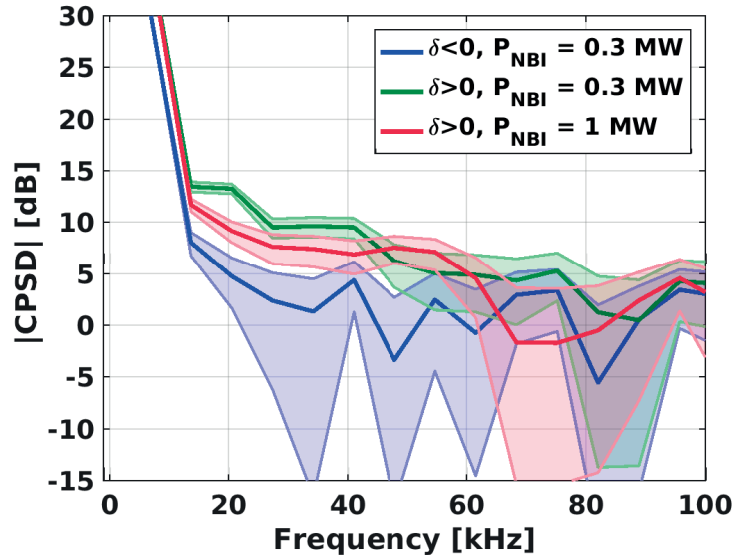


Figure 5.10 – Cross power spectral density of fluctuations for two neighbouring channels at  $\rho_{vol} \sim 0.75$ .



## 5.2. Development of matching NBI heated discharges with positive and negative $\delta$

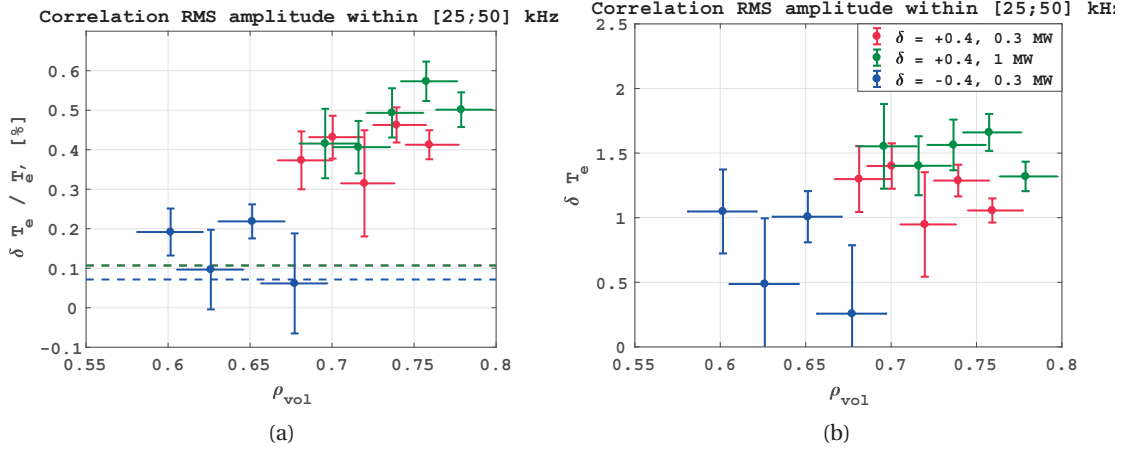


Figure 5.11 – Relative (a) and absolute (b) amplitude of the fluctuations obtained by integrating the CPSD of neighbouring channels between 25 and 50 kHz.

already successfully applied on DII-D [96] and Alcator C-Mod [97] for the study of fluctuations in H-mode and I-mode respectively. With the next upgrade phases planned in TCV, a second NBI will be installed in the opposite direction as the one current available. At that point the effects of rotation and ion heating could be probed separately.

### 5.2.2 Linear GENE simulations

Due to the similarity in pressure profiles and equilibrium, apart from the triangularity, these discharges are good models for simulations using gyrokinetic codes. Linear, flux-tube GENE [25] simulations were run using the profiles of the  $\delta < 0$  discharge during the NB phase, in three different radial positions, corresponding to  $\rho_{tor} = [0.6, 0.685, 0.8]$ . This was done for both the negative and positive  $\delta$  equilibria, keeping the profiles unaltered. As the simulations presented in chapter 4, these runs used three kinetic species (with carbon profiles calculated from CXRS measurements), kept into account collisions and electromagnetic effects.

In figure 5.13 the normalized growth rate  $\gamma * R/c_s$  and frequency  $\omega * R/c_s$  of the most unstable mode are shown for a range of wavenumbers at the three different radial positions. In the normalization  $R = 0.88$  m is the major radius and  $c_s = \sqrt{t(T_e/m_D)}$ . Full and hollow markers represent modes propagating in the electron and ion diamagnetic directions, indicating TEM/ETG and ITG modes respectively. As already observed [6][4], negative  $\delta$  lowers the linear growth rate of the most unstable mode for low  $k_y$ . This effect is stronger towards the plasma edge, consistent with the fact that, for these flux-tube simulations, triangularity is a local parameter whose magnitude quickly reduces when moving towards the plasma core. While in previous simulations electron driven modes (in particular TEMs) were found to be dominant at all wavenumbers and radial locations, in these NBI heated discharges ion branches (ITG) appear dominant for low wavenumbers, especially for  $\rho_{tor} = 0.6$  and 0.685. For all radii and

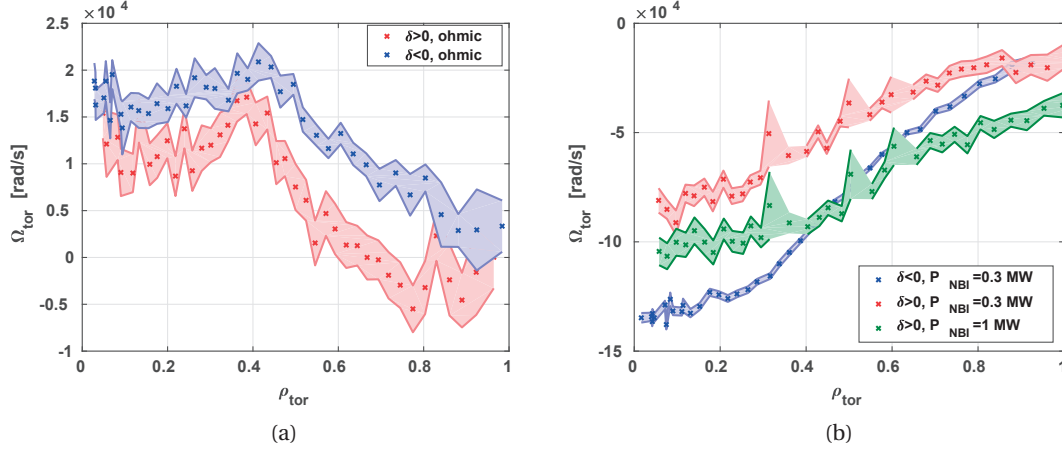


Figure 5.12 – Toroidal angular speed of the carbon ions in the plasma as measured by the CXRS in the ohmic discharges presented in paragraph 4.3 (a) and in the NBI heated discharges presented in this chapter (b).

shapes, electron temperature gradient (ETG) modes become dominant for high wavenumbers. As is especially visible in figure 5.14, the linear growth rates for unstable modes in negative triangularity plasmas, especially for low wavenumbers and large  $\rho_{\text{tor}}$ , are lower than in the cases where the positive triangularity equilibrium was used. This is similar to what had been observed in chapter 4. It is important to stress that, in this cases, negative triangularity displays a stabilizing effect for low wavenumber modes also when ion driven modes are dominant.

These simulations, together with those presented in chapter 4, suggest that negative triangularity influences the fluctuations that are driven in tokamak plasmas, with less unstable modes at low wavenumber, normally associated with larger contributions to overall particle and heat transport. This is consistent with the experimental observations in which higher fluctuations amplitude has been measured for the positive  $\delta$  plasma in a pair of discharges with matched profiles. In particular this effect was observed not to be limited just to discharges in which electron modes were the dominant source of instabilities. In fact, it could be observed also in discharges in which the unstable modes were a mix of ITG and TEM.

The  $E \times B$  shearing rate was estimated also for these cases and is shown in figure 5.14 as horizontal lines in the linear growth rate plots, where dashed line correspond to the uncertainty. Also in this case, due to the large uncertainty in the measurements, especially for the high power phase of the positive triangularity discharge, a direct effect of triangularity on  $\omega_{E \times B}$  could not be identified.

### Sensitivity to the impurity content

The results of these simulations were found to be particularly sensitive to the impurity content of the plasma. Figure 5.15 shows the effects of different settings of  $Z_{\text{eff}}$  on the simulations

## 5.2. Development of matching NBI heated discharges with positive and negative $\delta$

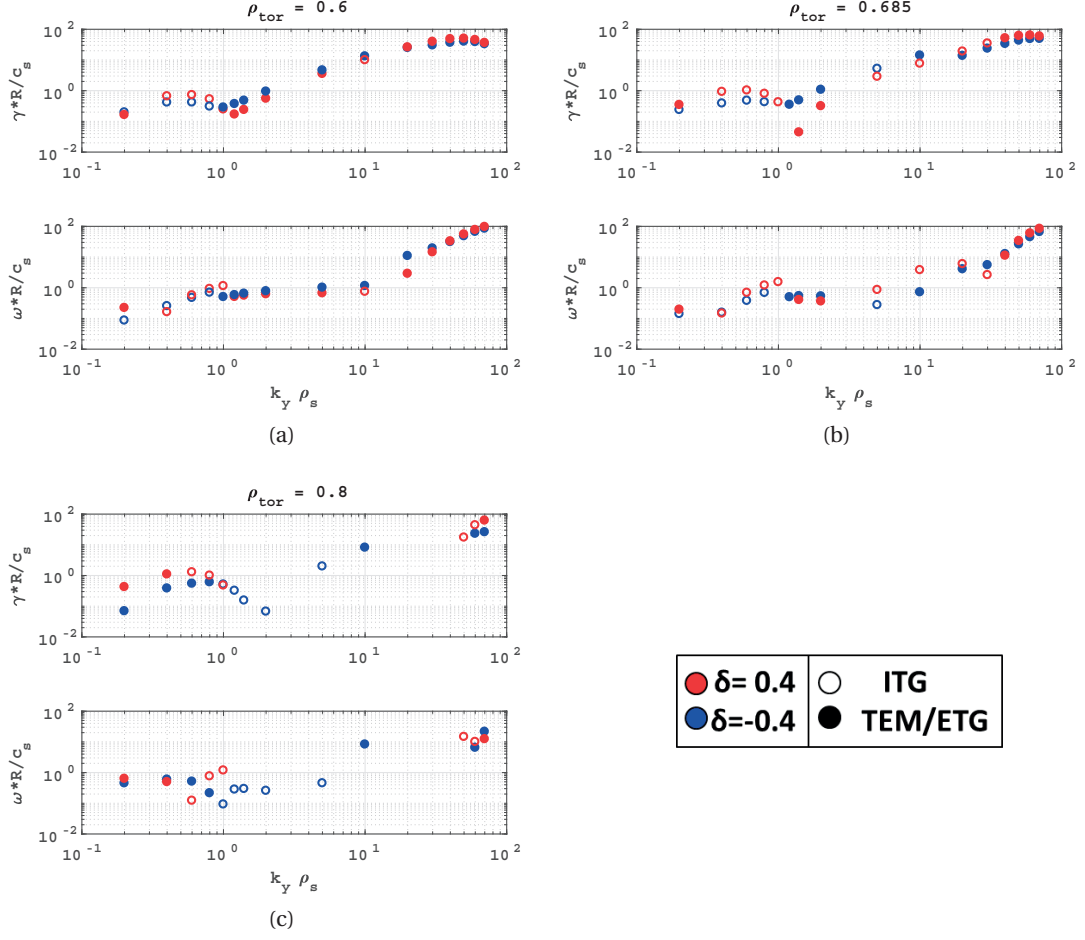


Figure 5.13 – Normalized linear growth rate ( $\gamma * R/c_s$ ) and frequency ( $\omega * R/c_s$ ) of the most unstable mode for each wavenumber in three radial positions:  $\rho_{tor} = 0.6$  (a),  $\rho_{tor} = 0.685$  (b),  $\rho_{tor} = 0.8$  (c). In the  $\omega$  plots, full markers correspond to modes that propagate in the electron diamagnetic direction (TEM or ETG).

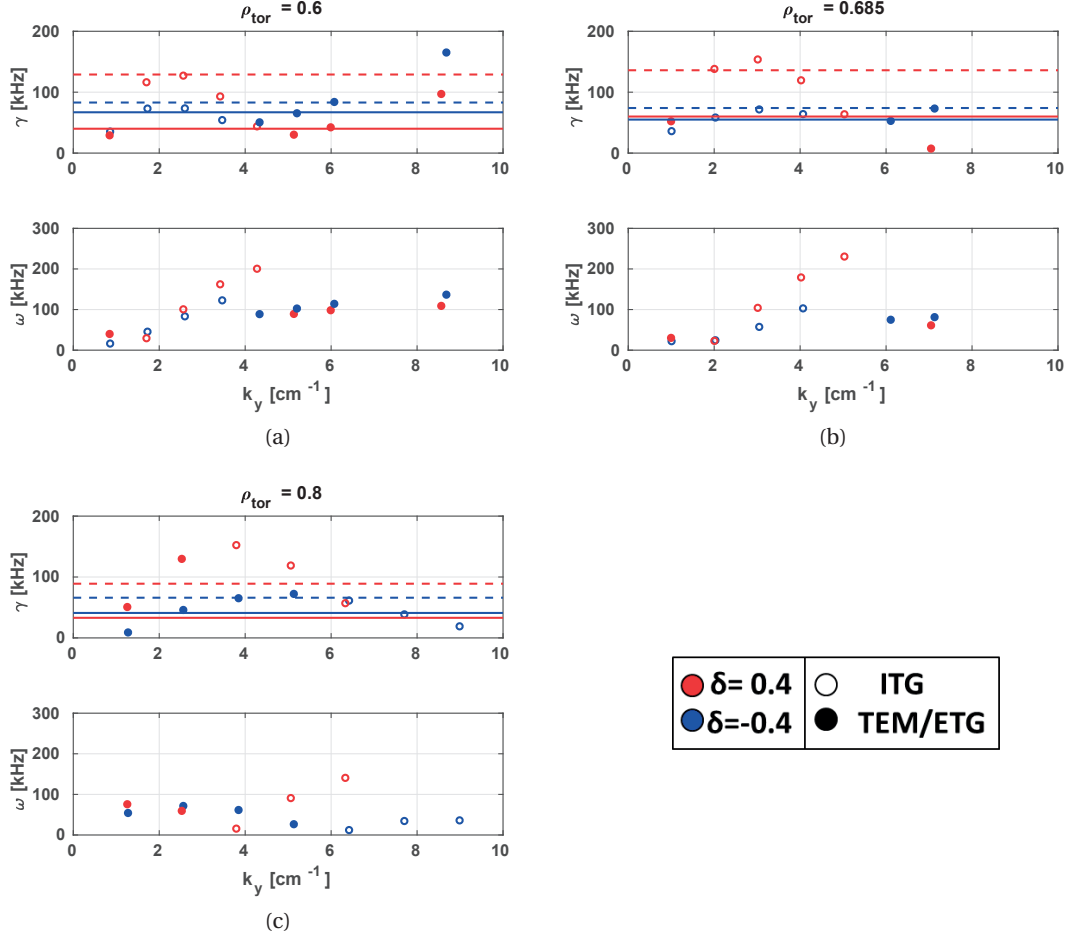


Figure 5.14 – Linear growth rate ( $\gamma$ ) and frequency ( $\omega$ ), in real units, of the most unstable mode for each wavenumber in three radial positions:  $\rho_{tor} = 0.6$  (a),  $\rho_{tor} = 0.685$  (b),  $\rho_{tor} = 0.8$  (c). In the  $\omega$  plots, full markers correspond to modes that propagate in the electron diamagnetic direction (TEM or ETG). Simulations have been run using the same electrons and ions profiles, changing the plasma equilibrium from negative triangularity (blue) to positive triangularity (red). Horizontal lines in the  $\gamma$  plots represent the estimated  $E \times B$  shearing rate, with its uncertainty shown as the dashed line.

## 5.2. Development of matching NBI heated discharges with positive and negative $\delta$

results. It is particularly evident how the addition of carbon in the simulations influences the growth rate of the most unstable mode, lowering it substantially with respect to a simulation with just two active species (squares versus circles).

As already mentioned, the results presented in figure 5.13 were obtained using the carbon concentration measured by the CXRS measurements, resulting in  $Z_{eff} = 1.3$ . This solution is consistent with the assumption that carbon is the only impurity in the plasma, normally realistic in a carbon wall machine such as TCV. This assumption is challenged for these discharges, since use of NBI in TCV is believed to cause the injection of metal impurities in the plasma, mainly coming from the beam duct [98]. An estimation of  $Z_{eff}$  independent of the CXRS measurements is routinely obtained on TCV through the use of current density balance:  $I_p = I_{ohm} + I_{CD} + I_{BS}$ . The bootstrap current  $I_{BS}$  is calculated from plasma profiles using a neoclassic model [99][100] by assuming a stationary plasma over the current diffusion time. The current drive  $I_{CD}$ , from both ECRH and NBI, is calculated using TORAY and ASTRA, respectively. From the measurement of loop voltage  $V_{loop}$ , then, it is possible to estimate the  $Z_{eff}$  that would give the plasma a resistivity suitable to achieve the correct value of  $I_{ohm}$  according to the neoclassical model. In the discharges discussed in this chapter and in chapter 4,  $Z_{eff}$  calculated in this way is always found to be higher than the value obtained taking into account solely the carbon content measured by CXRS. For the negative  $\delta$  discharge, this estimation results in  $Z_{eff} = 2.91$ , much higher than what has been estimated using carbon as the only impurity (1.3). To avoid running a simulation where this effective charge has to be reached by unrealistically increasing the carbon content, thus diluting the main ion species, a test has been performed with four active species. Using iron ( $Z = 26$ ) as a fourth active species it has been possible to match  $Z_{eff} = 2.91$ , while maintaining the realistic carbon profiles measured by CXRS. In doing so, it is assumed that  $T_{Fe} = T_C$  and  $R/L_{T_{Fe}} = R/L_{T_C}$   $R/L_{n_{Fe}} = R/L_{n_C}$  while  $n_{Fe}$ ,  $n_D$  and  $R/L_{n_D}$  are calculated imposing charge neutrality. The results of these simulations are shown in figure 5.15. While adding iron as an active species does not influence the growth rate for low wavenumbers with respect to using only carbon, according to the CXRS measurements, it is interesting to notice that the sign of the frequency for these modes becomes negative, implying that, linearly, the electron drive has become dominant.

Taking into account the presence of impurities other than carbon is thought to be the more realistic approach to study these discharges, but non-linear simulations are necessary to understand which of these two methods leads to more realistic saturated heat fluxes. This may ideally require taking into account also fluctuations at the electron scale, since the growth rates for high  $k_y$  seem to be affected by the different way of treating  $Z_{eff}$ .

Extensive non-linear simulations are necessary to pursue an in depth study of the effects of shape on the stability of turbulent modes in these discharges, as was done for example in [4]. Global, non-linear simulations would also help understand the nature of the non local influence that negative triangularity seems to exert on fluctuations. Flux-driven simulations, in particular, would reduce the impact of the profiles measurements uncertainty on the final

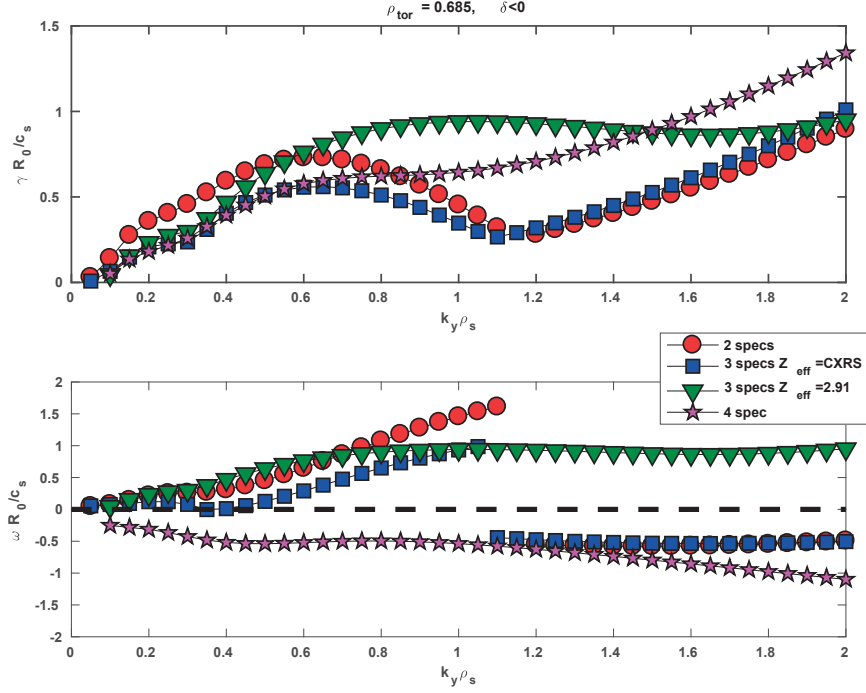


Figure 5.15 – Normalized linear growth rate ( $\gamma$ ) and frequency ( $\omega$ ) of the most unstable mode for each wavenumber with different impurity content of the plasma: no impurities (circles); carbon in concentration measured by CXRS (squares); carbon in concentration to match  $Z_{eff} = 2.91$  (triangles); carbon with concentration measured by CXRS and iron to match  $Z_{eff} = 2.91$  (stars). The simulations have been run using the profiles of the  $\delta = -0.4$  plasma at  $\rho_{tor} = 0.685$

saturated state. The results of these simulations which are beyond the scope of this thesis, could be processed with a synthetic diagnostic for the CECE diagnostic [101] and compared with the experimental measurements.

### 5.3 Conclusions

A pair of positive and negative  $\delta$  discharges, heated with NBI, were developed with comparable density and current profiles. The negative  $\delta$  plasma discharge exhibits higher confinement with respect to the positive triangularity one, also in presence of ion heating. To obtain comparable temperature profiles, almost 1.5 times total effective power had to be used in the positive  $\delta$  plasma with respect to the negative  $\delta$  one, as shown in table 5.1. Radiative temperature fluctuation measurements using the CECE diagnostic found fluctuation amplitudes to be almost twice as large in the positive  $\delta$  cases with respect to the negative  $\delta$ , see figure 5.11. It was excluded that the suppression of fluctuation could be associated exclusively to spectral broadening caused by a change in the toroidal rotation. Future works, after the installation

of a second NBI on TCV, could properly investigate the effects of rotation and ion heating on fluctuations separately.

Flux-tube, linear GENE simulations suggest that, in these plasmas, fluctuations are mixed TEM/ITG. The dominant turbulence regime strongly depends on the amount and type of impurities. Negative triangularity has been found to reduce the linear growth rates of low wavenumber modes, with a stronger effect in outer radial positions, suggesting reduced saturated transport also in these NBI heated discharges where  $T_e/T_i \sim 1$ . Estimates of the  $E \times B$  shearing rate suggest that shear may have important effects on the saturated state of turbulence, but no direct effect of triangularity on  $\omega_{E \times B}$  was observed. Non-linear and global simulations are necessary to further investigate the underlying causes of these effects and the influence of triangularity in positions closer to the plasma core.





# 6 Effects of collisionality and $T_e/T_i$ on fluctuations in positive and negative $\delta$ plasmas

## 6.1 Introduction

It has already been reported, in Chapter 4, how shape, and in particular triangularity, can affect fluctuations and transport in different sets of plasma conditions. Past experiments on TCV [3] highlighted that high collisionality reduces the relative improvement of confinement observed in negative with respect to positive triangularity plasmas. For high density, ohmic discharges, no difference in  $\chi_e$  was observed. This suggests that different plasma parameters can affect the way negative triangularity influences transport. Plasma conditions are known to strongly affect the type and intensity of turbulence developed during a discharge. For example, collisionality has a stabilizing effect on trapped electron modes (TEMs) [102] and the ratio  $T_e/T_i$  constitutes an important term in determining the relative strength of the ion and electron instability drives. A first experimental investigation into the combined effects of triangularity and collisionality on fluctuations has been already conducted in [7]. The aim of the present work is to study the behaviour of fluctuations in a large parameter space, including a variety of plasma shapes, collisionality and  $T_e/T_i$  values.

For this purpose, a database has been built putting together a series of discharges where density, ECRH and NB heating are varied in plasmas with positive and negative triangularity. In all of these discharges, radiative temperature fluctuations are measured using the CECE diagnostic.

Building a database of discharges with different heating schemes and density, in particular including discharges in which  $T_e/T_i \sim 1$ , allows one to verify if the effects of negative  $\delta$  already discovered in previous studies [17][16][23][7] are also found in conditions that are closer to those of a reactor [28][84].

In addition, it is interesting to experimentally investigate the effect of triangularity on the threshold for the onset of fluctuations [103] and the dependence of the fluctuations amplitude on the normalized temperature gradients [5][6][26]. While in this study the local temperature gradient has not been tailored by varying the on and off-axis ECH power in a single discharge,

## Chapter 6. Effects of collisionality and $T_e/T_i$ on fluctuations in positive and negative $\delta$ plasmas

---

as was done in [103], the variety of plasma discharges in the database allows measuring temperature fluctuations in equilibrium situations with different normalized temperature scale lengths for otherwise very similar plasma conditions. Temperature fluctuation measurements can then be used to investigate the effects of triangularity on critical gradients and stiffness.

### 6.2 Experimental method

The database contains 50 limited, L-mode discharges, 32 with positive triangularity ( $\delta = .0.4$ ) and 18 with negative triangularity ( $\delta = -0.4$ ). The shaping was not perfectly symmetrical for all discharges. Elongation varied between 1.4 and 1.5 in both shapes. Plasma current was kept fixed in all discharges at 230 kA, causing differences in the safety factor profiles ( $q_{95} \sim 3.3$  and  $q_{95} \sim 3.8$  for the negative and positive triangularity discharges respectively). In these plasmas the line averaged density, calculated along the central chord of the FIR, is varied from  $1 \cdot 10^{-19}$  to  $3.5 \cdot 10^{-19} \text{ m}^{-3}$ . EC heating is applied using one or two gyrotrons (using both an equatorial and an upper lateral launcher), pointing slightly off the plasma axis but still inside the  $q = 1$  surface, in order to reduce the impact of sawteeth [104]. Plasmas included in the database where ECH was applied, are heated using either one gyrotron at 365 kW, two gyrotrons at 365 kW or two gyrotrons at 475 kW. Neutral beam heating is applied to some of the negative (300 kW) and positive (300 or 950 kW) triangularity discharges. Taking into account also the ohmic power, the total nominal power (without taking into account of effective absorption of NBI power) in plasmas varies between 150 and 1500 kW. In all discharges the plasma axis is set at  $z = 0$  cm in order to have on-axis NB injection when the heating beam is used and CXRS measurements across the whole plasma profile. The discharges studied have confinement times varying between 2 and 20 ms.

CECE measurements are taken using the  $z = 0$  horizontal line of sight, with channels spaced by 300 MHz. The dedicated RF stage of the CECE diagnostic ( $f_{LO} = 61$  GHz) was temporarily connected to the  $z = 0$  horizontal line of sight instead of the standard ECE radiometer RF stage ( $f_{LO} = 64$  GHz), in order to extend the fluctuations measurements further towards the plasma edge. For all of these discharges, the flat top between 0.5 and 1.5 s was divided into 100 ms intervals (much larger than the energy confinement time for all considered discharges, varying from 2 to 17 ms). The plasma in one of these intervals was considered stationary, thus appropriate for correlation analysis, if the plasma density did not vary more than 15% and the heating power and mixture did not change. Equilibrium and current density were also checked to not vary during the selected intervals.

The amplitude of the fluctuations was calculated from cross-correlation analysis, as introduced in paragraph 3.6, integrating the CPSD over the 20-50 kHz range, obtaining, for each time interval, fluctuations measurements in five different radial positions. In some of the discharges, especially when auxiliary heating was applied, quasi-coherent modes could be observed in the 20-25 kHz range in the CPSD, similar to those visible in figure 5.10 for the negative triangularity discharge. To exclude their contribution from the fluctuations amplitude calculation, they

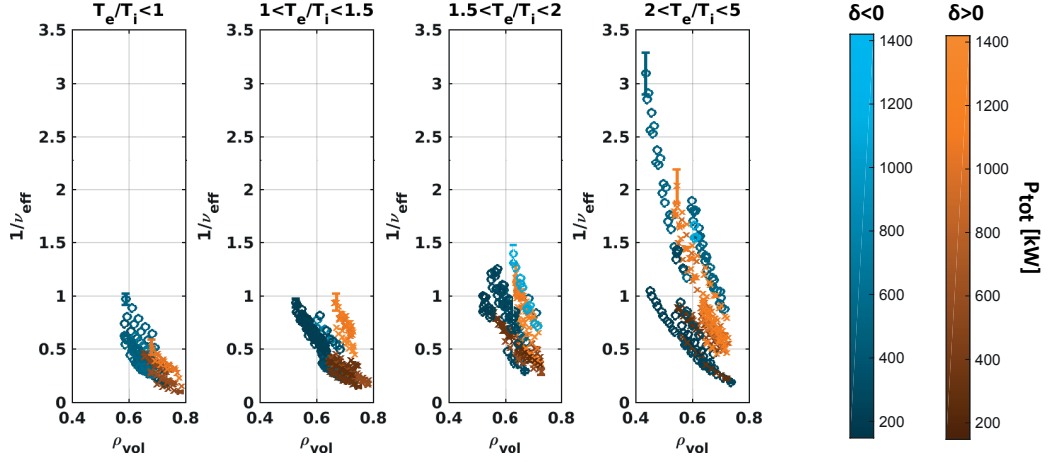


Figure 6.1 – Inverse effective collisionality  $1/\nu_{eff}$  for each channel time interval and discharge included in the database, plotted versus the radial location of the measurement. The different subfigures represent different windows of  $T_e/T_i$ . The shade of color is related to the total nominal power in the discharge ( $P_{ECH} + P_{NBI} + P_{Ohm}$ ).

have been identified, and their amplitude subtracted with respect to the background spectra around them.

The database contains a total of 1774 points, of which 1179 in positive  $\delta$  discharges and 595 in negative  $\delta$  ones. The local plasma conditions at the measurement points cover the ranges  $0.55 < \rho_{vol} < 0.75$ ,  $0.1 < 1/\nu_{eff} < 2$ ,  $0.5 < T_e/T_i < 5$ . As already defined in 4.1, effective collisionality is defined as the ratio between the electron-ion collision rate and the electron curvature drift frequency and it is approximated as  $\nu_{eff} \sim 0.1 R Z_{eff} n_e / T_e^2$  (with  $T_e$  in keV,  $n_e$  in  $10^{-19} m^{-3}$  and  $R$  in m). The parameter space covered is shown in figure 6.1 where each point represents the measurement of a single channel in one stationary time interval. In that figure the values of  $1/\nu_{eff}$ , for different values of  $T_e/T_i$  (both taken at the measurement points) are plotted versus their radial location. The color of the points is related to plasma triangularity while its hue to the nominal total power ( $P_{ECH} + P_{NBI} + P_{Ohm}$ ) applied in the specific discharge and time interval.

The upper boundary for the contribution of density fluctuations to the radiative temperature fluctuation measurements included in the database, calculated as in paragraph 3.3.2, varied between 3% and 22%.

## 6.3 Results

In all plasmas considered in this study, negative triangularity discharges show better confinement than positive triangularity ones for comparable plasma conditions. Figure 6.2 shows how the H-factor  $H_{98}(y,2)$  [105] is always higher for negative triangularity discharges with respect to positive triangularity ones in plasmas with similar characteristics, summarized by  $\nu_{eff}$  at

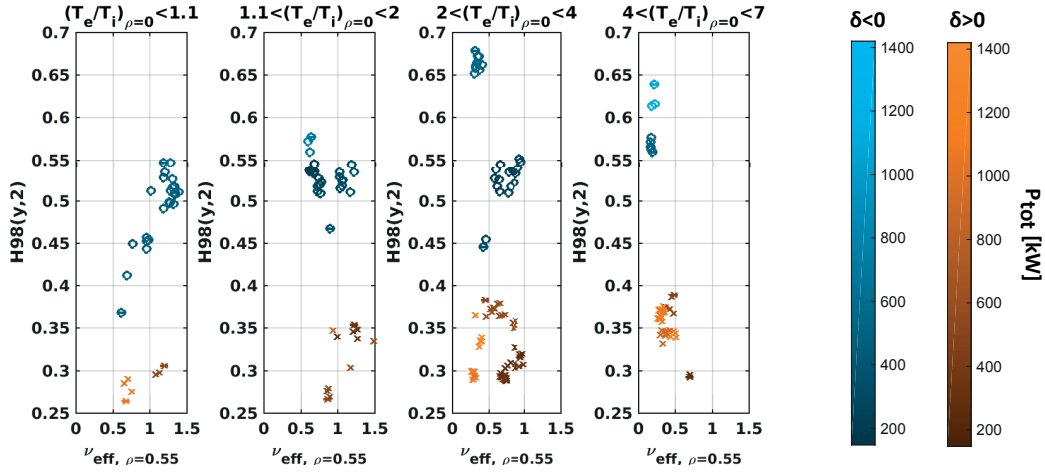


Figure 6.2 – H-factor  $H98(y,2)$  for each time interval and discharge considered in the database. The data are divided in windows according to the electron-ion temperature ratio at the plasma core.

$\rho_{vol} = 0.55$  (as was done in [3]) and  $T_e/T_i$  at the plasma core. Most interestingly, this includes plasmas with high collisionality and low  $T_e/T_i$ . In this database, though, not high enough values of collisionality were reached to probe the part of the parameter space where the relative confinement improvement in negative triangularity compared to positive triangularity discharges was strongly reduced in [3] ( $\nu_{eff, \rho=0.55} \sim 2$ ). In this figure each point represents the plasma conditions in a stationary time interval for one of the database discharges. Plasmas with comparable conditions should present similar H-factors so the difference that is observed between positive and negative  $\delta$  discharges can only be due to triangularity effects not accounted for in the scaling law.

One commonly accepted explanation for the rise in the value of  $\chi_e$  at lower  $\nu_{eff}$  is the reduced stabilization of turbulent fluctuations. As was done in [7], the fluctuation measurements have been plotted in figure 6.3 against the corresponding local  $1/\nu_{eff}$ , for all channels, time intervals and discharges. At all  $\nu_{eff}$  values, in comparable radial positions, fluctuations are higher in positive  $\delta$  than in negative  $\delta$  plasmas. In both shapes, fluctuation amplitude decreases with increasing collisionality with the difference between positive and negative triangularity reducing strongly for high  $\nu_{eff}$  values. This result is consistent with previous observations for density fluctuations [7] and with the behaviour of electron heat conductivity [3] mentioned earlier. It is important to notice that all fluctuation amplitudes below the diagnostic sensitivity level (represented by the solid horizontal black line in the plot) are characterized by relatively large uncertainties and represent measurements where no meaningful fluctuation was detected.

A possible explanation for the relative suppression of fluctuations decreasing at higher collisionality can be produced by assuming that the beneficial effect of negative triangularity on transport stems from the stabilization of fluctuations that, in turn, reduces the anomalous

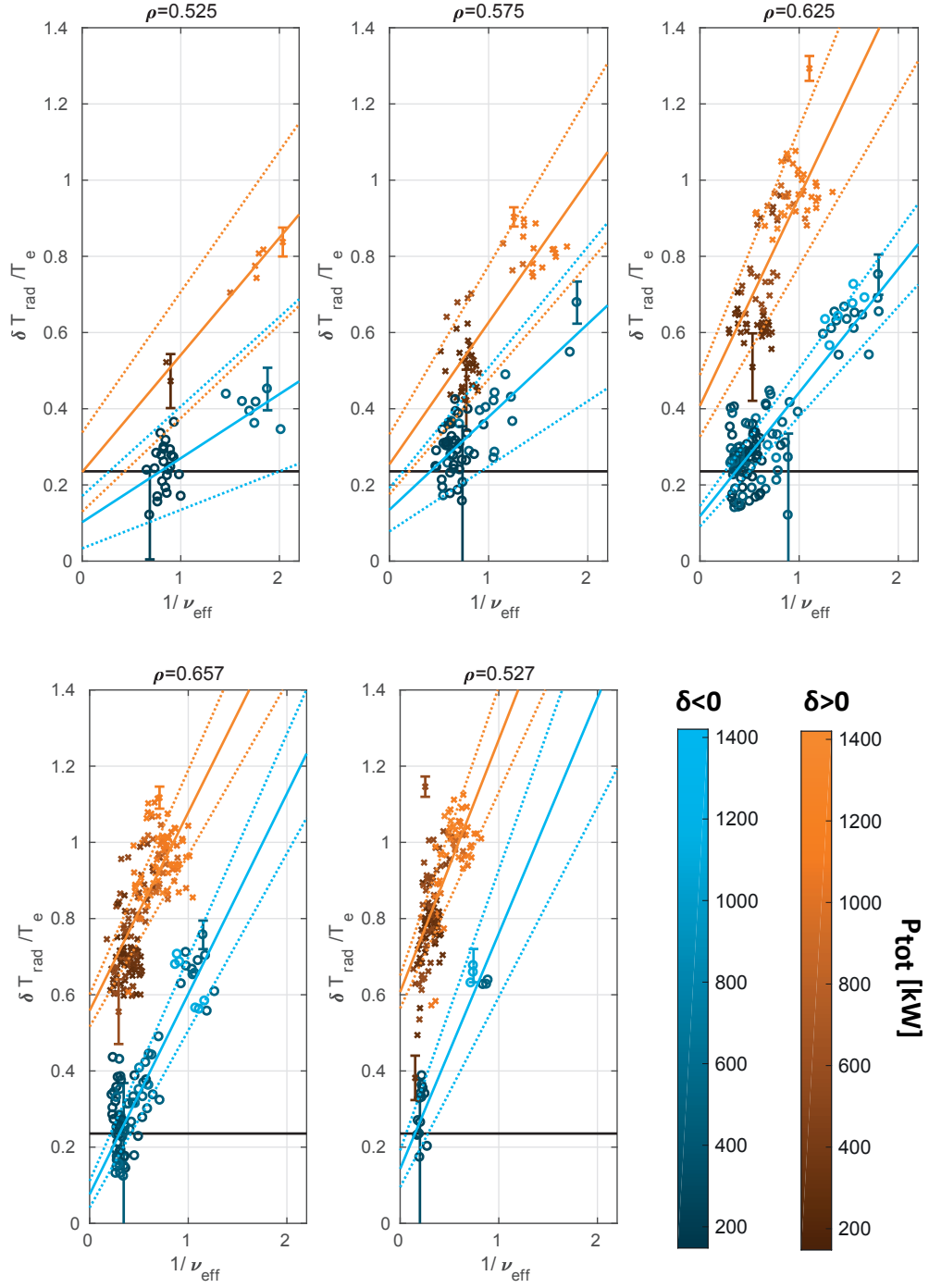


Figure 6.3 – Relative  $T_e$  fluctuations (in %) in positive and negative triangularity as a function of  $1/\nu_{eff}$  for various radial positions ( $\Delta\rho = 0.05$ ). The colors of the different points are related to the nominal power ( $P_{ohm} + P_{ECH} + P_{NBI}$ ) used in the discharges, with lighter colors corresponding to higher power. The black lines represent the estimated sensitivity limit for fluctuations detection, below which fluctuations are indistinguishable from noise.

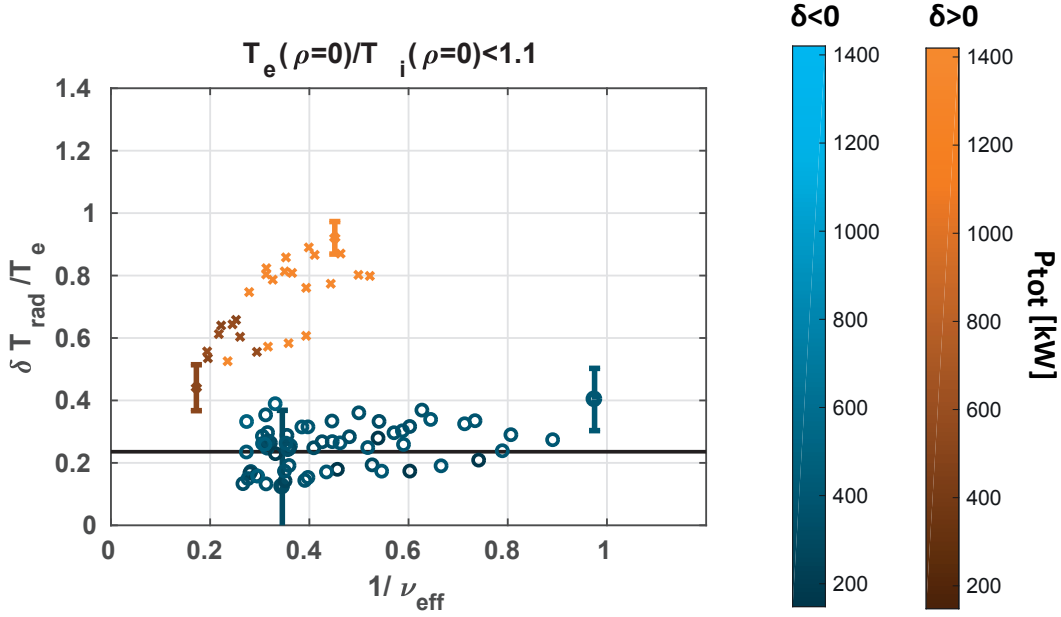


Figure 6.4 – Relative  $T_e$  fluctuations (in %) in positive and negative triangularity as a function of  $1/\nu_{eff}$  for all radial positions. The colors of the different points are related to the nominal power ( $P_{ohm}+P_{ECH}+P_{NBI}$ ) used in the discharges, with lighter colors corresponding to higher power. The black lines represent the estimated sensitivity limit for fluctuations detection, below which fluctuations are indistinguishable from noise. Only points corresponding to discharges for which  $T_e/T_i \leq 1.1$  at the core are plotted.

transport in the plasma. Since collisionality has also a damping effect on turbulence drive (especially for TEM) [102], its increase could reduce the relative confinement improvement provided by negative  $\delta$  by reducing the relative influence of fluctuations on transport. It is of particular interest to notice that also for plasmas where  $T_e/T_i \leq 1$ , obtained using NBI heating, fluctuations are higher in positive  $\delta$  cases for a large range of collisionalities. This is highlighted in figure 6.4, where only points in which  $(T_e/T_i)_{\rho=0} \leq 1.1$  are shown. For the negative  $\delta$  discharges, the amplitude of the measured fluctuations is so low that they can hardly be distinguished from noise. This does not exclude the existence of an underlying trend that the CECE in this specific configuration could not observe.

The data gathered in this database also allow to observe the effects of varying  $T_e/T_i$ , an important factor in determining the drive of different turbulent modes, on the fluctuations amplitude. Plotting the same set of data as in figure 6.3 directly against  $T_e/T_i$ , shown in figure 6.5, no clear trend can be identified for any of the combinations of radial position and collisionality. While a positive correlation between  $\delta T_e/T_e$  and  $T_e/T_i$  could be deduced by some of the plots in figure 6.3, that is partly related to the dependence of relative fluctuations on  $T_e$  alone, shown in figure 6.6. This latter dependence is to be expected due to the dependence of fluctuations amplitude on  $\nu_{eff}$  illustrated in figure 6.3. If that is taken into account, the temperature ratio does not seem to have a direct effect on fluctuations for the parameter space

studied in this database.

Suppression of fluctuations in negative  $\delta$  plasmas can still be observed across the whole range of  $T_e/T_i$  explored. Only in few cases the measurements in positive and negative  $\delta$  show comparable levels of fluctuations for similar  $T_e/T_i$ . In conclusion, from the data collected in these experiments, a direct effect of  $T_e/T_i$  on fluctuations could not be determined. This can be due to not exploring plasma conditions where these effects would have been visible, or to the limited sensitivity of the diagnostic to small fluctuating structures. It is observed, though, that negative triangularity causes suppression of the fluctuations for all  $T_e/T_i$  values explored in these experiments.

As already mentioned in paragraph 4.1.2, gyrokinetic simulations, run for a pair of positive and negative  $\delta$  plasmas with identical profiles, suggest that negative triangularity could act on the gradient threshold necessary for the onset of turbulent modes [6]. To elucidate this effect, the fluctuations amplitude is plotted with respect to the local normalized electron temperature scale length ( $\frac{R}{L_{Te}} = \frac{R}{\nabla T_e/T_e}$ ) for different radial positions and collisionality. In figure 6.7 it is possible to observe how fluctuations in negative  $\delta$  discharges are, in almost all cases, lower than in positive  $\delta$  ones for comparable normalized gradients. This suggests that mechanisms such as those sketched in figure 4.5 [6] could be at play for temperature fluctuations. Negative triangularity could increase the gradient threshold for the onset of turbulence, decrease the dependence of fluctuations amplitude on the driving gradient or a combination of both these effects. To properly test these hypothesis, though, dedicated experiments with varying amounts of ECH power deposited inside and outside the measurement location, as was done in [103], are necessary.

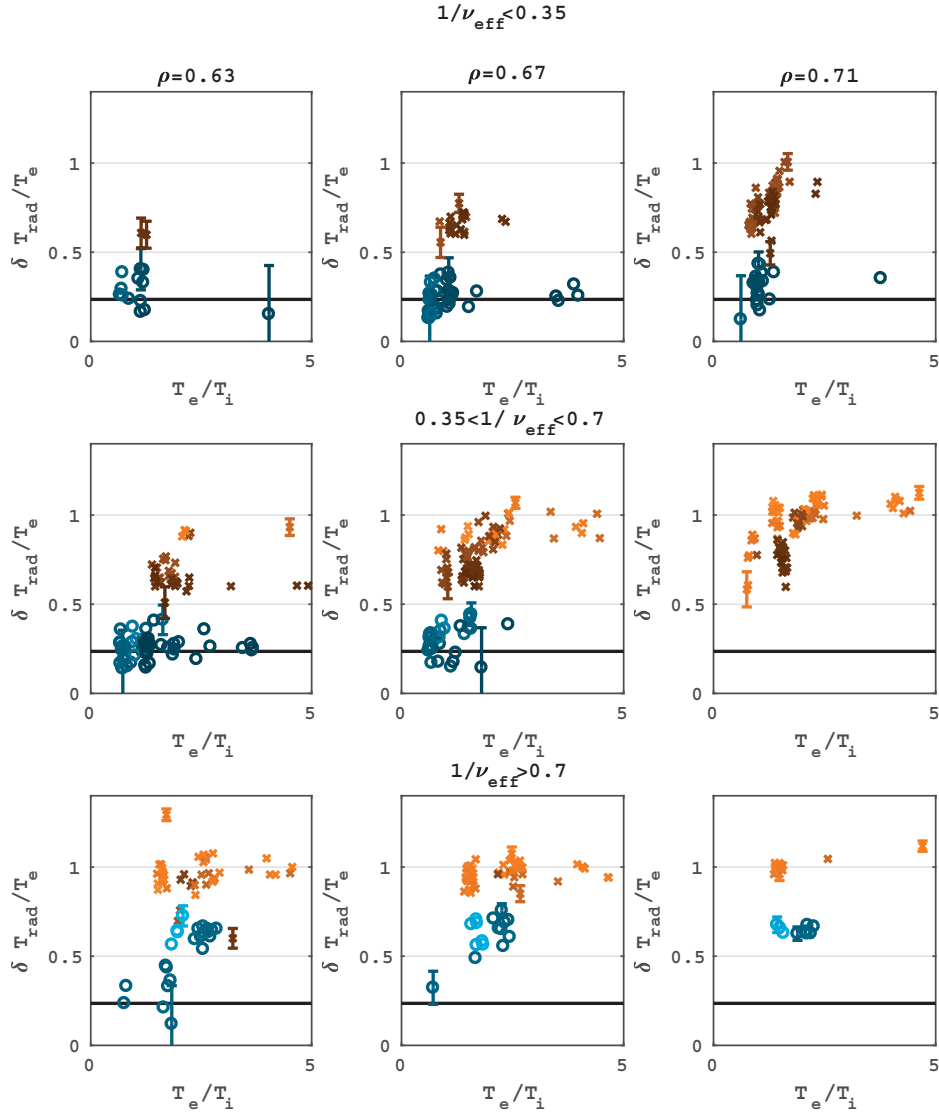


Figure 6.5 – Relative  $T_e$  fluctuations (in %) in positive and negative triangularity as a function of  $T_e/T_i$  for different combinations of radial positions ( $\Delta\rho = 0.05$ ) and  $1/\nu_{eff}$ . The colors of the different points are related to the nominal power ( $P_{ohm} + P_{ECH} + P_{NBI}$ ) used in the discharges, with lighter colors corresponding to higher power. The black lines represent the estimated sensitivity limit for fluctuations detection, below which fluctuations are indistinguishable from noise.



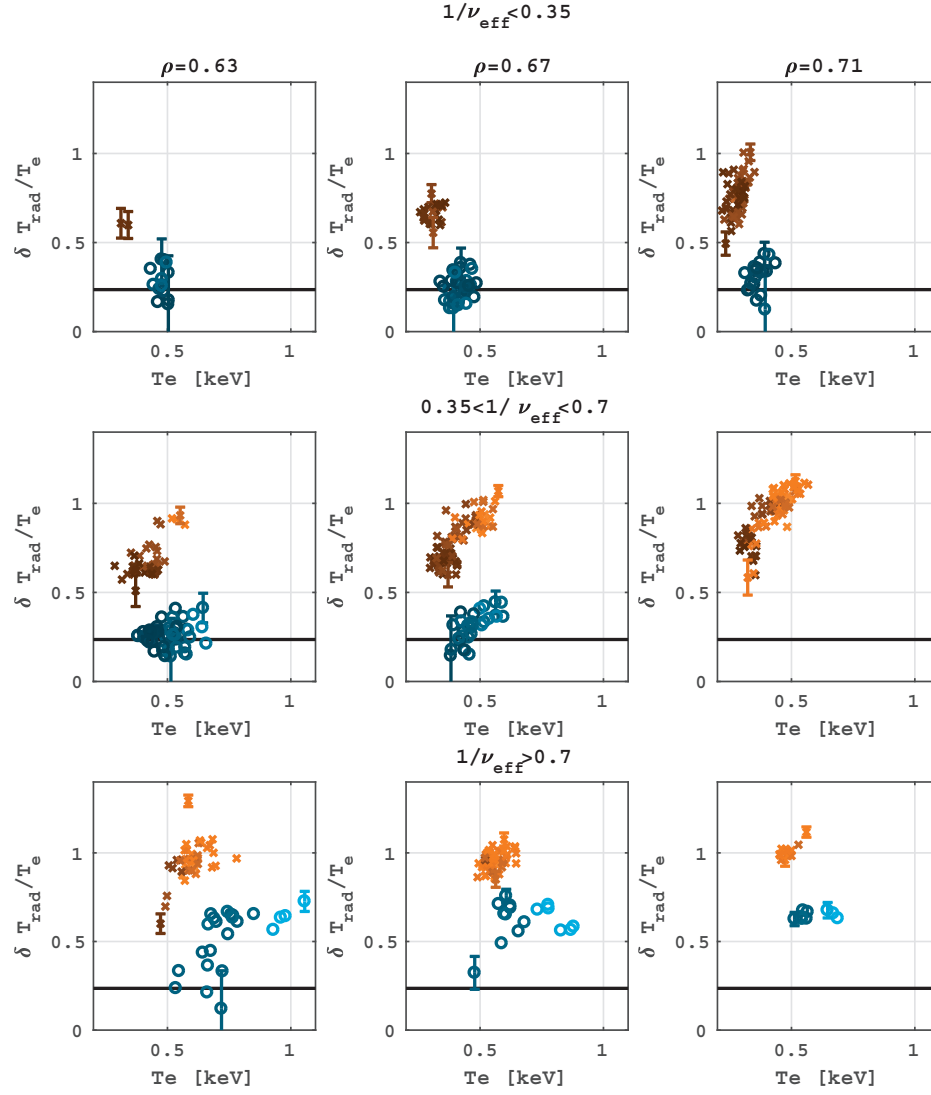


Figure 6.6 – Relative  $T_e$  fluctuations (in %) in positive and negative triangularity as a function of  $T_e$  for different combinations of radial positions ( $\Delta\rho = 0.05$ ) and  $1/\nu_{eff}$ . The colors of the different points are related to the nominal power ( $P_{ohm}+P_{ECH}+P_{NBI}$ ) used in the discharges, with lighter colors corresponding to higher power. The black lines represent the estimated sensitivity limit for fluctuations detection, below which fluctuations are indistinguishable from noise.

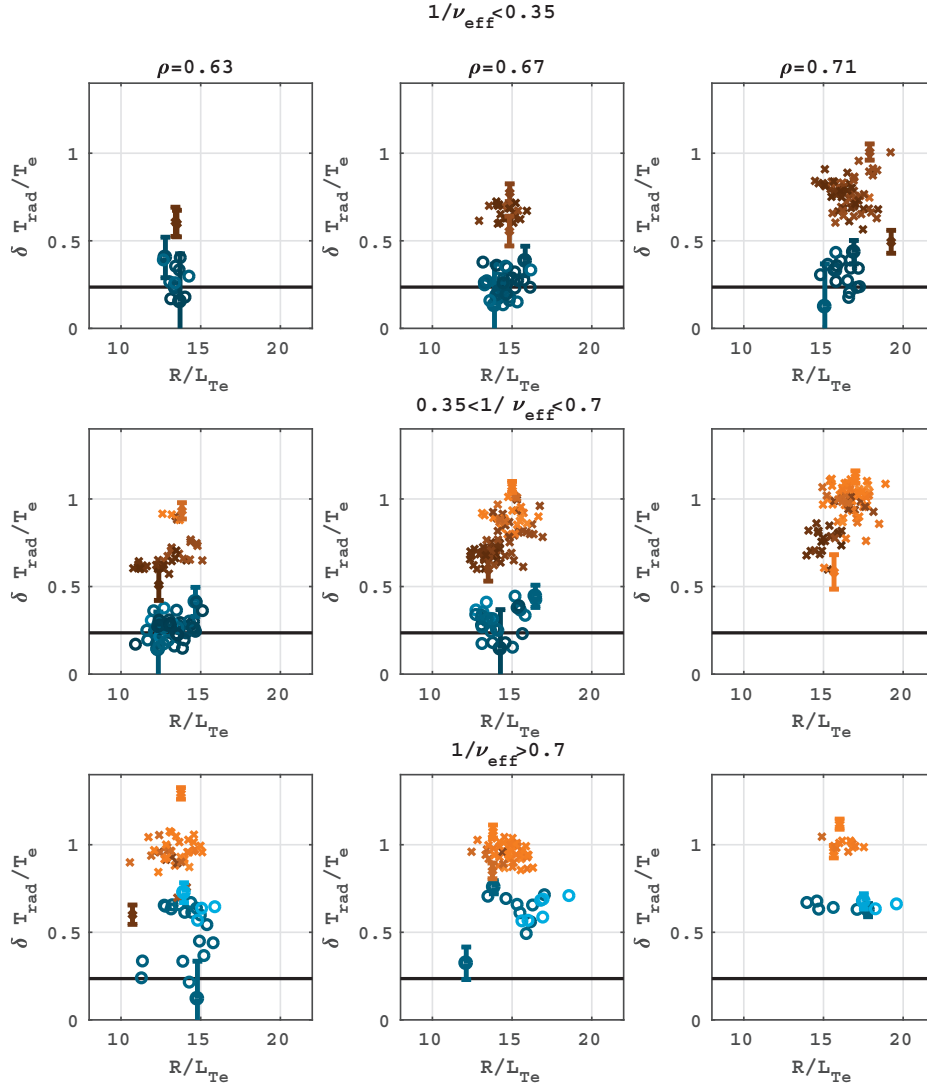


Figure 6.7 – Relative  $T_e$  fluctuations (in %) in positive and negative triangularity as a function of  $R/L_{T_e}$  for all radial positions. The colors of the different points are related to the nominal power ( $P_{\text{ohm}} + P_{\text{ECH}} + P_{\text{NBI}}$ ) used in the discharges, with lighter colors corresponding to higher power.

## 6.4 Conclusions

A database of  $T_e$  fluctuation measurements in positive and negative  $\delta$  discharges was constructed across a wide range of parameters. The effective collisionality  $\nu_{eff}$  and the  $T_e/T_i$  ratio have been varied by changing the plasma density and by combining the ECH and NBI systems of TCV at various power levels. In all discharges radiative temperature fluctuations have been measured using the CECE diagnostic looking at the plasma through the  $z=0$  horizontal line of sight. Negative triangularity is found to improve the confinement time in all cases corresponding to comparable plasma conditions. This holds true also at high collisionality and low  $T_e/T_i$  values, regimes previously not explored experimentally on TCV.

The fluctuation measurements confirm the suppressing effect of collisionality on fluctuations and, in particular, recover the reduction of relative improvement of negative  $\delta$  plasmas with respect to the positive  $\delta$  ones at high collisionality [3][7]. Most importantly, these effects appear also when  $T_e/T_i \sim 1$ , making these observations fully relevant to reactor-like machines. No correlation is found, in the discharges composing this study, between  $T_e/T_i$  and fluctuation amplitude. It is noted that this could be due to the limits of the parameter space explored, or to specific limitations of the diagnostic sensitivity.

Finally, fluctuations in negative  $\delta$  plasmas are found to be of lower amplitude than in positive  $\delta$  ones for similar  $R/L_{Te}$ , in all the explored combinations of collisionality and radial positions. This points toward the fact that negative triangularity affects the onset mechanism of fluctuations, as already suggested by numerical simulations results in [6]. This experimental observation could be explained, in fact, on the basis of a higher critical gradients for negative  $\delta$  plasmas, lower stiffness in the dependence of fluctuation amplitudes upon  $R/L_{Te}$  (as sketched in figure 4.5), or a combination of both.



## 7 Conclusions and outlook

By using the CECE diagnostic on TCV, which allows measuring low amplitude, large bandwidth fluctuations, this thesis studied the influence of various plasma parameters and plasma shaping, on radiative temperature fluctuations in a tokamak. To take advantage the variety of plasma configurations available to TCV, the CECE diagnostic is connected to three different lines of sight. The upper lateral, dual-axis steerable one has an antenna pattern that allows the study of a larger spectrum of fluctuations, including higher wavenumbers than the horizontal one. Furthermore, the six YIG IF filters and two RF stages with different LO frequencies grant great freedom in the choice of the channel location.

The unparalleled shaping flexibility of TCV, together with the versatility of the CECE diagnostic, allowed the study of radiative temperature fluctuations in positive and negative triangularity, L-mode limited discharges, in a variety of plasma conditions.

In a series of low density ohmic discharges, with the same plasma current and comparable density profiles, negative triangularity plasmas have higher temperature than those with positive triangularity over the whole radial profile, despite the fact that the magnitude of triangularity quickly vanishes when moving towards the plasma core. The resulting profiles suggest the existence of a stiff region in the plasma (approximately  $0.45 < \rho_{vol} < 0.75$  for these discharges) where  $R/L_{Te}$  is insensitive to changes in various plasma parameters (in this case triangularity). On the other hand, in the region just outside ( $\rho_{vol} > 0.75$ ), gradients vary in response to changes in the plasma conditions [5]. In these discharges, temperature fluctuations were measured in both of these regions. Fluctuations were found to be strongly suppressed in negative triangularity discharges in the non stiff region, with the difference between the two shapes quickly decreasing inside the stiff region of the plasma. A possible explanation for these observations is that the improvement in confinement caused by negative  $\delta$ , revealed by a steepening of the pressure gradient, is localized in the non stiff region closer to the plasma edge, where the magnitude of triangularity is larger. Higher pressure across the whole radial profile results then from the fact that the normalized scale length in the stiff region remains constant. These results qualitatively agree with previous experiments in TCV that found that negative triangularity discharges are characterized by reduced fluctuations

and improved confinement in low collisionality plasmas with high  $T_e/T_i$  ratio [89][23][3][7].

This work was the first on TCV to employ the NBI heating system to obtain negative triangularity plasmas where,  $T_e/T_i \sim 1$  over a large fraction of the radial profiles. For this purpose, a pair of discharges with matched density, safety factor profiles, elongation and opposite triangularity were realized and heated with NBI, successfully reaching  $T_e/T_i \leq 1$ . Also in these cases, the negative triangularity discharge presented higher electron and ion temperature profiles across the whole normalized radius than the positive triangularity one, despite the fact that the two plasmas were subjected to 330 kW and 435 kW of effective heating power, respectively. Comparable electron temperature profiles were achieved by using  $\sim 470$  kW in the positive triangularity discharge and  $\sim 330$  kW in the negative triangularity one. Also in this case, radiative temperature fluctuations, measured using the CECE diagnostic, are suppressed in the negative  $\delta$  case.

Linear gyrokinetic simulations, based on the experimental profiles, show a reduction of the linear growth rates for low wavenumber modes in negative  $\delta$  plasmas. The reduction is stronger for radial positions closer to the plasma edge, where the magnitude of the triangularity is higher. According to the simulations, the unstable modes are a mix of ITG and TEM, a different situation with respect to the pure TEM turbulence found for plasmas with  $T_e/T_i > 1$  in previous studies. Non linear simulations are necessary to study also the saturated state of turbulent instabilities in these plasmas. The simulations confirmed the important effect of impurities on the linear instability spectrum. Impurities mainly have a stabilizing effect on low wavenumber modes ( $k_y \rho_s < 1$ ) but, depending on the quantity and on which impurity species are actually used in the simulation, they can change the linear dominant turbulence from ITG to TEM. These results highlight how important is a thorough characterization of the impurity content of TCV plasmas in order to run simulations whose results can be directly compared with the experimental measurements.

To further extend the parameter space of the investigation, a series of discharges were realized, in which large ranges of collisionality values and  $T_e/T_i$  ratios were obtained for positive and negative triangularity discharges. Temperature fluctuations were measured in all parameter combinations using the CECE diagnostic. These measurements showed that negative triangularity improves plasma confinement and reduces fluctuations across a wide range of  $\nu_{eff}$  and  $T_e/T_i$  values. Collisionality was found to be the main actor in controlling by how much fluctuations are suppressed in negative  $\delta$  plasmas, with the strongest effect observed for the lowest collisionality. The ratio  $T_e/T_i$  was not found to have a strong effect on the fluctuation amplitudes for any combination of the parameters explored in this work. Naturally it cannot be excluded that  $T_e/T_i$  plays a more important role in a different parameters space, or on fluctuations whose wavenumbers fall outside the diagnostic sensitivity limits. Measurements in comparable radial positions, for plasmas with similar collisionality and the same normalized scale lengths, show higher fluctuation amplitudes in positive triangularity discharges. These observations suggest that the stabilizing effect of negative  $\delta$  on fluctuations could take the form of a higher critical threshold gradient for the onset of fluctuations, a weaker

---

proportionality between gradient and fluctuation amplitude, or a combination of both [6].

For the continuation of the studies on the effects of plasma conditions on core turbulent fluctuations in TCV, the use of additional diagnostic techniques could be very beneficial. For example the recently commissioned reflectometer system [65] and the tangential phase contrast imaging (TPCI) [7], for which a substantial upgrade is planned in the coming years, could provide density fluctuation measurements in a wider range of plasma densities, with the possibilities of quantifying also the fluctuations' wavenumber spectrum. The possibility of studying discharges using the CECE together with these other fluctuation diagnostics would provide a more complete characterization of turbulent modes. In particular, the shared line of sight between the CECE and the reflectometer can be used to perform density-temperature fluctuations cross-phase measurements [66][101], of particular interest for comparing experimental measurements with the results of gyrokinetic simulations [106]. Furthermore, reflectometry and TPCI can be used to extend the study of fluctuations to higher density plasmas, in which the CECE was unable to take measurements due to cutoff blocking access to the resonance layers. In the coming year the installation of a second 1 MW NBI is planned on TCV, injecting particles in the opposite direction with respect to the first one. This, in addition to further extending the parameter space accessible to TCV, will allow the study of the effects of ion heating and rotation on fluctuations separately.

Despite extended experimental efforts, the underlying causes for the suppression of fluctuations in negative triangularity discharges are not fully understood yet. An extensive set of numerical simulations is necessary. Global, non-linear simulations are considered to be necessary in order to reproduce the confinement improvement also for inner radii where triangularity is vanishing. Non-linear flux-tube simulations can also be used to verify if the same mechanisms already observed for the pure TEM discharges [4][26] also apply to mixed TEM/ITG plasmas, as identified by the linear simulations. Finally, once a good match is achieved between the simulated and experimentally measured heat fluxes, the application of a synthetic CECE diagnostic can provide further ways to validate the numerical results.

The measured suppression of fluctuations in negative triangularity plasmas compared to positive triangularity ones, and the simultaneous confinement improvement, can be likened to past studies of H-mode plasmas in DIII-D [96] and I-mode plasmas in Alcator C-Mod [97]. There, in fact, a reduction of core fluctuations amplitude was observed when transitioning into the high confinement regime. While in the case of H-mode it is commonly accepted that the transport barrier is related to changes in the  $E \times B$  shearing rate at the plasma edge, it has also been observed that, in the L-H transition, the stiff region of the plasma (as defined in [5]) extends up to the pedestal [107]. This draws further analogies with the results presented in this and past works, which suggest that the improved confinement in negative triangularity can be partly due to a change in the stiffness characteristics close to the plasma edge. These similarities could be the addressed in future works.

In conclusion, this thesis work provides a characterization of radiative temperature fluctua-

tions over the largest parameter space ever explored in TCV in this kind of study. In addition to quantities more commonplace in studies performed in other tokamaks, the shaping flexibility of TCV allowed the study of the effects of negative triangularity on transport and confinement. The obtained results corroborate the conclusions of past experiments and extend the parameter range of observations to low  $T_e/T_i$  ratio plasmas, of particular interest for future reactor-like tokamaks. Negative triangularity is found to have strong, beneficial effects on confinement in all parameters combinations in the database. Most importantly, the range of parameters explored in these experiments includes regions of interest for future, large reactor-like tokamaks, namely low collisionality and  $T_e/T_i \sim 1$ . Linear gyrokinetic simulations predict a stabilizing effect for negative  $\delta$  also in cases in which the dominant instabilities were a mix of ITG and TEM. These results are particularly interesting in the frame of the building interest in the fusion field towards negative triangularity. The possibility of designing a future reactor-like tokamak with negative  $\delta$  was already explored in the past [84][27][28] and beneficial effects were foreseen, such as more frequent, less intense ELMs and the possibility of having the strike point laying on the LFS, significantly increasing the surface area available for management of the plasma power exhaust. Recently, for the first time in a machine other than TCV, experiments have been performed where negative  $\delta$  plasmas showed better confinement and suppressed fluctuations in a variety of heating schemes [29]. The idea that it could be possible to obtain H-mode like levels of confinement in L-mode plasmas with negative triangularity is obviously attractive since it would potentially resolve the problem of the control of edge localised modes [30]. The piling up of evidence, from multiple tokamaks and covering a large parameter space, of the beneficial effects of negative  $\delta$  supports the investigation of negative  $\delta$  tokamaks as a viable alternative for future reactor-like machines. Opening up the possibility of studying negative  $\delta$  plasmas on a larger machine, designed so that different diverted configurations could be easily explored, may be the next step towards an innovative solution to some of the long standing issues that trouble the development of a tokamak reactor.



# A Calculation of the emission volumes position

Calculating the emission volumes of the ECE diagnostics channels is a fundamental step for data analysis. This appendix details how this procedure is carried out in TCV.

The magnetic equilibrium of the plasma in the selected time window is obtained using the CHEASE code [108]. This allows one to map the flux surfaces in real space:  $\rho(\mathbf{r})$ . Electron temperature and density, obtained from the Thomson scattering measurements, are also fit over the flux surface coordinate yielding  $T_e(\rho(\mathbf{r}))$ ,  $n_e(\rho(\mathbf{r}))$ . TORAY is used to propagate a set of rays inside the plasma starting from the line of sight geometry parameters. For each channel, a model for the gaussian beam at the channel's frequency is created using  $N_{rays}$  rays (normally  $N_{rays} = 40$ ). In a far-field approximation, the beam is considered to be generated by a point source whose position and cone aperture angle are derived by the geometry of the line of sight in use. Each ray carries the same power fraction in/from the antenna, and their starting locations are distributed around the axis of the cone according to a gaussian distribution. An example of the rays' starting points distribution for a discharge in which the  $z=0$  line was selected is shown in figure A.1. The red points represent the central ray and the boundaries that contain 95% of the emitted power. From these starting points the rays are propagated inside the plasma at a given frequency, until the power is completely absorbed. In this way one obtains the path of each ray as  $\mathbf{r}(s)$ , where  $s$  is the curvilinear coordinate following each ray. The temperature and density profiles, obtained from the Thomson scattering measurements, and the magnetic field are then interpolated over each ray trajectory:  $T_e(s)$ ,  $n_e(s)$ ,  $B(s)$ . Using these quantities, the emissivity for second harmonic, X-mode ECE ( $G(s)$ ) is calculated along each ray trajectory.

$$G(s) = T_e(s)\alpha(s)e^{-\tau(s)} \quad (\text{A.1})$$

where  $\alpha$  is the absorption coefficient of the plasma and  $\tau$  is the optical depth, defined as:

$$\tau(s) = \int_0^s \alpha(s') ds' \quad (\text{A.2})$$

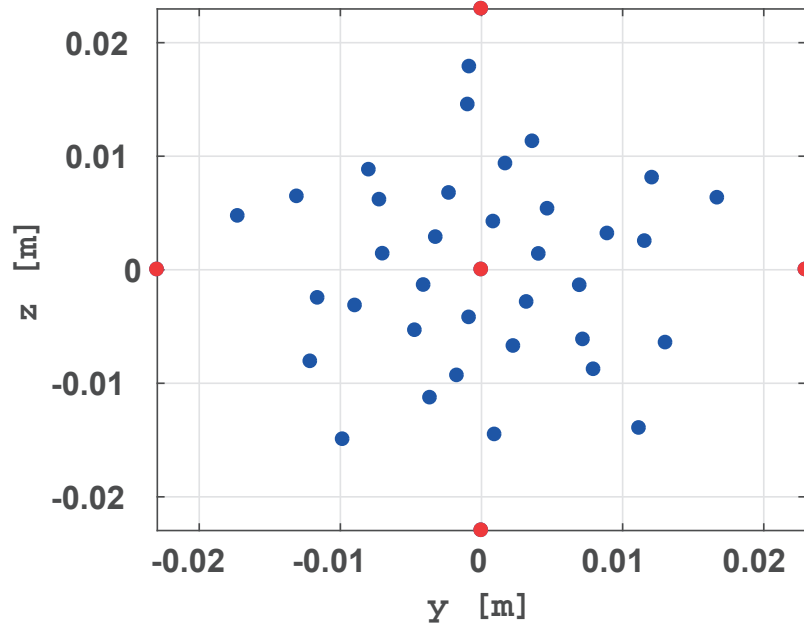


Figure A.1 – Starting positions of the rays generated by TORAY ( $s = 0$ ). The red points represent the central ray and the four extremes that contain 95% of the emitted/collected power. In this plot  $z$  is the vertical direction and  $y$  a direction tangential to the magnetic axis.

The absorption coefficient for the  $n^{th}$  harmonic of X-mode emission along each ray can be

calculated using the formulas found in [40], chapter 3:

$$\begin{aligned}
\alpha_n^X &= A_n \alpha_{n,0}^X \\
\alpha_{n,0}^X &= \frac{n^{2n-1}}{2^n n!} \left( \frac{\omega_p}{\Omega_c} \right)^2 \left( \frac{v_{th}}{c} \right)^{2(n-2)} \frac{\Omega_c}{c} [-F''_{n+3/2}(z_n)] \\
A_n &= N_{\perp}'^{(2n-3)} |1 + a_n|^2 b_n \\
a_n &= \frac{\left( \frac{\omega_p}{\Omega_c} \right)^2}{n \left[ n^2 - 1 - \left( \frac{\omega_p}{\Omega_c} \right)^2 \right]} \\
b_2 &= |1 + \frac{1}{2} \left( \frac{\omega_p}{\Omega_c} \right)^2 (1 + a_2)^2 F'_{7/2}(z_2)|^{-1} \\
N_{\perp}'^2 &= \frac{1 - \left( \frac{\omega_p}{\omega} \right)^2}{|1 + \frac{1}{2} \left( \frac{\omega_p}{\Omega_c} \right)^2 F'_{7/2}(z_1)|} \\
F_q(z) &= \sum_{\nu=0}^{\infty} (-z^{\nu}) \frac{\Gamma(q-1-\nu)}{\Gamma(q)} - i \frac{\pi}{\Gamma(q)} (-z)^{q-1} e^z \\
z_n &= \left( \frac{c}{v_{th}} \right)^2 \frac{\omega - n\Omega_c}{\omega} \text{ if } \omega > n\Omega_c \\
z_n &= 0 \text{ otherwise}
\end{aligned} \tag{A.3}$$

In these equations  $N'$  and  $N''$  are respectively the real and imaginary parts of the refractive index,  $\omega$  is the wave angular frequency,  $v_{th} = \sqrt{\frac{T_e}{m_e}}$  is the thermal velocity of electrons.

To take into account the effect of the intermediate frequency filters bandwidth ( $B_{IF}$ ) on the radial extension of the emission volumes, the emissivity profiles along the rays are calculated for a number of frequencies between  $[f - B_{IF}/2, f + B_{IF}/2]$ , where  $f$  is the central frequency of the filters. This approach assumes that refraction is constant for changes in frequency of the order of  $B_{IF}$ . The emissivity profiles obtained for each of these frequencies are then summed in a single emissivity profile for each channel, along each ray.

For each ray the emission region is identified as the interval  $[s_1, s_2]$  that contains 95% of the integral emissivity, such that:

$$\frac{\int_0^{s_1} G(s') ds'}{\int_0^{\infty} G(s') ds'} = 2.5\% \quad \text{and} \quad \frac{\int_0^{s_2} G(s') ds'}{\int_0^{\infty} G(s') ds'} = 97.5\% \tag{A.4}$$

In between  $s_1$  and  $s_2$  a number  $N_s$  of points is defined such that increments of the fraction of the integral of  $G$  are constant between them. The union of these segments over all rays defines the emission volume for a single channel. The mean of the plasma characteristics ( $T_e$ ,  $n_e$ ,  $B$ ,  $\mathbf{r}$ ,

## Appendix A. Calculation of the emission volumes position

---

$\rho$ ) are calculated over these points for every channel as:

$$\langle f \rangle = \frac{1}{N_{rays}} \frac{1}{N_s} \sum_{s_i=s_1}^{s_2} f(s_{i,j}) \quad (A.5)$$

Finally, the normalized signal for each channel is multiplied by  $\langle T_e \rangle$  to obtain a calibrated signal for the temperature fluctuations.

As mentioned in paragraph 3.6.2, the dimension  $d$  of the emission volumes obtained in this manner can be used to estimate the wavenumber sensitivity of the diagnostic. In equation 3.10 the spatial response of the diagnostic has been described with a gaussian characterized by its  $1/e$  folding lengths  $w$  and its standard deviation  $\sigma = w/\sqrt{2}$ . The square of this distribution, characterized by its standard deviation  $\sigma_p = \sigma/\sqrt{2}$ , describes the power collected by the antenna. Since the rays generated by TORAY contain 95% of the beam power, the extension of the emission volumes that have been calculated correspond to  $2\sigma_p$  on each side of the center of the beam:  $d = 4\sigma_p = w/2$ . According to equation 3.12, this leads to  $k \leq 2/(d_{x,y,z}/2)$

## **B Commissioning of the radiometers**

Part of this thesis work consisted in the characterization and assembly of some components of the ECE and CECE diagnostics in TCV. These measurements have been performed with a Keysight N5224A PNA Microwave Network Analyzer, 10 MHz-43.5 GHz. Its frequency range has been expanded using two pair of VDI VNA extender modules, covering the 50-75 GHz (WR-15) and 75-110 GHz (WR-10) frequency ranges respectively. The setup is calibrated at every use with dedicated VDI calibration kits.

### **B.1 LFS ECE transmission lines**

During the 2013-2014 TCV shutdown, the lines of sight of the LFS ECE have been moved in a different toroidal sector and, thus, the transmission lines have been completely redesigned. After their installation, their insertion loss has been tested using the PNA and the WR10 extender modules. The extender heads have been adapted to the circular waveguides using a rectangular-to-circular waveguide transition. Results of these measurements are shown in figure B.1.

### **B.2 CECE RF stage**

The insertion loss of the components of the two new independent RF sections of the CECE diagnostic (61 and 82 GHz local oscillators) has been tested over the 67-79 and 88-100 GHz frequency ranges respectively. The two couples of VDI extender modules, WR15 for the low frequency branch and WR10 for the high frequency one, have been employed for this measurement. The S21 parameters showed in figure B.2 represent the insertion loss of the notch filters (necessary to protect the system from ECRH power), the directional coupler that splits power between the two front ends, and the high pass filter before each mixer (as shown in figure 3.7 and figure 3.8). Including the 3 dB loss due to the directional coupler connecting the two, both front ends lose less than 6 dB in the pre-mixing phase. The strong attenuation at the lower frequencies is the effect of the high-pass, image reject filters of the two

## Appendix B. Commissioning of the radiometers

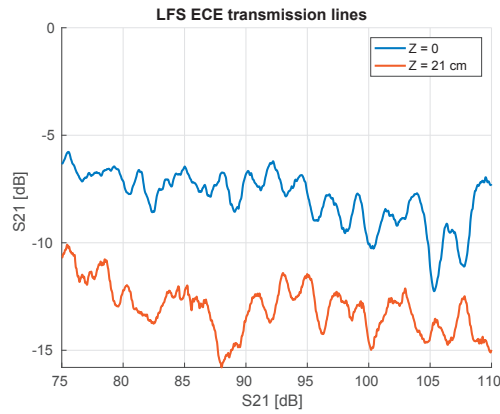


Figure B.1 – Transmission loss in the LFS ECE transmission lines from the TCV vessel to the radiometer input.

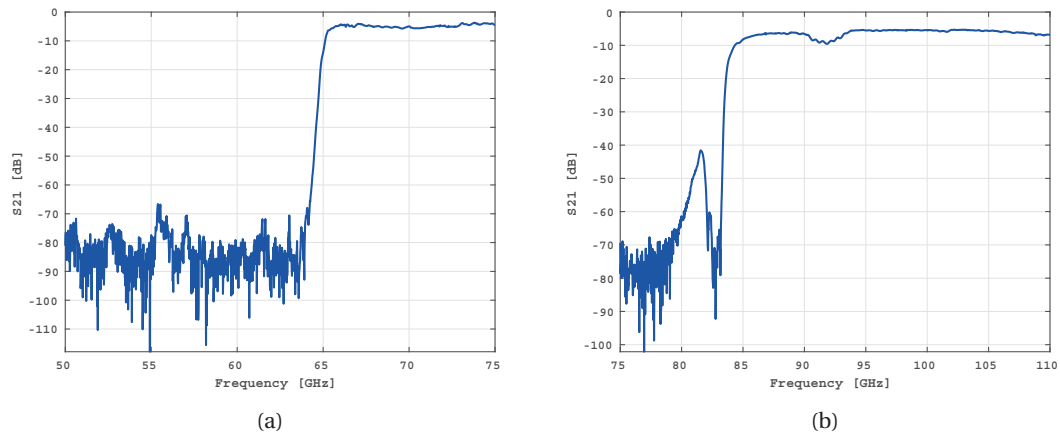


Figure B.2 – Transmission loss in the pre-mixing stage of the two independent CECE front ends. The measurements include the notch filters (82.7 and 118.3 GHz), a directional coupler splitting the power between the two front ends and the image reject high-pass filter.

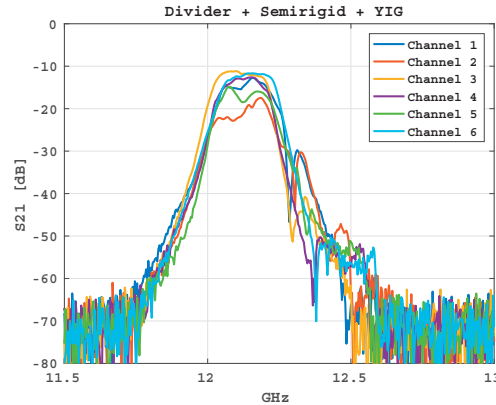


Figure B.3 – Insertion loss for the six channels of the CECE centered around the same frequency (12.1 GHz).

radiometers. In figure B.2b, it is possible to see the effect of the 82.7 GHz notch filter, protecting the system from X2 ECRH power.

After testing the functionality of the mixers and amplifiers, the radiometers have been assembled and connected to the telescope as described in 3.5.1.

### B.3 CECE IF stage

The transmission in the IF stage of the CECE has also been tested using the PNA. The frequency range of operation of the YIG IF filters varies between 6 and 18 GHz so, in this case, use of the extender modules has not been necessary. These tests included the core of the CECE IF section: the power divider, the YIG IF filters and three semirigid cables connecting them to the multiplexer. The center frequencies of the filters have been scanned, recording the S21 parameter at each step. These measurements have been used to assess the difference in performance of the different CECE channels (especially the YIG filters), across the whole frequency band. The results of these tests are shown for a single frequency step (figure B.3) and for the whole frequency range, in dB (figure B.4), and in real units (figure B.5).

#### B.3.1 Routine testing the IF stage of the Correlation ECE

These detailed measurements have been followed by a simpler weekly test routine for several months, in order to verify eventual degradation of the channels' response. These tests involved the whole IF stage, from the power divider to the acquisition, as shown in figure 3.12.

A HP 8350B Sweep Oscillator has been used to produce 1 mW sweeping across the 5-18 GHz frequency range over 500 ms. It has been connected to the input of the CECE IF stage with about 2 meters of coaxial cable. Attenuators summing up to 32 dB have been added before the insertion. The acquisition of the CECE channels has been manually triggered and the data

## Appendix B. Commissioning of the radiometers

---

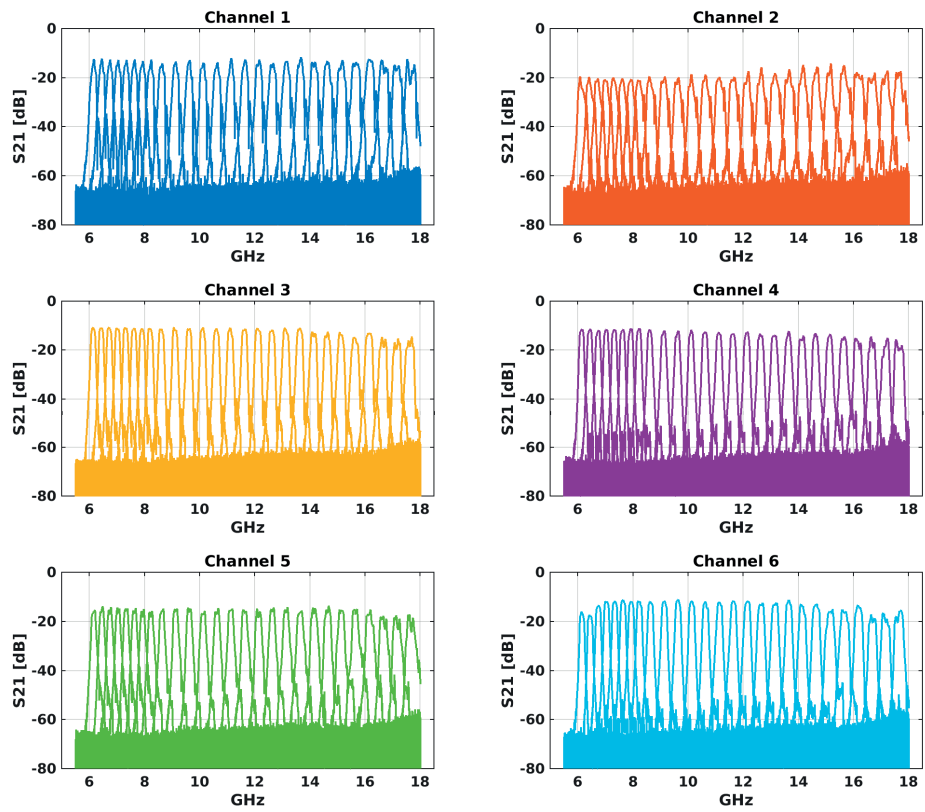


Figure B.4 – Insertion loss of the CECE channels for various frequencies setting of the YIG filters, in dB.



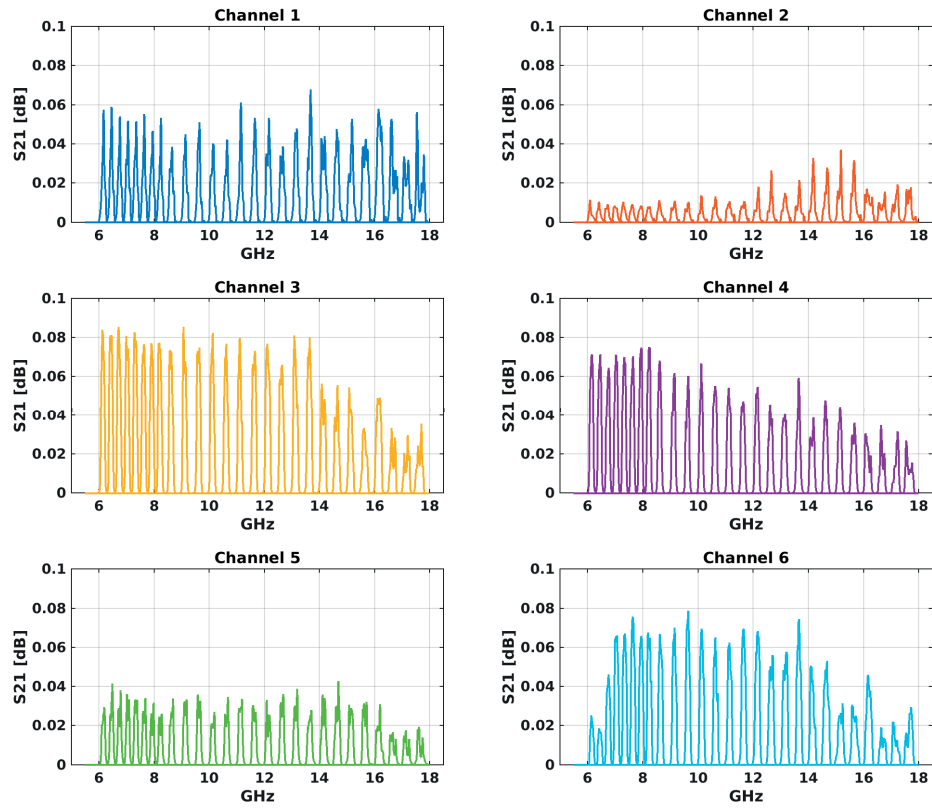


Figure B.5 – Insertion loss of the CECE channels for various frequencies setting of the YIG filters, in real units.

## **Appendix B. Commissioning of the radiometers**

---

collected and compared with the previous weeks. These tests found the performance of the six channels to be constant in time. The stability of the system (including also the RF section) can be further verified by comparing the signals collected during the TCV standard discharge, repeated identical everyday at the beginning of the operations.

# C Estimation of the propagation velocity of fluctuations using CECE measurements

## C.1 Principles

When performing cross-correlation analysis between the CECE signals coming from different channels, the phase difference gives an idea which of the two detects the fluctuations first. If it is possible to calculate the distance  $\Delta s$  that the fluctuations have to cross between the two channels, then an estimation of the velocity of propagation of the fluctuations is possible. The procedure proposed here is based on these assumptions:

- Fluctuating structures are strongly elongated along the field lines ( $k_{\parallel} \ll k_{\perp}$ );
- In the directions perpendicular to the field lines these structures are large enough to be detectable by a pair of neighbouring CECE volumes;

This estimation can be attempted starting from the phase difference between two channels or from the time delay of maximum correlation, estimated from their correlation coefficient.

## C.2 Estimation of $\Delta s$

The choice of  $\Delta s$  depends on the expected direction of propagation of the fluctuating structures. Two reasonable choices are:

- the separation of the emission volumes along the line of sight, corresponding to a radial propagation
- the distance separating the two emission volumes along a flux surface, corresponding to a purely poloidal propagation.

The separation of the emission volumes along the line of sight is easily calculated using the definition of the channels' position introduced in appendix A. If  $(\bar{x}_1, \bar{y}_1, \bar{z}_1)$  and  $(\bar{x}_2, \bar{y}_2, \bar{z}_2)$  are the mean coordinates of the two emission volumes,  $\Delta s = \|(\bar{x}_2 - \bar{x}_1, \bar{y}_2 - \bar{y}_1, \bar{z}_2 - \bar{z}_1)\|$

## Appendix C. Estimation of the propagation velocity of fluctuations using CECE measurements

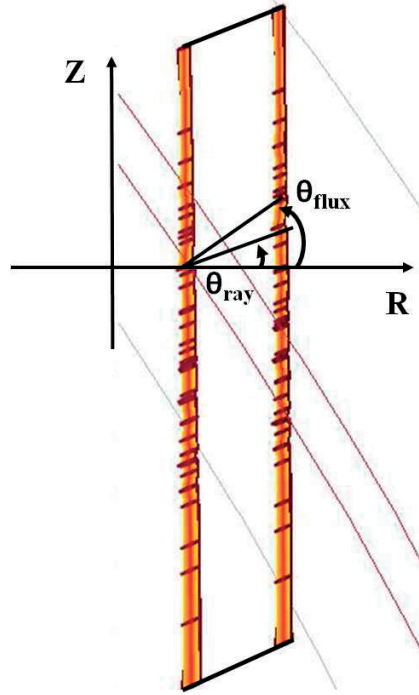


Figure C.1 – Definition of the angles used in the estimation of the propagation velocity.

To evaluate the poloidal propagation of the fluctuations along the magnetic surfaces, it is necessary to take into account the relative angle between the line of sight and the magnetic flux surface of interest.

Starting from the calculations presented in appendix A, we can define the angle between neighbouring emission volumes as:

$$\theta_{ray} = \arctan\left(\frac{\overline{z_1} - \overline{z_2}}{\overline{r_1} - \overline{r_2}}\right), \quad (C.1)$$

where 1 and 2 are indexes for different emission volumes,  $r = \sqrt{x^2 + y^2}$  and  $(\overline{\cdot})$  represents an average over the emission volume. This angle must be compared with the gradient of the flux surfaces in between the emission volumes  $\theta_{flux}$ . An example of how these angles are defined is shown in figure C.1. These two angles define  $\theta_{rf} = \theta_{flux} - \theta_{ray}$ . Then,  $\Delta s$  for a given couple of channels can be calculated as shown in figure C.2:

$$\Delta s = \Delta r \sin(\theta_{rf}). \quad (C.2)$$

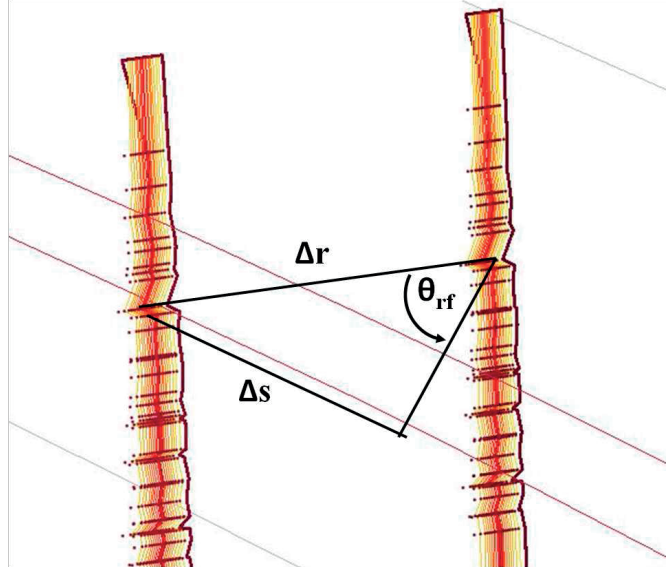


Figure C.2 – Definition of  $\theta_{rf}$  and representation of the distance separating two emission volumes in the R/Z plane ( $\Delta r$ ) and along a flux surface ( $\Delta s$ ).

### C.3 Propagation velocity estimate

The phase difference observed between two CECE channels due to the propagation of the fluctuating structure can be modelled simply as:

$$\Phi(f) \propto \omega(f) \Delta t \quad (C.3)$$

$$\propto 2\pi f \frac{\Delta s}{v(f)} \quad (C.4)$$

Where  $\Delta t$  is the time necessary to cross the  $\Delta s$  separating the detection volumes. This time interval can be expressed as the ratio between  $\Delta s$ , defined above, and the propagation velocity  $v$  of the fluctuations.

Knowing the phase difference between the oscillations in two neighbouring CECE channels, the propagation velocity of the fluctuations can be simply calculated as:

$$v(f) = 2\pi f \frac{\Delta s}{\Phi(f)} \quad (C.5)$$

When using this method, the sign of the velocity calculated using C.5 depends on the relative signs of  $\Phi$  and  $\theta_{rf}$ . Remembering that the chosen convention produces a positive phase when the fluctuations are detected first in the channel with the highest frequency of the couple, the simple picture used in this model can be used to determine if the fluctuations at a given

## Appendix C. Estimation of the propagation velocity of fluctuations using CECE measurements

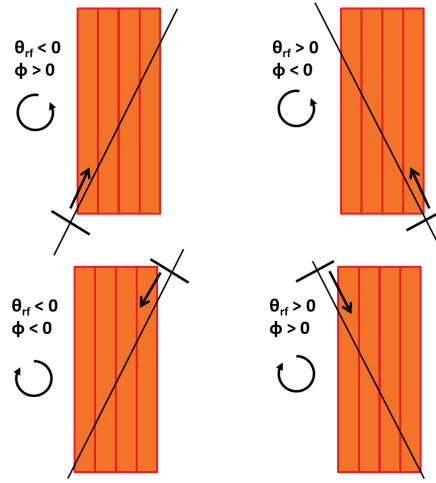


Figure C.3 – Schematic representation of the four different cases corresponding to the combinations of signs for  $\theta_{rf}$  and  $\Phi$ . The sign of the resulting velocity can be interpreted as the direction of propagation of the fluctuation along the flux surface. A negative velocity corresponds to counter-clockwise rotation, while negative velocity to clockwise.

frequency are rotating clockwise or counter-clockwise. The different cases are schematically represented in figure C.3. A positive velocity corresponds to clockwise rotation and viceversa (in agreement with TCV coordinate conventions COCOS17 [109]).

The same principles can be used to estimate the propagation velocity based on the correlation coefficient  $\rho(t)$ . The time delay  $\Delta t$  separating the detection of the fluctuating structures between two CECE channels can be assumed to be the time delay  $\tau_{max}$  corresponding to the maximum correlation  $\rho_{max} = \rho(\tau_{max})$ .

Computing the separation of the two volumes ( $\Delta s$ ) as described above, the speed of propagation of the fluctuations can be simply calculated as  $v = \Delta s / \tau_{max}$ . Contrary to the value obtained using the phase difference, this is the result of an integration over frequencies, performed during the calculation of the correlation function. To compare the two methods,  $v(f)$  must hence be averaged over the same frequency range considered when calculating the correlation function.

Using either of these procedures on pairs of neighbouring channels, one can obtain an estimation of the propagation speed, along a specific direction, for varying  $\rho$ . An example of their application in an ohmic discharge is shown in figure C.4, where the two different methods of calculation produce consistent results.

### C.4 Comparison with CXRS measurements

The estimation of propagation speed obtained with this method has been compared with the CXRS rotation measurements in TCV. To do so, a discharge has been chosen in which

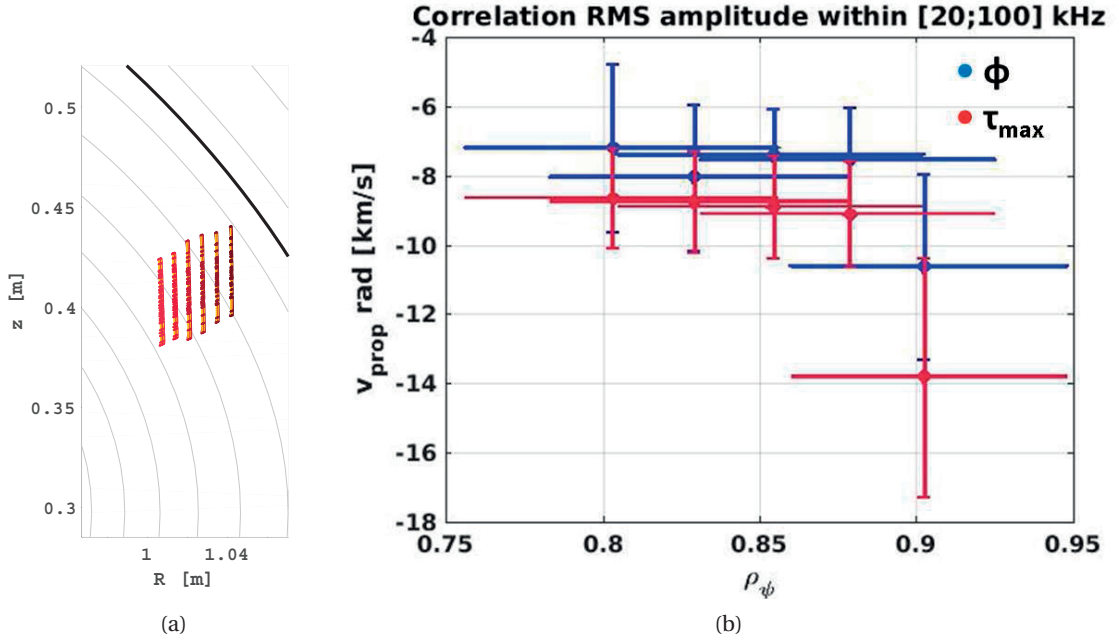


Figure C.4 – Comparison of the propagation velocity of fluctuations estimated using the phase difference between neighbouring channels (blue) or the time of maximum correlation (red).

the ECE emission volumes, shown in figure C.5, were as perpendicular as possible to the magnetic flux surface. Due to the position of the emission volumes, it is assumed that the main component of the propagation speed that could be detected is the poloidal one. In this discharge, two phases are compared: one with 900 kW of NBI heating, and one ohmic. The CXRS measurements show that the NBI injection causes a strong toroidal acceleration of the impurity ions, in counter-current direction, while no effects are observed on the poloidal velocity, as shown in figure C.6.

The phase difference between the two CECE channels, shown in figure C.7a, for fluctuations between 30 and 60 kHz, changes sign after the beam is turned on, suggesting a change in the direction of propagation of the fluctuating structures from counter-clockwise to clockwise. The propagation velocity has been estimated using C.5, calculating  $\Delta s$  along the flux surfaces, as explained in C.2. The frequency dependent velocities calculated in this way are shown in figure C.7b.

Integrating  $v(f)$  over the 30-60 kHz range, an estimation of the propagation poloidal velocity can be obtained for the two different time intervals.

To compare this result with CXRS measurements, it is necessary to make some assumptions. If the fluctuations are considered to be frozen to the magnetic field lines, their poloidal propagation would only be due to the background plasma rotation. The poloidal velocity of the intersection of a magnetic field line with the plasma cross section is a composition of both

## Appendix C. Estimation of the propagation velocity of fluctuations using CECE measurements

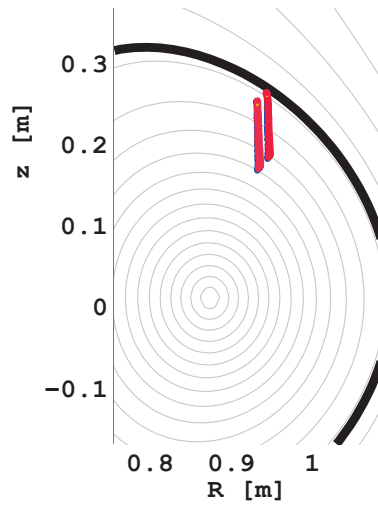


Figure C.5 – Volumes 53667.

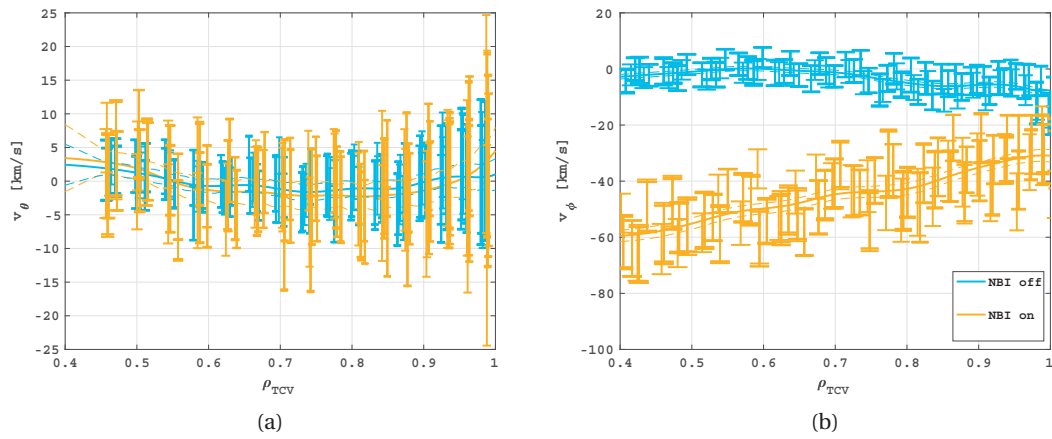


Figure C.6 – Poloidal and toroidal velocities of the carbon ions in TCV in the two phases where the NBI was on (yellow) and off (blue) respectively.



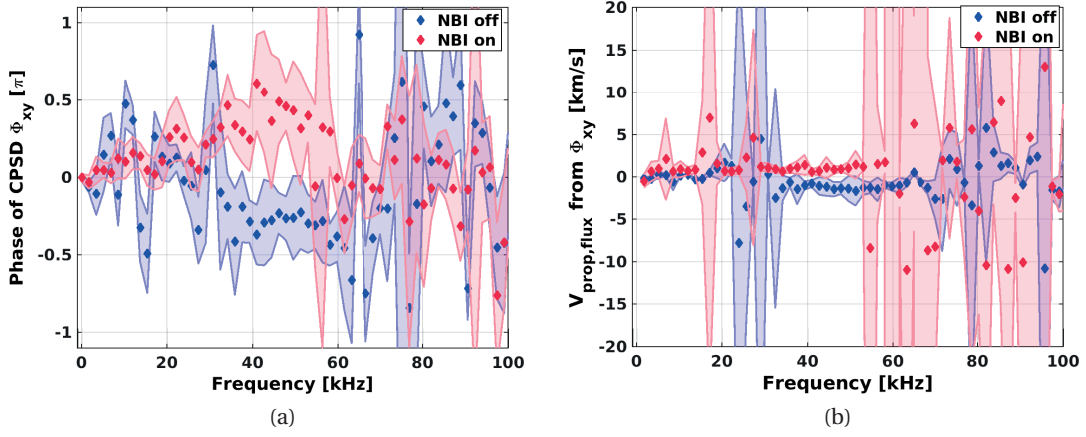


Figure C.7 – Phase and vflux 53667.

toroidal and poloidal plasma rotation velocities:

$$v_{prop} = v_{\theta} + \tan(\alpha) v_{\phi} \quad (C.6)$$

In this expression  $\alpha$  is the pitch angle of the magnetic field lines. In the convention used in TCV, positive values are for clockwise poloidal rotation and counter-clockwise toroidal rotation. Due to this, the sign of  $\alpha$  depends on the relative sign between the toroidal and poloidal (opposite to the plasma current) magnetic fields. If they have the same direction then  $\alpha$  is positive, otherwise is negative. For this comparison, the CXRS measurements of the carbon ions velocity have been used to infer the plasma rotation velocity. While this is very simple approach, it is known that, in regions where second derivatives in the ion temperature are high, there can be strong differences between the rotation of the impurities and the main ions [110].

The comparison between the propagation velocities estimated from the CXRS measurements and the CECE data is shown in figure C.7a. It show that the qualitative trend of increase in rotation velocity when the NBI is turned on is reproduced in the CECE based estimation as in the CXRS calculations. The quantitative results, though, differ significantly. If the assumption of fluctuations being frozen to the magnetic field lines is dropped, but they are still considered to be propagating only poloidally, the difference between the two results could be interpreted as the velocity of the fluctuations with respect to the background plasma rotation. If the values so obtained are compared with the poloidal rotation velocity of the carbon ions, we find values well inside the error bar of the experimental measurements, as shown in figure C.8b.

Appendix C. Estimation of the propagation velocity of fluctuations using CECE measurements

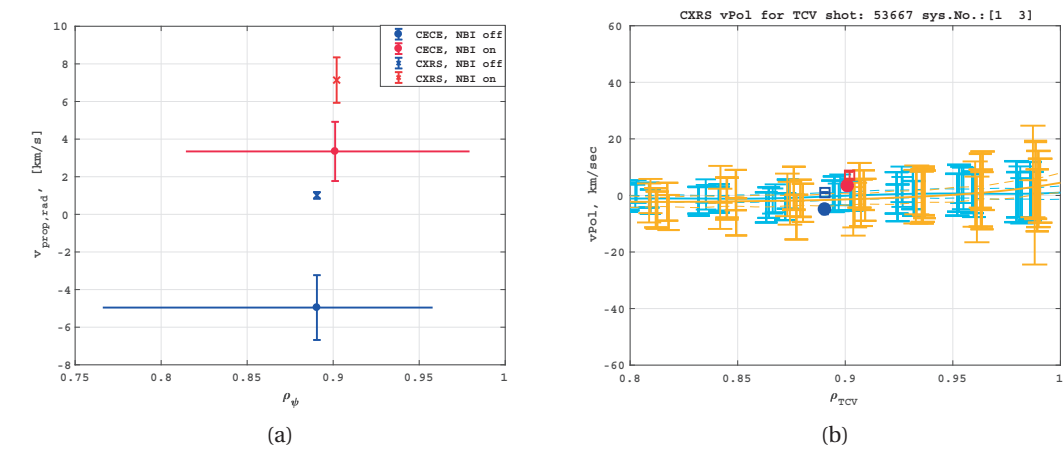


Figure C.8 – Phase and vflux 53667.

## D Simple modelling of fluctuations and application of a synthetic diagnostic

A correlation electron cyclotron emission (CECE) diagnostic is sensitive only to fluctuating structures large enough that their contribution is not averaged out inside the emission volume of a single channel, as explained in 3.3.1. To represent this effect and study how it affects the different lines of sight available to the CECE in TCV, a simple 2D model of fluctuations in the plasma cross section is developed, together with a synthetic CECE diagnostic. The main goal of this work is to investigate the sensitivity of the diagnostic to fluctuating structures of different sizes in an simplified representation, yet taking into account the real characteristics of the diagnostic and its lines of sight.

### D.1 Simple model for fluctuations

A model for the fluctuating field is constructed on the basis of a real plasma equilibrium. For any given TCV discharge, the magnetic equilibrium is reconstructed using CHEASE [108]. This provides, among other things, a mapping of the poloidal flux  $\Psi$  over the plasma cross section. In this way, every point of the plasma cross section can be identified by a  $[\rho(R, Z), \theta(R, Z)]$  pair, where  $\rho = \rho_\psi$  is defined as in equation 1.11 and  $\theta = \arctan[(Z - Z_{axis})/(R - R_{axis})]$ .

On this grid, the spatial structure of the fluctuations is modelled as a superposition of a number of different poloidal modes characterized by a poloidal number  $m$ :

$$A_m(R, Z) = \exp[i \cdot m \cdot \theta(R, Z)]. \quad (\text{D.1})$$

In this simple model, modes of higher order,  $m$ , represent turbulence with shorter wavelengths in the poloidal direction. As an example, in figure D.1a the pattern of a mode with  $m=4$  is shown. Each component is associated with a different frequency, proportional to  $m$ , such that at time  $t$ :

$$A_{mt}(R, Z, t) = A_m(R, Z) \cdot \exp[i \cdot m \cdot \omega(m) \cdot t] \quad (\text{D.2})$$

where  $\omega$  is an arbitrary coefficient defining the angular frequency of each mode.

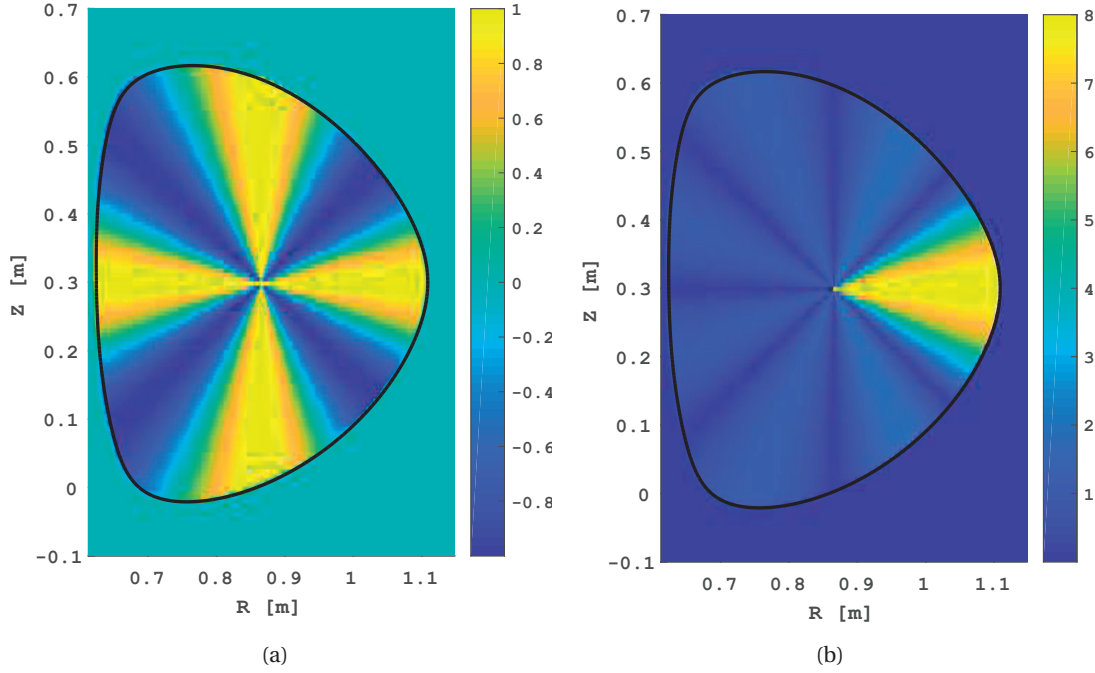


Figure D.1 – (a) Real part of the mode  $m=4$  as defined in D.1. (b) Norm of a superposition of modes with  $m$  going from 1 to 8 from equation D.3 with  $A_0(R, Z) = 1$ .

Once all the  $n$  different modes are summed, the final form of the fluctuating field is obtained.

$$A(R, Z, t) = A_0(R, Z) \cdot \sum_{j=1}^n A_{mt}^j(R, Z, t) \quad (\text{D.3})$$

The result of superimposing modes with  $m$  from 1 to 8 is shown in figure D.1b. In this case the norm of the sum of the fluctuations is shown instead of the oscillating parts. In equation D.3,  $A_0$  is used to further tailor the spatial structure of the fluctuations. For example, it can be used to create fluctuations whose amplitude decays moving away from the outboard midplane in the poloidal direction to mimic the ballooning structure of turbulent fluctuations.

## D.2 CECE synthetic diagnostic

Once the plasma equilibrium and the fluctuating structures have been defined, the CECE diagnostic can be modelled. The emission volumes for the synthetic channels are calculated as detailed in appendix A. The characteristics of the lines of sight are used as inputs in TORAY. Synthetic channels are defined by fixing their frequency or their position with respect to a flux surface. In the latter case, the intersection between the line of sight and the desired flux surface is found, assuming no refractive effects, and the synthetic channels are centred around the corresponding ECE resonance frequency. The channels bandwidth is normally set to 100 MHz to reproduce the actual diagnostic, but it can be changed arbitrarily. The

### D.3. Applications of the fluctuations model and the synthetic diagnostic

density and temperature profiles necessary for the calculation of refraction and the emissivity profiles can be taken from the same discharge from which the equilibrium is reconstructed, or they can be modified if necessary. An example of emission volumes obtained in this way for two channels using the horizontal line of sight characteristics, is shown in figures D.2a and D.2b. The channels are superimposed on a fluctuating structure generated using equation D.3. Notice that in this case  $A_0$  has been used to introduce a radial and poloidal decay when moving away from  $\theta = 0$  and  $\rho = 1$  respectively:

$$A_0(R, Z) = \exp \left[ -\frac{(\rho(R, Z) - 1)^2}{2 \cdot \sigma_\rho^2} \right] \cdot \exp \left[ -\frac{\theta(R, Z)^2}{2 \cdot \sigma_\theta^2} \right]. \quad (\text{D.4})$$

The fluctuating field, defined as described in paragraph D.1, is then interpolated on the points composing each emission volume. A weight is associated to each of these points corresponding to the value of emissivity  $G$ , calculated as in appendix A. Examples of the interpolation of the fluctuations and of the emissivity over the emission volumes are shown in figures D.2b and D.2c respectively. The weighted sum of the fluctuations over these points, for each time  $t$ , generates the synthetic CECE signal for each channel. In order to use this model as a synthetic diagnostic, signals are generated using the real CECE temporal resolution (1.75 MHz) and they are low pass filtered using a fifth order Butterworth at 450 kHz, which represents the video bandwidth of the radiometers' electronics. These parameters can be adjusted if necessary. Artificial, white, gaussian noise can then be added to each channel with arbitrary signal to noise ratio.

The standard data analysis procedure for CECE, introduced in paragraph 3.6, is then applied to every couple of neighbouring channels. This allows the calculation of CPSDs, common fluctuations amplitude and correlation length as it would be done for the actual experimental data. The results obtained using these synthetic signals can be used to verify how basic characteristics of the fluctuating structures influence the detection capabilities of the diagnostic in various configurations. Some examples of these applications are presented in the next section.

## D.3 Applications of the fluctuations model and the synthetic diagnostic

### D.3.1 Emission volume size and wavenumber sensitivity

The synthetic CECE diagnostic was applied in different cases to a fluctuating field consisting of the superposition of modes with  $m$  from 1 to 32, with  $A_0(R, Z) = 1$ , rotating at a constant  $\omega = 25 \cdot 10^3 \pi$  rad/s. The fluctuations were superimposed on the equilibrium of one of the positive  $\delta$  plasmas discussed in paragraph 4.3. Two CECE channels centred around  $\rho_{psi} = 0.7$  ( $f_1 = 70$  GHz,  $f_2 = 70.5$  GHz) and separated by 500 MHz, were modelled. These collect radiation

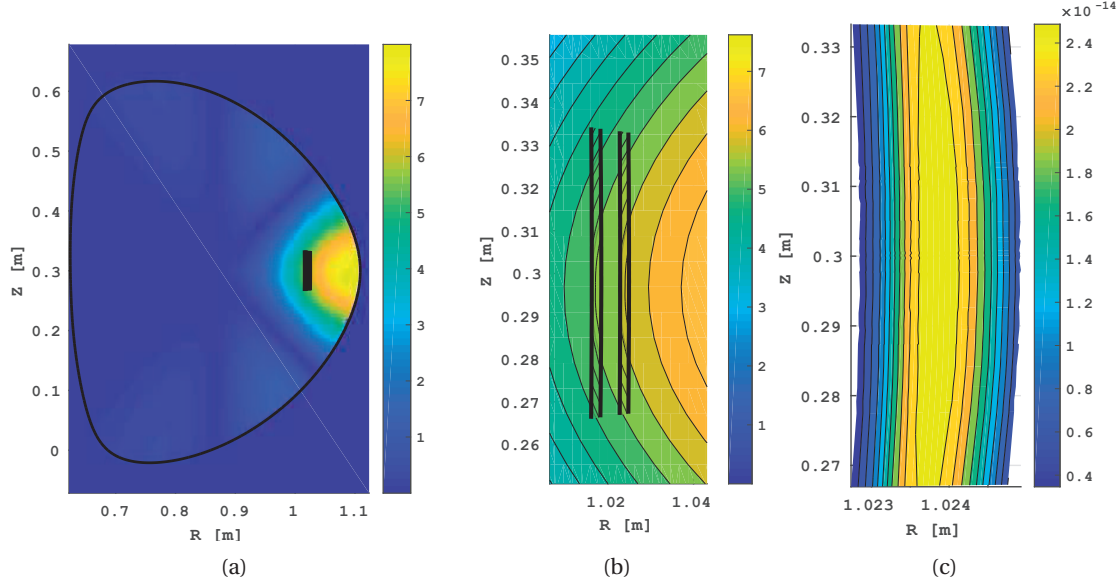


Figure D.2 – (a) Norm of a superposition of modes with  $m$  going from 1 to 8 from equation D.3 with  $A_0(R, Z)$  composed by two gaussians in both poloidal and radial directions. The former is centered on  $\theta = 0$  and the latter on  $\rho = 1$ . (b) Norm of the fluctuating structure shown in a interpolated over two emission volumes. (c) Emissivity  $G$  over one of the emission volumes.

through the horizontal line of sight, aligned with the plasma axis. White gaussian noise was added to the synthetic signals in order to obtain a signal to noise ratio of 1. Using the actual characteristics of the CECE in TCV ( $B_{IF} = 100$  MHz,  $f_{acq} = 1.75$  MHz,  $B_{vid} = 450$  kHz), the CPSD between the two channels, shown in figure D.3, shows differences in sensitivity for structures of different sizes. In this case, where each peak in the CPSD corresponds to a different mode  $m$ , with higher order modes appearing as higher frequency peaks, it is clear how the diagnostic loses sensitivity for smaller fluctuating structures. It is important to notice that this is not an effect of the radiometer characteristics since higher order peaks disappear into the noise before 450 kHz, where the video low-pass filter rolls over.

In fact the cause for the reduced sensitivity of the diagnostic to smaller fluctuating structures is the finite extension of the emission volumes, as already mentioned in 3.3.1. A simplified configuration of the diagnostic model was then applied to further study this effect. The same fluctuating field and channel configurations were retained except for the removal of noise and of the low-pass video filter and the aperture angle of the horizontal line of sight was varied from  $2^\circ$  to  $5^\circ$  (for the real line of sight  $\alpha = 3.05^\circ$ ).

The CPSD between the two channels was calculated separately for each poloidal mode component ( $A_{mt}$ ) and integrated over the whole frequency range, to obtain the common power generated by a single mode. This power has been used to estimate the relative sensitivity of the different optics configurations to the different modes. As expected, larger antenna patterns degrade the sensitivity of the diagnostic to smaller fluctuating structures (higher  $m$  modes).

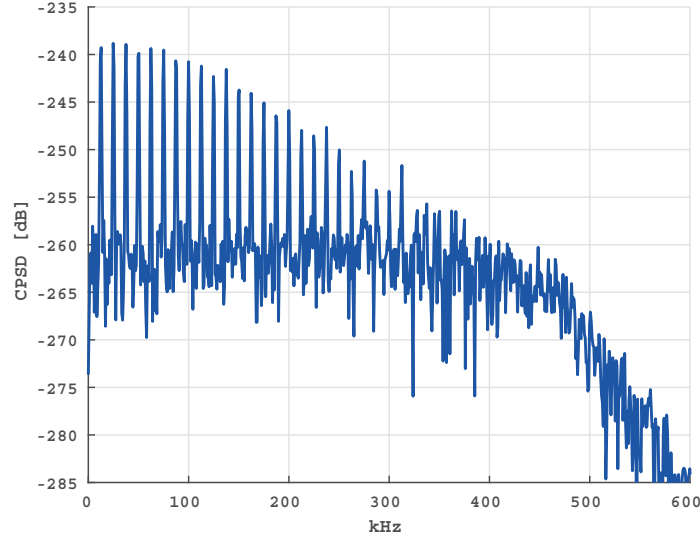


Figure D.3 – CPSD of two synthetic channels at  $\rho_{psi} = 0.7$  separated by 500 MHz, looking at fluctuations generated by m modes with m from 1 to 32, rotating at constant angular velocity  $\omega$ . The actual characteristics of the CECE diagnostic of TCV have been used in this test (optics,  $B_{IF}$ ,  $f_{acq}$ ,  $B_{vid}$ ).

Figure 4.21, showing these results, has been reproduced here in figure D.4 for convenience.

To verify the consistency of these results with the model of [8], introduced in paragraph 3.3.1, a series of simulations in which the angle  $\alpha$  was changed from  $0.1^\circ$  to  $8^\circ$  was run. The resulting fluctuation amplitudes for modes of different order as a function of the vertical size of the emission volumes are shown in figure D.5. According to the model of [8], the measured amplitude of the fluctuations should decrease as  $\exp(-\frac{(kw)^2}{2})$  where in this case  $k$  is the poloidal wavenumber of the fluctuations and  $w$  the vertical size of the emission volume. The points have been fit with:  $C_m \exp(-B_m \Delta Z^2)$ , where  $C_m$  and  $B_m$  are constants for each mode. As shown in figure D.5 the model fits very well the results of the simulations. This confirms that the observed decreased sensitivity for smaller fluctuating structures when using the synthetic diagnostic, can be attributed to the finite size of the emission volumes.

#### D.3.2 Wavenumber sensitivity of different lines of sight

The same combination of plasma equilibrium, profiles and modes was used to test the different sensitivity of the upper lateral and horizontal lines of sight of the CECE. Both lines have been simulated using their actual characteristics (except for the vertical position of the horizontal one, again set at  $z = 30$  cm). For the upper lateral line of sight, the angles used in the specific TCV discharge have been selected ( $\theta = 25^\circ$ ,  $\phi = 0^\circ$ ). Also in these cases two channels have been simulated around the  $\rho_\psi = 0.7$  flux surface, separated by 500 MHz. What is observed is that the upper lateral line of sight is less sensitive to the lowest order modes ( $m < 5$ ) with respect

## Appendix D. Simple modelling of fluctuations and application of a synthetic diagnostic

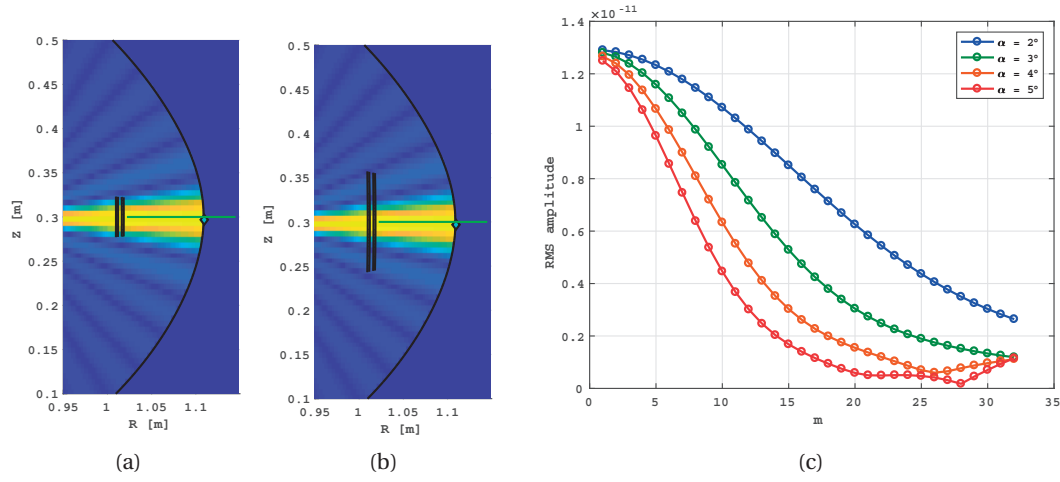


Figure D.4 – Examples of the changes in the emission volumes extension when changing the aperture angle of the horizontal line of sight from  $2^\circ$  (a) to  $5^\circ$  (b). The emission volumes are represented over the norm of the fluctuating structure obtained superimposing modes with m from 1 to 32. (c) Sensitivity of the diagnostic to varying m modes for increasing line of sight aperture angle. The sensitivity to higher order modes is reduced while the antenna pattern is widened.

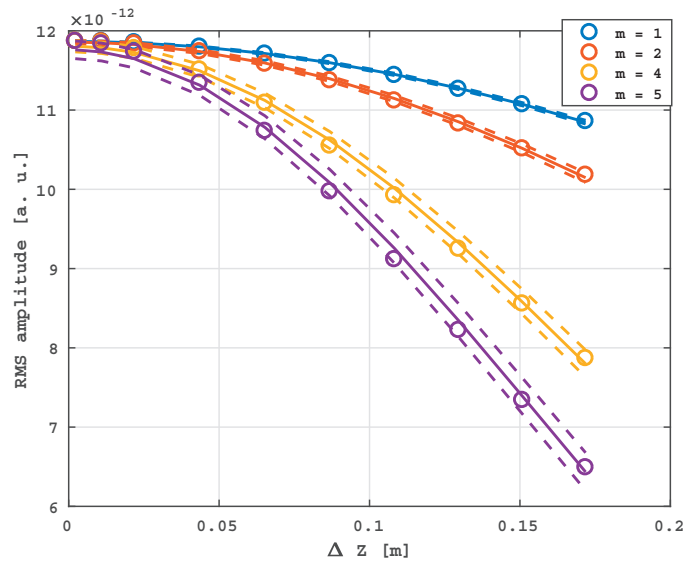


Figure D.5 – Amplitude of the fluctuations measured for varying aperture angle  $\alpha$  for several poloidal modes and corresponding fits with confidence intervals, calculated according to the model in [8].



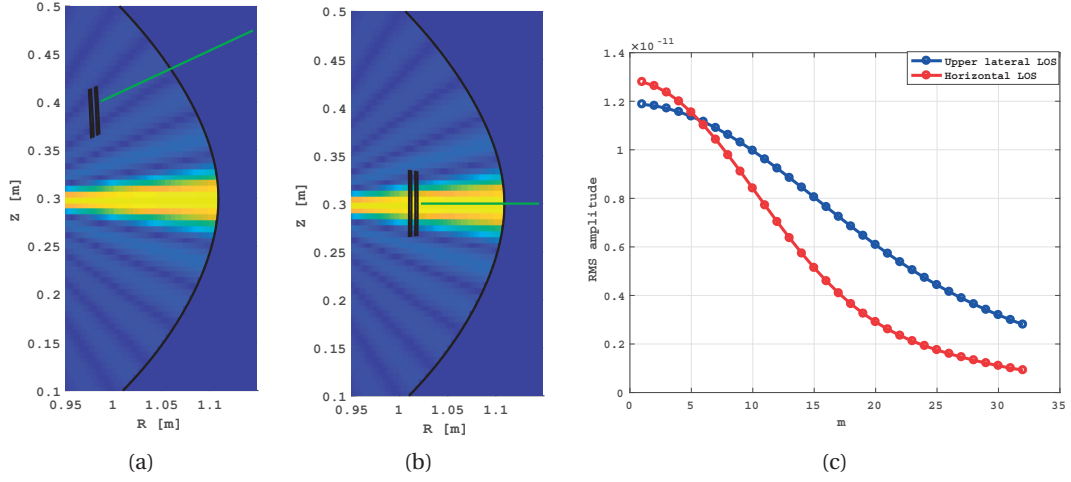


Figure D.6 – Norm of the fluctuating field (m from 1 to 32) and emission volumes for the simulation of the the upper lateral (a) and horizontal (b) lines of sight looking at  $\rho_\psi = 0.7$ . (c) Estimated sensitivity to the different modes for the two lines of sight.

to the horizontal one but, as m grows, it becomes relatively more and more sensitive. This simple model provides a possible explanation for the different fluctuation levels that have been observed in the experiments reported in paragraphs 4.2 and 4.3. The higher level of fluctuations measured when using the upper lateral line of sight in extremely similar plasmas is a consequence of its better spatial resolution (i.e. smaller spot size in the plasma). These results have already been shown in figure 4.22, but are reproduced in figure D.6 for convenience.

#### D.3.3 Effects of positive and negative $\delta$ equilibria on wavenumber sensitivity

Simulations have also been run using the equilibria and profiles of the pair of positive and negative  $\delta$  discharges introduced in paragraph 4.3. The goal was to see if the difference in equilibria and flux surface compression of positive and negative triangularity discharges has an influence on the detection of fluctuating structures of different size. Also in this case the horizontal line of sight was simulated (this time at the vessel midplane), with two channels separated by 500 MHz around  $\rho_\psi = 0.7$ . The emission volumes and the norm of the fluctuating field over the two plasma cross sections are shown in figures D.7a and D.7b. The differences in relative sensitivity to modes of different order, for positive and negative  $\delta$  plasmas, shown in figure D.7c, are very small. It is interesting to notice that experimentally measured fluctuations in negative  $\delta$  are significantly lower than in positive  $\delta$  plasmas even though the former shows  $\sim 20\%$  higher sensitivity to low order modes. It can then be excluded that different sensitivity of the diagnostic to modes of different sizes can be the source of the difference in fluctuations amplitude measured experimentally between positive and negative  $\delta$  plasmas.

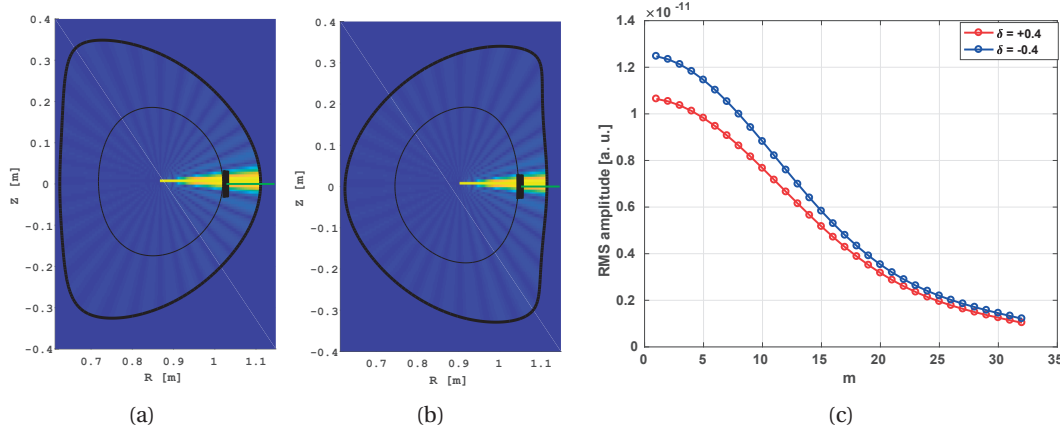


Figure D.7 – Norm of a superposition of modes with  $m$  going from 1 to 32 from equation D.3 with  $A_0(R, Z) = 1$  over the equilibria of positive (a) and negative (b)  $\delta$  plasmas, together with the simulated emission volumes. (c) Fluctuations amplitude of modes of order  $m$  obtained in the two cases.

## D.4 Conclusions

A simple model for studying the sensitivity of the different lines of sight available to the CECE diagnostic of TCV has been developed. The diagnostic is modelled taking into account as closely as possible the true characteristics of its optics and radiometer. Using this model, it has been possible to highlight the detrimental effects of wider antenna patterns on the diagnostic sensitivity to small fluctuating structures. Very good agreement has been found between these simulations and the model in [8]. The sensitivities of the horizontal and upper lateral lines of sight have been compared using this method, finding that, using the latter, smaller modes are better detected. This is in qualitative agreement with the experimental results presented in chapter 4. Simulations of identical fluctuating structures in positive and negative triangularity plasmas show that the diagnostic should present similar sensitivity to modes in both shapes. Diagnostic effects alone, related to differences in the equilibria and flux surfaces compression, thus can not explain the strong reduction in fluctuations amplitude observed in chapters 4 and 6.

While the simple model of fluctuations developed in this chapter is certainly insufficient to describe a realistic turbulent configuration inside a tokamak plasma, it allows to study the influence of the fluctuating structures size on the CECE sensitivity.

# Bibliography

- [1] J.-M. Moret, F. Buhlmann, D. Fasel, F. Hofmann, and G. Tonetti. Magnetic measurements on the TCV Tokamak. *Review of Scientific Instruments*, 69(6):2333–2348, June 1998.
- [2] Claudio Marini. *Poloidal CX visible light rotation diagnostics in TCV*. PhD thesis, EPFL, 2017.
- [3] Y. Camenen, A. Pochelon, R. Behn, A. Bottino, A. Bortolon, S. Coda, A. Karpushov, O. Sauter, G. Zhuang, and the TCV team. Impact of plasma triangularity and collisionality on electron heat transport in TCV L-mode plasmas. *Nucl. Fusion*, 47(7):510, 2007.
- [4] A. Marinoni, S. Brunner, Y. Camenen, S. Coda, J. P. Graves, X. Lapillonne, A. Pochelon, O. Sauter, and L. Villard. The effect of plasma triangularity on turbulent transport: modeling TCV experiments by linear and non-linear gyrokinetic simulations. *Plasma Phys. Control. Fusion*, 51(5):055016, 2009.
- [5] O. Sauter, S. Brunner, D. Kim, G. Merlo, R. Behn, Y. Camenen, S. Coda, B. P. Duval, L. Federspiel, T. P. Goodman, A. Karpushov, A. Merle, and Tcv Team. On the non-stiffness of edge transport in L-mode tokamak plasmas. *Physics of Plasmas*, 21(5):055906, May 2014.
- [6] G. Merlo, S. Brunner, O. Sauter, Y. Camenen, T. Görler, F. Jenko, A. Marinoni, D. Told, and L. Villard. Investigating profile stiffness and critical gradients in shaped TCV discharges using local gyrokinetic simulations of turbulent transport. *Plasma Phys. Control. Fusion*, 57(5):054010, 2015.
- [7] Zhouji Huang. *Experimental study of plasma turbulence in the TCV tokamak*. PhD thesis, EPFL, 2017.
- [8] R. Bravenec and A. Wootton. Effects of limited spatial resolution on fluctuation measurements (invited). *Review of Scientific Instruments*, 66(1):802–805, January 1995.
- [9] J. D. Lawson. Some Criteria for a Power Producing Thermonuclear Reactor. *Proc. Phys. Soc. B*, 70(1):6, 1957.
- [10] John Wesson. *Tokamaks*. International Series of Monographs on Physics. Oxford University Press, Oxford, New York, fourth edition edition, October 2011.

## Bibliography

---

- [11] S. Coda, T. P. Goodman, M. A. Henderson, F. Hofmann, Z. A. Pietrzyk, O. Sauter, S. Alberti, C. Angioni, K. Appert, R. Behn, P. Blanchard, P. Bosshard, R. Chavan, A. Degeling, B. P. Duval, D. Fasel, A. Favre, I. Furno, P. Gomez, P. Gorgerat, J.-P. Hogge, P.-F. Isoz, B. Joye, P. Lavanchy, J. B. Lister, X. Llobet, J.-C. Magnin, A. Manini, B. Marlétaz, P. Marmillod, Y. Martin, An Martynov, J.-M. Mayor, J. Mlynar, J.-M. Moret, P. Nikkola, P. J. Paris, A. Perez, Y. Peysson, R. A. Pitts, A. Pochelon, H. Reimerdes, J. H. Rommers, E. Scavino, A. Sushkov, G. Tonetti, M. Q. Tran, H. Weisen, and A. Zabolotsky. High-power ECH and fully non-inductive operation with ECCD in the TCV tokamak. *Plasma Phys. Control. Fusion*, 42(12B):B311, 2000.
- [12] T. C. Luce. An analytic functional form for characterization and generation of axisymmetric plasma boundaries. *Plasma Phys. Control. Fusion*, 55(9):095009, 2013.
- [13] R. L. Miller and R. W. Moore. Shape Optimization of Tokamak Plasmas to Localized Magnetohydrodynamic Modes. *Phys. Rev. Lett.*, 43(11):765–768, September 1979.
- [14] F. Troyon, R. Gruber, H. Saurenmann, S. Semenzato, and S. Succi. MHD-Limits to Plasma Confinement. *Plasma Phys. Control. Fusion*, 26(1A):209, 1984.
- [15] S. A. Sabbagh, A. C. Sontag, J. M. Bialek, D. A. Gates, A. H. Glasser, J. E. Menard, W. Zhu, M. G. Bell, R.E. Bell, A. Bondeson, C. E. Bush, J. D. Callen, M. S. Chu, C. C. Hegna, S. M. Kaye, L. L. Lao, B. P. LeBlanc, Y.Q. Liu, R. Maingi, D. Mueller, K. C. Shaing, D. Stutman, K. Tritz, and C. Zhang. Resistive wall stabilized operation in rotating high beta NSTX plasmas. *Nucl. Fusion*, 46(5):635, 2006.
- [16] A. Pochelon, T. P. Goodman, M. Henderson, C. Angioni, R. Behn, S. Coda, F. Hofmann, J.-P. Hogge, N. Kirneva, A. A. Martynov, J.-M. Moret, Z. A. Pietrzyk, F. Porcelli, H. Reimerdes, J. Rommers, E. Rossi, O. Sauter, M. Q. Tran, H. Weisen, S. Alberti, S. Barry, P. Blanchard, P. Bosshard, R. Chavan, B. P. Duval, Y.V. Esipchuck, D. Fasel, A. Favre, S. Franke, I. Furno, P. Gorgerat, P.-F. Isoz, B. Joye, J. B. Lister, X. Llobet, J.-C. Magnin, P. Mandrin, A. Manini, B. Marlétaz, P. Marmillod, Y. Martin, J.-M. Mayor, J. Mlynar, C. Nieswand, P. J. Paris, A. Perez, R. A. Pitts, K. A. Razumova, A. Refke, E. Scavino, A. Sushkov, G. Tonetti, F. Troyon, W. Van Toledo, and P. Vyas. Energy confinement and MHD activity in shaped TCV plasmas with localized electron cyclotron heating. *Nucl. Fusion*, 39(11Y):1807, 1999.
- [17] J.-M. Moret, S. Franke, H. Weisen, M. Anton, R. Behn, B. P. Duval, F. Hofmann, B. Joye, Y. Martin, C. Nieswand, Z. A. Pietrzyk, and W. van Toledo. Influence of Plasma Shape on Transport in the TCV Tokamak. *Phys. Rev. Lett.*, 79(11):2057–2060, September 1997.
- [18] A. J. Wootton, B. A. Carreras, H. Matsumoto, K. McGuire, W. A. Peebles, Ch. P. Ritz, P. W. Terry, and S. J. Zweben. Fluctuations and anomalous transport in tokamaks. *Physics of Fluids B: Plasma Physics*, 2(12):2879–2903, December 1990.

- 
- [19] G. Giruzzi, R. F. Steimle, D. R. Roberts, D. Sing, and A. J. Wootton. Identification and measurement of core plasma turbulence by observation of fast electrons in TEXT-U. *Plasma Phys. Control. Fusion*, 38(9):1593, 1996.
- [20] Ch. P. Ritz, H. Lin, T. L. Rhodes, and A. J. Wootton. Evidence for confinement improvement by velocity-shear suppression of edge turbulence. *Phys. Rev. Lett.*, 65(20):2543–2546, November 1990.
- [21] W. L. Rowan, C. C. Klepper, C. P. Ritz, R. D. Bengtson, K. W. Gentle, P. E. Phillips, T. L. Rhodes, B. Richards, and A. J. Wootton. Global particle confinement in the Texas Experimental Tokamak. *Nucl. Fusion*, 27(7):1105, 1987.
- [22] S. Coda and The TCV team. Overview of the TCV tokamak program: scientific progress and facility upgrades. *Nucl. Fusion*, 57(10):102011, 2017.
- [23] Y. Camenen, A. Pochelon, A. Bottino, S. Coda, F. Ryter, O. Sauter, R. Behn, T. P. Goodman, M. A. Henderson, A. Karpushov, L. Porte, and G. Zhuang. Electron heat transport in shaped TCV L-mode plasmas. *Plasma Phys. Control. Fusion*, 47(11):1971, 2005.
- [24] Mike Kotschenreuther, G. Rewoldt, and W. M. Tang. Comparison of initial value and eigenvalue codes for kinetic toroidal plasma instabilities. *Computer Physics Communications*, 88(2):128–140, August 1995.
- [25] F. Jenko, W. Dorland, M. Kotschenreuther, and B. N. Rogers. Electron temperature gradient driven turbulence. *Physics of Plasmas*, 7(5):1904–1910, April 2000.
- [26] Gabriele Merlo. *Flux-tube and global grid-based gyrokinetic simulations of plasma microturbulence and comparisons with experimental TCV measurements*. PhD thesis, EPFL, 2016.
- [27] M. Kikuchi, S. Medvedev, T. Takizuka, A. Fasoli, Y. Wu, P. Diamond, X. Duan, Y. Kishimoto, K. Hanada, L. Villard, O. Sauter, S. Coda, B. Duval, H. Reimerdes, S. Brunner, G. Merlo, J. Jiang, M. Wang, M. Ni, D. Chen, H. Du, W. Duan, Y. Hou, A. Ivanov, A. Martynov, Y. Poshekhonov, Y. Ueda, L. Yan, X. Song, G. Zheng, J. Liu, K. Nagasaki, K. Imadera, K. Mishra, A. Fujisawa, K. Nakamura, H. Zushi, Mj Pueschel, X. Xu, P. Zhu, D. Told, G. Q. Li, M. Furukawa, T. Ozeki, K. Shimizu, K. Kawashima, H. Urano, M. Honda, T. Ando, and M. Kuriyama. Perspective of negative triangularity tokamak as fusion energy system. European Physical Society (EPS), January 2015.
- [28] S. Yu Medvedev, M. Kikuchi, L. Villard, T. Takizuka, P. Diamond, H. Zushi, K. Nagasaki, X. Duan, Y. Wu, A.A. Ivanov, A. A. Martynov, Yu Yu Poshekhonov, A. Fasoli, and O. Sauter. The negative triangularity tokamak: stability limits and prospects as a fusion energy system. *Nucl. Fusion*, 55(6):063013, 2015.
- [29] M. E. Austin, A. Marinoni, M. L. Walker, M. W. Brookman, J. S. deGrassie, A. W. Hyatt, G. R. McKee, C. C. Petty, T. L. Rhodes, and C. Sung. Exploration of negative triangularity discharges on DIII - D. *44th EPS conference on plasma physics*, 2017.

## Bibliography

---

- [30] A. Marinoni, M. E. Austin, M. L. Walker, E. M. Davis, A. W. Hyatt, C. C. Petty, M. Porkolab, J. C. Rost, O. Sauter, K. E. Thome, and the DIII-D Team. Reduced fluctuations in high confinement plasmas at negative triangularity on DIII-D. Prague, 2018.
- [31] Alexander N. Karpushov, René Chavan, Stefano Coda, Vladimir I. Davydenko, Frédéric Dolizy, Aleksandr N. Dranitchnikov, Basil P. Duval, Alexander A. Ivanov, Damien Fasel, Ambrogio Fasoli, Vyacheslav V. Kolmogorov, Pierre Lavanchy, Xavier Llobet, Blaise Marlétaz, Philippe Marmillod, Yves Martin, Antoine Merle, Albert Perez, Olivier Sauter, Ugo Siravo, Igor V. Shikhovtsev, Aleksey V. Sorokin, and Matthieu Toussaint. Neutral beam heating on the TCV tokamak. *Fusion Engineering and Design*, 123:468–472, November 2017.
- [32] F. Hofmann. FBT - a free-boundary tokamak equilibrium code for highly elongated and shaped plasmas. *Computer Physics Communications*, 48(2):207–221, February 1988.
- [33] F. Hofmann and G. Tonetti. Tokamak equilibrium reconstruction using Faraday rotation measurements. *Nucl. Fusion*, 28(10):1871, 1988.
- [34] J. M. Moret, B. P. Duval, H. B. Le, S. Coda, F. Felici, and H. Reimerdes. Tokamak equilibrium reconstruction code LIUQE and its real time implementation. *Fusion Engineering and Design*, 91:1–15, February 2015.
- [35] S. Barry. *The extension of the FIR interferometer of TCV to a polarimeter and measurements of the Faraday rotation caused by the poloidal magnetic field*. PhD thesis, EPFL, 1999.
- [36] J. Hawke, Y. Andrebe, R. Bertizzolo, P. Blanchard, R. Chavan, J. Decker, B. Duval, P. Lavanchy, X. Llobet, B. Marlétaz, P. Marmillod, G. Pochon, and M. Toussaint. Improving spatial and spectral resolution of TCV Thomson scattering. *J. Inst.*, 12(12):C12005, 2017.
- [37] I. H. Hutchinson. *Principles of Plasma Diagnostics*. July 2002.
- [38] G. Bekefi. *Radiation Processes in Plasmas*, 1966.
- [39] Christopher Watts. A Review of ECE Correlation Radiometry Techniques for Detection of Core Electron Temperature Fluctuations. *FST*, 52(2):176–192, August 2007.
- [40] M. Bornatici, R. Cano, O. De Barbieri, and F. Engelmann. Electron cyclotron emission and absorption in fusion plasmas. *Nucl. Fusion*, 23(9):1153, September 1983.
- [41] A. J. Lichtenberg, S. Sesnic, and A. W. Trivelpiece. Measurement of the Synchrotron Radiation Spectrum from a Hot Plasma. *Phys. Rev. Lett.*, 13(13):387–388, September 1964.
- [42] F. Engelmann and M. Curatolo. Cyclotron radiation from a rarefied inhomogeneous magnetoplasma. *Nucl. Fusion*, 13(4):497, 1973.

- 
- [43] C. M. Celata and D. A. Boyd. Cyclotron radiation as a diagnostic tool for tokamak plasmas. *Nucl. Fusion*, 17(4):735, 1977.
- [44] A. E. Costley, R. J. Hastie, J. W. M. Paul, and J. Chamberlain. Electron Cyclotron Emission from a Tokamak Plasma: Experiment and Theory. *Phys. Rev. Lett.*, 33(13):758–761, September 1974.
- [45] S. Schmuck, J. Fessey, T. Gerbaud, B. Alper, M. N. A. Beurskens, E. de la Luna, A. Sirinelli, and M. Zerbini. Electron cyclotron emission measurements on JET: Michelson interferometer, new absolute calibration, and determination of electron temperature. *Review of Scientific Instruments*, 83(12):125101, December 2012.
- [46] H. J. Hartfuss, T. Geist, and M. Hirsch. Heterodyne methods in millimetre wave plasma diagnostics with applications to ECE, interferometry and reflectometry. *Plasma Phys. Control. Fusion*, 39(11):1693, 1997.
- [47] G. Cima. Correlation properties of black-body radiation in the context of the electron cyclotron emission of a magnetized plasma. *Il Nuovo Cimento D*, 16(4):359–364, April 1994.
- [48] G. Cima. Core temperature fluctuations and related heat transport in the Texas Experimental Tokamak-Upgrade. *Physics of Plasmas*, 2(3):720–726, March 1995.
- [49] H. J. Hartfuß, M. Häse, C. Watts, M. Hirsch, T. Geist, and the W7-AS Team. Temperature fluctuation measurements with ECE on W7-AS. *Plasma Phys. Control. Fusion*, 38(12A):A227, 1996.
- [50] M. Fontana, L. Porte, and P. Molina Cabrera. Correlation electron cyclotron emission diagnostic in TCV. *Review of Scientific Instruments*, 88(8):083506, August 2017.
- [51] C. Sung, A. E. White, J. H. Irby, R. Leccacorvi, R. Vieira, C. Y. Oi, W. A. Peebles, and X. Nguyen. Design of a correlation electron cyclotron emission diagnostic for Alcator C-Mod. *Review of Scientific Instruments*, 83(10):10E311, July 2012.
- [52] S. J. Freethy, G. D. Conway, I. Classen, A. J. Creely, T. Happel, A. Köhn, B. Vanovac, and A. E. White. Measurement of turbulent electron temperature fluctuations on the ASDEX Upgrade tokamak using correlated electron cyclotron emission. *Review of Scientific Instruments*, 87(11):11E102, November 2016.
- [53] A. E. White, L. Schmitz, W. A. Peebles, T. A. Carter, T. L. Rhodes, E. J. Doyle, P. A. Gourdain, J. C. Hillesheim, G. Wang, C. Holland, G. R. Tynan, M. E. Austin, G. R. McKee, M. W. Shafer, K. H. Burrell, J. Candy, J. C. DeBoo, R. Prater, G. M. Staebler, R. E. Waltz, and M. A. Makowski. A correlation electron cyclotron emission diagnostic and the importance of multifield fluctuation measurements for testing nonlinear gyrokinetic turbulence simulations. *Review of Scientific Instruments*, 79(10):103505, October 2008.



## Bibliography

---

- [54] Y. Kogi, T. Higashi, N. Tamura, H. Tsuchiya, D. Kuwahara, Y. Nagayama, A. Mase, K. Takehara, and T. Tokuzawa. Observation of electron temperature turbulence with a correlation electron cyclotron emission radiometer on LHD. *J. Inst.*, 11(01):C01072, 2016.
- [55] T. D. Rempel, R. F. Gandy, and A. J. Wootton. Density fluctuation effects on electron cyclotron emission correlation measurements in optically gray plasmas. *Review of Scientific Instruments*, 65(6):2044–2048, June 1994.
- [56] C. Janicki. Electron temperature measurement from the ECE diagnostics in tokamak plasmas under transient conditions. *Nucl. Fusion*, 33(3):513, 1993.
- [57] R. Behn, J. H. Rommers, R. A. Pitts, Z. A. Pietrzyk, R. Chavan, and B. Marletaz. A Thomson scattering diagnostic for measurements in the divertor region of TCV. *Review of Scientific Instruments*, 70(1):768–771, January 1999.
- [58] I. Klimanov, L. Porte, S. Alberti, P. Blanchard, A. Fasoli, and T. P. Goodman. Electron cyclotron emission spectrometry on the Tokamak à Configuration Variable. *Review of Scientific Instruments*, 76(9):093504, September 2005.
- [59] P. Blanchard, S. Alberti, S. Coda, H. Weisen, P. Nikkola, and I. Klimanov. High field side measurements of non-thermal electron cyclotron emission on TCV plasmas with ECH and ECCD. *Plasma Phys. Control. Fusion*, 44(10):2231, October 2002.
- [60] W. W. Eshetua, L. Porte, A. Fasoli, O. Sauter, S. Coda, T. P. Goodman, and The TCV Team. Vertical Electron Cyclotron Emission Diagnostic for TCV Plasmas. *EPJ Web of Conferences*, 32:03011, 2012.
- [61] T. C. Luce, P. C. Efthimion, and N. J. Fisch. Superthermal electron distribution measurements from polarized electron cyclotron emission (invited). *Review of Scientific Instruments*, 59(8):1593–1598, August 1988.
- [62] T. P. Goodman, V. S. Udintsev, I. Klimanov, A. Mueck, O. Sauter, and C. Schlatter. First Measurements of Oblique ECE with a Real-Time Movable Line of Sight on TCV. *FST*, 53(1):196–207, January 2008.
- [63] Miguel Silva, Timothy Goodman, Federico Felici, and Laurie Porte. Fast polarizers installation for ECRH and ECE in TCV. *Fusion Engineering and Design*, 86(6–8):1256–1259, October 2011.
- [64] Federico Felici. ECPOL: equations and Matlab tools for EC wave reflection and polarization calculations. Technical Report 174984, EPFL-CRPP, 2012.
- [65] P. Molina Cabrera, S. Coda, L. Porte, N. Offeddu, P. Lavanchy, M. Silva, and M. Toussaint. V-band Doppler backscattering diagnostic in the TCV tokamak. *Review of Scientific Instruments*, 89(8):083503, August 2018.



- 
- [66] A. E. White, W. A. Peebles, and T. L. Rhodes. Measurements of the cross-phase angle between density and electron temperature fluctuations and comparison with gyrokinetic simulations. *Physics of Plasmas*, 17(5):056103, March 2010.
- [67] K. Matsuda. Ray tracing study of the electron cyclotron current drive in DIII-D using 60 GHz. *IEEE Transactions on Plasma Science*, 17(1):6–11, February 1989.
- [68] Ronald H. Cohen. Effect of trapped electrons on current drive. *The Physics of Fluids*, 30(8):2442–2449, August 1987.
- [69] P. Welch. The use of fast Fourier transform for the estimation of power spectra: A method based on time averaging over short, modified periodograms. *IEEE Transactions on Audio and Electroacoustics*, 15(2):70–73, June 1967.
- [70] Motoki Nakata, Masanori Nunami, Hideo Sugama, and Tomo-Hiko Watanabe. Isotope Effects on Trapped-Electron-Mode Driven Turbulence and Zonal Flows in Helical and Tokamak Plasmas. *Phys. Rev. Lett.*, 118(16):165002, April 2017.
- [71] Julius S. Bendat and Allan G. Pierson. *Random Data: Analysis and Measurement Procedures*. Wiley, 1971.
- [72] R. E. Waltz, G. M. Staebler, W. Dorland, G. W. Hammett, M. Kotschenreuther, and J. A. Konings. A gyro-Landau-fluid transport model. *Physics of Plasmas*, 4(7):2482–2496, July 1997.
- [73] A. Bottino, A. G. Peeters, O. Sauter, J. Vaclavik, and L. Villard. Simulations of global electrostatic microinstabilities in ASDEX Upgrade discharges. *Physics of Plasmas*, 11(1):198–206, December 2003.
- [74] X. Garbet, P. Mantica, F. Ryter, G. Cordey, F. Imbeaux, C. Sozzi, A. Manini, E. Asp, V. Parail, R. Wolf, and the JET EFDA Contributors. Profile stiffness and global confinement. *Plasma Phys. Control. Fusion*, 46(9):1351, 2004.
- [75] E. D. Fredrickson, J. D. Callen, K. McGuire, J. D. Bell, R. J. Colchin, P. C. Efthimion, K. W. Hill, R. Izzo, D.R. Mikkelsen, D. A. Monticello, V. Paré, G. Taylor, and M. Zarnstorff. Heat pulse propagation studies in TFTR. *Nucl. Fusion*, 26(7):849, 1986.
- [76] J. Stober, O. Gruber, A. Kallenbach, V. Mertens, F. Ryter, A. Stäbler, W. Suttrop, W. Treutler, and the ASDEX Upgrade Team. Effects of triangularity on confinement, density limit and profile stiffness of H-modes on ASDEX upgrade. *Plasma Phys. Control. Fusion*, 42(5A):A211, 2000.
- [77] J. W. Hughes, B. LaBombard, J. Terry, A. Hubbard, and B. Lipschultz. Edge profile stiffness and insensitivity of the density pedestal to neutral fuelling in Alcator C-Mod edge transport barriers. *Nucl. Fusion*, 47(8):1057, 2007.
- [78] B. J. D. Tubbing, N. J. Lopes Cardozo, and M. J. Van der Wiel. Tokamak heat transport – a study of heat pulse propagation in JET. *Nucl. Fusion*, 27(11):1843, 1987.

## Bibliography

---

- [79] L. Porte, S. Coda, C. A de Mejere, Z. Huang, P. Hennequin, A. Kramer-Flecken, L. Vermare, V. Vuille, S. Brunner, J. Dominsky, F. Margairaz, G. Merlo, T. Vernay, and L. Villard. Multi-Diagnostic Study of Core Turbulence and Geodesic Acoustic Modes in the TCV Tokamak. *Proceedings of the 25th IAEA FEC*, October 2014.
- [80] Alessandro Bortolon. Plasma rotation and momentum transport studies in the TCV tokamak based on charge exchange spectroscopy measurements. 2009.
- [81] H. Reimerdes, A. Pochelon, O. Sauter, T. P. Goodman, M. A. Henderson, and An Martynov. Effect of triangular and elongated plasma shape on the sawtooth stability. *Plasma Phys. Control. Fusion*, 42(6):629, 2000.
- [82] M. E. Austin, R. F. Ellis, and T. C. Luce. Determination of wall reflectivity for ECE frequencies in DIII-D. Article, January 1997.
- [83] P. W. Terry. Suppression of turbulence and transport by sheared flow. *Rev. Mod. Phys.*, 72(1):109–165, January 2000.
- [84] Mitsuru Kikuchi, Tomonori Takizuka, and Masaru Furukawa. Negative Triangularity as a Possible Tokamak Scenario. In *Proceedings of the 12th Asia Pacific Physics Conference (APPC12)*, volume 1 of *JPS Conference Proceedings*. Journal of the Physical Society of Japan, March 2014.
- [85] R. A. Pitts, S. Carpentier, F. Escourbiac, T. Hirai, V. Komarov, S. Lisgo, A. S. Kukushkin, A. Loarte, M. Merola, A. Sashala Naik, R. Mitteau, M. Sugihara, B. Bazylev, and P. C. Stangeby. A full tungsten divertor for ITER: Physics issues and design status. *Journal of Nuclear Materials*, 438:S48–S56, July 2013.
- [86] A. Loarte, B. Lipschultz, A. S. Kukushkin, G. F. Matthews, P. C. Stangeby, N. Asakura, G. F. Counsell, G. Federici, A. Kallenbach, K. Krieger, A. Mahdavi, V. Philipps, D. Reiter, J. Roth, J. Strachan, D. Whyte, R. Doerner, T. Eich, W. Fundamenski, A. Herrmann, M. Fenstermacher, P. Ghendrih, M. Groth, A. Kirschner, S. Konoshima, B. LaBombard, P. Lang, A. W. Leonard, P. Monier-Garbet, R. Neu, H. Pacher, B. Pegourie, R.A. Pitts, S. Takamura, J. Terry, E. Tsitrone, the ITPA Scrape-off Layer, and Divertor Physics Topical Group. Chapter 4: Power and particle control. *Nucl. Fusion*, 47(6):S203, 2007.
- [87] F. Wagner, G. Becker, K. Behringer, D. Campbell, A. Eberhagen, W. Engelhardt, G. Fussmann, O. Gehre, J. Gernhardt, G. v. Gierke, G. Haas, M. Huang, F. Karger, M. Keilhacker, O. Klüber, M. Kornherr, K. Lackner, G. Lisitano, G. G. Lister, H. M. Mayer, D. Meisel, E. R. Müller, H. Murmann, H. Niedermeyer, W. Poschenrieder, H. Rapp, H. Röhr, F. Schneider, G. Siller, E. Speth, A. Stäbler, K. H. Steuer, G. Venus, O. Vollmer, and Z. Yü. Regime of Improved Confinement and High Beta in Neutral-Beam-Heated Divertor Discharges of the ASDEX Tokamak. *Phys. Rev. Lett.*, 49(19):1408–1412, November 1982.
- [88] H. Zohm. Edge localized modes (ELMs). *Plasma Phys. Control. Fusion*, 38(2):105, 1996.

- 
- [89] A. Pochelon, P. Angelino, R. Behn, S. Brunner, S. Coda, N. Kirneva, S. Yu Medvedev, H. Reimerdes, J. Rossel, O. Sauter, L. Villard, D. Wagner, A. Bottino, Y. Camenen, G. P. Canal, P. K. Chattopadhyay, B. P. Duval, A. Fasoli, T. P. Goodman, S. Jolliet, A. Karpushov, B. Labit, A. Marinoni, J.-M. Moret, A. Pitzschke, L. Porte, M. Rancic, V. S. Udintsev, and the TCV Team. Recent TCV Results - Innovative Plasma Shaping to Improve Plasma Properties and Insight. *Plasma and Fusion Research*, 7:2502148–2502148, 2012.
  - [90] A. Merle, O. Sauter, and S. Yu Medvedev. Pedestal properties of H-modes with negative triangularity using the EPED-CH model. *Plasma Phys. Control. Fusion*, 59(10):104001, 2017.
  - [91] M. Faitsch, R. Maurizio, A. Gallo, S. Coda, T. Eich, B. Labit, A. Merle, H. Reimerdes, B. Sieglin, C. Theiler, the Eurofusion MST1 Team, and the TCV Team. Dependence of the L-Mode scrape-off layer power fall-off length on the upper triangularity in TCV. *Plasma Phys. Control. Fusion*, 60(4):045010, 2018.
  - [92] Fabio Riva, Emmanuel Lanti, Sébastien Jolliet, and Paolo Ricci. Plasma shaping effects on tokamak scrape-off layer turbulence. *Plasma Phys. Control. Fusion*, 59(3):035001, 2017.
  - [93] M. Fontana, L. Porte, S. Coda, O. Sauter, and The TCV Team. The effect of triangularity on fluctuations in a tokamak plasma. *Nucl. Fusion*, 58(2):024002, 2018.
  - [94] G. M. Staebler, J. E. Kinsey, and R. E. Waltz. A theory-based transport model with comprehensive physics. *Physics of Plasmas*, 14(5):055909, May 2007.
  - [95] G. V. Pereverzev and P. N. Yushmanov. ASTRA - Automated System for TRansport Analysis. Technical Report IPP report, Max-Planck-Institut Für Plasmaphysik, 2002.
  - [96] L. Schmitz, A. E. White, T. A. Carter, W. A. Peebles, T. L. Rhodes, K. H. Burrell, W. Solomon, and G. M. Staebler. Observation of Reduced Electron-Temperature Fluctuations in the Core of H-Mode Plasmas. *Phys. Rev. Lett.*, 100(3):035002, January 2008.
  - [97] A. E. White, M. Barnes, A. Dominguez, M. Greenwald, N. T. Howard, A. E. Hubbard, J. W. Hughes, D. R. Mikkelsen, F. I. Parra, M. L. Reinke, C. Sung, J. Walk, and D. G. Whyte. Reduction of core turbulence in I-mode plasmas in Alcator C-Mod. *Nucl. Fusion*, 54(8):083019, 2014.
  - [98] Alexander N. Karpushov. Estimation of metal injection/deposition/accumulation in the TCV vacuum vessel from heating neutral beam. Technical report, 2018.
  - [99] O. Sauter, C. Angioni, and Y. R. Lin-Liu. Neoclassical conductivity and bootstrap current formulas for general axisymmetric equilibria and arbitrary collisionality regime. *Physics of Plasmas*, 6(7):2834–2839, June 1999.
  - [100] O. Sauter, C. Angioni, and Y. R. Lin-Liu. Erratum: “Neoclassical conductivity and bootstrap current formulas for general axisymmetric equilibria and arbitrary collisionality

## Bibliography

---

- regime” [Phys. Plasmas 6, 2834 (1999)]. *Physics of Plasmas*, 9(12):5140–5140, November 2002.
- [101] A.e. White, W.a. Peebles, T.l. Rhodes, G. Wang, L. Schmitz, T.a. Carter, J.c. Hillesheim, E.j. Doyle, L. Zeng, C.h. Holland, G.r. McKee, G.m. Staebler, R.e. Waltz, J. Candy, J.c. DeBOO, C.c. Petty, and K.h. Burrell. Correlation ece measurements of turbulent electron temperature fluctuations in diii-d. In *Electron Cyclotron Emission and Electron Cyclotron Resonance Heating (EC-16)*, pages 168–173. WORLD SCIENTIFIC, February 2011.
- [102] F. Ryter, C. Angioni, A. G. Peeters, F. Leuterer, H.-U. Fahrbach, W. Suttrop, and ASDEX Upgrade Team. Experimental Study of Trapped-Electron-Mode Properties in Tokamaks: Threshold and Stabilization by Collisions. *Phys. Rev. Lett.*, 95(8):085001, August 2005.
- [103] J. C. Hillesheim, J. C. DeBoo, W. A. Peebles, T. A. Carter, G. Wang, T. L. Rhodes, L. Schmitz, G. R. McKee, Z. Yan, G. M. Staebler, K. H. Burrell, E. J. Doyle, C. Holland, C. C. Petty, S. P. Smith, A. E. White, and L. Zeng. Observation of a Critical Gradient Threshold for Electron Temperature Fluctuations in the DIII-D Tokamak. *Phys. Rev. Lett.*, 110(4):045003, January 2013.
- [104] C. Angioni, T. P. Goodman, M. A. Henderson, and O. Sauter. Effects of localized electron heating and current drive on the sawtooth period. *Nucl. Fusion*, 43(6):455, 2003.
- [105] ITER Physics Expert Group on Confinement and transport, ITER Physics Expert Group on Confinement Modelling and Database, and ITER Physics Basis Editors. Chapter 2: Plasma confinement and transport. *Nucl. Fusion*, 39(12):2175, 1999.
- [106] S. J. Freethy, T. Görler, A. J. Creely, G. D. Conway, T. Happel, C. Koenen, P. Hennequin, and A. E. White. Validation of gyrokinetic simulations with measurements of electron temperature fluctuations and density-temperature phase angles on ASDEX Upgrade. *Physics of Plasmas*, 25(5):055903, March 2018.
- [107] Choongki Sung. *Experimental study of turbulent heat transport in Alcator C-Mod*. Thesis, Massachusetts Institute of Technology, 2015.
- [108] H. Lütjens, A. Bondeson, and O. Sauter. The CHEASE code for toroidal MHD equilibria. *Computer Physics Communications*, 97(3):219–260, September 1996.
- [109] O. Sauter and S. Yu. Medvedev. Tokamak coordinate conventions: COCOS. *Computer Physics Communications*, 184(2):293–302, February 2013.
- [110] D. Testa, C. Giroud, A. Fasoli, and K.-D. Zastrow. On the measurement of toroidal rotation for the impurity and the main ion species on the Joint European Torus. *Physics of Plasmas*, 9(1):243–250, December 2001.

# Matteo FONTANA

## PERSONAL DATA

---

PLACE AND DATE OF BIRTH: Italy, 09 March 1989  
CURRENT ADDRESS: 29, Chemin des Abbesses, Lonay-1027, Switzerland  
PHONE: +39 3490877649  
EMAIL: [matteo.fontana@epfl.ch](mailto:matteo.fontana@epfl.ch)

## WORK EXPERIENCE

---

2014-Now	Physics PhD student, SWISS PLASMA CENTER, ECOLE POLYTECHNIQUE FEDERALE DE LAUSANNE, Switzerland. "Turbulence characterization with Correlation Emission Cyclotron Diagnostic on TCV" Experience in plasma microwave diagnostics operation and data analysis Teaching assistant for General physics and Human Sciences bachelor courses
----------	---

## EDUCATION

---

2014	Master in NUCLEAR ENGINEERING, Politecnico of Milan, Italy. 110/110 cum laude
2011	Bachelor in MATERIALS AND NANOTECHNOLOGY ENGINEERING, Politecnico of Milan, Italy. 110/110 cum laude

## AWARDS

---

2017	Kyushu University Itoh Project Prize November 2017, trip to Japan where I presented a talk titled: "Triangularity effects on fluctuations" at Kyushu University and NIFS
2013	International Engineering Competition, Calgary, Canada "Engineering Impact Award"; 2 <sup>nd</sup> place in Case Study category
2012	European BEST Engineering Competition, Zagreb, Croatia 1 <sup>st</sup> place in Italian finals, "Case Study" category, Naples, Italy

## SELECTED PUBLICATIONS

---

M. Fontana et al., *The effect of triangularity on fluctuations in a tokamak plasma*, Nuclear Fusion, **58**, 2, 2018

M. Fontana et al., *Correlation electron cyclotron emission diagnostic in TCV*, Review of Scientific Instruments, **88**, 2017

## PERSONAL SKILLS

---

LANGUAGES	ITALIAN: native    ENGLISH: fluent (TOEFL C2)    FRENCH: fluent
ORGANIZATION	Used to teamwork, team managing and deadlines, excellent learning skills
COMMUNICATION	Experienced in public speaking (engineering competitions, seminars)
INFORMATICS	Excellent use of: Linux, Ubuntu, <del>La</del> TEX, Office package (ECDL 2007), Good programming skills on Matlab. Basics of Python



# Acknowledgements

It is safe to say that this PhD would not have been possible if not for the help of many individuals. What I have achieved in these four years is largely thanks to you.

First of all I want to mention Laurie and Ambrogio. Laurie has been a very dedicated supervisor, always available for discussion even when I was troubled by the stupidest issue. He quite literally taught me everything I know about microwave technology and if I will continue working in this field it is undoubtedly his merit (or fault, depending on the outcome). Ambrogio too, despite all of his other responsibilities, was genuinely interested in what I was working on and always ready to advise and guide me when necessary. I also have to thank Ambrogio and Ivo for having me working with you in the Global Issues course. Not only the course itself was really interesting but it was nice to discuss these topics with you and work more directly with the students compared with other classes.

Thanks also to Prof. Anne White and Dr. Tim Happel for having participated to my private defence with many interesting and insightful suggestions, really making it into a great growing opportunity for me.

Together with my supervisors, there have been many other members of the scientific SPC staff I have been consistently helped by: Stefano, Olivier, Stephan, Ivo, Antoine, Alexander, Duccio, Laurent, just to name a few. The possibility of asking for informations, advice or even just an opinion at any time and to anyone is, for me, one of the most valuable things here at SPC.

Being an experimental physicist that has spent quite a lot of hours in the control room, I am very much in debt with all the people that make TCV run, including all physics, gyrotrons, beam operators, diagnosticians, informatics, control people, engineers and the ateliers. I have bothered each and everyone of you multiple times for, quite literally, years. Thank you for your help! Merci beaucoup!

Thanks to Gabriele and Ajay who help me immensely with the GENE simulations. If it were not for you this thesis would be a bit shorter indeed.

During these four years the SPC has been for me an incredible environment, full of the kindest, funniest people around: always ready to help and joke and help some more when needed. My first years here would not have been the same without some of the older PhD students (now

## Acknowledgements

---

doctors) and I owe sincere gratitude to all of them. Thank you Gabriele (again), Federico and Claudio for the great help each of you has given me during these four years, for the evenings spent together and for the many 'una birra solo una'.

Thanks to all those that during these years were part of PPH 277, clearly the best office of SPC: Jeremy the SGALSPC, Dahye, Hugo, Roberto, Federico, Rogerio, Emmanuel, Noé, Zhouji, Himank, Falk, Joseph, together with Samuel and Stéphane (by adoption).

Thanks to everyone that really helped making these four memorable years: Francesco, Nico, Lorenzo, Paola, Oulfa, Umar, Hamish, Pedro, Kevin, Dario, Filippo, Avelino, Philippe, Maurizio, Eduardo, André, Alberto, Arsène and so many others that I am losing count already. Thanks to all of you.

Grazie di cuore ad Aberto, il mio dottorato non sarebbe stato lo stesso senza le tue visite qui a Losanna. Proprio un assaggio di altri tempi.

Grazie a Lobia, Mare, Sappi e Mattia, compagni di avventura che, in tutti questi anni, non hanno mai smesso di interessarsi alle storie che avevo da raccontare insieme a loro.

Grazie a Giorgio, Arianna, Claudio, Eleonora, Anna, Giovanni e tutti gli altri amici che ogni weekend aiutavano a buttare via la stanchezza.

Grazie a Red e Silvio. Potere giocare con voi ancora dopo 25 anni (!) è una gioia vera.

Grazie Nicolò ed Anna. Anche dopo esser partiti siete sempre i più vicini.

Grazie ai miei genitori per la pazienza infinita e il supporto in ogni momento. Se davvero il compito dei genitori è dare ai figli ali e radici direi che dovrete proprio essere fieri del lavoro che avete fatto.

Grazie a Marta per le attenzioni e la cura che mi hai dedicato in questi anni. In quattro anni non c'è stato un giorno in cui non abbia sentito il tuo amore. Grazie di tutto.

*Lausanne, 10 October 2018*

Matteo



